



HAL
open science

Channel optical chirowaveguides for enantioselective sensors

Hoshang Sahib

► **To cite this version:**

Hoshang Sahib. Channel optical chirowaveguides for enantioselective sensors. Physics [physics]. Université de Lyon, 2022. English. NNT : 2022LYSE1134 . tel-03856102

HAL Id: tel-03856102

<https://theses.hal.science/tel-03856102>

Submitted on 16 Nov 2022

HAL is a multi-disciplinary open access archive for the deposit and dissemination of scientific research documents, whether they are published or not. The documents may come from teaching and research institutions in France or abroad, or from public or private research centers.

L'archive ouverte pluridisciplinaire **HAL**, est destinée au dépôt et à la diffusion de documents scientifiques de niveau recherche, publiés ou non, émanant des établissements d'enseignement et de recherche français ou étrangers, des laboratoires publics ou privés.



N° National de Thèse : 2022LYSE1134

THESE de DOCTORAT DE L'UNIVERSITE DE LYON
opérée au sein de
l'Université Claude Bernard Lyon 1

Ecole Doctorale N° 52
PHYSIQUE ET ASTROPHYSIQUE (PHAST)

Discipline: **Physique**

Présentée et soutenue publiquement le 13/07/2022

par: **Hoshang SAHIB**

**Channel optical chirowaveguides for
enantioselective sensors**

Sous la direction de: PROF. STÉPHAN GUY

Co-endcadrants: DR. ALBAN GASSENQ et DR. AMINA BENSALAH-LEDOUX

Devant la commission d'examen formée de :

Prof. Stéphane GUY	<i>Université Claude Bernard Lyon 1</i>	Directeur
Prof. Pascale CHANGENET	<i>Ecole Polytechnique</i>	Rapportrice
Prof. Yann BATTIE	<i>Université de Lorraine</i>	Rapporteur
Prof. Christelle MONAT	<i>École Centrale de Lyon</i>	Examinatrice
Prof. Emmanuel BENICHOU	<i>Université Claude Bernard Lyon 1</i>	Examinateur
Prof. Benoit BOULANGER	<i>Université Grenoble Alpes</i>	Examinateur



N° National de Thèse : 2022LYSE1134

THESE de DOCTORAT DE L'UNIVERSITE DE LYON

Délivré par:

l'Université Claude Bernard Lyon1

Ecole Doctorale N° 52

PHYSIQUE ET ASTROPHYSIQUE (PHAST)

Discipline: **Physique**

Laboratoire: INSTITUT LUMIÈRE MATIÈRE (ILM)

Présentée et soutenue publiquement le 13/07/2022

par: **Hoshang SAHIB**

Channel optical chirowaveguides for enantioselective sensors

Sous la direction de: PROF. STÉPHAN GUY

Co-endcadrants: DR. ALBAN GASSENQ et DR. AMINA BENSALAH-LEDOUX

Devant la commission d'examen formée de :

Prof. Stéphane GUY	<i>Université Claude Bernard Lyon 1</i>	Directeur
Prof. Pascale CHANGENET	<i>Ecole Polytechnique</i>	Rapportrice
Prof. Yann BATTIE	<i>Université de Lorraine</i>	Rapporteur
Prof. Christelle MONAT	<i>École Centrale de Lyon</i>	Examinatrice
Prof. Emmanuel BENICHOU	<i>Université Claude Bernard Lyon 1</i>	Examineur
Prof. Benoit BOULANGER	<i>Université Grenoble Alpes</i>	Examineur

Acknowledgments

First and foremost, I would like to thank **Prof. Stéphan GUY** who guided and supported me throughout this PhD. The high theoretical and experimental knowledge of Prof. Stéphan prepared me to become an independent researcher for my future career. I thank you very much Stéphan for sharing all the knowledge with me, for giving me your time, for letting me work independently and for helping me whenever I got stuck. I will never forget the hours we spent together, the advices you gave me, and your sense of humor even in the most challenging moments. When I think about leaving ILM laboratory, the first thing I regret is leaving Stephan's advices. Thanks to Stephan, I gained knowledge that I had not even imagined obtaining during these four years.

I owe my knowledge of microfabrication to my co-supervisor, **Dr. Alban GASSENQ**, who worked hard with me during the first year of my PhD. Alban taught me how to work efficiently, how to do research in a systematic way. I was always impressed with Alban's energy and efficiency when we worked together. Although after the first year we didn't do experiments together because the project moved to another stage, Alban was always there to discuss the results we were getting, the problems we were encountering, and to help me by giving me clues to understand. Thank you, Alban, for all your advices, for not giving up on me in the occasions when I didn't work as you expected.

My journey with the chirality team started with my co-supervisor, **Dr. Amina BENSALAH-LEDOUX**, who accepted me for my master's internship. I owe my PhD to Dr. Amina, when I was about to finish the master's program, I was hesitating to pursue the PhD, she was the main reason that motivated me to continue, with her guidance, any student can finish the PhD. Thank you, Amina, for all your positive advices, for checking every time that everything was fine? Thank you for encouraging me by telling me Hoshang, you will have the best thesis, I believe in you. I feel like I did a good job during this PhD, but I'm sure I wasn't as good as your efforts with me, your unmatched guidance will make anyone great. I will keep your example of kindness for my life, I will try to help all my students as you helped me.

I would also like to thank Dr. Laure GUY, known as our collaborator, but she was like my fourth supervisor. Fortunately, I had the honor to work with her at ENS Lyon doing multiple experiments. Thank you, Laure, for maintaining the chirality project with your great competence as the only chemist of the team. Thank you for making all those samples and making my PhD productive even though I was not very good at organizing the samples.

I want to thank Dr. Bruno BAGNARD for his valuable remarks during the team discussions. Many thanks to Dr. Gilles LEDOUX for his help in the realization of my experiments by letting me borrow his equipments each time I needed them. I also enjoyed the working conditions within the MNP team, everyone being always ready to help, thank you Prof. Joël BELLESSA, Dr. Antonio PEREIRA, Dr. Cécile LE LUYER, Prof. Anne PILLONNET, Dr. Jean-Michel BENOIT, Dr. Clémentine SYMONDS and the two other PhD students Vincent TOANEN and Antoine BARD. I am grateful to the members of the jury for having accepted to be the jury of my thesis, I thank you for your kind comments and remarks during the day of defense. I am particularly thankful to the two reviewers, Prof. Pascale CHANGENET and Prof. Yann BATTIE, for the time they devoted to review my manuscript.

I am very indebted to my cousin Mr. Bestoon NAKSHBANDY and his wife Mrs. Shokhan NAKSHBANDY, thank you for being the closest family and never letting us feel far from home. Your continuous support for the six years of masters and doctorate was exceptional, your lovely family will always remain in my memory. I would also like to thank Mr. Léon CARIN and his wife Mrs. Sylvie Carin for having been there every time I needed help. Thank you very much especially for your warm support even on the day of the defense of the PhD, I am very grateful to have known you.

I would like to express my deepest gratitude to my family in Iraq, my parents and my brothers (Dashty, Barham, and Sarhang). Their constant support has always accompanied me to overcome the obstacles I have encountered throughout my academic journey in France. Finally, I thank my wife Didar Abas FATAH, thank you for keeping your positive attitude through all the challenging times of a PhD student's life. Thank you for raising our two children (Haroon and Dawaa) and for taking care of me during this PhD period. I share the honor of this PhD with you, you deserve it as much as I do.

Dedication

To my father, my mother, Didar, Haroon and Dawaa.

Résumé

La photonique intégrée est une technologie qui utilise la lumière comme vecteur d'information, à la manière des signaux électriques utilisés dans les circuits intégrés électroniques. Les éléments de base de la photonique intégrée sont les guides d'ondes canaux, qui sont des structures optiques rectangulaires fabriquées sur des substrats planaires (souvent appelés puces). La symétrie planaire des puces photonique impose une biréfringence linéaire (LB) qui génère des modes propres de polarisation linéaire transverses (les modes dit TE et TM pour transverse électrique et magnétique). Cette biréfringence complique l'utilisation d'onde de polarisation non TE/TM à cause des battement de polarisation. Par conséquent, toute application nécessitant d'autres polarisations, tel que la polarisation circulaire, polarisation clé pour la détection chirale, ne peut profiter des avantages de l'optique intégrée en terme de miniaturisation et robustesse...etc. Une façon de surmonter cette limitation, est d'utiliser des guides d'ondes faits de matériaux chiraux à biréfringence circulaire (CB), connus sous le nom de guides d'ondes chiroptiques.

Dans cette thèse, nous présentons l'étude théorique, la réalisation et la caractérisation optique de guides chiroptiques canaux supportant des modes propres de polarisations autres que TE/TM. En utilisant la théorie des modes couplés, on montre que les modes propres sont polarisation elliptique dont l'ellipticité est proportionnelle au rapport CB/LB. Pour un CB donnée lié au matériau chiral, on peut donc moduler l'ellipticité des modes propres en variant LB. Des simulation numériques, basées sur cette théorie, nous ont permis de cibler les meilleures structures guidantes afin d'obtenir des modes propres de polarisation circulaire. Nous avons étudié différentes façons de produire des guides d'ondes à partir de dépôts par PLD (Pulsed Laser Deposition) et par dip-coating sol-gel de couches chirales. La microfabrication des couches déposées par PLD et la gravure par RIE des couches déposées par sol-gel n'ont pas donné de bons résultats. Nous avons alors, développé une technique d'embossage, à l'aide de moules en PDMS, sur un matériau sol-gel pour produire des guides d'ondes canaux de bonne qualité. Nous avons pu fabriquer de façon simple, des guides d'ondes canaux de différentes géométries et, par conséquent, moduler leur LB. En mettant au point un polarimètre de Stokes, la polarisation des modes guidés dans ces systèmes a été mesurée et on a pu montrer que les guides chiroptiques canaux ont bien des modes propres dont la polarisation varie de linéaire à quasi-circulaire, en fonction de leur géométrie. De ce fait, on démontre expérimentalement, que l'optique intégrée n'est plus limitée aux seules polarisations rectilignes TE et TM. De plus, nous mettons en évidence l'extrême sensibilité du matériau à l'humidité et, grâce à notre montage optique, nous identifions et quantifions avec précision les biréfringences présentes dans les guides d'ondes: contraintes de traction et de compression ainsi que contributions asymétriques. Les résultats de cette thèse ouvrent le champ d'application de la technologie photonique intégrée à tous les domaines où la polarisation circulaire est nécessaire.

Abstract

Integrated photonics is the technology that uses light as an information carrier, similar to the electrical signals used in electronic integrated circuits. Integrated photonics building blocks are channel optical waveguides that are rectangular optical structures fabricated on planar substrates (often called chips). The planar symmetry makes integrated photonics waveguides linear birefringent which imposes linearly polarized eigenmodes, namely the transverse electric (TE) and the transverse magnetic (TM) modes. This birefringence complicates the use of non-TE/TM polarized light waves due to polarization beating. As a consequence, any application requiring other polarizations, such as circular polarization (the key polarization in chiral sensing), cannot take advantage of integrated photonics technology, in terms of miniaturization, robustness, etc. . . . One way to overcome this linear birefringence (LB) limitation, is to use waveguides made of chiral materials having circular birefringence (CB), known as chirowaveguides.

In this thesis, we present the realization as well as the theoretical and experimental study of channel chirowaveguides having polarization eigenmodes other than TE/TM. Using the coupled mode theory to study the light polarization properties in chirowaveguides, we show that these waveguides have elliptically polarized eigenmodes whose ellipticity is proportional to the CB/LB ratio. For a given CB related to the chiral material, we can therefore modulate the ellipticity of the eigenmodes by varying the LB. Numerical simulations are then used to design low LB structures to obtain channel chirowaveguides with circularly polarized eigenmodes. Different microfabrication methods are investigated to fabricate channel chirowaveguides based on pulsed laser deposition and sol-gel dip coating thin films. Microfabrication of pulsed laser deposited layers and reactive ion etching of sol-gel derived layers did not give us good results. Therefore, PDMS-based imprint lithography method on the sol-gel material is developed to produce high quality channel waveguides. With this method, we were able to fabricate in a simple way, channel waveguides of different geometries and, consequently, to modulate their LB. By setting up a Stokes polarimeter, the polarization of the guided modes is measured, and we show that the channel chirowaveguides have eigenmodes with polarization varying from linear to quasi-circular, depending on their geometry. Furthermore, we put into evidence the extreme sensitivity of the sol-gel derived material to humidity and thanks to our Stokes polarimeter setup we accurately identify and quantify the birefringences arising in the waveguides: tensile and compressive stress as well as asymmetric contributions. Our experimental results demonstrate that the integrated photonics is no longer limited to the linear TE and TM polarizations modes. The results of this thesis open the field of application of integrated photonics technology to all domains where circularly polarized light is relevant.

This page intentionally left blank

List of Figures

1.1	A snapshot of the electric field oscillation of a light wave in two linear polarization states when it is a) horizontally polarized b) Vertically polarized.	6
1.2	Snapshot of a light wave having the two components E_x and E_y with a phase difference $\phi = -\frac{\pi}{2}$. It represents a right circularly polarized light wave and obeys the right hand rule. The green color traces the tip of the resulting electric field which represents the helical trajectory of a circularly polarized wave.	8
1.3	Polarization ellipse of a general (elliptically polarized) wave.	8
1.4	Graphical representation of SOP of light in 3D space (Poincaré sphere). a) The infinite states of polarization are mapped to a 3D sphere of axes S_1 , S_2 , and S_3 . Each point on the sphere surface corresponds to particular (unique) SOP. The sphere contains a graphical representation of all the SOP on its surface, with the linearly polarized states placed around the equator, and the two circularly polarized states at the poles. b) Locus of a radius vector with spherical coordinates $(DOP, 2\psi, 2\chi)$ points to particular point on the sphere that represent a polarization ellipse (inset) of ellipticity χ and azimuth ψ	16
1.5	Graphical representation of the polarization states of light in 2D space in two case of the polarization ellipse. a) Evolution of polarization azimuth ψ as a function of Stokes parameters S_2 and S_1 when ellipticity $\chi=0$ ($S_3 = 0$). b) Evolution of polarization ellipticity χ as a function of Stokes parameters S_3 and S_1 when azimuth $\psi = 0$ ($S_2=0$).	18
1.6	Poincaré sphere representation of evolution of polarization of light when propagates through a birefringence system. It is a periodic rotation on a circular orbit perpendicular to an axis connecting orthogonal eigenmodes.	20
1.7	Structure of a typical planar waveguide with z-axis as the propagation direction and step refractive index in x -axis.	21
1.8	Evolution of effective refractive index of the guided modes of a planar waveguide as a function of waveguide's thickness h , for two refractive index contrasts ($\Delta n = n_g - n_b$)	25

1.9	Birefringent effect of planar optical waveguides, Poincaré sphere representation of polarization beating for left handed circular polarization (LHCP) and linear horizontally polarization inputs.	26
1.10	Structure of a typical channel waveguide with z-axis as the propagation direction.	27
1.11	Computed guided light field components distribution in channel waveguides using a full-vector finite-difference numerical computation method for a) quasi-TE ₀₀ mode, and b) quasi-TM ₀₀ mode.	29
1.12	Top) Cross-section and Bottom) Computed guided field distribution of the fundamental mode in five types of channel waveguides.	30
1.13	Evolution of effective refractive indices of guided modes as function of width of w and height in a) diffused, b) ridge, and c) rib waveguides. The TE ₀₀ and TM ₀₀ curves intersect at the position indicated by the black circle.	31
1.14	Chiral objects a) Our hands, b) Some molecules (Amino acid), and c) Circularly polarized light.	32
1.15	Birefringent effect of bulk chiral media, Poincaré sphere representation of polarization beating for left handed circular and linear horizontally polarization inputs.	35
1.16	Behaviour of chirowaveguides deduced from coupled mode theory. a) Coupling matrix. b) Graphical representation of the coupling, it shows how the presence of chirality couples the TE/TM eigenmodes of the single mode waveguide and thus the eigenmodes of a chirowaveguide are left/right handed elliptically polarized modes (L/RHEP). c) Evolution of a chirowaveguide eigenmodes polarization ellipticity as a function of $\frac{CB}{LB}$	41
1.17	Birefringent effect of chirowaveguides, Poincaré sphere representation of polarization beating for left handed circular and linear horizontally polarization inputs.	42
1.18	Cross-section of different channel waveguides for sensing applications.	44
1.19	Evolution of LB in different types of channel waveguides as function of channel width w , height h , rib thickness d , refractive index difference $\Delta n = n_g - n_b$	44
2.1	structures of chiral molecules deposited by PLD (a) bridged binaphtol and (b) helicene like molecule.	49
2.2	Schematic representation of pulsed laser deposition setup	50
2.3	Scheme of PLD setups to control thickness homogeneity , a) homogeneity control in one axis, b) homogeneity control in both axis.	51
2.4	photograph PLD films with their 3D profile , a) Regular PLD film, b) PLD films with homogeneity in one axis, c) PLD films with in two axis.	51

2.5	Chemical structures of a) tetraethoxysilane (TEOS), and b) methyltriethoxysilane (MTEOS).	53
2.6	Chemical structure of ORMOSIL films.	54
2.7	Schematic representation of dip coating technique	55
2.8	Thickness of a single coated films obtained from a (-)P1-46%MTeos_50g/L solution as a function of dip coating withdrawal speed. The films are baked at 120°C on a hotplate for 20h.	55
2.9	Thickness and refractive index evolution of the ORMOSIL films as a function of baking time at 120°C.	56
2.10	Refractive index evolution of the ORMOSIL films measured at 543nm as a function of MTEOS/R-SiO ₂ ratio for films baked at 120°C for 20h on hotplate.	57
3.1	The principle of channel waveguide fabrication from PLD based films a) Patterned substrate b) Deposited PLD on patterned substrates. c-d) ridge and diffused PLD channel waveguide ($n = 1.71$) with numerically simulated guided modes intensity for a $2 \times 3 \mu\text{m}^2$ channels if SU-8 material ($n = 1.6$) is used as buffer substrate.	60
3.2	SU-8 photolithography process flow	61
3.3	Effect of edge beads on SU-8 trench patterns a) with edge bead b) without edge beads. Note that the photolithography process parameters for both samples were all the same.	62
3.4	Three light exposure systems a) EVG 620 NT used for b) UV-KUB 2 c) upg101 laser exposure system.	64
3.5	SU-8 Pattern width evolution as a function of exposure dose for $3 \mu\text{m}$ thick photoresist when its exposed through $2 \mu\text{m}$ opening of a photomask.	64
3.6	High aspect ratio SU-8 patterns. a) a width= $2 \mu\text{m}$:height= $10 \mu\text{m}$ ridge. b) a width= $4 \mu\text{m}$:height= $10 \mu\text{m}$ trench.	67
3.7	SEM image of a PLD ridge channel fabricated by depositing the PLD material on a patterned SU-8 substrate. Note that the SEM image is taken at a 45° tilted angle.	67
3.8	SEM images of PLD films on SU-8 channel patterns , a) PLD film cleave imperfection, b) PLD reorganisation barriers.	68
3.9	ORMOSIL dry etching process flow.	69
3.10	Schemes of typical etched structures of the different reactive ion etching processes. a) Sample to be etched b) Chemically etched , b) Physically etched c) combined chemical and physical etching by optimizing RIE etching process parameters.	70

3.11	Photograph of an RIE equipment. inset) 3D Schematic representation of an ideal RIE equipment. Note that the 3D schematic is not to scale.	71
3.12	Schematic representation of etch rate measurement experimental protocol steps, a) Sample with PDMS mask b) Etched sample with PDMS mask b) Etched sample after liftoff the PDMS mask d) An experimental measure of etched step measurement by profilometer.	72
3.13	Effect of O ₂ flow on AZ5214E photoresist mask and ORMOSIL etch rate for two different RF powers (top: RF power =50Watt, bottom: RF power =75Watt) at constant chamber pressure (25 mTorr) and SF ₆ gas flow (10 sccm).	73
3.14	Optical microscope images of ORMOSIL layers etched at a) 50 Watt and b) 75 Watt RF power while other parameters O ₂ :SF ₆ =30sccm:10sccm, pressure 25 mTorr are constant.	74
3.15	Effect of RIE chamber pressure on AZ5214E photoresist mask and ORMOSIL etch rate at constant RF power and O ₂ :SF ₆ =30sccm:10sccm.	74
3.16	ORMOSIL film cracking during channel fabrication by RIE a) Cracks during soft mask fabrication. b) Crack by the RIE Ultra high vacuum. c) Crack during the etching process.	75
3.17	Scanning electron microscope images of RIE process a) Photoresist mask on ORMOSIL, b) 5 minutes RIE etched ORMOSIL, and c) 8 minutes RIE etched ORMOSIL. The process parameters are pressure=50 mTorr, RF power=50 W, O ₂ :SF ₆ flow rate 30:10 sccm.	76
3.18	Imprint lithography on ORMOSIL films process flow	77
3.19	Photograph of three imprint samples.	78
3.20	Two methods for master mold fabrication for PDMS replication a) SU-8 master mold and b) Silicon master mold.	79
3.21	SEM image of silicon master mold fabricated by RIE. note that the the image is taken at 45°.	80
3.22	PDMS mold fabrication process flow.	81
3.23	Photograph of the experimental facility for master mold silanization.	81
3.24	Photographs of last two steps in replicating the PDMS mold from the master mold a) Curing of the liquid PDMS on the master mold placed on a petri dish. b) PDMS molds removed and cut out.	82
3.25	SEM image of a pdms mold	83
3.26	SEM images of ORMOSIL structures fabricated by imprint lithography a) rib waveguides with different width and b) a fabricated ORMOSIL channel with width ($w=2.7\pm0.1\mu\text{m}$), height ($h=2.1\pm0.1\mu\text{m}$) and rib slab thickness $d=0.2\pm0.1\mu\text{m}$	83

4.1	Schematic description of a) Prism coupler, b) Grating coupler, and c) End-fire coupler. The schematics are not to scale.	88
4.2	a) Schematic representation of the optical setup for light coupling using end-fire coupler. b) Photograph of guided light in planar (left) and channel (right) waveguides using the setup. Note that propagation direction is from left to right (white arrow).	90
4.3	Experimental images of the intensity profile of guided modes in channel waveguides of different sizes. Note that the images are shown false colors	91
4.4	Losses measurement for a $2.1 \times 5.1 \mu\text{m}^2$ channel waveguide. top) Photograph of scattered light intensity in false color. bottom) Scatted light intensity variation with propagation length.	92
4.5	2D schematic representation of a) Glan laser linear polarizer b) Babinet–Soleil compensator.	94
4.6	a) Schematic of Glan-laser polarizer and Babinet–Soleil compensator polarization preparation setup. b) Poincaré representation of the polarization modulation by a Babinet-Soleil compensator. c) Some possible polarization states prepared by the combination.	95
4.7	General configuration of retarder and polarizer for polarization measurement. . .	96
4.8	Rotating quarter-wave plate-polarizer optical system for polarization measurement.	98
4.9	Polarimetry setup for waveguide characterization	99
4.10	Comparison of reference and measured polarization states by the optical setup. a) Comparison plotted on Poincare sphere. b) Comparison of the Stokes parameters separately.	101
4.11	Polarization mapping of an elliptically polarized laser beam.	102
4.12	Poincaré sphere representation of the behavior of a half-wave plate.	103
4.13	Schematic of Wollaston polarizing beam splitter.	104
4.14	Schematic representation of the optical setup for instantaneous measurement of Stokes parameters. NBS, WPBS, D are abbreviations for non polarizing beam splitter, Wollaston polarizing beam splitter, and photo-diodes is polarizing beam splitter respectively.	105
4.15	Comparison of reference and measured polarization states by the optical setup. a) Comparison on Poincare sphere b) Comparison of the Stokes parameters separately.	107
4.16	Schematic representation of the Mach–Zehnder interferometer optical setup. . .	110
4.17	a) Interference fringes image. b) Interference fringes intensity profile.	110
4.18	Intensity profile for interference fringes temporal evolution.	111

5.1	Computed shape birefringence $LB_{\text{shape}} (n_{\text{TE00}}-n_{\text{TM00}})$ for a rib waveguide (inset) as function of w but constant $d = 0.2 \mu\text{m}$ $h=2.1 \mu\text{m}$, $n_c=1$, $n_g=1.625$, and $n_b=1.61$	114
5.2	a) SEM image of ORMOSIL rib waveguides fabricated by imprint lithography which have same height $h = 2.1 \pm 0.1 \mu\text{m}$, same slab thickness $d = 0.2 \pm 0.1 \mu\text{m}$ but different width. b), c), and d) are rib channel waveguides with $w = 2.1 \pm 0.1 \mu\text{m}$, $w = 2.7 \pm 0.1 \mu\text{m}$, and $w = 3.6 \pm 0.1 \mu\text{m}$ respectively. The buffer layer is $6 \mu\text{m}$ thick with a refractive index contrast $\Delta n_g - n_b = 1.625 - 1.61 = 0.015$	116
5.3	a) Simulated and b) Experimentally measured mode intensity profile for the three rib waveguides with same rib height $h = 2.1 \pm 0.1 \mu\text{m}$, same slab thickness $d = 0.1 \pm 0.1 \mu\text{m}$ but different width $w = 2.1, 2.7, 3.6 \pm 0.1 \mu\text{m}$ from left to right. Not that the intensity of the guided modes is shown in false color scale	117
5.4	Top surface of image and losses measurement for ORMOSIL rib waveguides with same height $h = 2.1 \mu\text{m}$ but different widths $w = 2.1, 2.4, 3.6 \pm 0.1 \mu\text{m}$	118
5.5	Optical measurement setup.	119
5.6	Eigenmodes ellipticity and polarization ellipses measured for different rib widths w at rib height $h=2.1 \mu\text{m}$, slab thickness $d=0.2 \mu\text{m}$, refractive index contrast is $\Delta n=0.015$, and working wavelength is 633 nm	120
5.7	Experimental linear birefringence LB deduced from the eigenmodes polarization. a) Principal axis orientation of the linear birefringence as the orientation (azimuth) of the polarization ellipse of the eigenmodes. b) $ LB $ deduced from the ellipticity of the eigenmodes. The green line is the CB value of our material.	122
5.8	Poincaré representation of the transformations of input SOPs (blue points) into output SOPs (green points) after propagation in the chirowaveguides. The black points are the best fitted values for a rotation of angle ϕ about a diameter axis (red arrow). The cyan curves highlight the link between the input and output SOPs. a) (-) enantiomer waveguides, b) (+) enantiomer waveguides and c) (+/-) racemic waveguides. All waveguides are rib channels with $w = 2.7 \mu\text{m}$, $d = 0.2 \mu\text{m}$, and $h=2.1 \mu\text{m}$	124
5.9	Different types of sensing in optical waveguides. a) Volume sensing: change of CB in the cladding layer of the waveguide. b) Surface sensing: targeted molecules are anchored on molecular binder resulting in a high CB enhance in the close vicinity of the waveguide. c) Molecular diffusion of the chiral molecules into the waveguide material.	126

5.10	Chirowaveguide evanescent sensor. In red (blue) the field profile of the left(right)-handed elliptically polarized guided modes. While the guided modes acquire a phase change during their propagation in the chirowaveguide, a change of the chirality in the over-cladding induces an additional phase variation. The additional phase leads to a variation of the output polarization angle.	128
6.1	Dynamic evolution of in-plane refractive index (n_{TE}), out-of-plane refractive index (n_{TM}) versus humidity from dry air with (RH=11%) to humid air (RH=75%) and back cycle.	132
6.2	Calculated $n_{TE}(\Delta n) - n_{TE}(0)$, $n_{TM}(\Delta n) - n_{TM}(0)$, and $LB = n_{TE} - n_{TM} \ll 10^{-3}$ variation in a $2\mu\text{m}$ thick planar waveguide as a function material refractive index variation.	133
6.3	Planar (-) enantiomer chirowaveguide slow eigenmode evolution as a function of humidity represented on Poincaré sphere.	135
6.4	Poincaré representation of phase change for a linear polarization a $+45^\circ$ input as a function of humidity. a) RH=11% to 16%. b) RH=18% to 22%. c) RH=64% to 68%. d) RH=69% to 73%.	137
6.5	LB variation versus relative humidity for a planar ORMOSIL chirowaveguide.	138
6.6	Optical microscope image of a planar ORMOSIL waveguides a) before and b) after humidity effect.	139
6.7	Channel chirowaveguides eigenmode evolution as a function of humidity plotted on Poincaré sphere. a) (-)-enantiomer, b) (+)-enantiomer, and c) (+/-)-racemic waveguide. With the exception of chirality, the other waveguides properties are similar with $w = 2.4\mu \pm 0.1\mu\text{m}$, $h = 2.1\mu \pm 0.1\mu\text{m}$, $n_g = 1.618$, $n_b = 1.605$	141
6.8	Calculated LB azimuth for a system mixing LB oriented at 0 and 45°	142
6.9	Channel waveguides a) LB variation and b) Eigenmodes polarization azimuth variation as a function of humidity for three waveguides with different chirality (- enantiomer, + enantiomer, and +/- racemic). Channels size $w = 2.4 \pm 0.1$, $h = 2.1 \pm 1$, $l = 0.2 \pm 0.1\mu\text{m}$	143
6.10	Channel waveguides a) LB variation and b) Eigenmodes polarization azimuth variation as a function of humidity for four waveguides with different width w but same height $h = 2.1 \pm 0.1\mu\text{m}$, and rib thickness $d = 0.2 \pm 0.1\mu\text{m}$	144
6.11	Poincaré sphere representation of the dynamic phase change for a left-hand circularly polarized input in an ORMOSIL channel waveguide as a function of humidity, from dry air (RH=11%) to humid air (RH=75%) and vice versa. Channel size properties are $h = 2.1 \pm 0.1\mu\text{m}$, rib slab thickness = $0.2 \pm 0.1\mu\text{m}$, and a) $w = 4.2 \pm 0.1\mu\text{m}$. b) $w = 2.7 \pm 0.1\mu\text{m}$	146

6.12	Dynamic evolution of channel chirowaveguides LB as a function of humidity from dry air with (RH=11%) to humid air (RH=75%) and back cycle.	147
6.13	Optical experimental to use chirowaveguide for chiral sensing.	152
6.14	Experimental setup to control LB in the chirowaveguides by thermo-optics effects.	153
6.15	Computed shape birefringence $LB_{\text{shape}} (n_{\text{TE00}}-n_{\text{TM00}})$ for buried and air cover rib waveguides as function of w but constant $d = 0.2 \mu\text{m}$, $h=2.1 \mu\text{m}$, $n_c=1$, $n_g=1.625$, and $n_b=1.61$	155

List of Tables

1.1	Possible states of polarization as a function of phase difference (ϕ) and relative amplitudes of the two components of the electric field (E_{0x}, E_{0y})	9
1.2	Jones matrices for some standard polarization elements.	12
1.3	Stokes vectors for some states of polarization and unpolarized.	14
1.4	Mueller matrices for some standard polarization elements.	15
2.1	Comparison of chiral films made by PLD and sol-gel method.	58
3.1	Optimised soft-baking time (min) at 95°C on a hotplate versus film thickness (μm) for SU-8 films.	63
3.2	Optimised exposure energy dose for three different thickness (μm) for SU-8 films for near-UV light of 362 wavelength	65
3.3	Comparison of three photography UV exposure systems.	65
3.4	Optimised post exposure bake time for three different thickness (μm) for SU-8 films baked on a hotplate at 95°C.	66
3.5	Development times for SU-8 film as a function of film thickness using (Propylene glycol methyl ether acetate) developer.	66
3.6	Comparison of different methods for the fabrication of channel chirowaveguides.	84
4.1	Summary of optical characterization setups described in this chapter.	112
6.1	Humidity LB parameters for channel waveguides of different chirality.	144
6.2	Channel waveguide of different width.	145

Contents

List of Figures	vii
List of Tables	xiv
General Introduction	1
Scope of thesis	3
1 Theory and Design	5
1.1 Polarization of Light	5
1.1.1 Derivation of Maxwell wave equation	6
1.1.2 Monochromatic plane waves	7
1.1.3 Polarization ellipse	8
1.1.4 Jones Calculus	10
1.1.5 Stokes Parameters	12
1.1.6 Poincaré Sphere	16
1.1.7 Evolution of Stokes parameters in optical systems	18
1.2 Planar Waveguides	21
1.2.1 Planar waveguides equations	21
1.2.2 Guided modes propagation equations	22
1.2.3 Polarization beating in planar waveguides	25
1.3 Channel Waveguides	27
1.3.1 Channel waveguide equations	27
1.3.2 Computation of guided modes in channel waveguides	28
1.3.3 Polarization beating in channel waveguides	31
1.4 Chirality and Light	32
1.4.1 Light propagation in bulk chiral media	33
1.4.2 Polarization beating in bulk chiral media	34
1.5 Chirowaveguides	35
1.5.1 Coupled mode theory of chirowaveguides	37
1.5.2 Polarization beating in chirowaveguides	42

1.6	Waveguide Design	43
1.6.1	Low linear birefringence channel waveguides	43
1.7	Conclusion	46
2	Chiral Films	47
2.1	Choice of chiral molecules	47
2.2	Synthesis of chiral films	48
2.3	Pure chiral films by Pulsed laser deposition	48
2.3.1	PLD deposition experimental setup	50
2.3.2	Optimizing thickness of PLD films	50
2.3.3	Properties of chiral films made by PLD	52
2.4	Hybrid silica films	53
2.4.1	Material Synthesis	54
2.4.2	ORMOSIL film deposition	54
2.4.3	Thin film baking	56
2.4.4	ORMOSIL film refractive index control	57
2.4.5	Properties of chiral ORMOSIL-films made by Sol-gel	58
2.5	Conclusion	58
3	Waveguide Microfabrication	59
3.1	Microfabrication of PLD films	60
3.1.1	SU-8 Photolithography	60
3.1.2	PLD deposition on patterned substrates	67
3.2	ORMOSIL dry etching by RIE	69
3.2.1	RIE etching principle	70
3.2.2	Optimising RIE process parameters for ORMOSIL etching	72
3.2.3	Crack control in ORMOSIL layers	75
3.2.4	Fabricated ORMOSIL channels	76
3.3	Imprint Lithography	77
3.3.1	Master mold fabrication	79
3.3.2	PDMS mold replication	81
3.3.3	Fabricated ORMOSIL channel by imprint lithography	83
3.4	Conclusion	84
4	Optical setups	86
4.1	Waveguides input-output coupling	86
4.1.1	Prism coupler	87
4.1.2	Grating coupler	87

4.1.3	End-fire(direct) coupler	88
4.2	Waveguide loss measurement	91
4.3	Polarimetry	92
4.3.1	Polarization preparation	93
4.3.2	Polarization measurement by retarder and polarizer	96
4.3.3	Setup calibration	98
4.3.4	Rotating quarter-wave plate and polarizer setup testing	101
4.3.5	Birefringence measurement using the setup	102
4.3.6	Advantages and drawbacks of the optical setup	103
4.3.7	Dynamic polarization measurement	104
4.4	Mach-Zehnder interferometer	108
4.4.1	Interferometry principle	108
4.4.2	Mach-Zehnder interferometer experimental Setup	109
4.5	Conclusion	112
5	Elliptical birefringent chirowaveguides	113
5.1	Design	113
5.2	Rib fabrication and testing	115
5.2.1	Rib fabrication	115
5.2.2	Optical propagation	116
5.2.3	Waveguide loss measurements	117
5.3	Polarization measurement results	119
5.3.1	Elliptical birefringence modulation	120
5.3.2	Sources of linear birefringence	121
5.3.3	Low linear birefringent chirowaveguides	123
5.4	Chiral sensor	125
5.4.1	Effect of a chiral molecule on the chirowaveguide	125
5.4.2	Measurement parameters of the sensor	127
5.5	Conclusion	129
6	Effect of humidity on sol-gel polymer waveguides	130
6.1	Experimental	131
6.2	Mach-Zehnder interferometer	132
6.3	Static effect	134
6.3.1	Measurement technique	134
6.3.2	Planar waveguides LB measurement	135
6.3.3	Humidity effect on channel waveguides	140
6.4	Dynamic effect	145

6.5 Conclusion	147
General Conclusion and perspectives	149
Summary and accomplishments	149
Future perspectives	151
6.5.1 Chiral sensing using chirowaveguides	151
6.5.2 Controlling LB of the waveguides by thermo-optics effects	153
6.5.3 Buried channel waveguides TE-TM mode convertors	154
Appendices	156
Appendix A Appendix	158
A.1 Measurement of Muller matrix of an optical element	159
Bibliography	161

General Introduction

The work described in this manuscript was carried out at the Laboratory of the Institut Lumière Matière (ILM), a joint CNRS-University of Lyon 1 research unit, and in strong collaboration with the Chemistry Laboratory at the École normale supérieure of Lyon. The work was one of the projects of the *Chirality team*, which is a collaborative team of researchers from ILM and the chemistry laboratory of the Ecole Normale Supérieure de Lyon. It was financially supported by the French National Research Agency (ANR) within the framework of the CAPTOR project.

LIGHT is one of the main information carriers we use in our lives. When we are looking at the world around us, we are receiving the information carried by light. Our eyes can sense different characteristics of light such as intensity and color (wavelength). The information is transmitted to our eyes by certain successive interactions (e.g. absorption, refraction, diffraction, diffusion) of the light with the surrounding objects which modify the intensity, the wavelength and the direction of propagation. Because of the interaction of light with surrounding objects, we can use light as a basic tool to build many powerful analytical devices. The basic principle of these devices is to use light of known intensity, wavelength and direction of propagation and to measure any changes in these characteristics to obtain information about the specimen being analyzed. However, the three characteristics mentioned are not sufficient to know all the information carried by the light. For example, two light beams have similar intensity, wavelength and direction of propagation, but they interact differently with the surrounding medium. One of the beams changes intensity, frequency and direction, or all three, relative to the other beam, simply because its polarization is different.

The polarization of light, a fundamental property of electromagnetic waves, is information about the direction of oscillation of the electromagnetic waves electric field. This property of light can be detected using certain optical elements known as polarization elements. By measuring polarization information, polarimetry devices are developed that have many applications in science and technology: astronomy [1], ecology and environmental studies [2], food

industry [3], drug control and development [4], biomedical diagnosis and imaging [5], materials science [6], . . . The reason for all these applications is that light can be polarized into a continuum of states known as polarization states, ranging from linear to circular polarization; each polarization state is an analytical tool. Among all the applications, an important application of polarimetric devices that use the circular polarization state as the analytical tool is chiral sensing [7].

Chirality is a fundamental property of the living world, many molecules in nature have chiral property, they have three-dimensional molecular structures that cannot be superimposed on their mirror image. Two mirror-image molecules, called enantiomers, have mostly identical physical and chemical properties (e.g. same melting point, boiling point, solubility, etc.). However, they interact differently with other chiral objects. Since most of the receptors in our body are chiral, our body reacts differently to each enantiomer; One enantiomer form of a chiral drug can be used to cure, its counterpart can be very toxic or useless [8]. As an example, thalidomide was a widely used drug for the treatment of nausea in pregnant women. One enantiomer of thalidomide was found to treat nausea while the other enantiomer caused severe birth defects in thousands of children [9]. Furthermore, many chiral pollutants such as pesticides or drugs are present in air, soil or water. As an example, the chiral toxaphene or chlordane pesticides belong to the “Dirty Dozen” list of most harmful persistent organic pollutants. Many reports warn about the effect of chiral pollutants on the ecosystems and on human health and underline the importance of the daily monitoring of the chirality [10–13]. Therefore, the detection(sensing) and distinction of enantiomers is a topic of primary importance.

Polarimetry devices used to date for chiral sensing are mainly based on optical elements of laboratory dimensions. However, it has been more than 5 decades since the technology of integrated photonics * has been developed, which can encompass a large number of optical functions in small chips [14, 15]. In recent years, very advanced prototypes of this technology are developed that contains 850 optical functions (photonic components) [16]. However, to date, to our knowledge, there is no chiral sensor in integrated photonics. Indeed, integrated photonics being linear birefringent devices, the polarization information transmitted by the integrated photonic components is not preserved, except for two linear polarization states called eigenmodes. The eigenmodes of integrated photonics are linearly polarized parallel and perpendicular to the plane of the chip surface (i.e. transverse electric (TE) and transverse magnetic (TM) eigenmodes). The linear birefringence limits the polarization field of integrated photonics to applications based on the two linear polarization states. Therefore, circular polarization, which is the key polarization to chiral sensing, cannot be used with integrated photonics.

*Integrated photonics is the technology that uses light as an information carrier, similar to the electrical signals used in electronic integrated circuits.

Several efforts have been made to overcome the limitations of linear birefringence in integrated photonics by attempting to fabricate integrated photonic components with zero linear birefringence [17–27]. Zero-linear birefringence property is proposed in these studies by designing integrated photonic optical waveguides with certain exact waveguide geometries. In all these examples, since they use standard (achiral) materials, the constraints of waveguide fabrication are tedious and the slightest deviation from the ideal channel geometry results in non-zero linear birefringence. Other researchers, including the *chirality team*, have tackled the problem by using chiral materials to fabricate waveguides, called chirowaveguides [28–31]. Since chiral materials are circularly birefringent, optical chirowaveguide possess both linear and circular birefringence and are therefore elliptical birefringent systems with elliptically polarized eigenmodes. The purpose of using chirowaveguides is to realize waveguides with circularly polarized eigenmodes. Such waveguides can only be obtained if their linear birefringence is small compared to the circular birefringence. Obtaining a waveguide with such a property is challenging because, in general, the circular birefringence coming from the material chirality is lower than the linear birefringence coming from the opto-geometric properties of the waveguide. Nevertheless, it is not possible to increase the circular birefringence ($\sim 10^{-5} - 10^{-6}$) to the order of the linear birefringence ($\sim 10^{-2} - 10^{-4}$) because the circular birefringence is defined by the interaction between the micrometer wavelength of light and the nanometer size of the chiral molecules of the material. Therefore, the linear birefringence of the waveguides has to be lowered ($\sim 10^{-6}$) by controlling the opto-geometrical properties of optical waveguides.

When I started my PhD, the *chirality team* had already realized planar chirowaveguides by decreasing linear birefringence of the chirowaveguides using planar chirowaveguides sandwiched between two thick cladding layers [31]. Although the chirowaveguides could be used to transfer information using any polarization state of light they had two limitations: i) These are planar waveguides, which means that they can only be used to guide (confine) light in one direction, while channel waveguides can be used to guide light in two directions. Thus, most integrated photonic components are built from channel waveguides. ii) The waveguides were sandwiched between two thick cladding layers that prevents using them for sensing applications. Therefore, the realization of channel chirowaveguides without cladding layer became the objective of this PhD research.

Scope of thesis

The structure of this manuscript is organized into six chapters. Chapter 1 presents the theories necessary to describe the subject of this thesis. Although some of the theories are well known, we describe them again in this chapter in order to keep the manuscript reasonably self-contained and readable by non-specialists. At the end of the chapter numerical simulation

studies will be presented that led to define the design of the chirowaveguides to be fabricated. In the chapter 2, the chiral materials used to fabricate the chirowaveguides are presented, including their fabrication methods and the studies performed on these materials during this thesis. Chapter 3 presents the experimental microfabrication methods used for the fabrication of channel chirowaveguides by discussing the principle of the methods and showing the results obtained by each method. Chapter 4 presents the experimental optical characterization techniques used for the characterization of the chirowaveguides. The way the optical setups are developed and used to perform the characterization techniques are discussed. Chapter 5 presents experimental results on the fabrication and optical characterization of channel waveguides ranging from channel waveguides with linearly polarized eigenmodes to channel waveguides with quasi-circularly polarized eigenmodes. Chapter 6 is devoted to present some experimental results on effect of humidity on one of the chiral materials that we used to fabricate the channel chirowaveguides that is a sol-gel derived originally modified silica material. The dynamic and static effect of humidity on planar and channel waveguides made of the material are investigated and presented in this chapter.

Finally, the general conclusion summarizes the results obtained during this thesis and the future perspectives opened by this work.

Theory and Design

OPTICAL waveguides are already used for sensing applications such as humidity sensors [32], gas sensors [33], and biosensors [34]. However, to date, these waveguides have never been used for chiral sensing because optical waveguides only support two linearly polarized eigenmodes, namely transverse electric (TE) and transverse magnetic (TM) modes, whereas circularly polarized eigenmodes are required. Our objective is to realize waveguides, made of chiral materials, that support circularly polarized eigenmodes so that they can be used for chiral sensing. Before describing our strategy for making such waveguides, we answer some basic questions about the subject, including: What is the polarization of light?, What are the mathematical methods for dealing with this property of light? How do we measure the polarization of light? Why do optical waveguides only support TE/TM eigenmodes? What is chirality? and how to use chiral materials to realize waveguides usable for chiral sensing?

This chapter is dedicated to answer these questions and to explain the basic concepts necessary to understand the results obtained during this thesis.

1.1 Polarization of Light

Light is an electromagnetic wave, it has two fields (electric and magnetic). When light travels in free space, the two fields oscillate perpendicular to each other and both perpendicular to the direction of propagation. The information about the oscillation of the electric field of the light wave is the so-called polarization property of light. The possible oscillation states of the tip of the vector that represents the electric field of a light wave are called states of polarization (SOP) of light. If the oscillation of the electric field is confined in a plane, the light is said to be linearly polarized, this plane can rotate by any angle as shown in Figure 1.1. It is called linear because the trace of time variation of electric field in space creates a straight (linear) line for an observer looking towards the wave. Linear polarization is one possible SOP while the electric

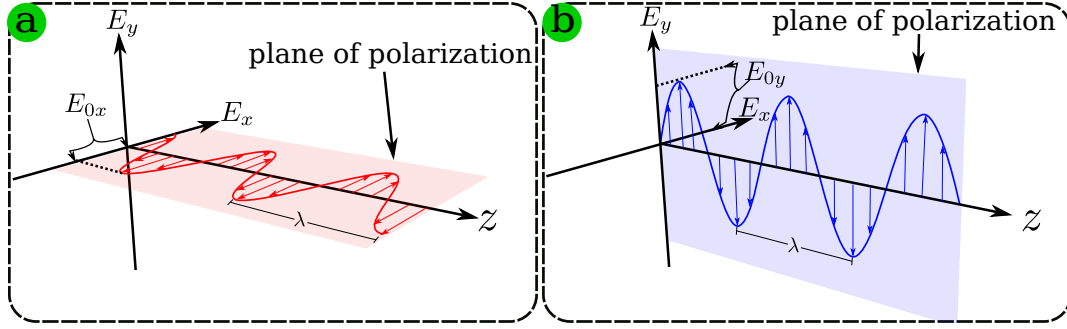


Figure 1.1: A snapshot of the electric field oscillation of a light wave in two linear polarization states when it is **a)** horizontally polarized **b)** Vertically polarized.

field can have many other possibilities to oscillate such as elliptical and circular polarization.

1.1.1 Derivation of Maxwell wave equation

Polarization of light can be easily described by Maxwell wave equation. The Maxwell equations in free space are:

$$\nabla \cdot \mathbf{E} = 0 \quad (1.1a)$$

$$\nabla \cdot \mathbf{H} = 0 \quad (1.1b)$$

$$\nabla \times \mathbf{E} = -\mu_0 \frac{\partial \mathbf{H}}{\partial t} \quad (1.1c)$$

$$\nabla \times \mathbf{H} = \varepsilon_0 \frac{\partial \mathbf{E}}{\partial t} \quad (1.1d)$$

where \mathbf{E} and \mathbf{H} are electric and magnetic field vectors respectively. The ε_0 and μ_0 are scalar variables describing the electric permittivity and magnetic permeability of free space. The $\nabla \cdot$ and $\nabla \times$ are divergence and curl of Del (nabla) operator respectively. To explain the polarization of light, we need to derive wave equation for the electric field of the light wave. By taking curl of equation 1.1c, then using equation 1.1d and nabla ∇ operator relations*, we obtain:

$$\nabla \times (\nabla \times \mathbf{E}) = -\mu_0 \frac{\partial}{\partial t} (\nabla \times \mathbf{H}) = -\nabla^2 \mathbf{E} \quad (1.2)$$

From equation 1.2, then using equation 1.1d, we get:

$$\begin{aligned} \varepsilon_0 \mu_0 \frac{\partial^2 \mathbf{E}}{\partial t^2} &= \nabla^2 \mathbf{E} \\ \frac{1}{c^2} \frac{\partial^2 \mathbf{E}}{\partial t^2} &= \frac{\partial^2 \mathbf{E}}{\partial x^2} + \frac{\partial^2 \mathbf{E}}{\partial y^2} + \frac{\partial^2 \mathbf{E}}{\partial z^2} \end{aligned} \quad (1.3)$$

Equation 1.3 is three-dimensional wave equation, where the electric field is $\mathbf{E} = \mathbf{E}(x, y, z, t)$, ∇^2 is vector Laplace operator, and c is velocity of light in free space being $c = \frac{1}{\sqrt{\varepsilon_0 \mu_0}}$.

* $\nabla \times (\nabla \times \mathbf{A}) = \nabla \cdot (\nabla \cdot \mathbf{A}) - (\nabla \cdot \nabla) \mathbf{A}$ & $\nabla \cdot \nabla = \nabla^2$

1.1.2 Monochromatic plane waves

A monochromatic plane wave is a particular solution of the wave equation. We assume that the light wave is a homogeneous monochromatic plane wave propagating with an angular frequency ω in the z direction with velocity c . Maxwell equation 1.1a implies the orthogonality of the electric field and the direction of propagation z for homogeneous plane waves, so the z component of the electric field is zero. Therefore, the electric field is described by only two components $E_x(z, t)$ and $E_y(z, t)$. The three-dimensional wave equation 1.3 in this case will be simplified to:

$$\frac{1}{c^2} \frac{\partial^2}{\partial t^2} \begin{bmatrix} E_x(z, t) \\ E_y(z, t) \end{bmatrix} = \frac{\partial^2}{\partial z^2} \begin{bmatrix} E_x(z, t) \\ E_y(z, t) \end{bmatrix} \quad (1.4)$$

$E_x(z, t)$ and $E_y(z, t)$ are decoupled and each one travels without affecting the other. If the electric field has only x component ($E_y = 0$), the equation 1.4 reduces to:

$$\frac{1}{c^2} \frac{\partial^2 E_x(z, t)}{\partial t^2} = \frac{\partial^2 E_x(z, t)}{\partial z^2} \quad (1.5)$$

We can write a simple traveling plane wave propagating in z direction as a solution of the wave equation 1.5:

$$E_x(z, t) = \Re[E_{0x} e^{i\phi_x} e^{i(\omega t - kz)}] = E_{0x} \cos(\omega t - kz + \phi_x) \quad (1.6)$$

where E_{0x} , ω , $k = \frac{\omega}{c}$, and ϕ_x are real quantities, they are maximum amplitude, angular momentum, wave vector, and absolute phase of the traveling wave respectively. Figure 1.1-a is a snapshot of such traveling wave at a particular moment in time. As shown, the electric field oscillates in a plane and is said to be linearly polarized.

If the electric field has only the y component ($E_x = 0$), then we can also write a traveling wave similar to the equation 1.6 as a solution for the wave equations but for E_y .

$$E_y(z, t) = \Re[E_{0y} e^{i\phi_y} e^{i(\omega t - kz)}] = E_{0y} \cos(\omega t - kz + \phi_y) \quad (1.7)$$

Figure 1.1-b is a snapshot of such traveling wave at a particular moment in time.

As the equations 1.6 and 1.7 are separately solutions of the wave equation, a traveling wave representing their linear combination is also a solution:

$$\mathbf{E}(z, t) = E_x(z, t)\hat{x} + E_y(z, t)\hat{y} = E_{0x} \cos(\omega t - kz)\hat{x} + E_{0y} \cos(\omega t - kz + \phi)\hat{y} \quad (1.8)$$

Here, \hat{x} and \hat{y} are unit vectors and $\phi = \phi_y - \phi_x$ is the phase difference between the two components of the electric field. The $\mathbf{E}(z, t)$, which is the resultant vector of $E_x(z, t)$ and $E_y(z, t)$ can describe all possible SOP, from linear to circular. We have plotted in Figure 1.2, the traveling wave of Equation 1.8 for the case when $E_{0x} = E_{0y}$ and $\phi = -\frac{\pi}{2}$, it is right handed circularly polarized wave. The figure shows in green color, how the tip of the resultant electric field traces a helical trajectory.

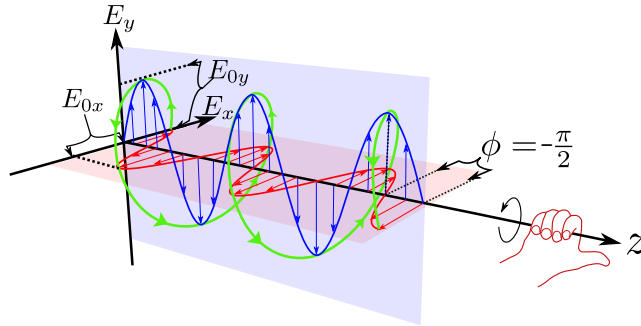


Figure 1.2: Snapshot of a light wave having the two components E_x and E_y with a phase difference $\phi = -\frac{\pi}{2}$. It represents a right circularly polarized light wave and obeys the right hand rule. The green color traces the tip of the resulting electric field which represents the helical trajectory of a circularly polarized wave.

1.1.3 Polarization ellipse

Using trigonometric identities, we can derive from equation 1.8 an equation for general case of light polarization:

$$\frac{E_x^2(z, t)}{E_{0x}^2} + \frac{E_y^2(z, t)}{E_{0y}^2} - 2\frac{E_x(z, t)E_y(z, t)}{E_{0x}E_{0y}} \cos \phi = \sin^2 \phi \quad (1.9)$$

Equation 1.9 is known as the polarization ellipse equation. The equation describes a rotated ellipse inscribed inside a rectangle in which the sides of the rectangle are oriented as the x and y axes of the electric field as shown in Figure 1.3. At a particular value of z , the tip of the electric field vector periodically traces out the ellipse in the $x - y$ plane. At a particular moment of time, the locus of the tip of the electric field vector follows a helical trajectory in

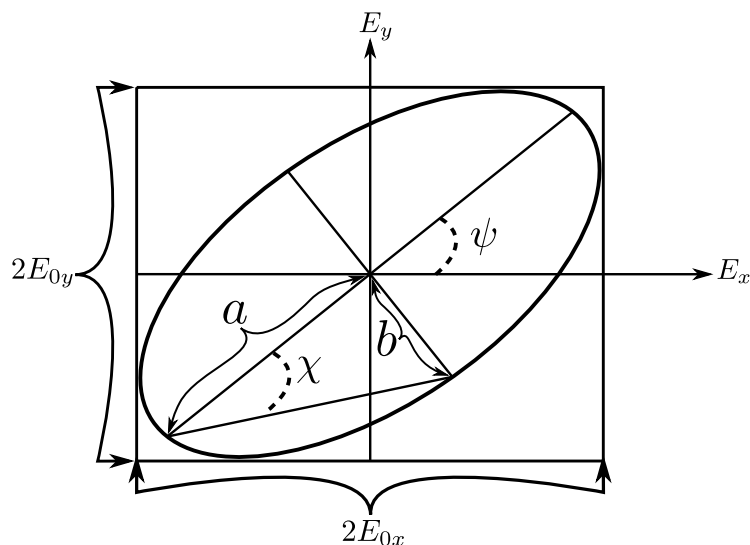


Figure 1.3: Polarization ellipse of a general (elliptically polarized) wave.

space that lies on the surface of an elliptical cylinder (A particular case where the cylinder is circular is shown in Figure 1.2).

The three parameters E_{0x} , E_{0y} , and ϕ are enough to completely describe the SOP of a fully polarized wave. Furthermore, the values of ϕ define the sense of rotation of the tip of the resultant electric field so-called polarization handedness. If $-\pi < \phi < 0$, the polarization is said to be right-handed polarized, the direction of rotation of tip of electric field obeys the right-hand rule (see Figure 1.2) while for left-handed polarized $0 < \phi < \pi$, it obeys left hand. The table 1.1 summarizes some possible SOPs according to the amplitude of the electric field components and their phase difference.

Table 1.1: Possible states of polarization as a function of phase difference (ϕ) and relative amplitudes of the two components of the electric field (E_{0x} , E_{0y})

$\phi =$	$-\pi$	$-\frac{\pi}{2}$	$-\frac{\pi}{4}$	0	$\frac{\pi}{4}$	$\frac{\pi}{2}$	π
$E_{0x}=1$ $E_{0y}=0$							
$E_{0x}=1$ $E_{0y}=0.5$							
$E_{0x}=1$ $E_{0y}=1$							
$E_{0x}=0.5$ $E_{0y}=1$							
$E_{0x}=0$ $E_{0y}=1$							

The convenient parameters to describe the polarization ellipse are polarization ellipticity angle χ (or just ellipticity for the sake of shortening) and the ellipse azimuth ψ as shown in Figure 1.3. The ellipticity χ is defined as the tangent of the ratio between the minor and major axes of the ellipse ($\tan \chi = \frac{b}{a}$), it defines the degree to which an ellipse is circle which takes the values of $-\frac{\pi}{4} < \chi < \frac{\pi}{4}$. The azimuth of the ellipse ψ is the angle of the major axis of the ellipse relative to the x -axis, it takes the values of $-\frac{\pi}{2} < \psi < \frac{\pi}{2}$. The relations between the electric field parameters (E_{0x} , E_{0y} , ϕ) and polarization ellipse parameters (χ , ψ) are [35]:

$$\sin 2\chi = \frac{2E_{0x}E_{0y}}{E_{0x}^2 + E_{0y}^2} \sin \phi \quad (1.10a)$$

$$\tan 2\psi = \frac{2E_{0x}E_{0y}}{E_{0x}^2 - E_{0y}^2} \cos \phi \quad (1.10b)$$

1.1.4 Jones Calculus

A simple method to deal mathematically with fully polarized light is to use the Jones calculus which was proposed by Robert Clark Jones in successive papers [36]. Here, we briefly go through this intuitive mathematical representation of polarized light.

1.1.4.1 Jones Vectors

We have defined a polarized electromagnetic wave as real part of a monochromatic plane traveling wave. With Jones calculus we deal with complex traveling wave, and we write the equation 1.8 as:

$$\mathbf{E}(z, t) = \begin{bmatrix} E_x(z, t) \\ E_y(z, t) \end{bmatrix} = \begin{bmatrix} E_{0x}e^{i\phi_x} \\ E_{0y}e^{i\phi_y} \end{bmatrix} e^{i(\omega t - kz)} \quad (1.11)$$

Jones calculus deals with complex amplitudes of the electric field components, then the Jones vector is:

$$\mathbf{J} = \begin{bmatrix} E_{0x}e^{i\phi_x} \\ E_{0y}e^{i\phi_y} \end{bmatrix} = \begin{bmatrix} E_{0x} \\ E_{0y}e^{i\phi} \end{bmatrix} \quad (1.12)$$

It is customary to use so-called normalized Jones vectors in which the vectors are reduced to their simplest form and have a magnitude of 1. The normalized form of Jones vectors are obtained by dividing the vector components by $(\sqrt{|E_{0x}|^2 + |E_{0y}|^2})$. Normalized Jones vectors for horizontally and vertically polarized waves are:

$$\mathbf{J}_x = \begin{bmatrix} 1 \\ 0 \end{bmatrix}, \quad \mathbf{J}_y = \begin{bmatrix} 0 \\ 1 \end{bmatrix} \quad (1.13)$$

For a linear polarization rotated by an angle of ψ with respect to the x axis, we must multiply the rotation matrix by \mathbf{J}_x , we obtain:

$$\mathbf{J}_x(\psi) = \begin{bmatrix} \cos \psi & -\sin \psi \\ \sin \psi & \cos \psi \end{bmatrix} \begin{bmatrix} 1 \\ 0 \end{bmatrix} = \begin{bmatrix} \cos \psi \\ \sin \psi \end{bmatrix} \quad (1.14)$$

From equation 1.14, we can obtain the normalized Jones vectors for $\pm 45^\circ$ linear polarized light that is:

$$\frac{1}{\sqrt{2}} \begin{bmatrix} 1 \\ \pm 1 \end{bmatrix} \quad (1.15)$$

In the case of left and right circularly polarized waves, the real amplitudes of the electric field components being equal and $\phi = \pm \frac{\pi}{2}$, normalized Jones vectors are:

$$\mathbf{J} = \begin{bmatrix} E_{0x} \\ E_{0y}e^{\pm i\frac{\pi}{2}} \end{bmatrix} = \frac{1}{\sqrt{2}} \begin{bmatrix} 1 \\ \pm i \end{bmatrix} \quad (1.16)$$

The Jones vector for a left and right elliptically polarized wave, whose major axis lies on the x -axis is:

$$\mathbf{J}(\psi = 0, \chi) = \begin{bmatrix} E_{0x} \\ E_{0y}e^{\pm i\frac{\pi}{2}} \end{bmatrix} = \begin{bmatrix} \cos \chi \\ \pm i \sin \chi \end{bmatrix} \quad (1.17)$$

Now, we can write general Jones vector for an arbitrary polarized wave, in term of polarization ellipse parameters, by multiplying rotation matrix to the equation 1.17

$$\mathbf{J}(\psi, \chi) = \begin{bmatrix} \cos \psi & -\sin \psi \\ \sin \psi & \cos \psi \end{bmatrix} \begin{bmatrix} \cos \chi \\ \pm i \sin \chi \end{bmatrix} = \begin{bmatrix} \cos \psi \cos \chi & \mp i \sin \psi \sin \chi \\ \sin \psi \cos \chi & \pm i \cos \psi \sin \chi \end{bmatrix} \quad (1.18)$$

1.1.4.2 Jones Matrix

Besides the simple representation of polarized light, Jones calculus can also be used to calculate and show how a polarized wave is modified when it interacts with any polarization element. Similar to the equation 1.18, when we have multiplied the rotation matrix to find out the effect of rotation, the effect of any polarization element on a polarized wave is assigned by multiplying a transformation matrix (Jones matrix) of that polarization element to the Jones vector of the wave. If an input polarized wave described by Jones vector $\mathbf{J}_{input} = \begin{bmatrix} E_{0x} \\ E_{0y}e^{i\phi} \end{bmatrix}$ which passes through a polarization element of Jones matrix \mathbf{M} , the Jones vector of the output wave is:

$$\mathbf{J}_{output} = \mathbf{M} \cdot \mathbf{J}_{input} = \begin{bmatrix} a_{11} & a_{12} \\ a_{21} & a_{22} \end{bmatrix} \begin{bmatrix} E_{0x} \\ E_{0y}e^{i\phi} \end{bmatrix} = \begin{bmatrix} a_{11}E_{0x} + a_{12}E_{0y}e^{i\phi} \\ a_{21}E_{0x} + a_{22}E_{0y}e^{i\phi} \end{bmatrix} \quad (1.19)$$

where a_{ij} are coefficients to be determined from the known properties of the polarization element encountered by the light. In table 1.2, we have listed Jones matrix for some standard polarization elements [37]. When a light wave passes through several polarization elements, it is only necessary to multiply the Jones vector of the input wave into the Jones matrix of each element, one after another.

The Jones calculus is a simple and powerful method to analyze and treat the polarization of light since the phase information of the electric field is preserved. However, this method can only be applied to fully polarized light and the elements of the Jones vector are not measurable quantities. In the remainder of this manuscript, we will mainly use the Stokes vectors (parameters) and Mueller calculus since the Mueller matrices for the polarization elements and the Stokes parameters for the state of the polarized light are measurable quantities.

Table 1.2: Jones matrices for some standard polarization elements.

polarization element	Jones matrix
linear polarizer at azimuth ψ	$\begin{bmatrix} \cos^2 \psi & \sin \psi \cos \psi \\ \sin \psi \cos \psi & \sin^2 \psi \end{bmatrix}$
linear phase retarder at azimuth $\psi = 0$ of the fast axis and phase retardation ϕ	$\begin{bmatrix} e^{i\frac{\phi}{2}} & 0 \\ 0 & e^{-i\frac{\phi}{2}} \end{bmatrix}$
linear phase retarder at azimuth ψ of the fast axis and phase retardation ϕ	$\begin{bmatrix} \cos^2 \psi e^{i\frac{\phi}{2}} + \sin^2 \psi e^{-i\frac{\phi}{2}} & 2i \sin \psi \cos \psi \sin \frac{\phi}{2} \\ 2i \sin \psi \cos \psi \sin \frac{\phi}{2} & \cos^2 \psi e^{-i\frac{\phi}{2}} + \sin^2 \psi e^{i\frac{\phi}{2}} \end{bmatrix}$
half wave plate at azimuth ψ	$\begin{bmatrix} \cos 2\psi & \sin 2\psi \\ \sin 2\psi & -\cos 2\psi \end{bmatrix}$
quarter wave plate at azimuth ψ	$\begin{bmatrix} \cos^2 \psi + i \sin^2 \psi & \sin \psi \cos \psi - i \sin \psi \cos \psi \\ \sin \psi \cos \psi - i \sin \psi \cos \psi & \sin^2 \psi + i \cos^2 \psi \end{bmatrix}$

1.1.5 Stokes Parameters

Another method to describe polarization of light is using a four column vector called Stokes vector or Stokes parameters. They owe their name to Sir George Stokes who described them long before Jones' parameters in 1851 [38]. This method is similar to Jones calculus in a way they both use a vector to describe the SOP of light while in Stokes vectors there are 4 elements rather than the 2 elements in Jones vectors. Also, the amplitude of an optical field used in Jones vectors cannot be measured. However, the time average of the square of the amplitude (intensity) is the quantity used in the Stokes parameters, which makes the Stokes parameters measurable quantities. Another important difference between the Stokes and Jones vectors is that the Stokes parameters give a complete description of the state of light, even if the light is partially polarized.

1.1.5.1 Derivation of Stokes parameters

To derive Stokes parameters, we start from equation 1.8 that represents electric field components of a monochromatic plane wave (E_x and E_y) with a certain phase ϕ between them. We can obtain a similar equation of polarization ellipse (equation 1.9) but for the time average of the electric field [39]:

$$\frac{\langle E_x^2 \rangle}{E_{0x}^2} + \frac{\langle E_y^2 \rangle}{E_{0y}^2} - 2 \frac{\langle E_x E_y \rangle}{E_{0x} E_{0y}} \cos \phi = \sin^2 \phi \quad (1.20)$$

We take time average $\langle \dots \rangle^\dagger$ of only the electric field since for a monochromatic wave the amplitude and phase difference are constant with time. From the definition of time average ($\langle f(t) \rangle = \frac{1}{T} \int_0^T f(t) dt$), the terms of equation 1.20 are written as:

$$\langle E_x^2 \rangle = \frac{1}{2} E_{0x}^2, \quad \langle E_y^2 \rangle = \frac{1}{2} E_{0y}^2, \quad \langle E_x E_y \rangle = \frac{1}{2} E_{0x} E_{0y} \cos \phi \quad (1.21)$$

Using these results in equation 1.20 and arranging the amplitudes of electric field components, we arrive at:

$$\underbrace{(E_{0x}^2 + E_{0y}^2)}_{S_0} = \underbrace{(E_{0x}^2 - E_{0y}^2)}_{S_1} + \underbrace{(2E_{0x}E_{0y} \cos \phi)}_{S_2} + \underbrace{(2E_{0x}E_{0y} \sin \phi)}_{S_3} \quad (1.22)$$

The four separate terms in brackets of this equation define the four Stokes parameters (S_0 , S_1 , S_2 , and S_3), they can be written as a column vector so-called Stokes vector:

$$\mathbf{S} = \begin{bmatrix} S_0 \\ S_1 \\ S_2 \\ S_3 \end{bmatrix} = \begin{bmatrix} E_{0x}^2 + E_{0y}^2 \\ E_{0x}^2 - E_{0y}^2 \\ 2E_{0x}E_{0y} \cos \phi \\ 2E_{0x}E_{0y} \sin \phi \end{bmatrix} \quad (1.23)$$

From equations 1.23 and 1.10, we can write polarization ellipse parameters χ and ψ as a function of four Stokes parameters

$$\tan 2\psi = \frac{S_2}{S_1} \quad (1.24a)$$

$$\sin 2\chi = \frac{S_3}{S_0} \quad (1.24b)$$

When the first time Sir George Stokes introduced Stokes parameters, he defined them based on experimental measurements [38]. S_0 is total intensity of a light wave (I_{total}). S_1 is intensity difference of the light wave when passed through a polarizer oriented in x and y axes (I_{\leftrightarrow} and I_{\updownarrow}). S_2 is intensity difference of light wave when passed through a polarizer oriented in 45° and -45° relative to x axis (I_{\nearrow} and I_{\nwarrow}). S_3 is intensity difference of light wave when passed through a left-handed circular polarizer to right-handed circular polarizer (I_{\odot} and I_{\ominus}). Therefore, we can also write Stokes vector as:

$$\mathbf{S} = \begin{bmatrix} S_0 \\ S_1 \\ S_2 \\ S_3 \end{bmatrix} = \begin{bmatrix} E_{0x}^2 + E_{0y}^2 \\ E_{0x}^2 - E_{0y}^2 \\ 2E_{0x}E_{0y} \cos \phi \\ 2E_{0x}E_{0y} \sin \phi \end{bmatrix} = \begin{bmatrix} I_{total} \\ I_{\leftrightarrow} - I_{\updownarrow} \\ I_{\nearrow} - I_{\nwarrow} \\ I_{\odot} - I_{\ominus} \end{bmatrix} \quad (1.25)$$

[†]Averaging over a long period of time (many photons), this is how photodetectors work.

1.1.5.2 Normalized Stokes parameters

Measurement of all four Stokes parameters requires an absolute intensity measurement. In practice, to avoid uncertainty of photodetectors, what we measure are normalized (or relative) unitless Stokes parameters. We normalize all the parameters to S_0 which is the total intensity of the light. The normalized Stokes vector is:

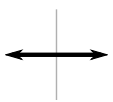
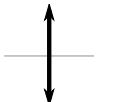
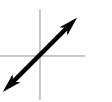
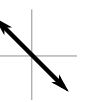
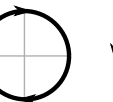
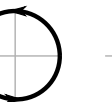
$$\tilde{S} = \begin{bmatrix} \tilde{S}_0 \\ \tilde{S}_1 \\ \tilde{S}_2 \\ \tilde{S}_3 \end{bmatrix} = \begin{bmatrix} 1 \\ \frac{S_1}{S_0} \\ \frac{S_2}{S_0} \\ \frac{S_3}{S_0} \end{bmatrix} = \begin{bmatrix} 1 \\ \frac{I_{\leftrightarrow} - I_{\updownarrow}}{I_{total}} \\ \frac{I_{\nearrow} - I_{\searrow}}{I_{total}} \\ \frac{I_{\circlearrowleft} - I_{\circlearrowright}}{I_{total}} \end{bmatrix} \quad (1.26)$$

The Stokes parameter \tilde{S}_1 is +1 and -1 for horizontally and vertically polarized light, \tilde{S}_2 is +1 and -1 for linear polarized at 45° and -45°, and \tilde{S}_3 is +1 and -1 for left and right handed circularly polarized light. For an elliptically polarized light, each parameter have a value less than one, the arithmetic average of the three is 1 ($\sqrt{\tilde{S}_1^2 + \tilde{S}_2^2 + \tilde{S}_3^2} = 1$). Therefore, the \tilde{S}_1, \tilde{S}_2 and \tilde{S}_3 are enough to completely describe SOP of light. Any additional measurement of light intensity is indirectly the measurement of the degree of polarization. In other words, if $\sqrt{\tilde{S}_1^2 + \tilde{S}_2^2 + \tilde{S}_3^2} < 1$, the light is not completely polarized. Degree of polarization (*DOP*) is defined as:

$$DOP = \frac{\sqrt{S_1^2 + S_2^2 + S_3^2}}{S_0} = \sqrt{\tilde{S}_1^2 + \tilde{S}_2^2 + \tilde{S}_3^2} \quad (1.27)$$

In Table 1.3, we have listed normalized Stokes vectors for some SOP of light.

Table 1.3: Stokes vectors for some states of polarization and unpolarized.

SOP								Unpolarized
Stokes vector	$\begin{bmatrix} 1 \\ 1 \\ 0 \\ 0 \end{bmatrix}$	$\begin{bmatrix} 1 \\ -1 \\ 0 \\ 0 \end{bmatrix}$	$\begin{bmatrix} 1 \\ 0 \\ 1 \\ 0 \end{bmatrix}$	$\begin{bmatrix} 1 \\ 0 \\ -1 \\ 0 \end{bmatrix}$	$\begin{bmatrix} 1 \\ 0 \\ 0 \\ 1 \end{bmatrix}$	$\begin{bmatrix} 1 \\ 0 \\ 0 \\ -1 \end{bmatrix}$	$\begin{bmatrix} 1 \\ -0.55 \\ 0.65 \\ 0.53 \end{bmatrix}$	$\begin{bmatrix} 1 \\ 0 \\ 0 \\ 0 \end{bmatrix}$

1.1.5.3 Mueller matrix

In general, when light passes through an optical element, its SOP and therefore its Stokes parameters change. Similar to Jones matrices used in Jones calculus to determine the effect polarization elements, we can also create a transfer matrix to calculate the effect of a polarization element on polarized light using Stokes parameters. When SOP of a light wave is described by a Stokes vector, the effect of any polarization element on such light wave can be calculated by

multiplying the input light wave's Stokes vector to a matrix that represents the optical element

$$S_{output} = M \cdot S_{input}$$

$$\begin{bmatrix} S_0(output) \\ S_1(output) \\ S_2(output) \\ S_3(output) \end{bmatrix} = \begin{bmatrix} m_{11} & m_{12} & m_{13} & m_{14} \\ m_{21} & m_{22} & m_{23} & m_{24} \\ m_{31} & m_{32} & m_{33} & m_{34} \\ m_{41} & m_{42} & m_{43} & m_{44} \end{bmatrix} \begin{bmatrix} S_0(input) \\ S_1(input) \\ S_2(input) \\ S_3(input) \end{bmatrix} \quad (1.28)$$

The matrix M is called Mueller matrix and m_{ij} are the coefficients to be determined from the known properties of the polarization element or medium encountered by the light. Mueller matrix is a 4×4 matrix corresponding to the 4 column Stokes vector. In literature, one can find Mueller matrices for some polarizing elements or for a medium that depolarizes light. In the table 1.4, as we did for Jones matrices, we list Mueller matrices for some usual polarization elements.

Table 1.4: Mueller matrices for some standard polarization elements.

polarization element	Mueller matrix				
linear polarizer at azimuth ψ	$\frac{1}{2}$	1	$\cos 2\psi$	$\sin 2\psi$	0
		$\cos 2\psi$	$\cos^2 2\psi$	$\sin 2\psi \cos 2\psi$	0
		$\sin 2\psi$	$\sin 2\psi \cos 2\psi$	$\sin^2 2\psi$	0
		0	0	0	0
linear phase retarder at azimuth $\psi = 0$ of the fast axis and phase retardation ϕ		1	0	0	0
		0	1	0	0
		0	0	$\cos \phi$	$\sin \phi$
		0	0	$-\sin \phi$	$\cos \phi$
linear phase retarder at azimuth ψ of the fast axis and phase retardation ϕ	1	0	0	0	0
	0	$\cos^2 2\psi + \cos \phi \sin^2 2\psi$	$(1 - \cos \phi) \sin 2\psi \cos 2\psi$	$\sin 2\psi \cos 2\psi$	$-\sin \phi \sin 2\psi$
	0	$(1 - \cos \phi) \sin 2\psi \cos 2\psi$	$\sin^2 2\psi + \cos \phi \cos^2 2\psi$	$\sin \phi \sin 2\psi$	$\sin \phi \sin 2\psi$
	0	$\sin \phi \sin 2\psi$	$-\sin \phi \sin 2\psi$	$\cos \phi$	$\cos \phi$
half wave plate at azimuth ψ		1	0	0	0
		0	$\cos 4\psi$	$\sin 4\psi$	0
		0	$\sin 4\psi$	$-\cos 4\psi$	0
		0	0	0	-1
quarter wave plate at azimuth ψ	1	0	0	0	0
	0	$\cos^2 2\psi$	$\sin 2\psi \cos 2\psi$	$-\sin 2\psi$	$-\sin 2\psi$
	0	$\sin 2\psi \cos 2\psi$	$\sin^2 2\psi$	$\cos 2\psi$	$\cos 2\psi$
	0	$\sin 2\psi$	$-\cos 2\psi$	0	0
Ideal depolarizer		1	0	0	0
		0	0	0	0
		0	0	0	0
		0	0	0	0

1.1.6 Poincaré Sphere

We have defined degree of polarization (DOP) and polarization ellipse parameters (χ and ψ) as a function of Stokes parameters in equations 1.24 and 1.27. We can summarize these relations as:

$$\mathbf{S} = \begin{bmatrix} S_0 \\ S_1 \\ S_2 \\ S_3 \end{bmatrix} = \begin{bmatrix} 1 \\ DOP \cos 2\psi \cos 2\chi \\ DOP \sin 2\psi \cos 2\chi \\ DOP \sin 2\chi \end{bmatrix} \quad (1.29)$$

By looking at the equation 1.29, we notice that the relation between Stokes parameters (S_1 , S_2 , and S_3) and polarization parameters (DOP , 2χ , and 2ψ) are very similar to the relation between cartesian (x , y , and z) and spherical (radius, latitude, and azimuth) coordinate systems. Therefore, in a 3D cartesian space whose axes represent S_1 , S_2 , and S_3 , all possible states of polarization of light can be described by points on the surface of a sphere of radius DOP . Such sphere is known as the Poincaré sphere, after the French scientist Henri Poincaré who, in 1892, discovered that infinite polarization states can be represented on a finite 3D sphere [40]. The sphere is shown in figure 1.4-a, each point on the sphere represents a particular SOP.

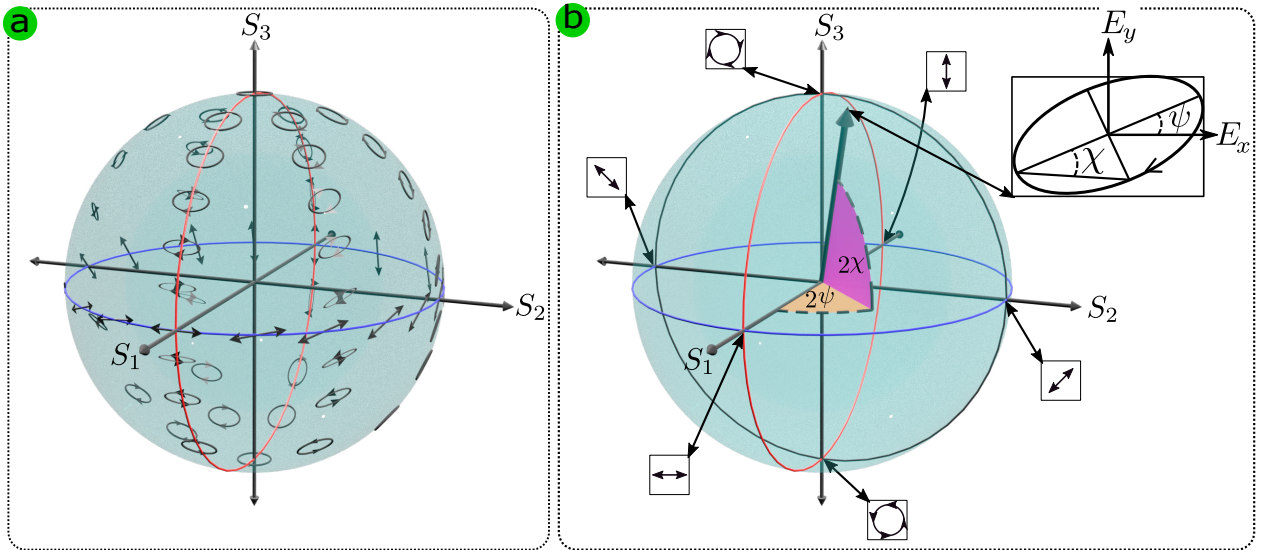


Figure 1.4: Graphical representation of SOP of light in 3D space (Poincaré sphere). **a)** The infinite states of polarization are mapped to a 3D sphere of axes S_1 , S_2 , and S_3 . Each point on the sphere surface corresponds to particular (unique) SOP. The sphere contains a graphical representation of all the SOP on its surface, with the linearly polarized states placed around the equator, and the two circularly polarized states at the poles. **b)** Locus of a radius vector with spherical coordinates (DOP , 2ψ , 2χ) points to particular point on the sphere that represent a polarization ellipse (inset) of ellipticity χ and azimuth ψ .

All states of the left elliptical polarization are located in the north hemisphere, with the left circular polarization being the extreme state located at the north pole (ellipticity $0 < \chi \leq \frac{\pi}{4}$). Polarization states with opposite handedness are on the south hemisphere and right handed circular polarization is located on south pole (ellipticity $0 > \chi \geq -\frac{\pi}{4}$). All the linear polarization states (ellipticity $\chi = 0$) are located on the 2D circle (the sphere equator) that connects the two hemispheres.

To present a SOP on the sphere of ellipticity χ and azimuth ψ , we draw a vector from the center to the surface of the sphere. This radius vector has spherical coordinates of distance= DOP , polar angle (latitude angle)= 2χ , and azimuth= 2ψ as shown in Figure 1.4-b. For fully polarized light, the radius of the sphere is one, it is smaller than one for partially polarized light while the radius converges to zero for unpolarized light.

Orthogonal polarization states on the Poincaré sphere

Polarization states whose characteristic points are at opposite ends of a diameter of the sphere are orthogonal. Three examples of orthogonal polarization states are shown in Figure 1.4-b. They are the intersections of the sphere with the 3D Cartesian space of the axes S_1 , S_2 , and S_3 at six points: i) the two points where the S_1 -axis intersects with the sphere are linear horizontally and vertically polarization states, ii) the two points where the S_2 -axis intersects with the sphere are $\pm 45^\circ$ rotated linear polarization states, and iii) the two points where the S_3 -axis intersects with the sphere are left and right circular polarization states. This is true for any two orthogonal states (states with perpendicular azimuths, opposite directions, but identical ellipticity), which means that any two orthogonal polarization states create a diametrical axis on the sphere.

Two cases of polarization states on Poincaré sphere

For a linear fully polarized light ($DOP=1$, $\chi = 0 \equiv S_3 = 0$), the azimuth ψ is a function of Stokes parameters S_1 and S_2 . The plot of ψ versus S_1 and S_2 creates a circle (blue circle in Figure 1.4) in which all the linear states of polarization are located on the circumference of the circle as shown in Figure 1.5-a. Each point on the blue circle represents a particular linear state of polarization. For polarization states whose major axes are located on x -axis (not rotated) and thereby $\psi = 0 \equiv S_2 = 0$, we can plot ellipticity χ as a function of S_3 and S_1 . The plot is also a circle in which polarization states from linear to circular (right and left handed) are located on the circumference of the circle as shown in Figure 1.5-b. In both plots, the radius of the circles is defined by DOP , if $DOP < 1$, then the radius of the circle is < 1 .

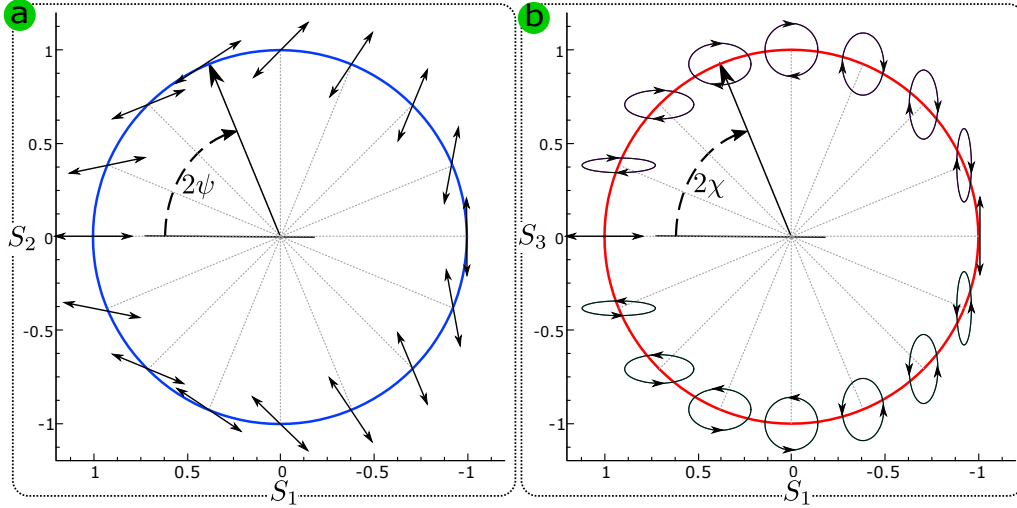


Figure 1.5: Graphical representation of the polarization states of light in 2D space in two case of the polarization ellipse. **a)** Evolution of polarization azimuth ψ as a function of Stokes parameters S_2 and S_1 when ellipticity $\chi=0$ ($S_3=0$). **b)** Evolution of polarization ellipticity χ as a function of Stokes parameters S_3 and S_1 when azimuth $\psi=0$ ($S_2=0$).

1.1.7 Evolution of Stokes parameters in optical systems

In the previous sections, when we discussed the polarization of light, we assumed that the light wave is propagating in free space. Since light is an electromagnetic wave, its properties change (e.g. wavelength, polarization) as it propagates through a material or device. If the material is optically isotropic[‡], lossless and dielectric (insulator), the only property of light that changes is its wavelength, and therefore its speed. The ratio between the speed of light in free space to the speed in a material ($\frac{c}{v}$) is called refractive index (n) of that material. Regarding polarization of an electromagnetic plane wave that is composed of two decoupled components (E_x and E_y), in isotropic materials, the two components of the wave interact symmetrically in all directions during their propagation. The interaction of light does not depend on the direction of propagation nor its SOP. Therefore, in an optically isotropic dielectric material, all SOP of the light wave and thus their Stokes parameters are maintained during propagation.

1.1.7.1 Birefringent systems

Birefringent systems are optical systems which are sensitive to polarization of light. Contrary to isotropic dielectric materials, in such systems, all SOP of the light wave and thus its Stokes parameters are modified during propagation, except for two orthogonal states called eigenmodes of the system. This means that if a light wave with the polarization of either of the eigenmodes propagates in the corresponding birefringent system, its polarization does not

[‡]The optical properties of the material are the same in all directions

change. However, in general, the two eigenmodes propagate in the corresponding birefringence system with different velocity and are known as the slow and fast eigenmodes (i.e., the slow and fast eigenmodes have different refractive indices). When a light wave whose polarization is different from that of the eigenmodes enters a birefringence system, it decomposes into two eigenmodes with a certain phase difference between them. As the two eigenmodes propagate at different speeds, the slow eigenmode is retarded with respect to the fast eigenmode (change in phase difference); the light that exits the system is a superposition of the two eigenmodes with a new (different) phase difference and therefore a different SOP. This behavior is used to build polarization elements (e.g. optical phase retarders work on this principle such as waveplates or Babinet-Soleil compensators). However, in integrated photonics, such behaviour is an issue since light wave with polarization other than the eigenmodes cannot propagate without being modified, it is known as polarization beating.

1.1.7.2 Birefringence systems and Poincaré sphere

The polarization beating corresponds to the periodic evolution of the light polarization along the propagation path inside a birefringent system. This evolution can be elegantly represented graphically using the Poincaré sphere. We have explained that points at opposite ends of a diameter axis of the Poincaré sphere represent two orthogonal polarization states. Since birefringence systems are characterized by two orthogonal eigenmodes, the two eigenmodes create a diameter axis of the Poincaré sphere as shown by the red arrow in Figure 1.6. If a light wave propagates in z -direction, the evolution of the polarization's Stokes parameters through the birefringence system is described by [41]:

$$\frac{\partial \mathbf{S}}{\partial z} = \boldsymbol{\Omega} \times \mathbf{S} \quad (1.30)$$

where $\boldsymbol{\Omega} = \frac{2\pi}{\lambda}(n_{slow} - n_{fast}) \cdot \mathbf{S}_{em}$. λ , n_{slow} , and n_{fast} are light wavelength in free space, refractive index of slow eigenmode, and refractive index of fast eigenmodes respectively. \mathbf{S}_{em} is slow eigenmode's Stokes vector with projections $S_{1(em)}$, $S_{2(em)}$, and $S_{3(em)}$ defined by the equation 1.29. Indeed, the eigenmodes of the system are the solutions of $\frac{\partial \mathbf{S}_{em}}{\partial z} = 0$. Equation 1.30 states that, when a light wave propagates through a birefringent system from any initial position, the evolution of the Stokes vector continuously traces a circular orbit perpendicular to the axis connecting the orthogonal eigenmodes on the Poincaré sphere, as shown in Figure 1.6. The magnitude of the evolution (i.e. phase retardation or polarization beating) is defined by:

$$\phi = |\boldsymbol{\Omega}| \cdot l = \frac{2\pi}{\lambda} \cdot (n_{slow} - n_{fast}) \cdot l \quad (1.31)$$

where l is the length of the birefringent system.

Briefly, if a light wave with particular SOP propagates in a birefringent system whose length and birefringence magnitude ($n_{slow} - n_{fast}$) are known, the SOP of the output light can

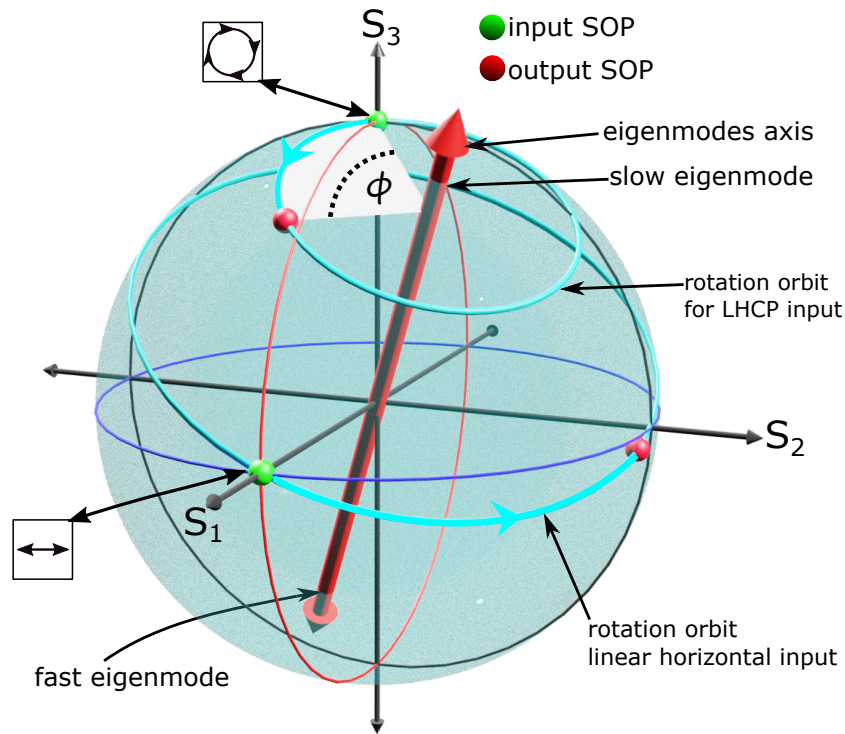


Figure 1.6: Poincaré sphere representation of evolution of polarization of light when propagates through a birefringence system. It is a periodic rotation on a circular orbit perpendicular to an axis connecting orthogonal eigenmodes.

be determined using Poincaré sphere by performing the following steps which are graphically shown in Figure 1.6

1. Locate the point on the sphere corresponding to the input light SOP, green point in the figure.
2. Define the eigenmodes axis of the system by assigning a diametric axis connecting the eigenmodes, red arrow on the figure.
3. Rotate the input SOP point about the eigenmodes axis in a perpendicular orbit by an angle defined by equation 1.31, to get the final point, red point in the figure.

The examples of the input SOPs in Figure 1.6 are left handed circular (LHCP) and horizontal linear polarizations. From the evolution of the two inputs we can see that, the more close to the eigenmodes axis, the smaller the rotation orbit and thereby, the smaller the polarization change. As stated by equation 1.30, the eigenmodes are the SOPs whose the size of rotation orbit is zero.

1.2 Light Guiding in Planar Optical Waveguides

Planar optical waveguides are optical systems that confine light waves in their structures made of a material with a high refractive index (compared to the surrounding). In this section, we will use electromagnetic theory to describe the behaviour of light waves in such structures and find the eigenmodes (guided modes) for the propagated waves.

1.2.1 Planar waveguides equations

To derive planar waveguide equations, we start by writing Maxwell equations 1.1c and 1.1d for homogenous lossless dielectric media:

$$\nabla \times \mathbf{E} = -\mu \frac{\partial \mathbf{H}}{\partial t} \quad (1.32)$$

$$\nabla \times \mathbf{H} = \varepsilon \frac{\partial \mathbf{E}}{\partial t} \quad (1.33)$$

where ε and μ are electric permittivity and magnetic permeability of the dielectric media. We have schematized in Figure 1.7 a typical structure of a planar waveguide. It is characterized by a plane-parallel refractive index limit in the (x) direction, but having infinite extent in the lateral (y and z) directions. Since the structure is infinite in the y and z directions, the electric and magnetic fields of the light propagating in such structure have the property of translational invariance in these directions. Therefore, the electric and magnetic fields of a wave propagating in z direction satisfying Maxwell wave equation are written as:

$$\mathbf{E} = \mathbf{E}_0(x) e^{i(\omega t - \beta z)} \quad (1.34a)$$

$$\mathbf{H} = \mathbf{H}_0(x) e^{i(\omega t - \beta z)} \quad (1.34b)$$

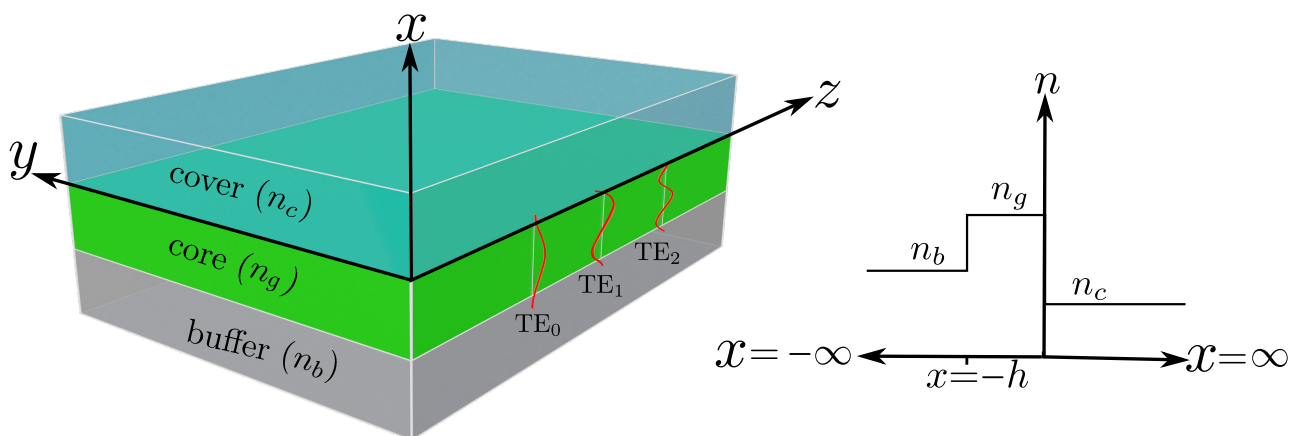


Figure 1.7: Structure of a typical planar waveguide with z -axis as the propagation direction and step refractive index in x -axis.

And, the nabla(also called Del) operator in equation 1.32 and 1.33 become:

$$\nabla = \begin{bmatrix} \frac{\partial}{\partial x} \\ 0 \\ -i\beta \end{bmatrix} \quad (1.35)$$

For non-magnetic dielectric materials $\mu = \mu_0$ and $\varepsilon = \varepsilon_0 n^2$. Inserting electric and magnetic field equations (1.34a, 1.34b) into the equations 1.32 and 1.33 and using the above relations we get:

$$\left. \begin{aligned} i\beta E_y &= -i\omega\mu_0 H_x \\ \frac{\partial E_y}{\partial x} &= -i\omega\mu_0 H_z \\ i\omega\varepsilon_0 n^2 E_y &= -\frac{\partial H_z}{\partial x} - i\beta H_x \end{aligned} \right\} \text{Transverse Electric} \quad (1.36)$$

$$\left. \begin{aligned} i\beta H_y &= i\omega\varepsilon_0 n^2 E_x \\ \frac{\partial H_y}{\partial x} &= i\omega\varepsilon_0 n^2 E_z \\ i\omega\mu_0 H_y &= \frac{\partial E_z}{\partial x} + i\beta E_x \end{aligned} \right\} \text{Transverse Magnetic} \quad (1.37)$$

The two equations 1.36 and 1.37 represent the two allowed propagated modes in planar waveguides which are Transverse Electric (TE) and Transverse Magnetic (TM) modes. For the TE, the E_y component of the field is transverse to the direction of propagation while the E_z and E_x are zero. For the TM, it is the H_y component of the magnetic field that is transverse; the H_z and H_x are zero. By observing the electric fields of the two modes, we deduce that the TE and TM modes are two orthogonal modes polarized parallel and perpendicular to the plane of the waveguide.

1.2.2 Guided modes propagation equations

1.2.2.1 TE mode

Mathematically speaking, a mode is a field distribution that is a solution of Maxwell wave equation. For the TE mode, $Ez = Ex = Hy = 0$, the transverse electric field E_y is the solution of the following wave equation

$$\frac{\partial^2 E_y}{\partial x^2} + [k^2 n^2(x) - \beta^2] E_y = 0 \quad (1.38)$$

where magnetic fields are related to the transverse electric field by $H_x = \frac{-\beta E_y}{\omega\mu_0}$ and $H_z = \frac{i}{\omega\mu_0} \frac{\partial E_y}{\partial x}$.

If we take the example of a planar waveguide shown in Figure 1.7. It consists of three layers (cover, core(guiding), and buffer) with refractive indices of n_c , n_g and n_b respectively. We can write TE-wave equations for each layer as:

$$\frac{\partial^2 E_y}{\partial x^2} + (k^2 n_c^2 - \beta^2) E_y = 0 \quad (\text{cover}) \quad (1.39a)$$

$$\frac{\partial^2 E_y}{\partial x^2} + (k^2 n_g^2 - \beta^2) E_y = 0 \quad (\text{core}) \quad (1.39b)$$

$$\frac{\partial^2 E_y}{\partial x^2} + (k^2 n_b^2 - \beta^2) E_y = 0 \quad (\text{buffer}) \quad (1.39c)$$

To simplify these equations, we assign wave vectors for each layer as $(k^2 n_c^2 - \beta^2) = -\Omega_c^2$, $(k^2 n_g^2 - \beta^2) = \Omega_g^2$, and $(k^2 n_b^2 - \beta^2) = -\Omega_b^2$. Inserting Ω_c , Ω_g , and Ω_b into equations 1.39 they become:

$$\frac{\partial^2 E_y}{\partial x^2} - \Omega_c E_y = 0 \quad (\text{cover}) \quad (1.40a)$$

$$\frac{\partial^2 E_y}{\partial x^2} + \Omega_g E_y = 0 \quad (\text{core}) \quad (1.40b)$$

$$\frac{\partial^2 E_y}{\partial x^2} - \Omega_b E_y = 0 \quad (\text{buffer}) \quad (1.40c)$$

For guided modes, the condition $kn_g > \beta > kn_{b,c}$ must be fulfilled, which means that the solutions of the above equations are sinusoidal in the core layer and exponentially decaying in the surrounding layers. In other words, a guided mode is a confined electromagnetic field with a propagated wave in the core layer and evanescent waves in the surrounding layers. Therefore, the field distribution of the TE mode can be written as [42]:

$$E_y = \begin{cases} Ae^{-\Omega_c x} & 0 \leq x < \infty & (\text{cover}) \\ B \cos(\Omega_g x) + C \sin(\Omega_g x) & -h \leq x \leq 0 & (\text{core}) \\ De^{\Omega_b(x+h)} & -\infty < x \leq -h & (\text{buffer}) \end{cases} \quad (1.41)$$

where A, B, C , and D are constants. Boundary conditions require the continuity of E_y field (which means H_x as well) and H_z (thereby $\frac{\partial E_y}{\partial x}$) at the boundaries of the core layer at $x = 0$ and $x = -h$. Using the boundary condition of continuity of $\frac{\partial E_y}{\partial x}$ at the interface $x = 0$, the equations 1.41 can be simplified to:

$$E_y = A \begin{cases} e^{-\Omega_c x} & 0 \leq x < \infty & (\text{cover}) \\ [\cos(\Omega_g x) - \frac{\Omega_c}{\Omega_g} \sin(\Omega_g x)] & -h \leq x \leq 0 & (\text{core}) \\ [\cos(\Omega_g h) + \frac{\Omega_c}{\Omega_g} \sin(\Omega_g h)] e^{\Omega_b(x+h)} & -\infty < x \leq -h & (\text{buffer}) \end{cases} \quad (1.42)$$

Now, by using the continuity of $\frac{\partial E_y}{\partial x}$ at the interface $x = -h$, from equation 1.42 we obtain

$$\tan(\Omega_g h) = \frac{\Omega_b + \Omega_c}{\Omega_g - \frac{\Omega_b \Omega_c}{\Omega_g}} \quad (1.43)$$

From definition of $\Omega_g = (k^2 n_c^2 - \beta^2)$, equations 1.43 is called propagation constant equation of TE mode, meaning that the propagation constant β of the TE mode satisfies this equation. The equation is a periodic function and repeats in $(m\pi, m \text{ is an integer } 0, 1, 2, \dots)$, signifying the discrete number of guided modes. In other words, there are discrete guided modes with propagation constants β_m, m being a positive integer $(0, 1, 2, \dots)$, are called fundamental, first, second mode respectively.

1.2.2.2 TM mode

What we have done so far for the TE mode, can also be repeated with the same procedure to obtain similar results for the TM mode (H_y field). The only difference in deriving propagation constant equation for TM compared to TE one is the difference in boundary conditions. For TM mode, the boundary conditions at the core interfaces $x = 0$ and $x = -h$ are continuity of H_y (and thereby of $\varepsilon_0 n^2 E_x$) and of E_z (and thereby of $\frac{1}{n^2} \frac{\partial H_y}{\partial x}$). If we apply these boundary conditions on TM wave equation, we get TM mode propagation equation

$$\tan(\Omega_g h) = \frac{\Omega_g(\bar{\Omega}_b + \bar{\Omega}_c)}{\Omega_g^2 - \bar{\Omega}_b \bar{\Omega}_c} \quad (1.44)$$

where $\bar{\Omega}_b = \frac{n_g^2}{n_b} \Omega_b$, and $\bar{\Omega}_c = \frac{n_g^2}{n_c} \Omega_c$.

1.2.2.3 Computation of propagation constant

Using equations 1.43 and 1.44, if the refractive indices of the waveguide layers and thickness of the core layer are known, the β (and thus the effective refractive index of the TE and TM mode) can be computed. After computation of β , we can use equation 1.42 to plot the field profile of TE guided modes as shown in Figure 1.7 for the three TE modes (TE₀, TE₁, TE₂). The profile of TM is mode (H_y field) is nearly identical to the one TE mode (E_y field) such that one can consider the profiles shown in Figure 1.7 as the three TM modes (TM₀, TM₁, TM₂). The integer m defines the number of lobes in the guided filed, for example TE₀ and TE₁ modes profile have one and two lobes respectively.

From the computations, we have plotted in Figure 1.8 dispersion curves of the guided modes for a planar waveguides at ($\lambda = 0.633, n_c=1, n_g = 1.61, \text{ and } n_b = 1.52$). It can be noted from the figure that TE and TM modes propagate with different effective refractive indices which verifies the birefringent nature of planar waveguides. For a constant wavelength, the number of the guided modes depend on the core thickness and refractive index contrast ($\Delta n = n_g - n_b$). Waveguides that supports only one guided modes of each polarization state (TE₀, TM₀), are called single-mode waveguides. Such kind of waveguides are preferable in integrated photonics. Indeed, manipulation of waveguides that are not single-mode is much more difficult since interaction of fundamental modes (TE₀, TM₀) with higher order mode sometimes gives undesirable effects. In what follows in this manuscript (the calculations and

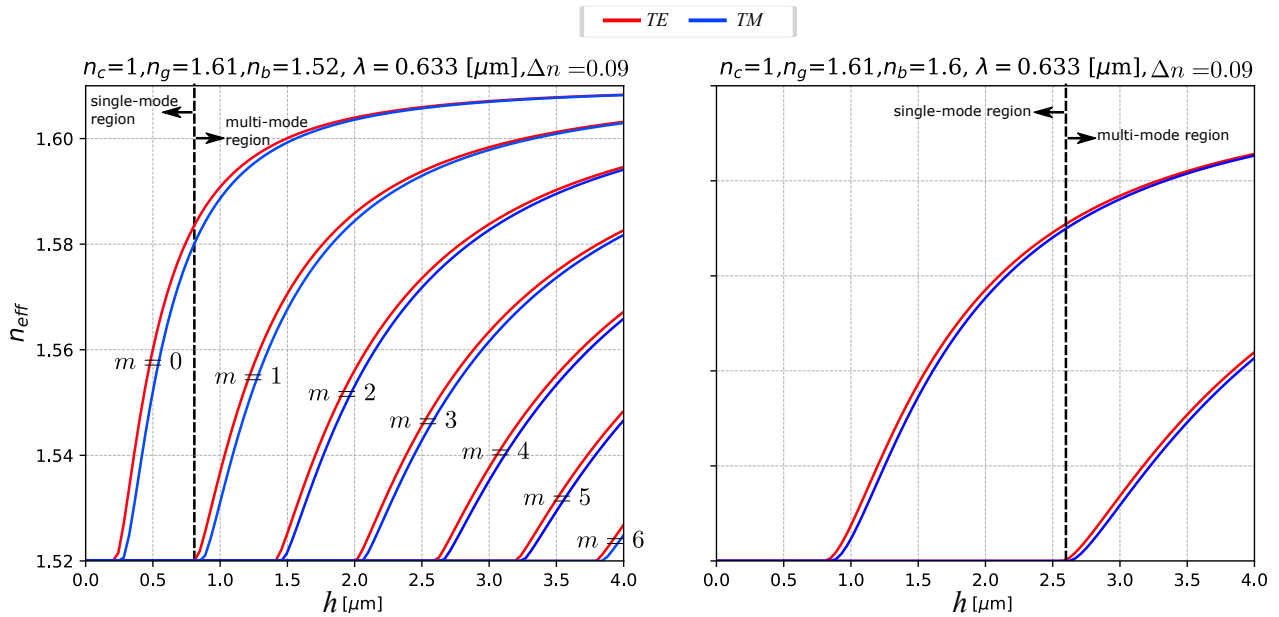


Figure 1.8: Evolution of effective refractive index of the guided modes of a planar waveguide as a function of waveguide's thickness h , for two refractive index contrasts ($\Delta n = n_g - n_b$)

experimental measurements), we consider that the waveguides are single mode. Since a single-mode waveguide supports only one TE and TM mode, which are linear polarization modes, the linear birefringence in planar waveguides is quantified as:

$$LB = n_{TE_0} - n_{TM_0} \quad (1.45)$$

LB depends on the thickness of the planar waveguide and decreases with increasing thickness as indicated by the space between the TE_0 and TM_0 curves in Figure 1.8. However, It decreases significantly by decreasing the refractive index contrast (Δn). Quantitatively, for a planar waveguide with properties ($n_c = 1, n_g = 1.61, \lambda = 0.633\mu\text{m}$, and thickness $h = 2\mu\text{m}$) $LB = 4 \times 10^{-4}$ if refractive index contrast $\Delta n = 0.09$, the LB value reduces to half ($LB = 2 \times 10^{-4}$) for $\Delta n = 0.01$. These theoretical results show the importance of a low Δn to obtain low LB planar waveguides.

1.2.3 Polarization beating in planar waveguides

We have shown that planar waveguides are birefringent systems with eigenmodes that are two linear polarization modes (TE and TM). Therefore, if a light wave is guided inside such waveguide, its SOP undergo a periodic modulation, unless its SOP corresponds to TE and TM. The polarization modulation which is known as polarization beating can be graphically presented using Poincaré sphere. As stated by equation 1.30, on the Poincaré sphere, the modulation corresponds to a rotation of the initial SOP about a diameter axis of the sphere

defined by the eigenmodes TE and TM. In Figure 1.9, we have shown the polarization beating for two guided waves if their initial polarization state is (left circular and horizontal linear). The linear horizontal polarization is not modified and its rotation orbit is zero since its polarization corresponds to one of the eigenmodes. However, the left handed circular polarization (LHCP) is modified to the highest extent and rotation orbit is the highest. The periodic polarization modulation of LHCP correspond to change in ellipticity χ from $\chi = \pm\frac{\pi}{4} \rightleftharpoons \chi = 0$.

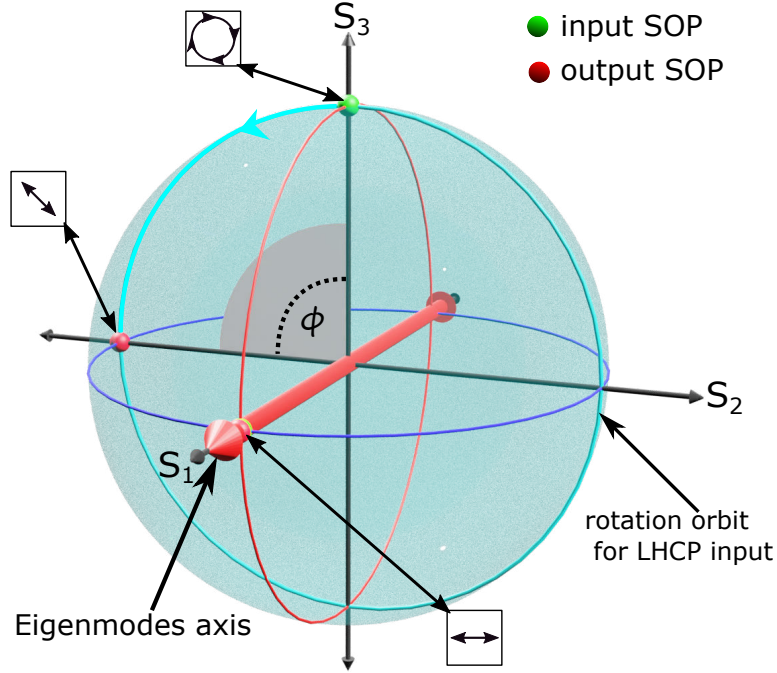


Figure 1.9: Birefringent effect of planar optical waveguides, Poincaré sphere representation of polarization beating for left handed circular polarization (LHCP) and linear horizontally polarization inputs.

Regarding the polarization beating magnitude in planar waveguides, since linear birefringence is defined by effective refractive index difference of TE and TM, the equation 1.46 become:

$$\phi = \frac{2\pi}{\lambda} \cdot (n_{TE} - n_{TM}) \cdot l = \frac{2\pi}{\lambda} \cdot \text{LB} \cdot l \quad (1.46)$$

This equation indicates that the magnitude of the polarization modulation (angle ϕ) in planar waveguides is proportional to the LB and the length of the waveguide (l). In the Figure 1.9, we have shown a particular case where $\phi = \frac{\pi}{2}$, the output polarization is a linear polarization at -45° with respect to x for left handed circularly polarized input. Because of this polarization modulation, it is practically impossible to handle circular polarization in planar waveguides or to use planar waveguides for circular polarization applications such as chiral sensing.

1.3 Channel Waveguides

Channel waveguides are rectangular optical structures whose dimensions are of the order of the wavelength of the light. In contrast to planar waveguides, channel waveguides provide confinement of light not only in x -direction, but in $x - y$ -directions. Furthermore, they can be designed to have zero birefringence property (i.e. equivalent interaction of TE and TM modes $n_{\text{TE}} = n_{\text{TM}}$) [18]. This makes channel waveguides a perfect waveguide structure for our objective of realizing waveguides that can support any polarization. In this section, we describe light confinement and properties of channel optical waveguides.

1.3.1 Channel waveguide equations

In Figure 1.10, we have shown the structure of a typical channel waveguide, it is characterized by a refractive index limit with respect to x and y directions, only having infinite extent in the longitudinal direction (z). A light wave propagating in such waveguides has the property of translation invariance in only z direction. The electric field and magnetic field equations of such wave propagating in z direction can be written as:

$$\mathbf{E} = \mathbf{E}_0(x, y) e^{i(\omega t - \beta z)} \quad (1.47a)$$

$$\mathbf{H} = \mathbf{H}_0(x, y) e^{i(\omega t - \beta z)} \quad (1.47b)$$

Thus, the nabla operator in Maxwell equations 1.32 and 1.33 is:

$$\nabla = \begin{bmatrix} \frac{\partial}{\partial x} \\ \frac{\partial}{\partial y} \\ -i\beta \end{bmatrix} \quad (1.48)$$

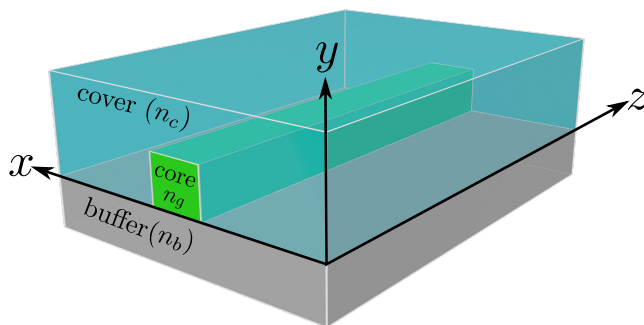


Figure 1.10: Structure of a typical channel waveguide with z -axis as the propagation direction.

Inserting electric and magnetic field equations (1.47a, 1.47b) into equations 1.32 and 1.33, and using the relation 1.48, we get:

$$\frac{\partial E_z}{\partial y} + i\beta E_y = -i\omega\mu H_x \quad (1.49a)$$

$$\frac{\partial E_z}{\partial x} + i\beta E_x = i\omega\mu H_y \quad (1.49b)$$

$$\frac{\partial E_y}{\partial x} - \frac{\partial E_x}{\partial y} = -i\omega\mu H_z \quad (1.49c)$$

$$\frac{\partial H_z}{\partial y} + i\beta H_y = i\omega\varepsilon(x, y)E_x \quad (1.49d)$$

$$\frac{\partial H_z}{\partial x} + i\beta H_x = -i\omega\varepsilon(x, y)E_y \quad (1.49e)$$

$$\frac{\partial H_y}{\partial x} - \frac{\partial H_x}{\partial y} = i\omega\varepsilon(x, y)E_z \quad (1.49f)$$

As it can be seen from these equations 1.49, in channel waveguides, the modes are no more TE, TM modes but hybrid modes. In these modes, the three components of the electric (E_x, E_y, E_z) and magnetic field (H_x, H_y, H_z) are all depending on each other. To our knowledge, to date, there are no analytical solutions for these equations. Therefore, the guided modes must be determined using numerical methods.

1.3.2 Computation of guided modes in channel waveguides

In our study, to find properties of guided modes in channel waveguide, we use a full-vector finite-difference method that has been fully documented elsewhere [43]. We have used an open-source Python computer programming language package that encompasses the method and give clear examples of using such method to find guided modes in dielectric channel waveguides [44]. Our task for using the method is creating a 2D matrix ε_{ij} that describes the waveguide structure in term of electric permittivity ε (and thereby refractive index n). Each element of the matrix defines the refractive index at that position which is associated with surrounding refractive indices. The computations shown in the following were performed by creating $15 \times 15 \mu\text{m}^2$ refractive index meshgrid with a 50nm step length. These conditions are chosen as an optimised conditions based on computation time and accuracy.

In Figure 1.11, we have plotted the computed field components of the fundamental modes for a rectangle waveguide with ($n_c = 1, n_g = 1.61, n_b = 1.52, w = 3\mu\text{m}$, and $h = 2\mu\text{m}$). It can be noted that, the guided modes of channel waveguides are not similar to TE and TM modes of planar since the longitudinal components of the electric and magnetic field are not zero. However, the guided mode shown in Figure 1.11-a is known as quasi-TE mode since $(E_y, E_z, H_x) \ll (E_x, H_y, H_z)$, and, the one in Figure 1.11-b is known quasi-TM mode since $(E_x, H_y, H_z) \ll (E_y, E_y, H_y)$. Furthermore, for the quasi-TE mode $H_z \ll (E_x, H_y)$,

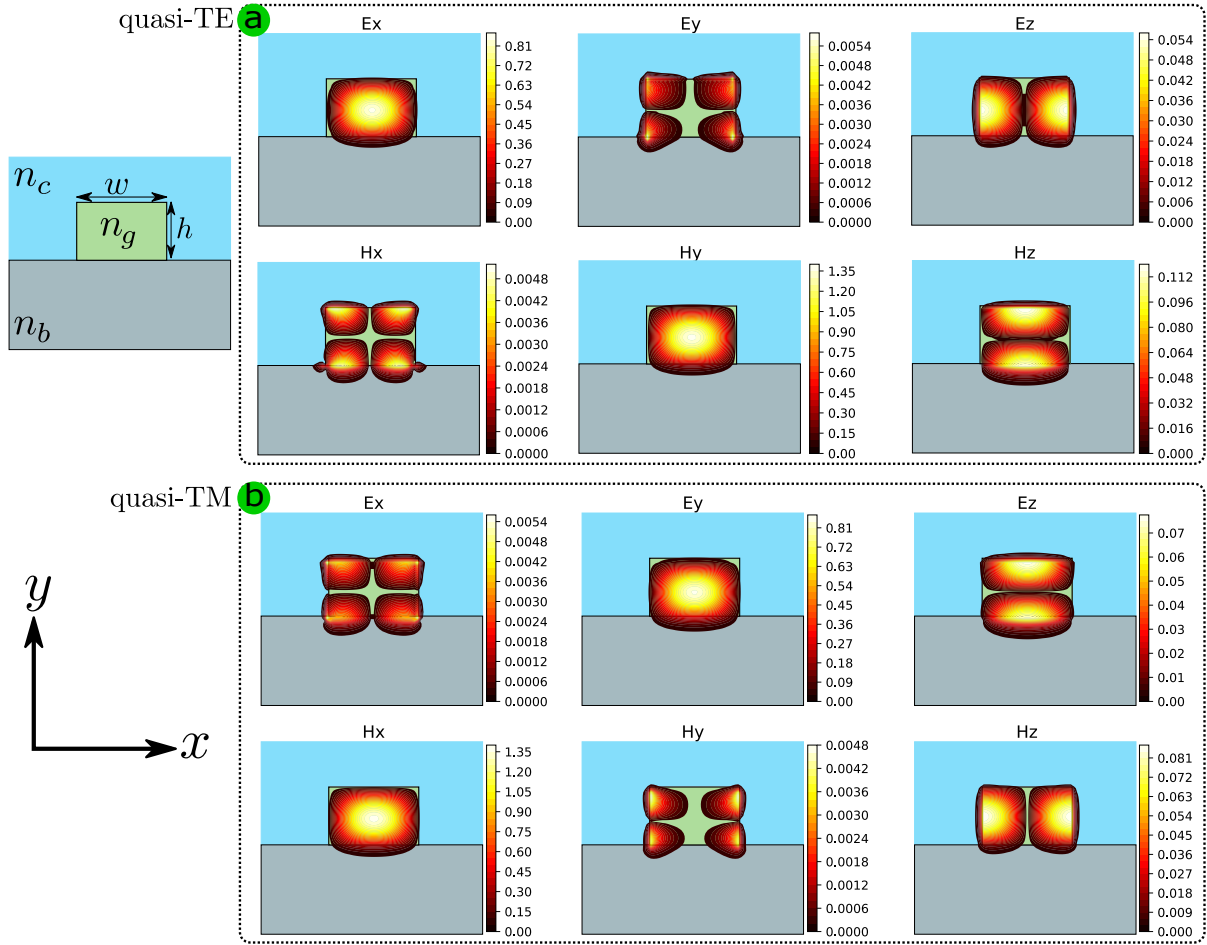


Figure 1.11: Computed guided light field components distribution in channel waveguides using a full-vector finite-difference numerical computation method for **a)** quasi- TE_{00} mode, and **b)** quasi- TM_{00} mode.

for the quasi-TM mode $E_z \ll (E_y, H_x)$. We therefore, consider the guided modes in the channel waveguides as two orthogonal plane waves so that we can treat them using plane wave considerations.

1.3.2.1 Classification of channel waveguides

Depending on the position of the waveguide core (relative to its surroundings) and its geometry, channel waveguides are classified into different types (the most common ones are buried, diffused, ridge, rib and strip-loaded). In Figure 1.12, we have drawn the typical cross-section and computed guided intensity distribution of the fundamental modes (TE_{00} and TM_{00}) in these five types of channel waveguides. Each type has its own advantage and disadvantage depending on the applications. Considering our objective, "channel waveguides for sensing applications", we shall not study the modal properties of buried and strip-loaded channels because the guided field is not in contact with the surrounding medium. Therefore, we only

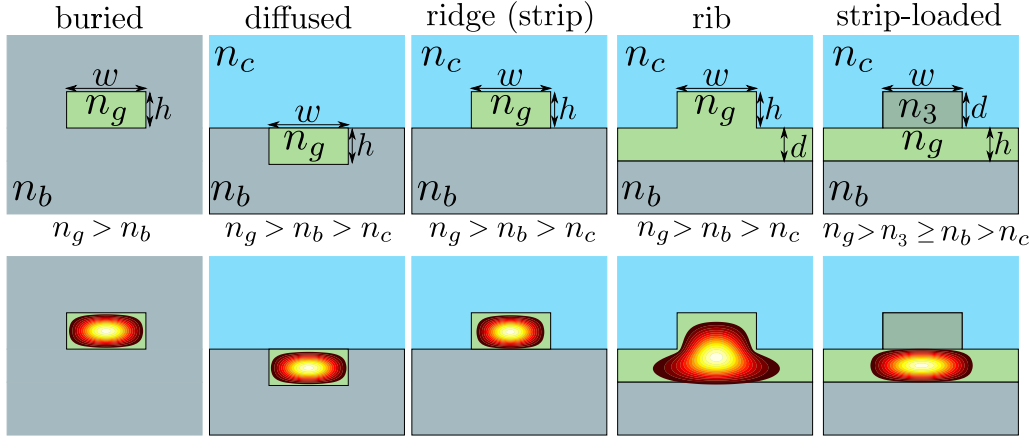


Figure 1.12: Top) Cross-section and Bottom) Computed guided field distribution of the fundamental mode in five types of channel waveguides.

study modal properties for diffused, ridge, and rib channel waveguides with the condition (cladding layer is air $n_c = 1$), the sky-blue region in Figure 1.12.

1.3.2.2 Guided modes dispersion curves in channel waveguides

To further investigate the behavior of the guided modes and determine their propagation constant for the three types of channels, we calculated the dispersion curves of the guided modes. In the computations, the cover is set to be air to satisfy the condition that the guided can interact with surrounding. The buffer layer is set to be glass as a conventional substrate for light guiding, and the waveguide core is set to have $n = 1.61$ that is the refractive index of the material we want to use. Figure 1.13 shows the effective refractive indices evolution of $TE_{00}(TM_{00})$ guided modes in diffused, ridge, and rib channel as a function of width and height of the channels. When the channel's dimensions are small, no guided modes are present, the channel start to support guided modes at certain dimensions. The behaviour of guided modes is not defined by only the dimensions and refractive index contrast ($n_g - (n_b, n_c)$) but also by the type of the channel. For instance, rib channel start to support guided modes at higher w compared to ridge and diffused channels.

From Figure 1.13, we can see that the effective refractive index curves for TE_{00} (red curves) and TM_{00} (blue curves) are different regardless of the channel type, indicating that the channel waveguides are birefringent. Since TE_{00} and TM_{00} are linearly polarized guided modes, linear birefringence LB is quantified as:

$$LB = n_{TE_{00}} - n_{TM_{00}} \quad (1.50)$$

Although the dispersion curves indicate that the channels are birefringent, in all three channels there are geometries in which the curves intersect (black circle in Figure 1.13). The intersections between the curves in Figure 1.13 means that channel waveguides can be fabri-

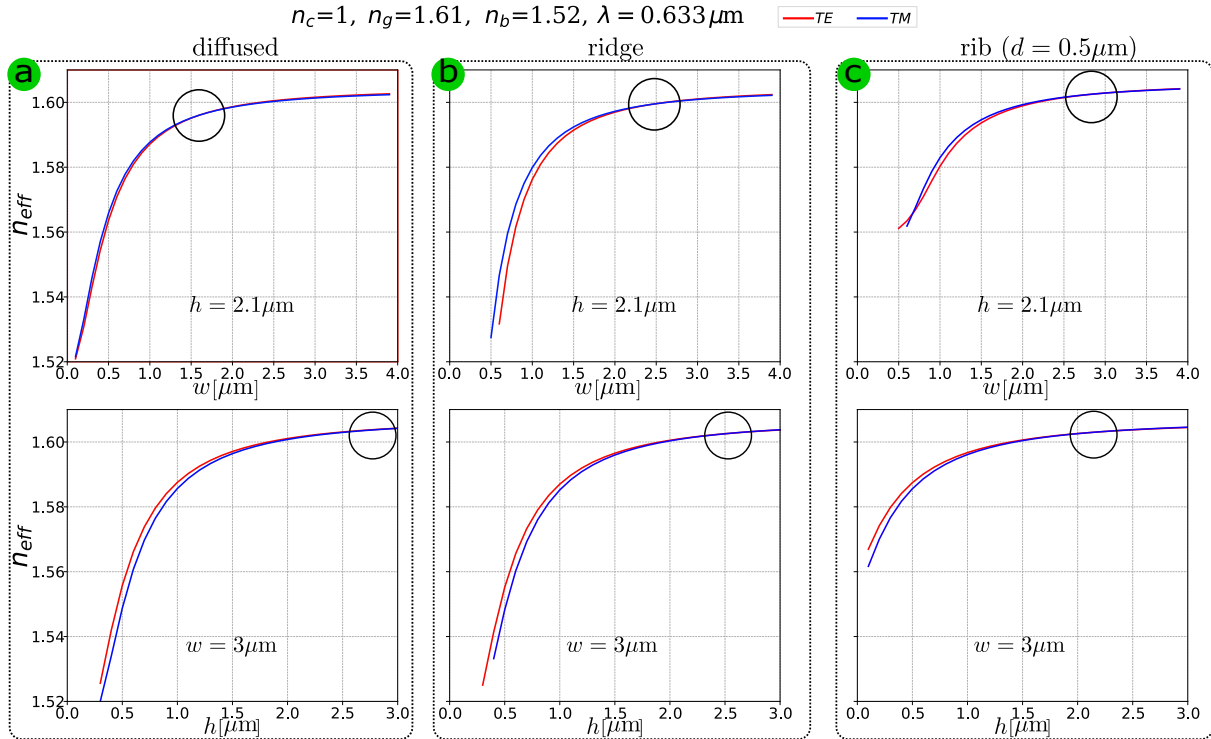


Figure 1.13: Evolution of effective refractive indices of guided modes as function of width of w and height in **a)** diffused, **b)** ridge, and **c)** rib waveguides. The TE_{00} and TM_{00} curves intersect at the position indicated by the black circle.

cated to have zero birefringence. The intersection also means that zero birefringence property of channel waveguides is only present for exact given geometries, the slightest deviation from the ideal channel geometry lead to non-zero LB. This behavior of channel waveguides makes the fabrication of channel waveguides with zero birefringence property a challenging technological task because the waveguide geometry must be maintained in centimeter length with nanometer precision. For such reason, channel waveguides are currently only used for polarization applications based on TE/TM polarizations. We will show in the upcoming sections, how channel optical waveguides can be used for circular polarization applications without zero birefringence condition if the waveguides are made of chiral material.

1.3.3 Polarization beating in channel waveguides

Channel waveguides are birefringent systems with TE/TM edgemodes similar to the planar waveguides. Therefore, the birefringent effect of such waveguides on polarization beating is identical to planar waveguides. To avoid repeating what we have already explained, we do not show the Poincaré sphere representation of the polarization beating in the channel waveguides, the reader can find the explanation in 1.2.3.

1.4 Chirality and Light

Chirality is a property of geometry and asymmetry, a chiral object is three-dimensional body which cannot be superimposed with its mirror image by any solid translation and rotation. The origin of the word chiral comes from the Greek word /Kheir/ "χξρι" which means "hand". Chirality is also called "handedness", our hands are non-superimpose mirror images as shown in Figure 1.14-a. The word chiral was first introduced by Lord Kelvin in the late 19th century in the following form: "I call any geometrical figure, or group of points, 'chiral', and say that it has chirality if its image in a plane mirror, ideally realized, cannot be brought to coincide with itself" [45].

The chiral property can also be found at the molecular level, some molecules look like non-superimposable images and are known as enantiomers (Figure 1.14-b). When a material or medium is composed of (+)/(-) enantiomers, it is said to have a chiral (+)/(-) property. A material containing the two enantiomers in equal amounts 50:50% is called racemic and has no chiral property. Since enantiomers have identical chemical composition, they share most of their physical and chemical properties. However, their interaction with other chiral objects is different, which is the behavior of any chiral object, including enantiomers. This behavior can be observed when light propagates through a chiral material, the polarization plane of linearly polarized light rotates in one direction for the (+) enantiomer and in the opposite direction for the (-) enantiomer. Indeed, light has a chiral property, circularly polarized light waves behave as chiral objects (Figure 1.14-c), left and right circularly polarized light waves interact differently with chiral materials. The phenomenon of plane of polarization rotation by chiral materials is known as optical activity. In the following, we will discuss the propagation of light in chiral materials and the physical principle behind the rotation of linear polarization.

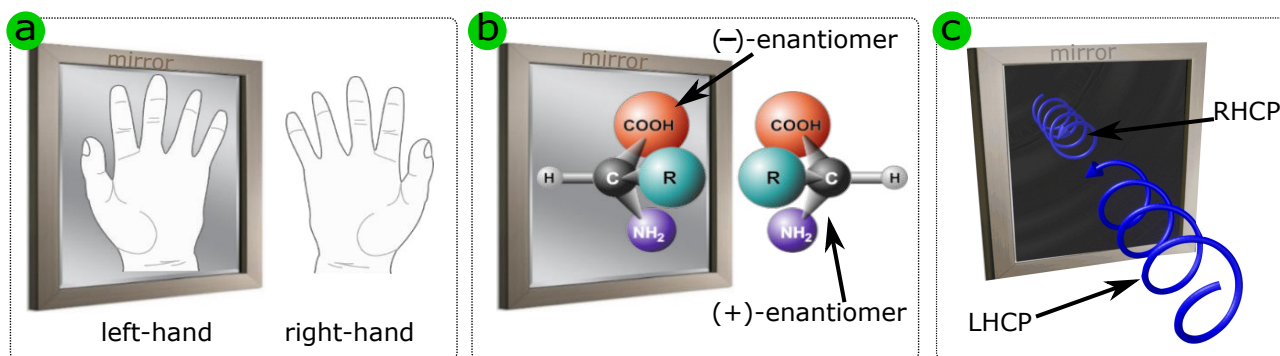


Figure 1.14: Chiral objects **a)** Our hands, **b)** Some molecules (Amino acid), and **c)** Circularly polarized light.

1.4.1 Light propagation in bulk chiral media

The behavior of light propagation in a bulk chiral medium can be described using Maxwell equations and the constitutive equations of chiral materials. Maxwell equations for the propagation of time-harmonic electromagnetic fields of $e^{-i\omega t}$ in a dielectric medium, known as Maxwell equations phasor forms, are the following:

$$\nabla \cdot \mathbf{D} = 0 \quad (1.51a)$$

$$\nabla \cdot \mathbf{B} = 0 \quad (1.51b)$$

$$\nabla \times \mathbf{E} = -i\omega \mathbf{B} \quad (1.51c)$$

$$\nabla \times \mathbf{H} = i\omega \mathbf{D} \quad (1.51d)$$

where \mathbf{D} and \mathbf{B} are electric field displacement and the magnetic flux density respectively. The constitutive equations for the vector fields \mathbf{D} and \mathbf{B} for an isotropic chiral material are known as Drude-Born-Fedorov equations [46, 47]:

$$\mathbf{D} = \varepsilon(\mathbf{E} + \gamma \nabla \times \mathbf{E}) \quad (1.52a)$$

$$\mathbf{B} = \mu(\mathbf{H} + \gamma \nabla \times \mathbf{H}) \quad (1.52b)$$

where γ is a first order parameter that describes the chirality of the material. We can see from equations 1.52a and 1.52b that chirality parameter γ couples electric and magnetic fields. Therefore, solving the above equations is rather complicated. An intuitive way to handle the difficulty of the problem is to decompose the vector fields (\mathbf{E}, \mathbf{H}) using the Bohren decomposition into two independent fields $(\mathbf{E}_+, \mathbf{H}_+)$ and $(\mathbf{E}_-, \mathbf{H}_-)$ [48–50]:

$$\mathbf{E} = \mathbf{E}_+ + \mathbf{E}_- \quad \text{with} \quad \mathbf{E}_\pm = \frac{1}{2}(\mathbf{E} \mp i\sqrt{\frac{\mu}{\varepsilon}}\mathbf{H}) \quad (1.53a)$$

$$\mathbf{H} = \mathbf{H}_+ + \mathbf{H}_- \quad \text{with} \quad \mathbf{H}_\pm = \frac{1}{2}(\mathbf{H} \pm i\sqrt{\frac{\varepsilon}{\mu}}\mathbf{E}) \quad (1.53b)$$

The introduced fields $(\mathbf{E}_+, \mathbf{H}_+)$ and $(\mathbf{E}_-, \mathbf{H}_-)$ are independent of each other and have simple solutions. Regarding the electric field, by using the equations 1.52a, 1.52b, 1.53a, and 1.53b we can obtain:

$$\nabla \times \mathbf{E}_\pm = kn_\pm \mathbf{E}_\pm \quad (1.54)$$

where $n_\pm = \frac{n}{1 \mp \gamma kn}$, k and n are free space wave vector and refractive index of the material respectively. If we take curl of the equations 1.54, we get Helmholtz wave equation for the \mathbf{E}_\pm vector field

$$\nabla^2 \mathbf{E}_\pm + k^2 n_\pm^2 \mathbf{E}_\pm = 0 \quad (1.55)$$

In bulk medium, the general solution of the equation 1.55 is a plane wave. By using equation 1.54 we can show that the equation of the plane wave is in the form:

$$\mathbf{E}_+ = (\hat{x} + i\hat{y})E_{0+}e^{-i\beta_+z} \quad (1.56a)$$

$$\mathbf{E}_- = (\hat{x} - i\hat{y})E_{0-}e^{-i\beta_-z} \quad (1.56b)$$

Note that equations 1.56a and 1.56b correspond to left and right handed circularly polarized (L/RHCP) plane waves propagating in z direction with propagation constants $\beta_{\pm} = kn_{\pm}$. The \hat{x} and \hat{y} are unit vectors, and n_{\pm} are the effective refractive indices of the propagated \mathbf{E}_{\pm} fields. By inserting the solutions of the \mathbf{E}_{\pm} fields (1.56a and 1.56b) into equation 1.53a, we get the equation of the light waves electric field propagating in a bulk chiral medium

$$\mathbf{E} = \mathbf{E}_+ + \mathbf{E}_- = (\hat{x} + i\hat{y})E_{0+}e^{-i\beta_+z} + (\hat{x} - i\hat{y})E_{0-}e^{-i\beta_-z} \quad (1.57)$$

This equation shows that a light wave propagates in a chiral medium as a superposition of two plane waves which are left and right circularly polarized waves. The interaction of the chiral medium with the two plane waves (L/RHCP) results in different interactions (i.e. they have different refractive indices). Therefore, a bulk chiral medium is a birefringent with L/RHCP eigenmodes, so-called circular birefringent medium. Circular birefringence (CB) is quantified as the difference of the effective refractive index of left and right circularly polarized light

$$\begin{aligned} \text{CB} &= n_+ - n_- = \frac{n}{1 - \gamma kn} - \frac{n}{1 + \gamma kn} \\ \text{CB} &\approx 2\gamma kn^2 \quad \text{for } (\gamma kn) \ll 1 \end{aligned} \quad (1.58)$$

This equation shows that CB is linearly proportional to the chirality parameter γ , the higher the chirality of the medium, the higher the CB.

1.4.2 Polarization beating in bulk chiral media

We have shown that chiral bulk materials are birefringent systems with left and right circularly polarized eigenmodes. Therefore, if a light wave propagates in a chiral material, its polarization state undergoes periodic modulation, unless its polarization corresponds to L/RHCP. As we have discussed before, the polarization modulation can be evaluated using the Poincaré sphere. The two eigenmodes create a diameter axis on the sphere that is located on the S_3 axis as shown in Figure 1.15. SOP modulation for a light propagating in chiral medium is a periodic rotation in a circular orbit in a plane perpendicular to the eigenmodes axis. In the figure, we have shown the polarization modulation (beat) for a left circular polarization and a linear horizontal polarization input. The left circular polarization is not modified and its rotation orbit is zero as it is one of the eigenmodes. However, the linear polarization input is rotated in an orbit on

the equator of the sphere, i.e. the azimuth of the polarization is changed. It is the well-known polarization rotation that occurs when light propagates in a chiral medium.

Regarding polarization modulation magnitude, since birefringence in a bulk chiral medium is defined by CB, the equation 1.31 become:

$$\phi = \frac{2\pi}{\lambda} \cdot \text{CB} \cdot l \quad (1.59)$$

This equation[§] indicate that polarization modulation magnitude (ϕ) in a bulk chiral medium is proportional to the CB and the length of the medium (l). In Figure 1.15, we have shown a particular case when $\phi = \frac{\pi}{2}$, then, a linearly polarized wave input is rotated by 45° .

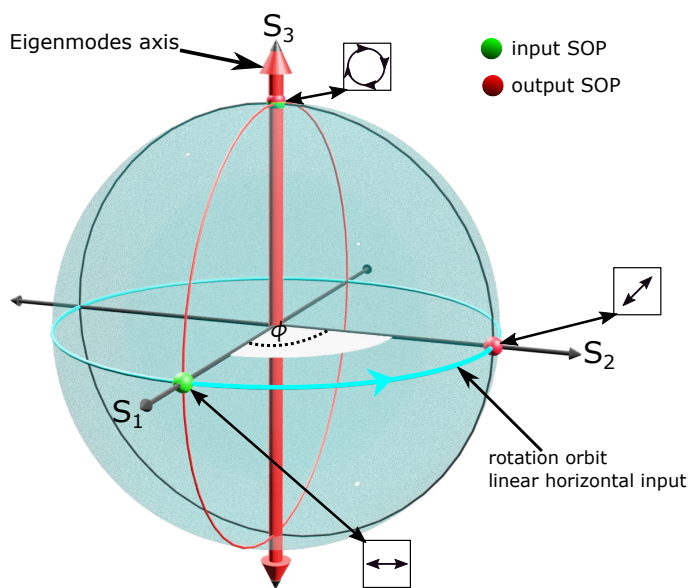


Figure 1.15: Birefringent effect of bulk chiral media, Poincaré sphere representation of polarization beating for left handed circular and linear horizontally polarization inputs.

1.5 Chirowaveguides

We have described that single-mode waveguides are linear birefringent systems with two mutually orthogonal linearly polarized eigenmodes (TE and TM). We have also described that bulk chiral media are circular birefringent media with two mutually orthogonal circularly polarized eigenmodes (LHCP and RHCP). Therefore, optical waveguides made of a chiral material have both LB and CB. These waveguides are known as chirowaveguides, they do not support TE/TM eigenmodes like achiral planar waveguides, nor circular eigenmodes as for bulk chiral materials, but elliptically polarized eigenmodes [51]. Understanding the properties of guided

[§]Note that ϕ in equation 1.59 is phase not polarization rotation in real space. The optical rotation in a chiral medium is $\phi/2$.

modes in chirowaveguides is rather a complex problem, as the presence of chirality and finite dimensions of the waveguides together introduces considerable additional mathematical complexity. However, the properties of the guided modes can be determined if the effect of chirality on the TE and TM modes is treated as a mode coupling mechanism [52–54].

In a standard (non-chiral) single-mode dielectric waveguide, the TE/TM eigenmodes propagate along the z direction independent of each other if the material properties remain independent of z . In the case when there is a perturbation (e.g. due to presence of chirality in the waveguide) the eigenmodes are coupled with each other. This means that in waveguides made of chiral material, if a pure TE eigenmode is excited at the beginning of the waveguide, part of its power is transferred to the TM eigenmode or vice versa. If the field distributions of the eigenmodes do not differ significantly before and after coupling, the propagation characteristics of the coupled TE-TM modes can be analyzed by the perturbation method and thereby coupled mode theory. Similarly, we can use the coupled mode theory to describe chirowaveguide since the chirality parameter γ of a chiral medium is small compared to $\sqrt{\frac{\epsilon}{\mu}}$ and it does not change the eigenmode field distribution.

In this section, we will use coupled mode theory to analyze the chirowaveguides on the basis of the following assumptions:

- In a standard dielectric material (achiral) waveguide system, the TE/TM eigenmodes have complex amplitudes ($a \cdot f(x, y)e^{-i\beta_{TE}z}$ and $b \cdot g(x, y)e^{-i\beta_{TM}z}$) of propagation constants β_{TE} and β_{TM} . Such system are considered as unperturbed system with two independent eigenmodes.
- In chirowaveguides, coupling is assumed to modify only the real amplitudes of eigenmodes such that they become function of z ($a(z)$ and $b(z)$), without affecting either transverse spatial distributions ($f(x, y)$ and $g(x, y)$) or their propagation constants (β_{TE} and β_{TE}).

Before using coupled mode theory for chirowaveguides, we need to derive coupling equations for the bulk chiral medium and describe eigenmodes complex amplitudes in the achiral optical waveguide that we will be using to derive the coupled mode equations.

Electric and magnetic field coupling equations in bulk chiral medium: We assume that the waveguide is made of a homogeneous, lossless, isotropic chiral material and the effect of chirality parameter γ is in the first order. By inserting the constitutive equations for the vector fields \mathbf{D} and \mathbf{B} of bulk chiral medium (1.52a and 1.52b) into the Maxwell equations (1.51d and 1.51c), we get:

$$\nabla \times \mathbf{E} = -i\omega\mu\mathbf{H} + \omega^2\mu\gamma\epsilon(\mathbf{E} + \gamma\nabla \times \mathbf{E}) \quad (1.60a)$$

$$\nabla \times \mathbf{H} = i\omega\epsilon\mathbf{E} + \omega^2\epsilon\gamma\mu(\mathbf{H} + \gamma\nabla \times \mathbf{H}) \quad (1.60b)$$

Since the chirality parameter γ is the first order parameter, the equations 1.60a and 1.60b will reduce to:

$$\nabla \times \mathbf{E} = -i\omega\mu\mathbf{H} + \omega^2\gamma\mu\epsilon\mathbf{E} \quad (1.61a)$$

$$\nabla \times \mathbf{H} = i\omega\epsilon\mathbf{E} + \omega^2\gamma\mu\epsilon\mathbf{H} \quad (1.61b)$$

Taking the curl of the above equations we get:

$$\nabla^2\mathbf{E} + \omega^2\mu\epsilon\mathbf{E} - 2i\gamma\omega^3\mu^2\epsilon\mathbf{H} = 0 \quad (1.62a)$$

$$\nabla^2\mathbf{H} + \omega^2\mu\epsilon\mathbf{H} + 2i\gamma\omega^3\mu\epsilon^2\mathbf{E} = 0 \quad (1.62b)$$

Using the relation $\omega^2\mu\epsilon = k^2n^2$, we write the equations 1.62a and 1.62b as:

$$\nabla^2\mathbf{E} + k^2n^2\mathbf{E} - 2ik^2n^2\gamma\omega\mu\mathbf{H} = 0 \quad (1.63a)$$

$$\nabla^2\mathbf{H} + k^2n^2\mathbf{H} + 2ik^2\gamma\omega\epsilon\mathbf{E} = 0 \quad (1.63b)$$

These two equations (1.63a and 1.63b) show how in a bulk chiral medium the usual wave equation is modified by terms proportional to $2ik^2n^2 \dots$. These terms are new source of polarization for the \mathbf{E} and \mathbf{H} fields, the \mathbf{H} adds new sources to \mathbf{E} and \mathbf{E} to \mathbf{H} . We will use these equations to derive the coupled mode equations in chirowaveguides.

Transverse field equations in an unperturbed achiral waveguide: For a single-mode achiral waveguide with given optical and geometrical properties, the eigenmodes are TE/TM of propagation constants β_{TE} and β_{TM} whose complex amplitudes are of the form:

$$E_y(x, y, z) = a f(x, y)e^{-i\beta_{TE}z} \quad (1.64a)$$

$$H_y(x, y, z) = b g(x, y)e^{-i\beta_{TM}z} \quad (1.64b)$$

where a and b are the real amplitudes which are constant, and $f(x, y), g(x, y)$ are transverse functions of the two eigenmodes. These complex amplitudes (1.64a and 1.64b) satisfy the Maxwell wave equations in the form:

$$\nabla_{\mathbf{t}}^2 f(x, y) + (k^2n^2(x, y) - \beta_{TE}^2)f(x, y) = 0 \quad (1.65a)$$

$$\nabla_{\mathbf{t}}^2 g(x, y) + (k^2n^2(x, y) - \beta_{TM}^2)g(x, y) = 0 \quad (1.65b)$$

where $\nabla_{\mathbf{t}}$ is the transverse gradient operator.

1.5.1 Coupled mode theory of chirowaveguides

Applying coupled mode assumptions, in a chirowaveguide, the real amplitudes of TE and TM given in equations 1.64a, and 1.64b become a function of z ($a(z)$ and $b(z)$) while their transverse

functions ($f(x, y)$, $g(x, y)$) and propagation constants (β_{TE} , β_{TM}) remain unchanged. Now, by inserting equations of the TE and TM complex amplitudes (1.64a and 1.64b) into the coupled equations of electric magnetic field in chiral media (1.63a and 1.63b), we get:

$$\begin{aligned} & \left[\nabla_{\mathbf{t}}^2 f(x, y) + (k^2 n^2(x, y) - \beta_{TE}^2) f(x, y) \right] a(z) e^{-i\beta_{TE}z} \\ & + \left[\frac{d^2 a(z)}{dz^2} - 2i\beta_{TE} \frac{da(z)}{dz} \right] f(x, y) e^{-i\beta_{TE}z} \\ & - 2ik^2 n^2(x, y) \gamma \omega \mu b(z) g(x, y) e^{-i\beta_{TM}z} = 0 \end{aligned} \quad (1.66a)$$

$$\begin{aligned} & \left[\nabla_{\mathbf{t}}^2 g(x, y) + (k^2 n^2(x, y) - \beta_{TM}^2) g(x, y) \right] b(z) e^{-i\beta_{TM}z} \\ & + \left[\frac{d^2 b(z)}{dz^2} - 2i\beta_{TM} \frac{db(z)}{dz} \right] g(x, y) e^{-i\beta_{TM}z} \\ & + 2ik^2 n^2(x, y) \gamma \omega \varepsilon a(z) f(x, y) e^{-i\beta_{TE}z} = 0 \end{aligned} \quad (1.66b)$$

By looking at these equations we notice that the first items of equation 1.66a and 1.66b are identical to the equation 1.65a and 1.65b which are solutions for the unperturbed systems, and they are marked out to zero. Since chirality perturbation is weak, we assume that the variation of the amplitudes $a(z)$ and $b(z)$ is slow such that $|\frac{d^2 a}{dz^2}| \ll |\beta_{TE} \frac{da}{dz} a|$, we neglect then the $(\frac{d^2 a}{dz^2}, \frac{d^2 b}{dz^2})$ [55]. Therefore, the equations 1.66a and 1.66b reduce to:

$$f(x, y) \frac{da(z)}{dz} = - \frac{k^2 n^2(x, y)}{\beta_{TE}} \gamma \omega \mu b(z) g(x, y) e^{i\Delta\beta z} \quad (1.67a)$$

$$g(x, y) \frac{db(z)}{dz} = + \frac{k^2 n^2(x, y)}{\beta_{TM}} \gamma \omega \varepsilon a(z) f(x, y) e^{-i\Delta\beta z} \quad (1.67b)$$

where $\Delta\beta = \beta_{TE} - \beta_{TM}$. So far, for TM, we have written the complex amplitude of the magnetic field component H_y . However, to know the polarization, we need to deal with the complex amplitude of the TM electric field E_x . Since we assumed the single-mode waveguides with TE/TM eigenmodes, E_x is:

$$E_x = - \frac{\beta_{TM}}{\omega \varepsilon} H_y = c(z) g(x, y) e^{-i\beta_{TM}z} \quad (1.68)$$

where $c(z) = \frac{\beta_{TM}}{-\omega \varepsilon} b(z)$. Inserting $b(z)$ into equations 1.67a and 1.67b, they become:

$$f(x, y) \frac{da(z)}{dz} = - \frac{k^2 n^2(x, y)}{\beta_{TE}} \gamma \omega \mu \left\{ \frac{-\omega \varepsilon}{\beta_{TM}} c(z) \right\} g(x, y) e^{i\Delta\beta z} \quad (1.69a)$$

$$g(x, y) \frac{d\left\{ \frac{-\omega \varepsilon}{\beta_{TM}} c(z) \right\}}{dz} = + \frac{k^2 n^2(x, y)}{\beta_{TM}} \gamma \omega \varepsilon a(z) f(x, y) e^{-i\Delta\beta z} \quad (1.69b)$$

Using the relation $\omega^2 \varepsilon \mu = k^2 n^2$, the equations 1.69a and 1.69b become:

$$f \frac{da(z)}{dz} = \frac{k^2 n^2(x, y)}{\beta_{TE}} \frac{k^2 n^2(x, y)}{\beta_{TM}} \gamma g(x, y) c(z) e^{i\Delta\beta z} \quad (1.70a)$$

$$g \frac{dc(z)}{dz} = - k^2 n^2(x, y) \gamma f(x, y) a(z) e^{-i\Delta\beta z} \quad (1.70b)$$

We can simplify more the above equations by inserting CB value (from equations 1.58) to both equations:

$$f \frac{da(z)}{dz} = \frac{k\text{CB}(x, y)}{2} \frac{n^2(x, y)}{n_{TE}n_{TM}} g(x, y) c(z) e^{i\Delta\beta z} \quad (1.71a)$$

$$g \frac{dc(z)}{dz} = - \frac{k\text{CB}(x, y)}{2} f(x, y) a(z) e^{-i\Delta\beta z} \quad (1.71b)$$

where $n_{TE} = \frac{\beta_{TE}}{k}$, $n_{TM} = \frac{\beta_{TM}}{k}$ are effective refractive indices of TE and TM. Multiplying both sides of equation 1.71a by $f^*(x, y)$, also multiplying both sides of equation 1.71b by $g^*(x, y)$, integrating both equations with respect to (x, y) then, using the fact that $f(x, y)$ and $g(x, y)$ are normalized so that their integral is unity, we finally obtain:

$$\frac{da(z)}{dz} = K_{ca} c(z) e^{i\Delta\beta z} \quad (1.72a)$$

$$\frac{dc(z)}{dz} = K_{ac} a(z) e^{-i\Delta\beta z} \quad (1.72b)$$

These equations (1.72a and 1.72b) are called coupled mode equations where K_{ca} and K_{ac} are the mutual coupling coefficients:

$$K_{ca} = \frac{k}{2} \int \frac{n^2(x, y)}{n_{TE}n_{TM}} \text{CB}(x, y) f^*(x, y) g(x, y) dx dy \quad (1.73a)$$

$$K_{ac} = - \frac{k}{2} \int \text{CB}(x, y) g^*(x, y) f(x, y) dx dy \quad (1.73b)$$

We assume that the field distributions of the two modes are equivalent such that $g(x, y) \equiv f(x, y)$:

$$K_{ca} = \frac{k}{2} \int \frac{n^2(x, y)}{n_{TE}n_{TM}} \text{CB}(x, y) |f(x, y)|^2 dx dy \quad (1.74a)$$

$$K_{ac} = - \frac{k}{2} \int \text{CB}(x, y) |f(x, y)|^2 dx dy \quad (1.74b)$$

These integrals can be divided into a material part where $\text{CB}(x, y) = \text{CB}$ and an outer part where $\text{CB} = 0$.

$$K_{ca} = \frac{k}{2} \text{CB} \int_{mat} \frac{n^2(x, y)}{n_{TE}n_{TM}} |f(x, y)|^2 dx dy + \frac{k}{2} \int_{out} \frac{n^2(x, y)}{n_{TE}n_{TM}} \cdot 0 \cdot |f(x, y)|^2 dx dy \quad (1.75a)$$

$$K_{ac} = - \frac{k}{2} \text{CB} \int_{mat} |f(x, y)|^2 dx dy - \frac{k}{2} \int_{out} 0 \cdot |f(x, y)|^2 dx dy \quad (1.75b)$$

Furthermore, for single-mode waveguides $n^2 \approx n_{TE}n_{TM}$ then the coupling coefficients can be written as:

$$K_{ca} = \frac{k}{2} \text{CB} \int_{mat} |f(x, y)|^2 dx dy \quad (1.76a)$$

$$K_{ac} = - \frac{k}{2} \text{CB} \int_{mat} |f(x, y)|^2 dx dy \quad (1.76b)$$

These equations of coupling coefficients indicate that, in chirowaveguides, the complex amplitudes of TE and TM are coupled as a result of the CB of the waveguides. However, compared to the bulk chiral material, in chirowaveguides the chiral coupling is reduced by the integral terms which represent the fraction of the field interacting with the chiral material. In a well-confined guided modes, the field is mainly inside the material and the integral can be approximated to 1. Therefore, the coupling coefficients (Equations 1.76a and 1.76b) can be written as:

$$K_{ca} \approx \frac{k}{2} \text{CB} \quad (1.77a)$$

$$K_{ac} \approx -\frac{k}{2} \text{CB} \quad (1.77b)$$

1.5.1.1 Eigenmodes in chirowaveguides

To find eigenmodes of chirowaveguides, we have to further simplify the coupling equations. This can be done by using variable transformation [56]. The idea is that, instead of writing the absolute complex amplitudes of the waveguide eigenmodes, we write their complex amplitudes relative to each other, so that:

$$\bar{a}(z) = a(z)e^{-i\frac{\Delta\beta}{2}z} \quad \bar{c}(z) = c(z)e^{i\frac{\Delta\beta}{2}z} \quad (1.78)$$

where $\bar{a}(z)$ is relative complex amplitude of TE eigenmode, $\bar{c}(z)$ is relative complex amplitude of TM. The variable transformation allows us to write the coupling equations (1.72a and 1.72b) straightforwardly in a more compact matrix form:

$$\frac{d}{dz} \begin{bmatrix} \bar{a}(z) \\ \bar{c}(z) \end{bmatrix} = \begin{bmatrix} -i\frac{\Delta\beta}{2} & \frac{k}{2}\text{CB} \\ -\frac{k}{2}\text{CB} & i\frac{\Delta\beta}{2} \end{bmatrix} \begin{bmatrix} \bar{a} \\ \bar{c} \end{bmatrix} \quad (1.79)$$

If we use relation $\Delta\beta = k(n_{TE} - n_{TM}) = k\text{LB}$, the above equation become:

$$\frac{d}{dz} \begin{bmatrix} \bar{a}(z) \\ \bar{c}(z) \end{bmatrix} = \frac{-ik}{2} \begin{bmatrix} \text{LB} & i\text{CB} \\ -i\text{CB} & -\text{LB} \end{bmatrix} \begin{bmatrix} \bar{a} \\ \bar{c} \end{bmatrix} \quad (1.80)$$

we recall here again that \bar{a} is the complex amplitude of TE mode and \bar{c} is the complex amplitude of TM mode. The coupling matrix $(\frac{-ik}{2} \begin{bmatrix} \text{LB} & i\text{CB} \\ -i\text{CB} & -\text{LB} \end{bmatrix})$ in equation 1.80 represents in a compact form the behaviour of eigenmodes in single-mode chirowaveguides. For an achiral waveguide (CB=0), and therefore, the eigenvalues and eigenvectors of the matrix correspond to the unperturbed waveguides which are TE and TM eigenmodes. When the chirality is present, the off-diagonal elements of the matrix couple the TE and TM, then TE and TM are no more eigenmodes.

Birefringence of chirowaveguides (modal birefringence (MB)) is the eigenvalues of the coupling matrix which quantifies the effective refractive index difference of the eigenmodes

$$\text{MB} = \pm\sqrt{\text{LB}^2 + \text{CB}^2} \quad (1.81)$$

The eigenvectors of the coupling matrix which means the eigenmodes of chirowaveguides are:

$$|+\rangle = \begin{bmatrix} 1 \\ \frac{-i(\text{LB} + \sqrt{\text{LB}^2 + \text{CB}^2})}{\text{CB}} \end{bmatrix} = \begin{bmatrix} 1 \\ \frac{-i(1 + \sqrt{1 + \frac{\text{CB}^2}{\text{LB}^2}})}{\frac{\text{CB}}{\text{LB}}} \end{bmatrix} \quad (1.82a)$$

$$|-\rangle = \begin{bmatrix} \frac{i\text{CB}}{\text{LB} + \sqrt{\text{LB}^2 + \text{CB}^2}} \\ 1 \end{bmatrix} = \begin{bmatrix} \frac{i\frac{\text{CB}}{\text{LB}}}{1 + \sqrt{1 + \frac{\text{CB}^2}{\text{LB}^2}}} \\ 1 \end{bmatrix} \quad (1.82b)$$

We can define these two eigenmodes as Jones vectors in term of polarization ellipticity χ , if we define:

$$\tan 2\chi = \frac{\text{CB}}{\text{LB}} \quad (1.83)$$

By using trigonometric identity ($\tan \chi = \frac{\tan 2\chi}{1 + \sqrt{1 + \tan^2 2\chi}}$), we get Jones vector for the two eigenmodes

$$\mathbf{J}_{|+\rangle} = \begin{bmatrix} \cos \chi \\ -i \sin \chi \end{bmatrix}, \quad \mathbf{J}_{|-\rangle} = \begin{bmatrix} \sin \chi \\ i \cos \chi \end{bmatrix} \quad (1.84)$$

Not that these two Jones vectors of the eigenmodes correspond to elliptical polarization when polarization ellipse major axis is located on x -axis (azimuth $\psi = 0$) (see equation 1.17).

Chirowaveguides behaviour based on coupled mode theory: In summary, from equations 1.80- 1.84, chirowaveguides are elliptical birefringent waveguides with (i) left/right handed elliptically polarized (L/RHEP) eigenmodes, (ii) the azimuth of the eigenmodes is identical to the axis of the linear birefringent waveguide (TE/TM axis), (iii) ellipticity of the eigenmodes related to the $\frac{\text{CB}}{\text{LB}}$ ratio and (iv) modal birefringence (MB) given as the arithmetic average of the LB and CB (Equation 1.81).

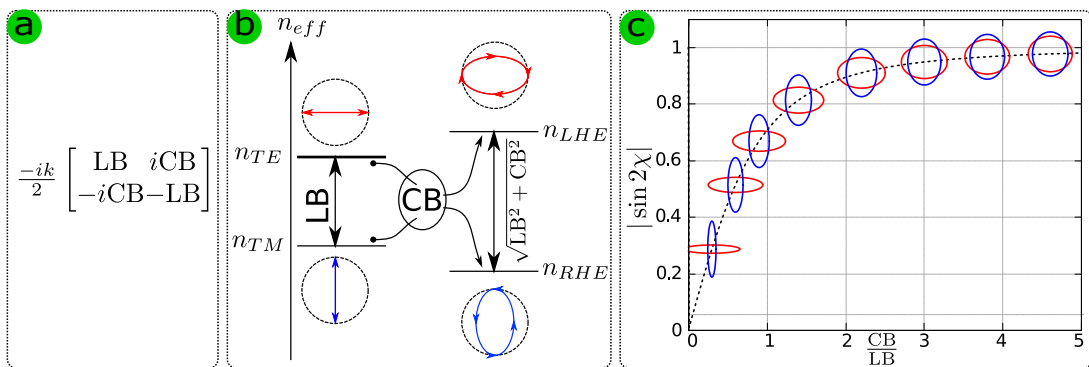


Figure 1.16: Behaviour of chirowaveguides deduced from coupled mode theory. a) Coupling matrix. b) Graphical representation of the coupling, it shows how the presence of chirality couples the TE/TM eigenmodes of the single mode waveguide and thus the eigenmodes of a chirowaveguide are left/right handed elliptically polarized modes (L/RHEP). c) Evolution of a chirowaveguide eigenmodes polarization ellipticity as a function of $\frac{\text{CB}}{\text{LB}}$.

We have shown in Figure 1.16-c the evolution of a chirowaveguide eigenmodes ellipticity as a function $\frac{CB}{LB}$. From the figure, we can deduce that for a chirowaveguide with a particular chirality property (CB), the ellipticity of the eigenmodes is controlled by changing the linear birefringence (LB) of the waveguide. Therefore, we can obtain optical waveguides that can be used for elliptically polarized light applications (from linear to circular) simply by having an LB of the order of CB without the need to fabricate waveguides with zero birefringence.

1.5.2 Polarization beating in chirowaveguides

We have shown that the eigenmodes of single-mode chirowaveguides, are two mutually orthogonal elliptically polarized eigenmodes (L/RHEP). Therefore, if a light wave is guided in a chirowaveguide, its SOP undergoes a periodic modulation, unless its polarization corresponds to one of the two eigenmodes. Such polarization modulation (beating) can be evaluated using the Poincaré sphere. The two eigenmodes create a diameter axis on the sphere that has "latitude" angle of 2χ with the equator of the sphere but at azimuth $\psi = 0$ as shown in Figure 1.17. The modulation of the SOP of a guided light is a periodic rotation on a circular orbit in a plane perpendicular to the eigenmodes axis.

We have shown graphically in Figure 1.17 how the SOP of guided light is modulated in a chirowaveguide if its initial polarization state is a horizontal linear or left circular polarization. In the figure, we have taken the example of a chirowaveguide whose eigenmodes have an ellipticity of $\chi = 30^\circ$ which corresponds to $\frac{CB}{LB} \approx 3$. In a chirowaveguide with such eigenmodes, the

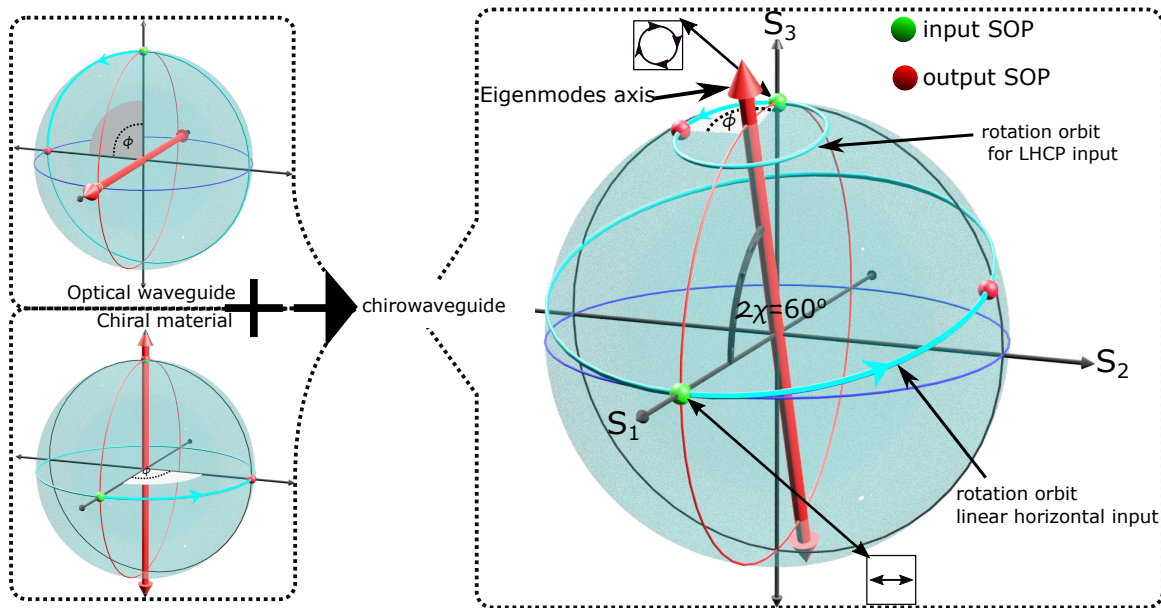


Figure 1.17: Birefringent effect of chirowaveguides, Poincaré sphere representation of polarization beating for left handed circular and linear horizontally polarization inputs.

polarization beating effect for a linear horizontal polarization input corresponds to a rotation orbit that is quite similar to that of bulk chiral media. On the other hand, the polarization beat for a left-hand circular polarization corresponds to a very small rotational orbit, indicating that in these waveguides, the circular polarization can be propagated while maintaining its polarization handedness. In addition, the eigenmodes are elliptical polarizations with high ellipticity, so they can be used as a chiral probe to realize optical waveguides for chiral sensing.

In chirowaveguides, as birefringence is defined by equation 1.81, the polarization modulation magnitude (ϕ) can be calculated as:

$$\phi = \frac{2\pi}{\lambda} \cdot \sqrt{\text{LB}^2 + \text{CB}^2} \cdot l \quad (1.85)$$

This equation indicates that the polarization modulation in a chirowaveguide is proportional to the magnitude of all birefringences present in the waveguides and the waveguide length.

1.6 Design of elliptical birefringent chirowaveguides

Our objective is to realize optical waveguide with eigenmodes that can be used for sensing applications. This corresponds to the eigenmodes with high polarization ellipticity, with a circular polarization at the highest level. We have described that chirowaveguides allow us to reach our objective while the ellipticity of the eigenmodes is defined by the ratio of the circular to linear birefringence of the waveguides ($\frac{\text{CB}}{\text{LB}}$). Our objective becomes the realization of waveguides composed of a material with high CB and a structure with low LB. The choice of the material is already made, we have two materials with chiral properties (see chapter 2). Our task, therefore, is to design and fabricate optical waveguides with low LB (in the order of the CB of the material). Hopefully, channel waveguides can be designed to have very low LB [18]. In this section, we use the numerical simulations to calculate LB in the types of channel waveguides that can be used for sensing applications (i.e. diffused, ridge, and rib channels).

1.6.1 Low linear birefringence channel waveguides

We begin our study by defining our objective LB. We target channel waveguides with a $\text{LB} \leq 1 \times 10^{-5}$ which corresponds to the CB of one of the materials we use, at $\lambda = 0.633\mu\text{m}$. The targeted chirowaveguides have eigenmodes with ellipticity $\chi=22.5^\circ$. Figure 1.18 shows cross section of the three type of channel waveguide we want to study. The parameters that affect the LB are shown in the figure, namely refractive indices of the cover (n_c), guide (n_g), and buffer (n_b) layers, the channels width (w), their height (h), and rib channel slab thickness (d). Since we want to use the waveguide for sensing, n_c is set to $n_c = 1$ (i.e. refractive index of air). We also fixed n_g and set this parameter to $n_g = 1.61$ as refractive index of one our chiral

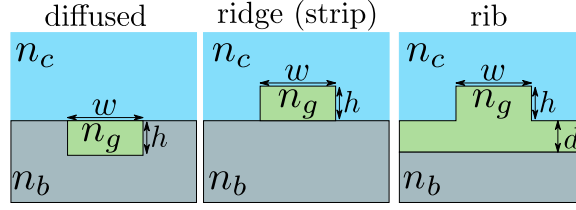


Figure 1.18: Cross-section of different channel waveguides for sensing applications.

material. Therefore the remaining parameters to study are n_b , w , h , and d .

Figure 1.19-a-c shows LB evolution as a function of w and h for the three different channels types while $n_b = 1.52$ is constant ($\Delta n = 0.09$). The blue lines are contour for channels dimensions with $LB \leq 1 \times 10^{-5}$. It is important to note that we have plotted the absolute value of LB because for our objective $LB = +1 \times 10^{-5}$ or $LB = -1 \times 10^{-5}$ are equally important, otherwise, LB is (-) in the upper part of the blue zone. The red lines are the contour for channels with $LB \leq 1 \times 10^{-4}$. It can be seen that for all three types of channels, there is always a zone in which the channels can be made to have the targeted property. The position of the blue area in the diagonal of the color map indicates that by changing h while w is fixed or by changing w while h is fixed, we can always obtain waveguides with $LB \leq 1 \times 10^{-5}$. In fabrication process, the later situation is preferred (changing w while h is fixed) as the microfabrication methods are usually work on patterning films that has fixed thickness. If we take one example of fixed $h = 2.1 \mu\text{m}$, we can see from the Figure 1.19-a-c that the fabricating tolerance in width Δw

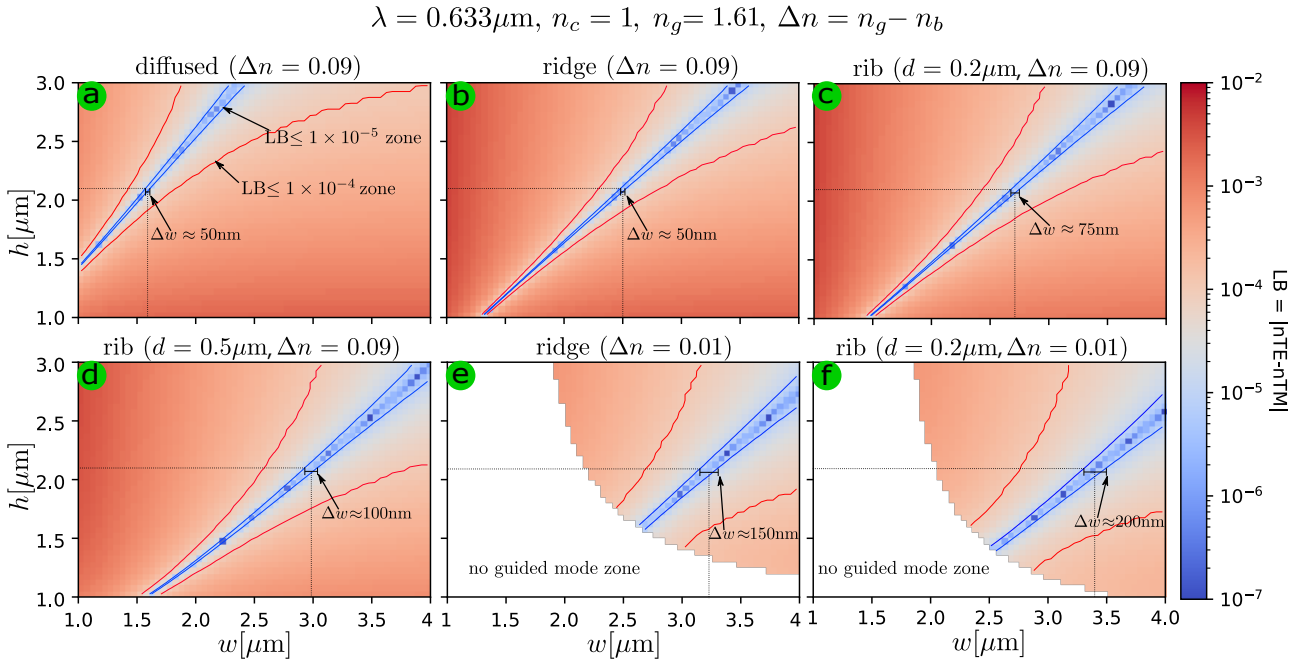


Figure 1.19: Evolution of LB in different types of channel waveguides as function of channel width w , height h , rib thickness d , refractive index difference $\Delta n = n_g - n_b$.

is 50nm for diffused and ridge channel while it is higher Δw is 75nm in rib waveguide with $d = 0.2\mu\text{m}$.

Regarding the effect of d in rib waveguides, the targeted LB area (blue area) shifts to higher w and it widens when d increases as shown in Figure 1.19-c-d. Quantitatively, for $d = 0.2\mu\text{m}$ rib waveguide, it has target LB value at $h = 2.1\mu\text{m}$ and $w = 2.7\mu\text{m}$ with $\Delta w = 75\text{nm}$ of fabrication tolerance. When $d = 0.5\mu\text{m}$, the target LB value move to $h = 2.1\mu\text{m}$ and $w = 3\mu\text{m}$, and the fabrication tolerance increase to $\Delta w = 100\text{nm}$.

The effect of buffer refractive index (n_b) relative to the guided layer refractive index (n_g) for rib and ridge channels is shown Figure 1.18-e-f. By comparing Figure 1.18-b with 1.18-e for ridge channels and Figure 1.18-c with 1.18-f for rib channels we can notice that the behaviour of the channels is highly changed. In both channels, the targeted LB area shifts to higher w and widens strongly when Δn reduces from 0.09 to 0.01. Quantitatively, for such change in Δn , at $h = 2.1\mu\text{m}$, the fabrication tolerance in width increase from $\Delta w = 50\text{nm}$ to $\Delta w = 150\text{nm}$ in ridge channels and from $\Delta w = 75\text{nm}$ to $\Delta w = 200\text{nm}$ in rib waveguides. The choice of Δn must be made considering that either the waveguides support guided modes or not. At very low Δn , the waveguide does not support guided modes as indicated by the white zone in Figure 1.18-e-f.

Note that in all the simulation results presented in Figure 1.18-a-f, the fabrication tolerance increases significantly if a material with higher circular birefringence is used (e.g. $\text{CB}=1 \times 10^{-4}$). This behavior is illustrated in the figure by the red lines that correspond to channels with $\text{LB} \leq 1 \times 10^{-4}$.

Based on the results of the numerical simulation, we can summarize our fabrication design as follows:

1. Diffuse, ridge and rib channel waveguides can all be fabricated with the LB of our objective.
2. The fabrication tolerance of the waveguide dimensions (h and w) is higher in the rib waveguides compared to the diffuse and ridge waveguides. Similarly, the higher the value of d , the higher the fabrication tolerance.
3. The refractive index contrast between the buffer layer and the guiding layer is a very important parameter for the fabrication tolerance in all three types of waveguides, it highly increases fabrication tolerance.
4. Finally, obviously, if the targeted LB is higher in the first place (i.e., using a material with a higher CB), the fabrication tolerance is higher for all channels.

1.7 Conclusion

In this chapter, we have aimed to answer the fundamental questions regarding the topic of this thesis. In the first sections, we have discussed the nature of light polarization using electromagnetic theory, the Jones mathematical method for describing light polarization, and the effect of materials on light polarization. Afterwards, we have described the Stokes parameters, which, along with Mueller matrices, are both sufficient to describe the polarization of light and the effect of any medium on polarization. The advantage of using Stokes parameters to treat the polarization of light over Jones vectors is that the Stokes parameters are practically measurable while the elements of Jones vectors are not. We then described the elegant Poincaré sphere graphical representation of light polarization represented by Stokes parameters. The Poincaré sphere allowed us to visualize light SOP and determine the effect of polarization sensitive elements such birefringence systems.

We then described the behavior of light waves when guided in a planar waveguide, which allowed us to provide the general idea of the behavior of light in integrated photonic components. By analytically solving Maxwell's equations, we have shown that the guided modes in planar waveguides are two orthogonal linear polarization modes (TE/TM), which limits the use of these waveguides for linear polarization applications. Afterwards, we described guided light behaviour in channel waveguides and different types channel waveguides. Using numerical simulations, we described the behavior of guided modes in channel waveguides and showed that standard (achiral) channel waveguides are also birefringent and are limited to TE/TM polarization applications.

By solving Maxwell equations for chiral bulk media, we have shown that these media are circular birefringent systems with left and right circular polarization eigenmodes. Our approach to determine the eigenmodes of waveguides made chiral materials (chirowaveguides) was the coupled mode theory which allowed us to define the eigenmodes by simple mathematical equations (equation 1.83). The equation states that the polarization ellipticity of the waveguides is proportional to CB/LB. Owing to this equation, for a given value of CB ($\sim 1 \times 10^{-5}$), then using numerical simulations, we have defined our design rules for the fabrication of channel chirowaveguides with elliptically polarized eigenmodes ($LB \leq CB$). We showed that rib, ridge, and diffuse channel chirowaveguides can be fabricated with such property, by varying the opto-geometrical parameters of the waveguides, such as channel width, height, and refractive index. Also, we showed that small refractive index difference between the guiding layer and the buffer layer allows to fabricate low LB channel waveguides with a better fabrication tolerance.

rings present intrinsic CB greater than the binaphthols family (i.e. 2 to 3 times greater when in solution) [58].

2.2 Synthesis of chiral thin films with high circular birefringence

From our description of chirowaveguides (see 1.5.1), the first requirement on chiral layers to realize chirowaveguides with circularly polarized eigenmodes is having high CB. Among the exploitable techniques for the deposition of chiral layers, thermal methods that risk to cause racemization (loss of chirality) and/or to degrade organic chiral molecules were discarded. Two techniques have been chosen: the sol-gel technique already known to design hybrid materials (organic-inorganic) [59] and Pulsed Laser Deposition (PLD) which has already given good results for the deposition of small organic molecules [60]. These two techniques have been adapted to the specificity of the deposition of layers containing chiral organic molecules: synthesis of new chiral sol-gel precursors based on binaphthyl-SiO₂ [61, 62] and in-situ control of the racemization in both cases [30, 63, 64].

Once the layers are realized, their properties are characterized by the appropriate techniques developed within the team. Thus, the thickness and the refractive index are measured by M-line spectroscopy, the optical quality is characterized by the measurement of the optical losses in guided mode, and their optical rotation (CB) is measured thanks to a rotatory optical dispersion setup.

2.3 Pure chiral films by Pulsed laser deposition

The laser ablation technique is a thin film synthesis method that was developed for the synthesis of superconductor thin films [65]. It consists in vaporizing a compound by focusing a pulsed UV laser on a target of compacted powders and to collect the ablated species on a substrate placed at a few centimeters. The deposition is performed in a vacuum or in a gaseous atmosphere.

The use of PLD method for the deposition of organic or even biological films is much more recent. Indeed, it was assumed for a long time that laser ablation was not a suitable method for the synthesis of organic films because the energy of the ablation laser was too high, which would lead to the breaking of the bonds of the organic molecules and thus to their degradation. Nevertheless, by controlling the deposition parameters, mainly the laser energy that must be sufficient to release the organic material from the target and not too high to avoid its degradation. In this case, the thin film deposition regime is not ablation but rather

desorption. Hence, PLD has allowed the deposition of films of organic molecules of various size and complexity without degradation [60]. In the case of the deposition of chiral organic molecules, the challenge is not only to degrade the molecule but also not to racemize it (switch from one enantiomer to the other) during the deposition by PLD. Indeed, the racemization of the chiral molecules deposited would lead, in the end, to a film whose chiroptical properties (CB) might be null. Starting from a target consisting of a single enantiomer of chiral molecules, it is therefore necessary to find the laser ablation conditions that allow to preserve both the integrity of the chiral molecule (no degradation) and its enantiopurity (no racemization) to obtain a purely chiral thin film with a CB and good optical quality.

Previously, the *Chirality team* has shown that thanks to the PLD technique, it was possible to realize purely chiral organic thin films made of only binaphthol-bridged molecules [30,63] or only helicenes-like molecules, transparent and with a very high CB [64]. For this, the essential parameter to control is the laser fluence which is the ratio of the laser beam energy to the beam cross-section on the target in mJ/cm^2 . Moreover, it has been shown that there is a range of laser fluence $[15-45]\text{mJ}/\text{cm}^2$, depending on the deposited chiral molecule, that allows to keep the integrity of the molecules and their enantiopurity. The transfer of chirality from the target to the thin film is not limited by thermal effects but rather by photochemical processes since the degradation of the molecules studied does not depend on the molecular structure whereas racemization does. Thus, the interest of PLD for these materials is its instantaneous nature (ultra short laser pulse) which allows the heated material to be immediately ejected and cooled before the racemization process [30,63]. During my Master 2 internship, we synthesized purely chiral films of bridged binaphthyl and helicene-like molecules presented in Figure 2.1.

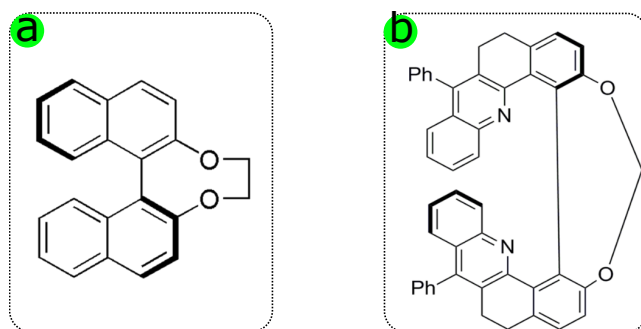


Figure 2.1: structures of chiral molecules deposited by PLD (a) bridged binaphthol and (b) helicene like molecule.

2.3.1 PLD deposition experimental setup

In our experiment, we have been using a KrF laser source (wavelength $\lambda = 248$ nm, pulse duration=5 ns) and operating frequency is set to 50 Hz. As it is shown schematically in Figure 2.2 the laser beam is focused on the target at an incident angle of 45° . The beam size on the target is set to be $4 \times 4 \text{ mm}^2$ and the optimised energy fluence is found to be $20 \text{ mJ} \cdot \text{cm}^{-2}$ for binaphthol-bridged molecules and $30 \text{ mJ} \cdot \text{cm}^{-2}$ for helicene-like molecules. The short (5ns) pulse-by-pulse duration of the technique prevents any thermal damage on the target. Furthermore, the target material is fixed on a rotating stage to avoid energy(heat) accumulation at the position of the beam. Thus, only the molecules on the upper surface of the target receive energy and do not transmit it to the lower molecules. The distance between the target to substrate was set to 4cm and deposition was carried out under a vacuum of $\sim 1 \times 10^{-6}$ mbar. Under these conditions, the deposition rate, using a fresh target, was found to be $\sim 70 \text{ nm/min}$ and $\sim 100 \text{ nm/min}$ for bridged-binaphthol and helicene-like molecules respectively. Thickness from few nm to few μm could be controlled depending on the deposition duration.

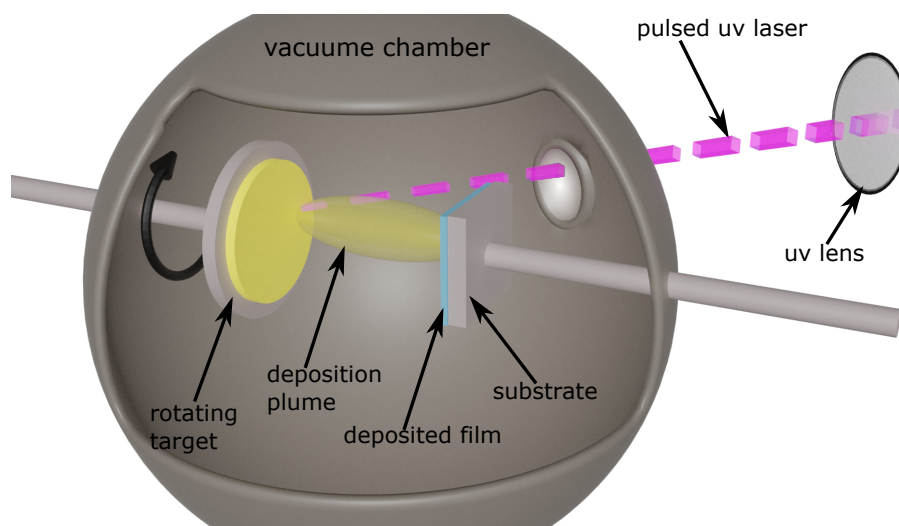


Figure 2.2: Schematic representation of pulsed laser deposition setup

2.3.2 Optimizing thickness of PLD films

Due to the in-homogeneity of the density of the species ejected from the target and their expansion in space, i.e. the plume geometry, the laser ablation deposition of the thin film is in-homogeneous in thickness, whatever the deposited material. Indeed, for a 4cm distance between the target and the substrate, by placing the substrate such that its center touches the center of the plume, a bell-shaped profile is obtained with a thickness variation of about 60% between the center of the film and the edges (in 1cm distance), as shown in Figure 2.4 (a).

The colored rings observed in photographs of the films (figures' insets) are the indication of thickness drop from the center to the border due to light interference by the thin film.

This in-homogeneity of the thickness is the main drawback of the films deposited by PLD as it induces modal scattering of the guided light. We followed two experimental techniques to improve the thickness homogeneity of the PLD films that are:

1. **Horizontal oscillation of the substrate relative to evaporation plume:** By means of a vacuum translation motor and a suitable mechanical support, the substrate is set to oscillate horizontally in front of the target during deposition, so that its position is periodically translated with respect to the fixed position of the plume. The schematic of the modified substrate holder is shown in Figure 2.3-a. This improves the film thickness profile along one axis. The obtained films, in this way, have half-cylinder shaped thickness profile, with a thickness inhomogeneity of $< 20\%$ in one direction, corresponding to the substrate horizontal oscillation axis, as shown in Figure 2.4-b. We also tried scanning

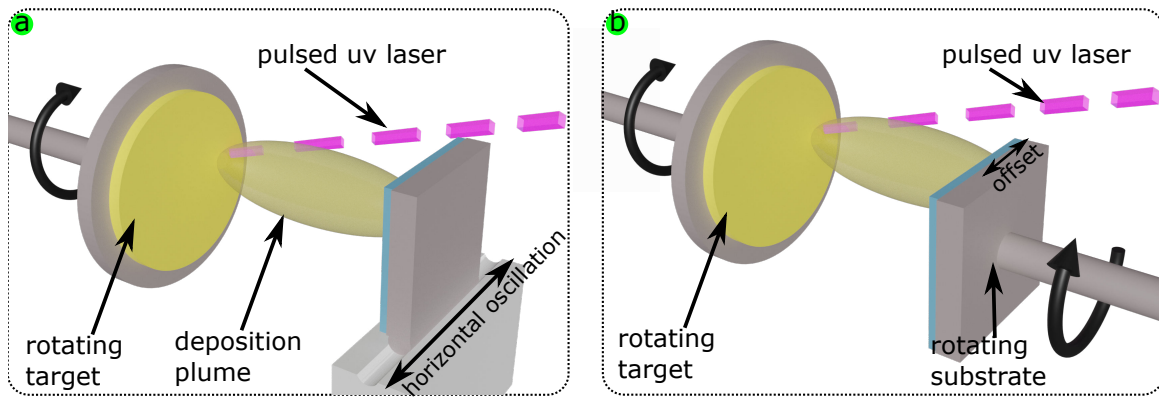


Figure 2.3: Scheme of PLD setups to control thickness homogeneity , a) homogeneity control in one axis, b) homogeneity control in both axis.

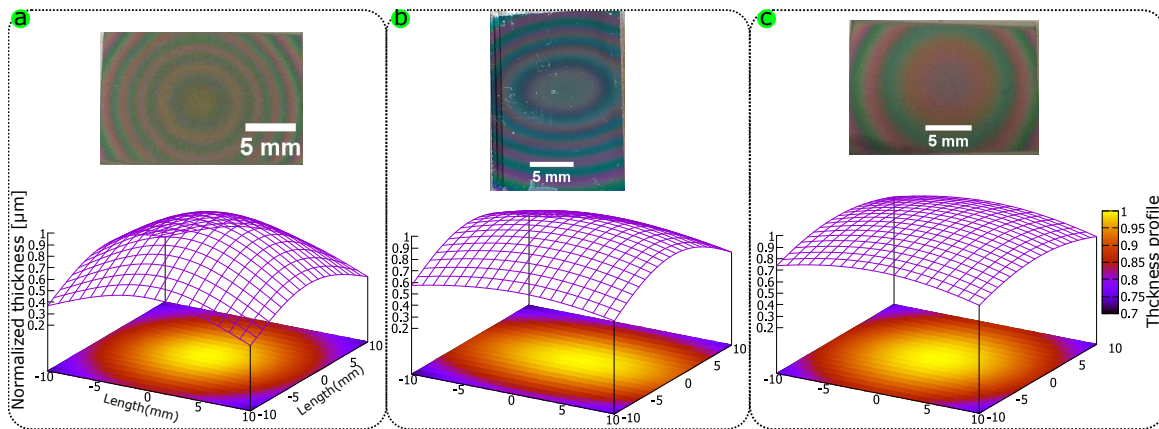


Figure 2.4: photograph PLD films with their 3D profile , a) Regular PLD film, b) PLD films with homogeneity in one axis, c) PLD films with in two axis.

horizontally the rotating target with the laser beam with fixed substrate, but the results were less good than the previous case.

2. Offset between evaporation plume and substrate while rotating the substrate:.

Increasing the distance between the target and the substrate enlarges the scale of thickness homogeneity, but it highly decreases the deposition rate. At reasonable target-substrate distance (4cm), a more homogeneous film is deposited by combining an offset between the fixed plume position and the initial position of the substrate, and rotation the substrate (see Figure 2.3-b). Offsetting the substrate allows for a higher deposition rate at the edge of the substrate than in its center, while continuous rotation of the substrate allows for a higher deposition rate in the center. Consequently, overall, the center and the edges get an equivalent deposited material. With this technique, we deposited PLD films with <20% inhomogeneity in thickness between the center and the edges over 1cm distance in 2D dimensions, as shown in Figure 2.4-c.

2.3.3 Properties of chiral films made by PLD

- Thanks to PLD, purely chiral thin films (composed only of chiral molecules), transparent, with good optical quality (no cracks or microscopic defects) are obtained. However, bridged binaphthol based films are mechanically more brittle and may exhibit post-deposition poly-crystallization while films based on helicene molecules are more stable.
- Thicknesses of 2 μm were achieved with thickness homogeneity (20 % difference between the center and the edges of the layer on a 4cm² layer). Such thickness inhomogeneity corresponds to a 400nm thickness change in the 2 μm thick film, which is a drawback for our study that requires high precision in thickness control. Therefore, further optimization of the thickness is required.
- As PLD deposited films are made of only chiral molecules, the high density of chiral molecules gives them high chiroptical properties. $CB \approx 2.5 \times 10^{-5}$ for chiral bridged-binaphthol films and $CB \approx 9 \times 10^{-5}$ for helicene-like molecules films at $\lambda = 633\text{nm}$ are obtained.
- The refractive index of the bridged-binaphthol films measured by M-line spectroscopy at $\lambda = 633\text{nm}$ is found to be $n = 1.71$ and isotropic (i.e. in-plane refractive index (n_{TE}) = out-of-plane refractive index (n_{TM})). However, the helicene-like molecules films are found to be anisotropic $n_{\text{TE}} = 1.72 \neq n_{\text{TM}} = 1.79$).

Although the helicene-like molecules films have higher CB, their anisotropy brings extra linear birefringence, and therefore, we only used bridged binaphthol chiral molecules films in the reminder of the thesis work.

2.4 Hybrid silica films

In parallel, an important work has been done on the deposition of chiral films by the sol-gel method to reach the required properties in particular, the conservation of CB as high as possible, a good optical quality, a thickness higher than $2\mu\text{m}$. To reach such thicknesses with the classical sol-gel technique, multilayer deposits ($\sim 100\text{nm}$ per deposition) with a thermal treatment between two depositions is necessary. This allows to evaporate the solvents and to dry the first layer so that it does not dissolve in the precursor solution during the next deposition. However, annealing even at relatively low temperature ($\sim 150^\circ\text{C}$) leads to the racemization of chiral molecules and to the loss of the CB of the layer. It was therefore necessary to develop a new process allowing to obtain a thick layer in one step and to determine the good temperature for the drying of the layer while keeping the highest chiral properties.

Through a new deposition protocol using a hybrid, organic-inorganic precursor containing the functionalized chiral molecule of binaphthol bind to the silica network and by developing a procedure for a pre-condensed solution with high viscosity, a stable, transparent layers with thicknesses up to $7\mu\text{m}$ in one deep-coating step has been achieved [62]. However, the films obtained in this way, could present cracks which is a drawback for the films. To improve the mechanical properties of the films and to limit cracking, the sol-gel solution was modified by replacing TEOS by MTEOS. As shown in Figure 2.5, in TEOS each silicon atom is linked to four oxygen atoms while in MTEOS, it is linked to three of them and one methyl CH_3 which does not take part in the bonding to the silica network. It confers thus, more plasticity to the network and better mechanical properties to the final thick layers. Therefore, it was necessary to optimise both the composition and the deposition conditions for this new solution in order to obtain layers with the appropriate properties (refractive indices, thickness, good optical quality and high CB) for the fabrication of chiro-waveguides and their study.

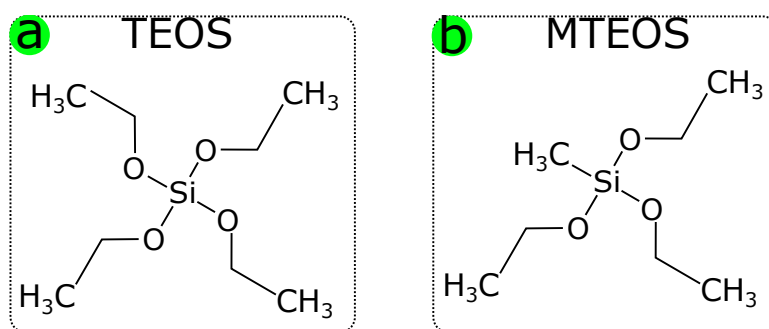


Figure 2.5: Chemical structures of a) tetraethoxysilane (TEOS), and b) methyltriethoxysilane (MTEOS).

2.4.1 Material Synthesis

The ORMOSIL sols are synthesized based on a polymerizable triethoxysilane precursor functionalized by a chiral binaphthol group $\text{RSi}(\text{OEt})_3$ using the approach previously published elsewhere [61] and replacing TEOS by MTEOS. The chemical structure of the ORMOSIL material is shown in Figure 2.6. As can be seen, the material is made of silica network for which each chiral molecule is attached to one silicon atom.

Two kinds of solutions containing binaphthol chiral molecules have been prepared: enantiopure solutions containing either $(+)\text{RSi}(\text{OEt})_3$ or $(-)\text{RSi}(\text{OEt})_3$ for the fabrication of the enantiopure chirowaveguide layers with opposite handedness and racemic solution by mixing $(+)\text{RSi}(\text{OEt})_3$ and $(-)\text{RSi}(\text{OEt})_3$ in equivalent proportions (50-50)%, for the fabrication of achiral waveguides. By adjusting the amounts of solvent and additives such as MTEOS and Polyéthylène glycol(PEG), the quality of final deposited layers as well as their refractive indexes are controlled.

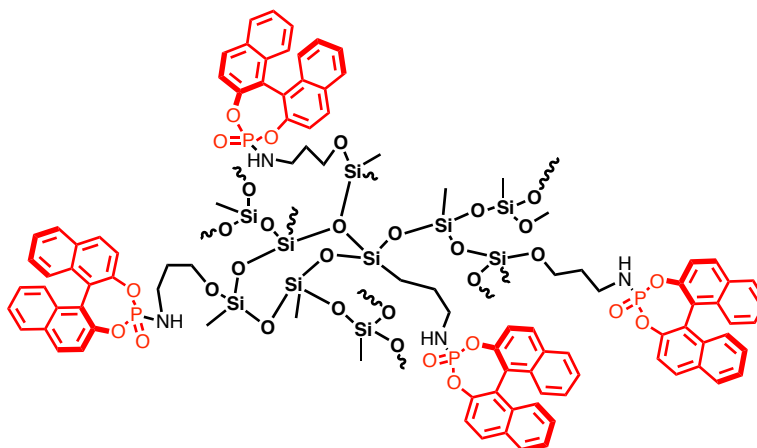


Figure 2.6: Chemical structure of ORMOSIL films.

2.4.2 ORMOSIL film deposition

The deposition of the ORMOSIL films is carried out using dip coating technique. It is an immersion-withdraw technique that can be used to deposit films of variety of materials including sol-gel films [66]. In this case, films are obtained by dip coating a substrate into the wet sol-gel and post-baking the deposited film to evaporate the solvents and to allow a full condensation of the material.

An ideal dip coater is schematically shown in Figure 2.7. Prior to dip-coating, silicon substrates are cleaned in a freshly prepared piranha solution in order to remove all the organics from the substrate surface and to activate the surface for ORMOSIL binding. The cleaned

substrate is immersed in the ORMOSIL solution, and after a few seconds of immersion, the substrate is withdrawn from the solution. A homogeneously spread film is deposited on the substrate during withdrawal. The thickness of the films depends on the concentration (which means viscosity) of the solution and the withdrawal speed. Figure 2.8 shows thickness of dip coated films as a function of withdrawal speed, at a given solution concentration. As it can be seen, thickness of the films is linearly proportional to dip coating withdrawal speed and film's thickness ranging from 1 to $2.6\mu\text{m}$ are obtained in a single immersions-withdrawal. These thicknesses are sufficient for the chiral guiding layer. To get more thick films at constant viscosity and withdrawal speed, multiple immersions-withdrawals are done and thickness as high as $20\mu\text{m}$ is obtained. To obtain guiding and buffer layers for optical waveguides, thick buffer layers with low refractive index are deposited first and baked, followed by layers with higher refractive index relative to the buffer, as shown in Figure 2.7.

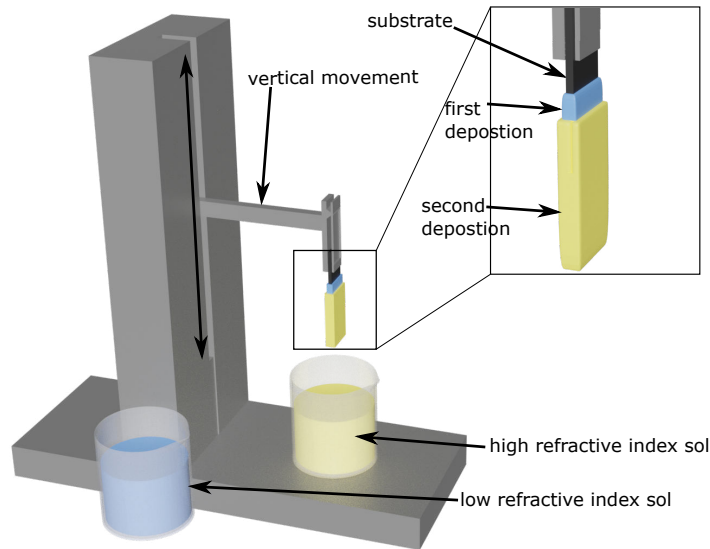


Figure 2.7: Schematic representation of dip coating technique

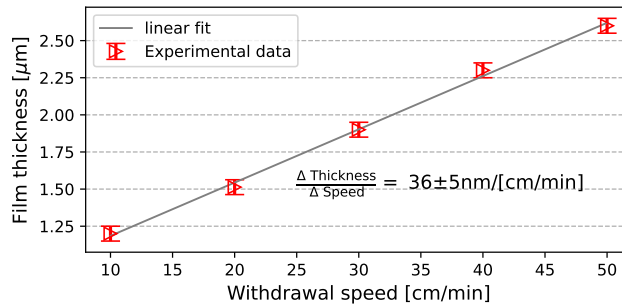


Figure 2.8: Thickness of a single coated films obtained from a (-)P1-46%MTeos_50g/L solution as a function of dip coating withdrawal speed. The films are baked at 120°C on a hotplate for 20h.

2.4.3 Thin film baking

The ORMOSIL dip coated layers are soft and not stable because they still contain solvent that must evaporate. Baking the layers is necessary to finish the polymerization, remove the solvents, dry the material, and obtain solid films. We have used hotplates to bake the layers instead of oven to shorten the drying time and avoid racemization of the chiral molecules. Indeed, baking with an oven creates a very thin layer on the surface of the films that prevents the solvent to evaporate and elongates the baking time. The baking temperature is set to 120°C as an optimised temperature since lower temperature is not effective to remove the solvents and higher temperature degrades the organic part of the material [62].

During baking, the properties of the layers change. Figure 2.9 shows the effect of baking time at constant temperature on thickness and refractive index of the baked films. It can be seen that the first 10 minutes of baking results in a rapid decrease in thickness and a rapid increase in the refractive index of the layers. After this time, the thickness becomes relatively constant while the refractive index continues to increase but at a much lower rate. The rapid increase in thickness and decrease in refractive index with baking time maybe related to the evaporation of the solvents (they have low refractive index). As the solvents evaporate, the silica network begins to polymerize and densify but at a slower rate because the Si atoms carry organic molecules that slow down the process due to steric hindrance. Although the thickness and refractive index of the films appears to be constant after 20 minutes of baking, complete condensation of the films required more than 3 hours. This is set by putting the films under high vacuum in order to check if the baked films are completely dried. If this is not the case, the remaining solvents removed by high vacuum from the films induce cracks.

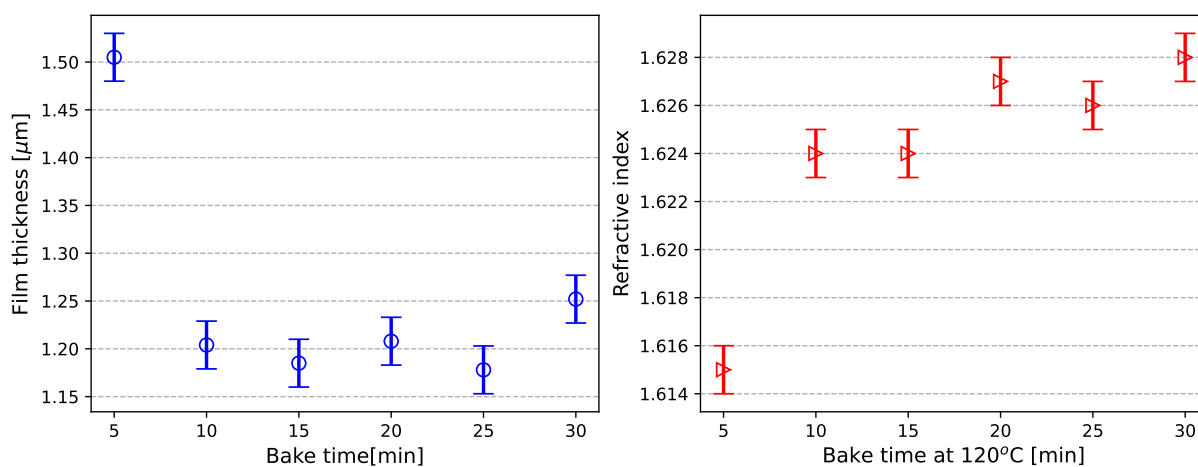


Figure 2.9: Thickness and refractive index evolution of the ORMOSIL films as a function of baking time at 120°C.

2.4.4 ORMOSIL film refractive index control

The hybrid structure of ORMOSIL films provides flexibility in controlling the final properties of the deposited film. The refractive index of a composite material is based on the refractive index of its constituents. As we discussed in chapter 1 (section 1.6), to achieve chirowaveguides with low linear birefringence, one important condition is to control the refractive indices of the guiding and the buffer layers in a way to get a refractive index contrast between these two layers as small as possible.

The refractive index of the final deposited films was controlled by adjusting the ratio of high to low refractive index components of the sol-gel solutions. Thus, in our case, by controlling the amount of MTEOS in the sol-gel solution, the refractive index of the deposited layers could be adjusted, and a refractive index contrast as low as 0.001 between the buffer and the guiding layers could be obtained.

After dip-coating of different films from different sol-gel solutions containing different amounts of MTEOS and baking all the obtained films at 120°C for 20h on hotplate, the refractive index of the films is measured by M-line.

The evolution of the refractive index as a function of MTEOS content is presented in Figure 2.10. It clearly indicates that the addition of MTEOS decreases the refractive index values of the final deposited film. The decrease in refractive index is linearly proportional to the MTEOS/R-SiO₂ ratio with -0.05 ± 0.01 ratio (slope).

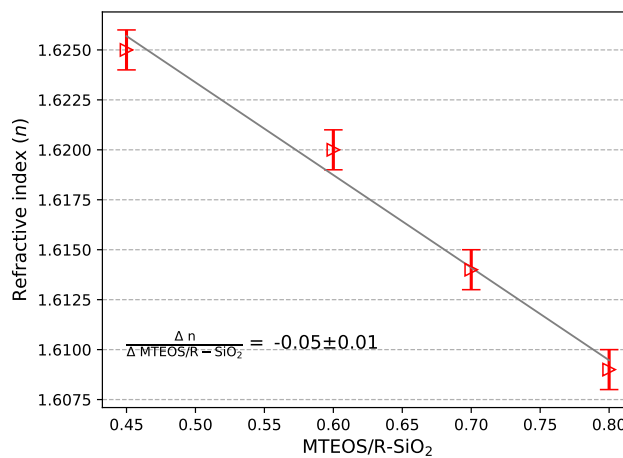


Figure 2.10: Refractive index evolution of the ORMOSIL films measured at 543nm as a function of MTEOS/R-SiO₂ ratio for films baked at 120°C for 20h on hotplate.

2.4.5 Properties of chiral ORMOSIL-films made by Sol-gel

- It is amorphous glass like material with very good optical quality with negligible optical losses above 600 nm wavelength.
- The refractive index of the material is adjustable such that it can be used to fabricate buffer and core(guiding) layer of waveguides with fine refractive index contrast as small as (~ 0.001).
- Homogeneous thick chiral and achiral films can be deposited with controlled thickness of $2\mu\text{m}$ and up to $10\mu\text{m}$.
- The key advantage of this material which allowed us to reach our objective, is that before baking, the dip coated layers are soft, and they can be stamped(imprinted) to fabricate any structure of the material including high quality channel waveguides.
- The baked (condensed) ORMOSIL films are stable and robust, they can be used to fabricate channel waveguides using etching microstructure techniques , if needed.
- Since the chiral molecules are diluted in the silica lattice, chiral films based on ORMOSIL show lower chirality($\text{CB} \sim 1 \times 10^{-5}$) compared to films made of similar chiral molecules but deposited by PLD. This is the only drawback of the ORMOSIL-films. However, this polymer material has the highest CB among amorphous polymer materials.

2.5 Conclusion

In this chapter, we have described two chiral films that will be used for channel waveguides fabrication. For both films, we have presented their synthesis and general properties. In Table 2.1, the comparison between the two methods in producing chiral films is presented.

Table 2.1: Comparison of chiral films made by PLD and sol-gel method.

PLD films	ORMOSIL films
Pure organic chiral films	Hybrid binaphthyl-SiO ₂
Fixed refractive index $n = 1.71$	Adjustable refractive index 1.6 – 1.63
High CB $\sim 2.5 \times 10^{-5}$	relatively lower CB $\sim 1 \times 10^{-5}$
Thickness inhomogeneity	Homogeneous thickness with high optical quality
Fragile films	Glass like robust films
Thickness control from few nm to few μm	Thickness control from 100nm to $\sim 20\mu\text{m}$

3.1 Microfabrication of PLD films

Since PLD films are deposited by flying molecules onto a substrate, they take the shape of the substrate on which they are deposited. This feature of PLD films allows us to fabricate channel structures in these films. In Figure 3.1, we have schematized the principle of fabricating microstructures from PLD-deposited materials which includes two processes. The first process is the fabrication of a patterned substrates as shown in Figure 3.1-a. The second process is the deposition of PLD layers on the patterned substrates as shown in Figure 3.1-b.

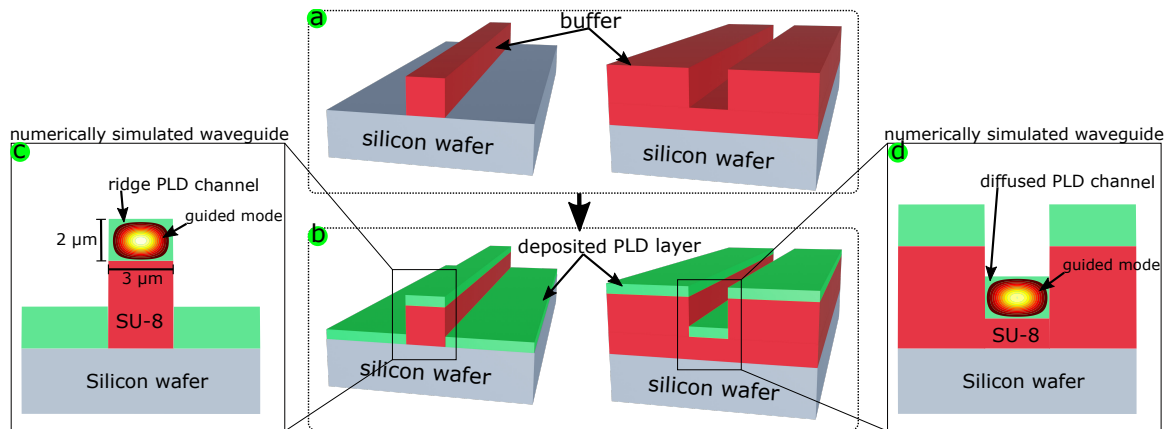


Figure 3.1: The principle of channel waveguide fabrication from PLD based films a) Patterned substrate b) Deposited PLD on patterned substrates. c-d) ridge and diffused PLD channel waveguide ($n = 1.71$) with numerically simulated guided modes intensity for a $2 \times 3 \mu\text{m}^2$ channels if SU-8 material ($n = 1.6$) is used as buffer substrate.

To use this method in optical waveguide fabrication, the patterned substrates must be transparent and have a lower refractive index than the PLD materials ($n=1.71$ at 633 nm). Based on these two conditions, we chose to fabricate SU-8 photoresist patterns on a silicon wafer because SU-8 is a transparent material and has a lower refractive index than PLD material ($n=1.6$ at 633 nm). By using different types of patterned SU-8 substrates (e.g., ridge and trench substrates), we can fabricate ridge and diffused PLD channels. Figures 3.1-c and 3.1-d show the cross-sectional design of ridge and diffuse PLD channels on SU-8 substrates with details of the channel waveguide and the guided modes simulated in such channels.

3.1.1 SU-8 Photolithography

SU-8 is a commercial negative photoresist with unique optical properties (transparent in visible and telecommunication wavelength) [72]. Its high performance in the fabrication of high aspect ratio patterns has attracted much attention for its use in many photonic applications [73, 74].

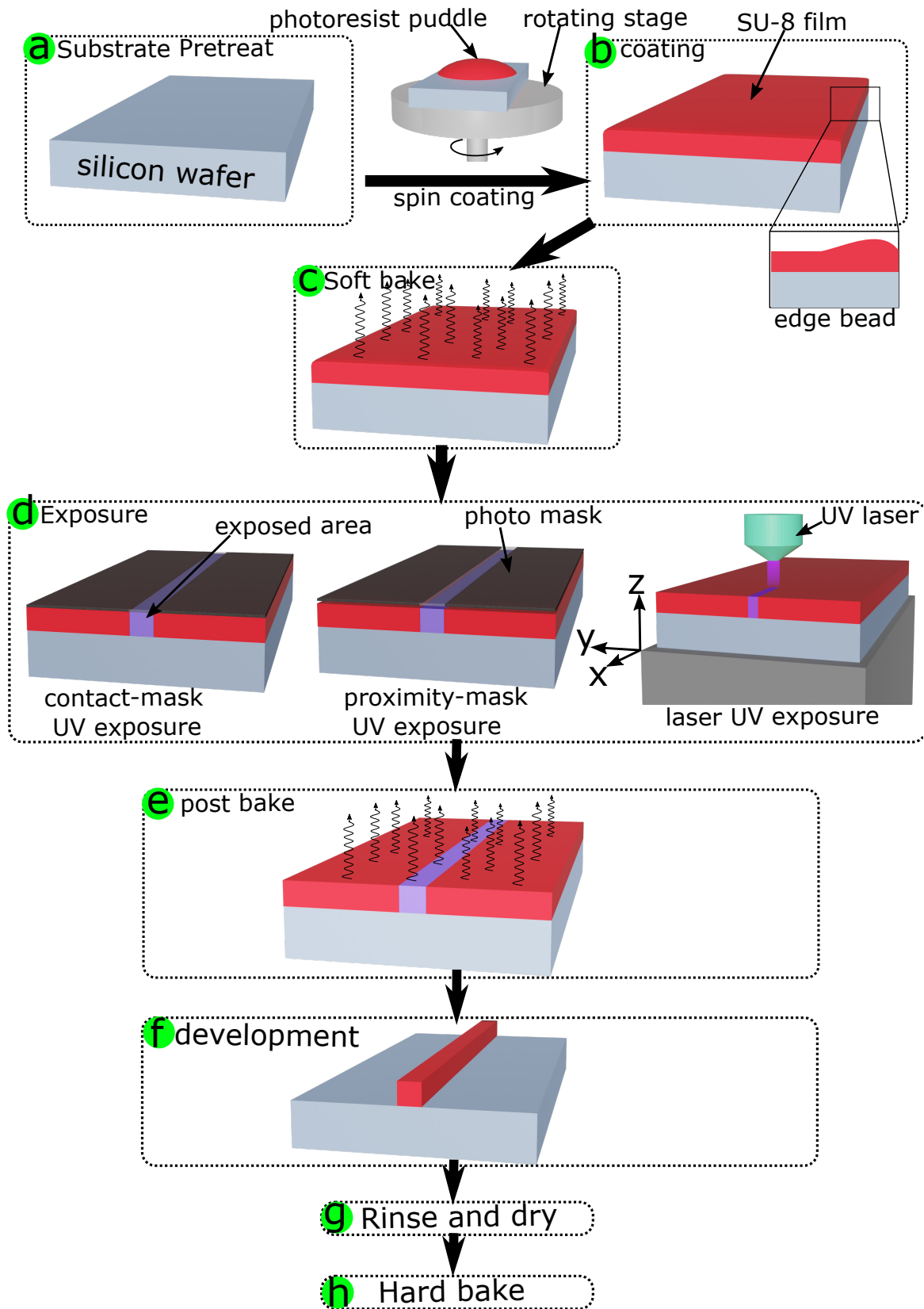


Figure 3.2: SU-8 photolithography process flow

The photoresist has been used in variety of applications from fabrication of very thick [75] to a very high resolution (nanometer scale) patterns [76]. Although the photoresist manufacturer provides a standard processing guide, the effective realization of SU-8 patterns requires the optimization of multiple processing parameters depending on the applications and instruments used in the process. We used the manufacturer's guidelines as a baseline to optimize the process parameters and fabricate the patterns for our objective. Figure 3.2 shows the flowchart of the SU-8 lithography process as recommended by the manufacturer [77], as well as 3D schematics of the samples at each step. The flow chart and 3D schematics have been modified to represent the procedure we followed during the time we worked on the fabrication of the SU-8 patterns. In the following parts of this section, we describe the different steps and present our studies on the influence of process parameters.

a) Substrate Pre-treatment(Figure 3.2-a): The lithography process starts with the preparation of the substrate. We have noticed that if the substrates are not clean or wet, the fabricated patterns can become detached during development. To avoid these problems, the silicon wafers are prepared by cleaning them with hot acetone in an ultrasonic bath, then washed with ethanol followed by purified water. They are then dried with a nitrogen blower. After this step, the wafers must be dry and free of any kind of particles (e.g. dust).

b) Photoresist film deposition(coating)(Figure 3.2-b): Typically, photoresists are coated by the spin coating method, in which a puddle of few drops of photoresist is poured onto the wafer and then spin-coated. However, SU-8 spin coatings are not homogeneous, during coating, protrusions are present on the edges of the films which are known as edge beads (see Figure 3.2-c inset). Figure 3.3 shows SEM images of trench patterns fabricated with SU-8 films with and without edge beads while all the other process parameters were equivalent. We see that presence

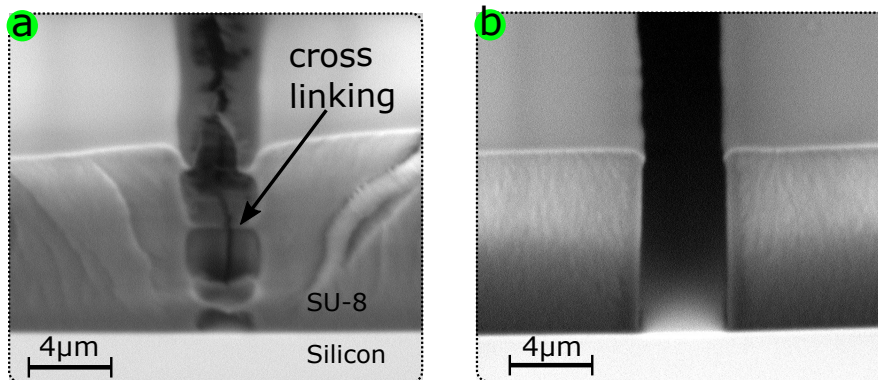


Figure 3.3: Effect of edge beads on SU-8 trench patterns a) with edge bead b) without edge beads. Not that the photolithography process parameters for both samples were all the same.

of edge beads decreases the resolution and performance of the photoresist because they cause a proximity effect when exposed to light. The cross-linking of the photoresist in the trench shown in Figure 3.3 with the edge beads is due to the fact that the edge beads limit the contact of the photomask with the coating and thus the light diffuses under the photomask. We have reduced the size of the edge beads by executing speed changing program in the spin-coater. For example, run the spinner at 500 rpm and 200 rpm/second acceleration for 10 seconds, then at 1000 rpm and 500 rpm/second for 10 seconds, then at 3000 rpm and 1000 rpm/second for 30 seconds [77]. Such technique highly reduces edge beads, especially if low thickness photoresist is used (e.g. 2 and 5 μm). To completely remove edge beads in thick SU-8 coatings (e.g., 10 μm), we cleaved the edges of the samples. These techniques allowed us to deposit homogeneous films of SU-8.

c) Soft-Bake(Figure 3.2-c): After the spin coating, the coating must be baked in order to evaporate the solvent. Complete evaporation of the solvent is necessary since the film may stick to the photomask (if photomask used) during exposure step. Although it is recommended by the photoresist manufacturer that soft baking should preferably be done in two steps, first at 65°C and then at 95°C on a hot plate, we found a single step baking directly at 95°C on a hot plate to be effective for our objective. We have optimized the soft baking time depending on the thickness of the resist, as listed in Table 3.1. The optimized values are obtained on the basis of the minimum resolution obtained and the baking time sufficient not to stick to the photomask.

Table 3.1: Optimised soft-baking time (min) at 95°C on a hotplate versus film thickness (μm) for SU-8 films.

Photoresist thickness (μm)	3 \pm 0.1	5 \pm 0.1	10 \pm 0.1
Optimized soft bake time (min)	1.5	2	2.3

d) UV-Light Exposure(Figure 3.2-d): Depending on the facilities available at the University Claude Bernard Lyon 1, we used three different exposure systems which are shown in Figure 3.4. The EVG 620 NT, UV-KUB 2, and upg101 allowed us to perform the light exposure step in hard contact mask, soft contact mask (proximity), and laser exposure respectively. The three exposure techniques are performed as follows:

1. In hard contact mask(Figure 3.2-d-left and 3.4-a), the photoresist is exposed to near-UV light through photomask * in which the photomask and the wafer (sample) are in contact.

*The photomask consists of patterns of a thin (< 50nm) layer of chromium made on a glass substrate. As SU-8 is a negative photoresist, the fabricated patterns are the negative image of the photomask patterns.

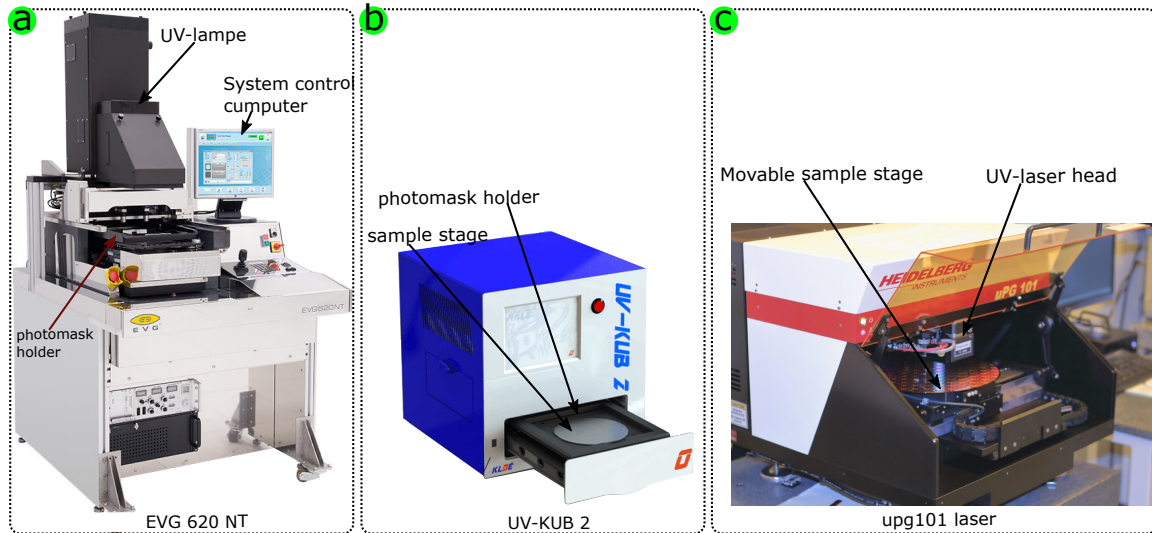


Figure 3.4: Three light exposure systems a) EVG 620 NT used for b) UV-KUB 2 c) upg101 laser exposure system.

A pressure is then applied to eliminate as much as possible the gap between the wafer and the photomask. We studied the effect of light exposure on the quality of channel and trench patterns in SU-8. Figure 3.5 presents the effect of exposure dose on pattern width for a $3\mu\text{m}$ thick photoresist when the resist is exposed through a $2\mu\text{m}$ opening in the photomask. The fabricated pattern width is seen to be very close to the feature size defined by the photomask if right energy dose is used. However, by increasing the energy dose, the width of the patterns increases significantly while the increase in width is less when the energy dose is far from the optimized value. It is therefore important to optimize this parameter because a high energy dose extends the polymerized area and limits the minimum size of the fabricated pattern. Using contact mask method minimum resolution for ridges and trenches are obtained at the optimized exposure dose which are listed in Table 3.2.

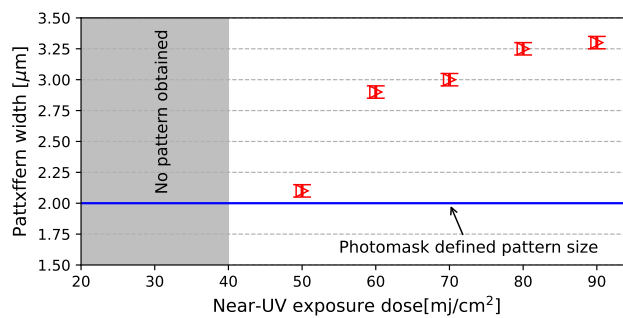


Figure 3.5: SU-8 Pattern width evolution as a function of exposure dose for $3\mu\text{m}$ thick photoresist when its exposed through $2\mu\text{m}$ opening of a photomask.

Table 3.2: Optimised exposure energy dose for three different thickness (μm) for SU-8 films for near-UV light of 362 wavelength

Photoresist thickness (μm)	3 ± 0.1	5 ± 0.1	10 ± 0.1
Optimized light exposure (mj/cm^2)	50	70	100

- In proximity photomask (Figure 3.2-d-middle and Figure 3.4-b): In proximity photolithography, there is a gap between the photomask and the resist. The gap is controlled by the mask holder system, it is usually in the micrometer range which limits the resolution of this method. The reason of using this method was that the system (Figure 3.4-b) is an effortless, fast and economical masking system. However, after much effort, we came to the conclusion that the system cannot be used to obtain SU-8 patterns smaller than $4\mu\text{m}$ because SU-8 is very sensitive to the photomask proximity effect.
- Laser exposure system (Figure 3.2-d-right and Figure 3.4-c): To fabricate patterns that were not available in photomask form, we used a laser light exposure system **uPG 101**. The system can be used for direct writing and uses a laser source at wavelength of 365nm with a micrometer scale beam size. Any pattern structures can be produced by this system and resolution down to micrometer is obtainable. The minimum resolutions of the obtained patterns are limited by the laser spot size. With this system, we have been able to fabricate high aspect ratio SU-8 patterns (10:2 in $10\mu\text{m}$ thick photoresist).

Based on the results obtained with the three light exposure systems, we have listed their advantages and disadvantages in the Table 3.3.

Table 3.3: Comparison of three photography UV exposure systems.

UV exposure model	Advantage	Disadvantage
EVG 620 NT (Figure 3.4-a)	Fast exposure	High cost
Contact mask exposure	High resolution	Photomask needed
UV-KUB 2 (Figure 3.4-b)	Fast exposure	Low resolution
Proximity mask exposure	Low cost	Photomask needed
upg101 (Figure 3.4-c)	Maskless exposure	High cost
laser exposure	High resolution	Long exposure time

e) Post-exposure bake (Figure 3.2-e): The photo-initiation by the UV light energy in the exposure step is assisted by the heat of the post-exposure bake. This step provides the additional energy needed to polymerize the exposed portion of the photoresist and therefore should be performed directly after the exposure step. Any delay between exposure and post-bake step will result in diffusion of photoacid from the exposed area and thus limit resolution [78]. In

addition, a short postbake time is not sufficient to polymerize the exposed area, whereas a long postbake time causes polymerization to continue outside the exposed area. Using a hotplate set at 95°C, we optimized the postbake time to obtain minimum resolution for three different photoresist thicknesses which are listed in Table 3.4.

Table 3.4: Optimised post exposure bake time for three different thickness (μm) for SU-8 films baked on a hotplate at 95°C.

Photoresist thickness (μm)	3 \pm 0.1	5 \pm 0.1	10 \pm 0.1
Optimized post bake time (min)	2	2	2.5

f) Development(Figure 3.2-e): Samples are allowed to cool (at room temperature) for at least one minute after post-baking before development, and then immersed in a developer provided by the photoresist manufacturer (propylene glycol methyl ether acetate). We also optimized this process parameter, the optimized development times for three SU-8 films of different thicknesses are listed in Table 3.5. We have seen that short development time is not sufficient to dissolve the unexposed area of the photoresist, while a long development time affects the sidewall angle of the fabricated patterns and also limits the minimum fabricated ridges. The optimized development times are expressed in seconds since it is important to develop the samples to the accuracy of seconds. Note that the speed of agitation of the sample in the developer solution changes development time (a faster agitation requires a shorter time and vice versa) and also affects the lithographic performance.

Table 3.5: Development times for SU-8 film as a function of film thickness using (Propylene glycol methyl ether acetate) developer.

Photoresist thickness (μm)	3 \pm 0.1	5 \pm 0.1	10 \pm 0.1
Development time (seconds)	50	90	150

g) Rinse and dry: Developed samples are sprayed (washed) with isopropyl alcohol for a few seconds to clean and remove developer residue, followed by a spray of purified water, then dried with a nitrogen blower.

h) Hard bake: All samples are baked after the rinsing and drying step for > 5 minutes on a hot plate at 95°C. This step is not critical, neither the baking time nor the baking temperature. We performed this step to ensure the stability of the SU-8 patterns when they will be used as substrates.

Lithographic performance: The SU-8 process explained in this section is sufficient to fabricate patterns up to one micrometer in $3\mu\text{m}$ and $5\mu\text{m}$ thick photoresist coatings. In the $10\mu\text{m}$ thick coatings, the minimum size obtained was $2\mu\text{m}$ ridges and $4\mu\text{m}$ trenches. SEM images of the minimum resolution obtained in the 10 micrometer thick coating are shown in Figure 3.6. Smaller features in the $10\mu\text{m}$ coating could not be obtained because ridges less than $2\mu\text{m}$ in width were detaching and trenches less than $4\mu\text{m}$ in width were cross-linking.

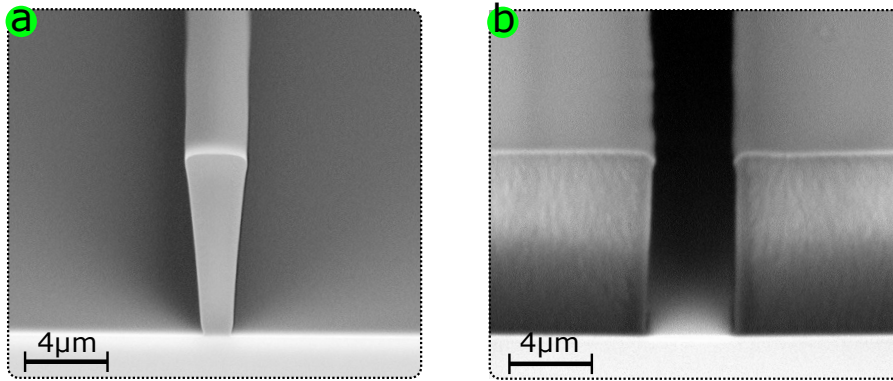


Figure 3.6: High aspect ratio SU-8 patterns. a) a width= $2\mu\text{m}$:height= $10\mu\text{m}$ ridge. b) a width= $4\mu\text{m}$:height= $10\mu\text{m}$ trench.

3.1.2 PLD deposition on patterned substrates

After fabrication of the patterned substrates from SU-8 photoresist, the next step is to fabricate the channel chirowaveguides by depositing the pure chiral material by PLD on the patterned substrate. Figure 3.7 shows deposited PLD of bridged-binaphthyle layer on ridge SU-8 patterns

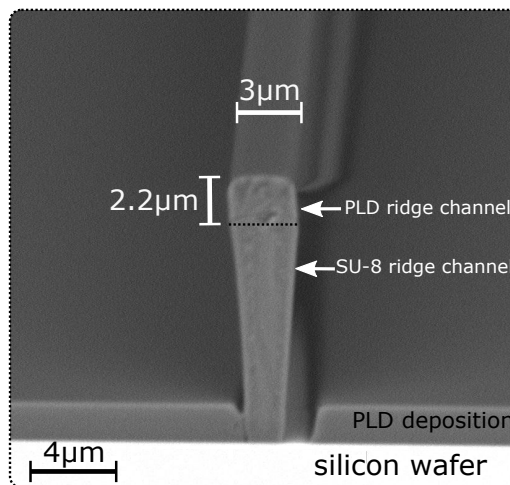


Figure 3.7: SEM image of a PLD ridge channel fabricated by depositing the PLD material on a patterned SU-8 substrate. Note that the SEM image is taken at a 45° tilted angle.

using the optimized PLD deposition parameters as described in 2.3.1. It can be seen that the PLD layer follows the substrate patterns and results in a PLD ridge channel. The width of the fabricated PLD ridge channel is defined by the patterns on the substrate while its height is defined by the thickness of the deposited layer. For the sample shown in the figure, the process ended up with a $2.2 \times 3 \mu\text{m}^2$ PLD ridge channel.

3.1.2.1 PLD channel waveguides performance

Although we have fabricated PLD channels made of pure chiral molecules, we have never been able to use them as waveguides. We studied the behavior of the channels and found that some obstacles prevented the coupling and propagation of light inside the channels. Figure 3.8-a shows a PLD channel after cleaving the sample. It can be seen that the PLD channels do not cleave like the rest of the sample, while the SU-8 patterns and the PLD layer on the wafer follow the cleavage of the silicon wafer[†]. The reason for this behavior of the PLD channels is probably the adhesive force between the SU-8 and the PLD organic layer. This behavior of the PLD channels prevented the coupling of light into the channels since we were using an end-fire coupler which requires a flat, smooth facet to couple the light.

In addition, although we could get sometimes, channels with smooth facet such as the one shown in Figure 3.7, the coupled light did not propagate, it scattered as soon as it entered the channels. Figure 3.7-b shows some parts of the PLD channels that were causing the light scattering. It appears that the molecules undergo a poly-crystallization process that deforms the shape of the PLD channels. Binaphthyl molecules are not stable in time, reorganize from amorphous material to poly-crystalline (>few days) and create therefore, uncontrollable barriers for light propagation.

[†]The sample shown in Figure 3.7 is one of the samples that PLD channels were cleaved to have flat facet while majority of the samples were cleaved as the one shown in Figure 3.8-a

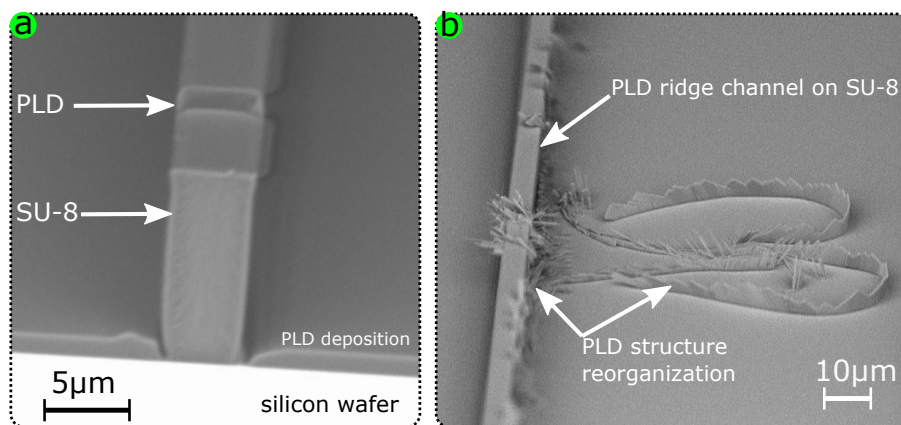


Figure 3.8: SEM images of PLD films on SU-8 channel patterns , a) PLD film cleave imperfection, b) PLD reorganisation barriers.

Considering the two problems in the fabrication of PLD channels, we decided to stop our studies on PLD films and to focus on ORMOSIL films, whose optical quality and stability over time have been demonstrated [62].

3.2 Microfabrication of ORMOSIL films by RIE

Fully condensed organically modified silica (ORMOSIL) films behave more like silica films and, therefore, we decided to investigate lithography methods suitable for silica films. One method that has proven effective in fabricating ORMOSIL microstructures is reactive ion etching (RIE) [69]. However, due to the unique properties of our ORMOSIL chiral films, we had to adapt the RIE process parameters and study the entire fabrication process.

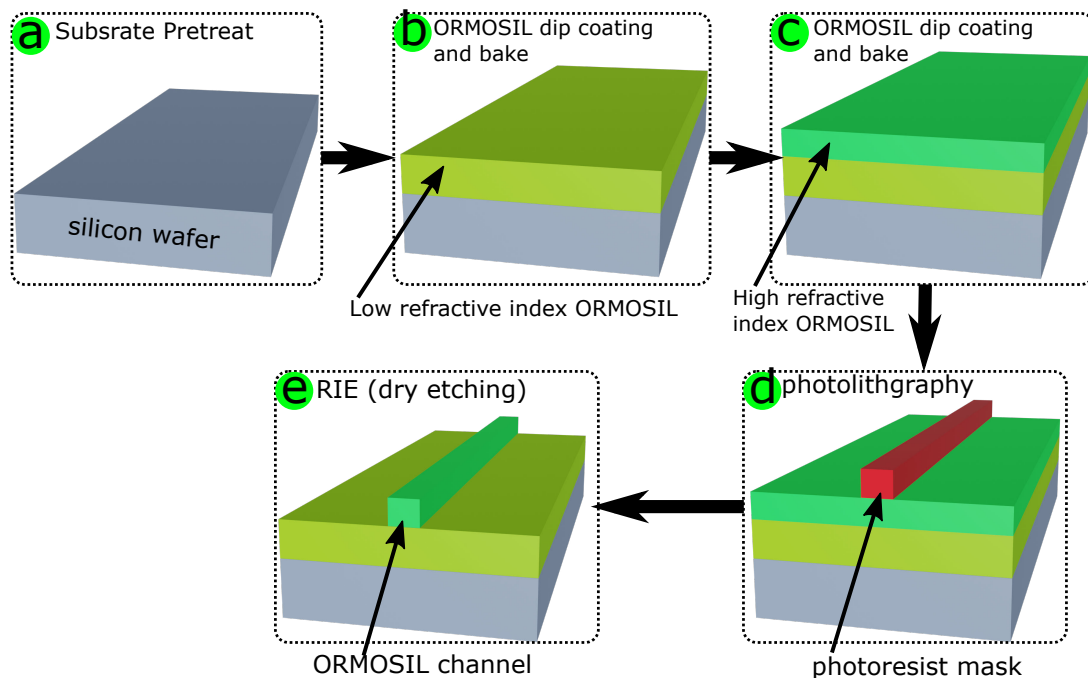


Figure 3.9: ORMOSIL dry etching process flow.

The basic idea of the RIE process is to transfer a structure defined by a mask (e.g. a photoresist) into a material that cannot be structured directly. In Figure 3.9, we have schematized the complete process we followed to fabricate ORMOSIL channel waveguides by RIE. It consists of five successive steps:

- First, silicon wafers are cleaned by soaking them in a fresh (prepared) pirhana solution to dissolve any attached pollution molecules (Figure 3.9-a).
- Thick films of low refractive index ORMOSIL (e.g. 80% of MTEOS) are then deposited on the clean wafer by dip coating, then the layers are baked for 20 hours at 120°C on a hotplate (Figure 3.9-b).

- (c) Prior to the deposition of the second ORMOSIL layers, the first layers are plasma cleaned to activate their surface, then the second layers which have a higher refractive index (compared to the first layer (e.g. 60% of MTEOS)) are deposited and the baking step is repeated (Figure 3.9-c).
- (d) In this step, photoresist patterns are fabricated on the double-layer ORMOSIL films using a commercial photoresist (AZ5214E), in which all photolithography parameters have already been optimized and a complete guide to photolithography on this photoresist is provided by the manufacturer [79] (Figure 3.9-d).

In this section, since we have previously described steps a-c (see 2.4), and in step d we have used the regular lithographic process, we discuss in detail only the RIE step (Figure 3.9-e) by explaining the basics of the method and presenting our experimental studies.

3.2.1 RIE etching principle

RIE is a dry etching mechanism that uses low pressure reactive plasmas containing ions and radicals to perform gas phase etching. The etching mechanism is divided into chemical and physical processes [80, 81]. Figure 3.10 shows the schematic of the typical etched structures based on the different processes of the etching mechanism. In the chemical etching process, a target material is etched chemically. The plasma contains reactive species (radicals) that are very active and very sensitive to the atomic bonds, they interact with the target materials surface and create volatile products. Chemical etching process is highly selective[‡] and results in an isotropic etched structure (figure 3.10-b). In the physical process, materials are etched by ion bombardment, in which energetic ions are directed at the material by an electric field. The directed ions transfer their energy to the atoms on the surface of the target materials, if the energy is high enough, the atoms of the target materials are sputtered. Therefore, the selectivity of this process is low compared to the chemical etching. Since the bombardment of the ions is directional, it produces a directional etching structure (Figure 3.10-c).

[‡]Selectivity is defined as the etch rate of the target material relative to the mask.

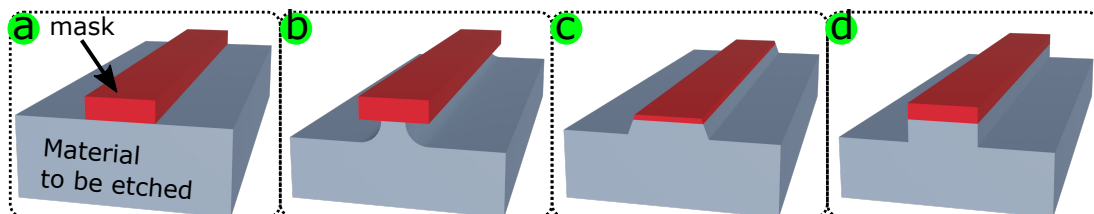


Figure 3.10: Schemes of typical etched structures of the different reactive ion etching processes. a) Sample to be etched b) Chemically etched, b) Physically etched c) combined chemical and physical etching by optimizing RIE etching process parameters.

The chemical and physical processes can be synergistically combined to overcome the limitations of both if the parameters of the RIE are optimized, as schematically shown in Figure 3.10-d. In such process, the reactive gases reduce the materials surface binding energy and enhance the sputtering, simultaneously, directed energetic ions create active sites to enhance chemical reaction of reactive gases with surface atoms and both together enhance the overall etching process [81, 82].

RIE equipment: The RIE process can be performed using RIE equipment (Figure 3.11). It consists of a high vacuum chamber controlled by a vacuum pump. Inside, there are two electrodes, the lower electrode (cathode, also serves as a sample holder) is connected to a radio frequency (RF) power, the upper electrode is grounded. After introducing reactive gases through the gas inlet, the plasma can be initiated by applying RF power (typically at 13.56 MHz) to the lower electrode (cathode) [83]. In the vacuum environment, the applied RF power causes a discharge between the two electrodes and this discharge dissociates and ionizes the gases in the chamber (i.e. the plasma). The plasma contains reactive gases and ions that are responsible for the chemical and physical etching processes. With the plasma initiation, the difference in ion and electron mobility makes the cathode electrode a negatively charged electrode; a DC bias voltage is then formed on the electrode. The electric field of the bias voltage attracts the positive ions from the plasma to the target material and causes the directional etching of the RIE.

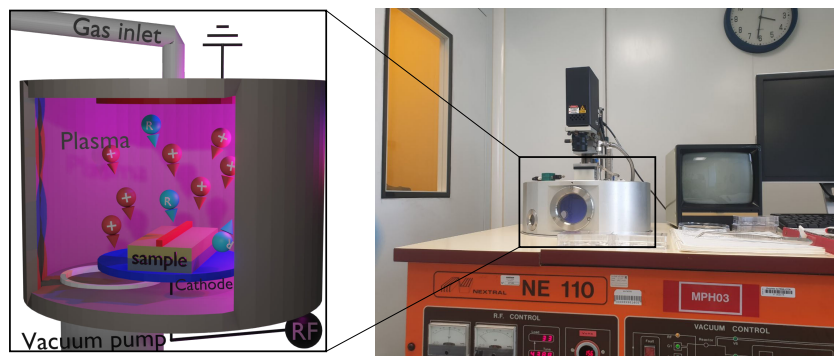


Figure 3.11: Photograph of an RIE equipment. inset) 3D Schematic representation of an ideal RIE equipment. Note that the 3D schematic is not to scale.

RIE process gases: The selection of reactive gases in the RIE is a key parameter for successful etching. Typically, different gases are used in the RIE to provide chemical and physical etching for the process. The reactive gas for chemical etching must be chosen so that the reaction product between the reactive species and the target material atoms is volatile. The ion etch gas (physical ion bombardment) should be selected based on the hardness or toughness

of the material to be etched and the mask. We are using RIE to etch ORMOSIL that is a silica based material. It has been shown that SF_6 and O_2 gas mixtures are suitable for etching silicon-containing materials [84]. SF_6 provides sufficient F-radicals to the plasma and creates volatile SiF_4 or SiF_x (x less than 4) gases while O_2 gas provides oxygen ions for physical etching. Therefore, we used a gas mixture (SF_6/O_2) as the process gases in the RIE etching of ORMOSIL films.

3.2.2 Optimising RIE process parameters for ORMOSIL etching

We explained that RIE incorporates both chemical and physical etching. It is important to optimize the process parameters so that the fabricated structure has the desired properties. In our experiments, we were using "Nextral NE110" RIE equipment (Figure 3.11), and, we chose to optimize three process parameters: the RF power (W), the gas flow rate, and the chamber pressure (mTorr) in order to achieve a high etch rate and selectivity ($\text{selectivity} = \frac{\text{ORMOSIL etch rate}}{\text{Photoresist etch rate}}$).

Experimental protocol to measure RIE etch rate: In our process optimization experiments, we used the experimental protocol shown in Figure 3.12 to measure the etch rates for ORMOSIL and photoresist. The experiment proceeds as follows: photoresist and ORMOSIL films are deposited on silicon wafers, a piece of PDMS is used to mask a part of the sample during the etching process (Figure 3.12-a). Afterwards, the sample is etched in a RIE process in which the PDMS mask protects one part of the layer and the process results into a step etched profile (Figure 3.12-b). The PDMS mask is then removed and the etching height is measured using a profilometer (Veeco Dektak 150) as shown in Figure 3.12-c and 3.12-d.

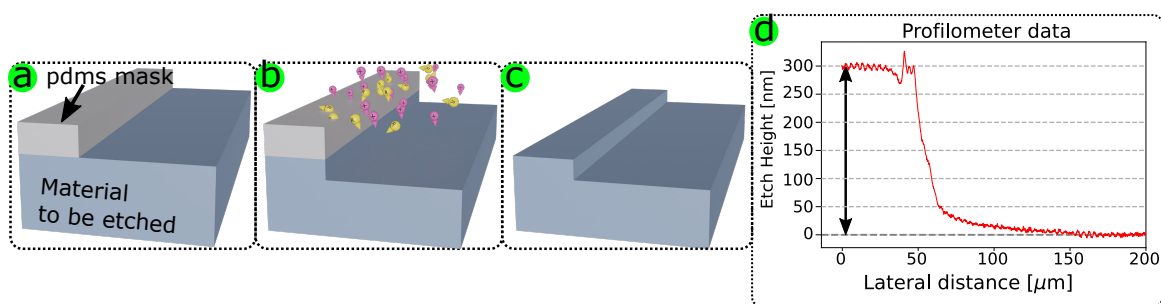


Figure 3.12: Schematic representation of etch rate measurement experimental protocol steps, a) Sample with PDMS mask b) Etched sample with PDMS mask b) Etched sample after liftoff the PDMS mask d) An experimental measure of etched step measurement by profilometer.

Experimental study: The first measurements were carried out using pure gases (SF_6 or O_2) to understand the etching process of ORMOSIL. We observed that if only pure SF_6 gas

is used in the RIE process, the ORMOSIL films become very rough. Also, in using pure O_2 gas, the process etched only the photoresist and the ORMOSIL etching was negligible. In pure SF_6 , the process results in very rough ORMOSIL films, probably because they are silica-based and SF_6 provides F-radicals that chemically interact with silicon atoms and destroy the silica network [85]. The high etch of the photoresist in pure O_2 is due to the fact that the photoresist is a pure organic material and organic materials (soft in general) can be easily etched during physical etching process.

Starting from equal gases ratio, Figure 3.13 shows the effect of oxygen gas flow on the etch rate (and selectivity) of photoresist and ORMOSIL at two different RF powers while the SF_6 is 10sccm and the chamber pressure is 25mTorr. When the RF power is 50Watt, the etch rate for ORMOSIL and photoresist increases by increasing the O_2 gas flow up to 30sccm, after which the etch rate decreases. However, for high RF power (75Watt), the etch rate always increases for ORMOSIL and photoresist. Regrading etching selectivity, at 50Watt of RF power, it is almost constant (~ 1.2) except for 20sccm of O_2 gas flow which it goes down to 0.95. At the 75Watt of RF power, selectivity goes down from 1.5 at 10sccm of O_2 flow for 1.2 at 40sccm of O_2 flow.

These results show that ORMOSIL and photoresist are primarily etched by oxygen ions since the O_2 flux increases the etch rate for both materials. The etching of both materials by

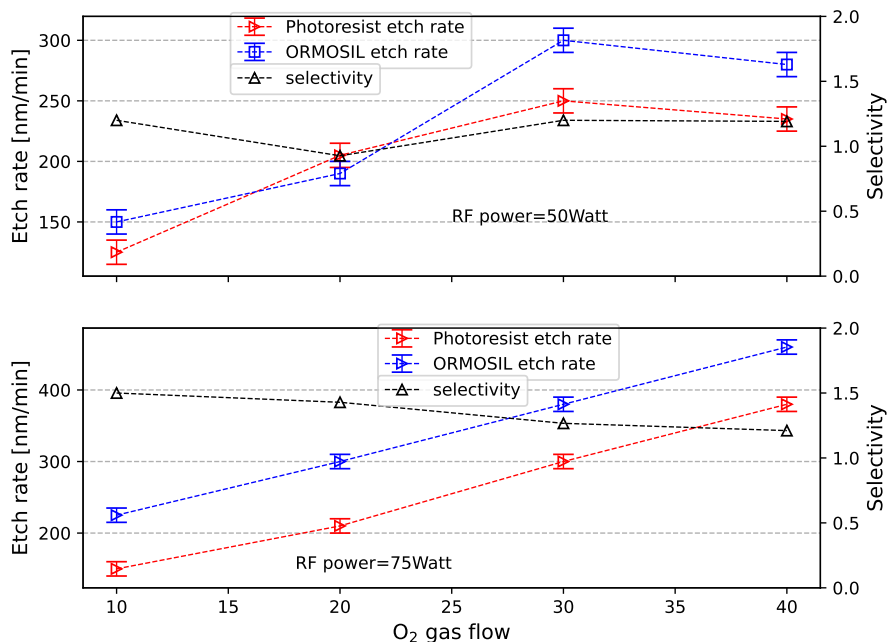


Figure 3.13: Effect of O_2 flow on AZ5214E photoresist mask and ORMOSIL etch rate for two different RF powers (top: RF power = 50Watt, bottom: RF power = 75Watt) at constant chamber pressure (25 mTorr) and SF_6 gas flow (10 sccm).

oxygen ions is also the reason for the increase in etch rate with RF power. Higher RF power creates a higher DC bias between the chamber electrodes and, therefore, the oxygen ions acquire a higher momentum and bombard the material surface with higher energy and, therefore, the etch rate is higher [86].

Although the higher RF power gives higher etch rate, high roughness is observed at higher RF power. Figure 3.14-a and 3.14-b show optical microscope images of two ORMOSIL layers that are etched at 50 and 75Watt of RF power respectively. This high roughness is probably caused by enhanced ion bombardment.

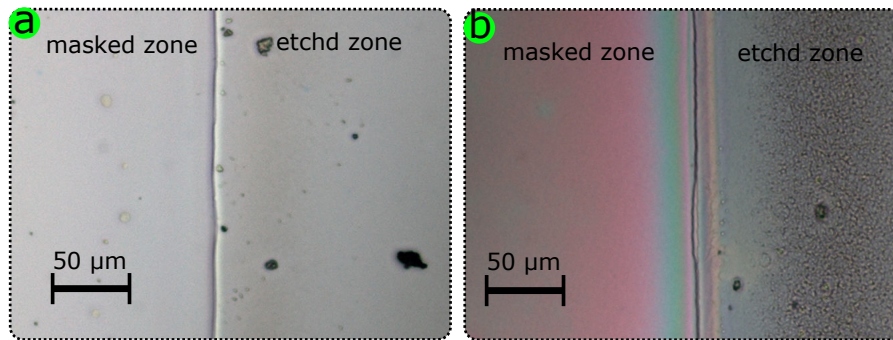


Figure 3.14: Optical microscope images of ORMOSIL layers etched at a) 50 Watt and b) 75 Watt RF power while other parameters $O_2:SF_6=30\text{sccm}:10\text{sccm}$, pressure 25 mTorr are constant.

To know the effect of RIE chamber gas pressure on etch rate, the other parameters are set constant (RF power=50Watt, $O_2:SF_6$ ratio: 30:10 sccm) and pressure of the chamber is varied. Figure 3.15 shows ORMOSIL and photoresist etch rate and selectivity as a function of RIE chamber gas pressure. As can be seen from the figure, the etch rate decreases as the pressure increases. This can be due to the fact that at high pressure, the density of the gas inside the chamber is high and the oxygen atoms lose their energy during collision before bombardment of

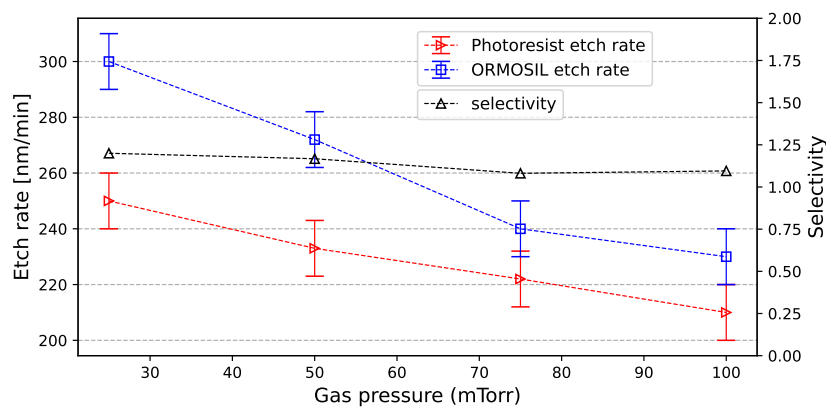


Figure 3.15: Effect of RIE chamber pressure on AZ5214E photoresist mask and ORMOSIL etch rate at constant RF power and $O_2:SF_6=30\text{sccm}:10\text{sccm}$.

the material surface [87]. Regarding selectivity, it is relatively constant in which it only changes from 1.2 to 1.1 by changing gas pressure from 25Torr to 100Torr.

Taking into account the conditions (low roughness, high etch rate and selectivity), the processing parameters were optimized as pressure=50 mTorr, RF power=50 W, O₂:SF₆ flow rate 30:10 sccm and photoresist:ORMOSIL etch rate=233±10:272±10 nm/min. The optimized parameters are selected based on the results presented here and other results obtained before I start my PhD, which showed that higher pressure decreases the roughness of the etched ORMOSIL layers but results in isotropic etching [88].

3.2.3 Crack control in ORMOSIL layers

Sol-gel based films have always suffered from the problem of film cracking [89]. Since our ORMOSIL films are also sol-gel derived films, they also had the problem of cracking, while for optical waveguides, a crack-free waveguide is an essential requirement. Throughout our work on ORMOSIL channel fabrication by RIE, we have encountered film cracking at all stages of the process.

Figure 3.16 shows three samples that cracked during the RIE process. The films are seen to crack during photolithography process of the photoresist soft mask fabrication (Figure 3.16-a). The cracking of the films in this step is due to the thermal shock of the lithography baking step. Some samples that were not cracked in the lithography step they directly cracked as soon as they were put under ultra high vacuum chamber of the RIE (Figure 3.16-b). The vacuum cracking occurred because the films were not completely condensed, and under vacuum, the remaining solvents in the films initiated cracks in the films. We were able to avoid cracking during these process steps by baking the ORMOSIL films on a hot plate to ensure that the films are fully condensed, whereas previously we were baking them in an oven.

In the final ORMOSIL etching process, the samples also cracked as shown in Figure 3.16-c. However, we have never been able to completely solve the film cracking problem in the RIE

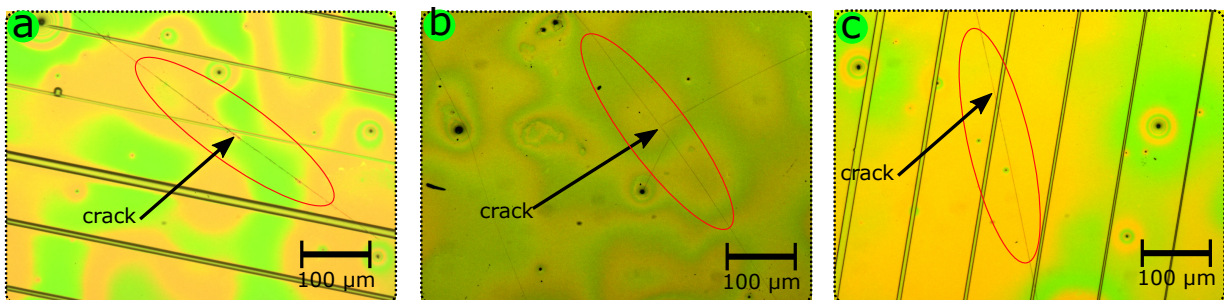


Figure 3.16: ORMOSIL film cracking during channel fabrication by RIE a) Cracks during soft mask fabrication. b) Crack by the RIE Ultra high vacuum. c) Crack during the etching process.

dry etching process, except for a few samples. As can be seen in the figure, the cracks cut the channels and prevent their use as waveguides.

3.2.4 Fabricated ORMOSIL channels

Figure 3.17 shows SEM images of a three-step RIE process on an ORMOSIL layer at the optimized process parameters. A $2.3 \pm 0.1 \mu\text{m}$ thick photoresist (AZ5214E) channel is fabricated on a thick ORMOSIL film (Figure 3.17-a). The sample is etched for 5 minutes, during this time $1.4 \pm 0.1 \mu\text{m}$ of ORMOSIL is etched while only $1.1 \pm 0.1 \mu\text{m}$ of photoresist mask is etched (Figure 3.17-b). The sample then etched again for an additional 3 minutes, during the total 8 minutes, $2.1 \pm 0.1 \mu\text{m}$ of ORMOSIL and $1.7 \pm 0.1 \mu\text{m}$ of photoresist are etched. In the two-step etching process selectivity is found to be constant $\sim 1.2 \pm 0.05$. The results show that the shape of the photoresist, including the sidewall angle, can be transferred to the ORMOSIL layer. However, the roughness of ORMOSIL and photoresist increases with etching time.

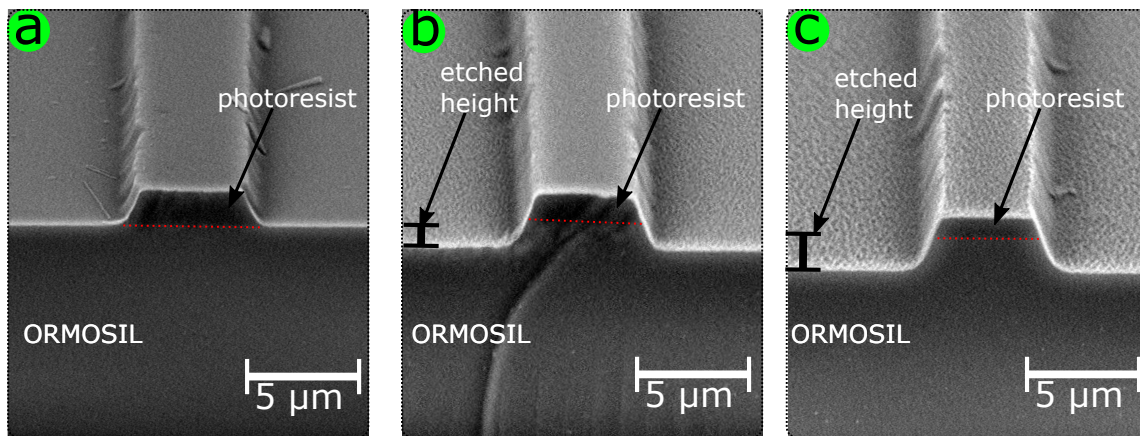


Figure 3.17: Scanning electron microscope images of RIE process a) Photoresist mask on ORMOSIL, b) 5 minutes RIE etched ORMOSIL, and c) 8 minutes RIE etched ORMOSIL. The process parameters are pressure=50 mTorr, RF power=50 W, $O_2:SF_6$ flow rate 30:10 sccm.

The results shown in Figure 3.17 are the best results I have obtained during the time I have been working on the fabrication of ORMOSIL structures by RIE. Although our latest results on ORMOSIL channel fabrication by RIE were quite promising, we decided to stop our study on this fabrication method for the following reasons:

1. We found another fabrication method that is much more efficient than RIE for our material (the new method is described in the next section- 3.3).
2. Most of the samples were cracking, which made the method very time-consuming.
3. Even at our optimized RIE process parameters, the roughness of the fabricated channels was still high.

3.3 Microfabrication of ORMOSIL by Imprint Lithography

We explained in the previous chapter (section 2.4) that ORMOSIL films are obtained by dip coating of sol-gel derived ORMOSIL solutions on substrates. Prior to baking, the ORMOSIL layers are wet and soft and can be patterned using imprint lithography method. The basic principle of imprint lithography is simple: transfer the structure of a mold to the soft ORMOSIL layers by imprinting (stamping) the mold on the surface of the layers [70]. In Figure 3.18 we have schematically shown the process flow of ORMOSIL channel waveguide fabrication by imprint lithography. The process is performed in five successive steps as described in the following:

- In the first step, silicon wafers are cleaned by soaking them in a fresh (prepared) pirhana solution to dissolve any attached pollution molecules(Figure 3.18-a).
- Thick layers of ORMOSIL are dip coated on the clean wafers, then baked for 20 hours at 120°C on a hotplate(Figure 3.18-b).
- Prior to the deposition of the second ORMOSIL layers, the first layers are plasma cleaned to activate their surface, then fresh ORMOSIL layer with high refractive index (relative to first layer) are dip coated(Figure 3.18-c).
- Directly after dip coating of the second ORMOSIL layers, PDMS molds are imprinted on to the fresh ORMOSIL by gently putting the PDMS mold on the layers. The size of PDMS molds must be smaller than the ORMOSIL layer otherwise the edge beads of the film prevent the mold to completely transfer the structures. To fix the mold on the layers, the ensemble (PDMS mold on ORMOSIL layer) is sandwiched between two glass slides

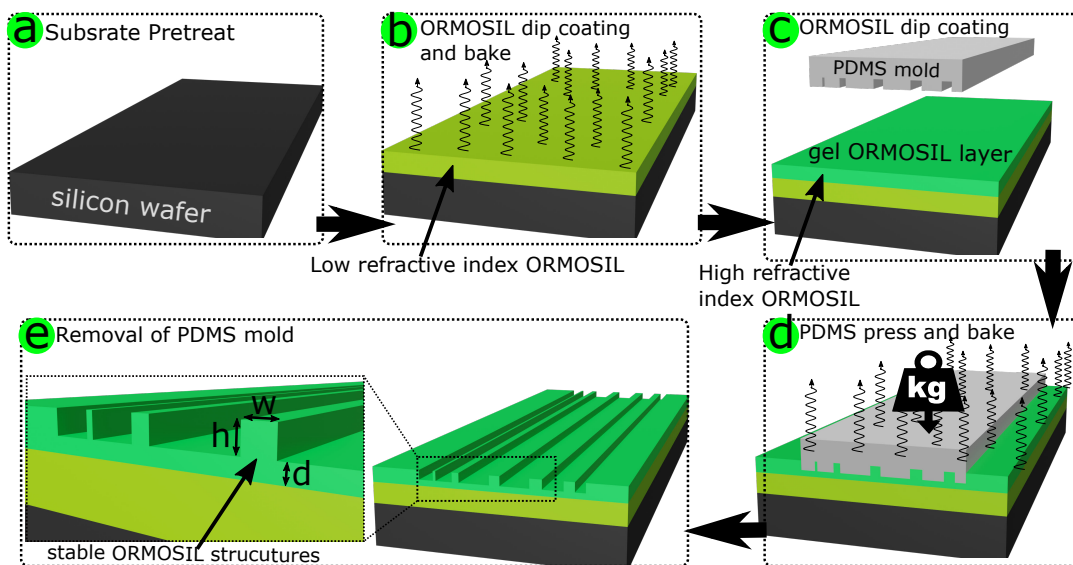


Figure 3.18: Imprint lithography on ORMOSIL films process flow

then clamped using foldback clips as shown in Figure 3.19. Glass slides are used in the clamping to ensure homogeneous distribution of the clamp pressure on the PDMS molds. We have studied the effect of load applied on the pdms mold (between 1–10Kg,) but we didn't see any obvious effect of different forces in that range on the resulted fabricated structures.

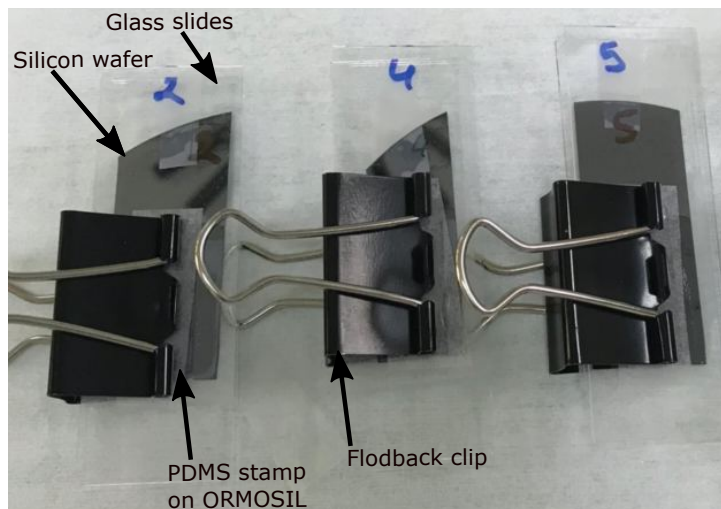


Figure 3.19: Photograph of three imprint samples.

The clamped samples were then baked in an oven at 120°C for 3.5 hours. Due to high permeability of PDMS to the diffusion of small molecules, including sol-gel solvents, it allows the drying of the structures [90]. The baking temperature of 120°C is chosen as the optimal temperature, because at lower temperatures the obtained ORMOSIL structures are not stable and higher temperatures the ORMOSIL material loss chirality [62]. Regarding the 3.5 hours bake time, a longer bake time complicates the removing of PDMS, and for a shorter bake time the fabricated structures are not stable.

- (e) After baking the samples, the clamps were released and the PDMS molds were removed from the samples by slowly pulling on one side of the mold. The removed PDMS molds are clean without having any ORMOSIL residues, they can be reused several times. At this step, ORMOSIL structures are fabricated that have negative image shape of the PDMS molds (Figure 3.18-e).

The success of the imprint lithography method lies in the fact that the mold does not bond to the ORMOSIL layer during the imprinting process. Based on this condition, we chose to use a polydimethylsiloxane (PDMS) mold because its low binding affinity to other materials has already been proven [91]. Although PDMS molds are simple to make, they can only be made by replicating the structure of other molds, called master molds. In the following subsections, we describe the experimental processes for i) fabrication of the master molds; ii) replication of the PDMS molds from the master molds.

3.3.1 Master mold fabrication

The structures obtained by PDMS-based imprint lithography are defined by the master molds, any imperfections in the master molds will be transferred by the PDMS molds to the fabricated ORMOSIL structures. During the time we used the imprint lithography method, we made master molds with two methods which are schematically shown in Figure 3.20. The first method is a direct fabrication of the targeted channel structures using SU-8 photoresist on a silicon wafer as shown in Figure 3.20-a. Such SU-8 master molds are fabricated by following the photolithography process explained in 3.1.1. The advantages of using SU-8 for master mold fabrication is that the process is fast, and it can be fabricated in one step. However, if the master mold is planned to be used for a long time and needs to be cleaned several times, it is better to use silicon molds. Therefore, we decided to fabricate silicon master molds and in the following, we give the experimental details of their fabrication.

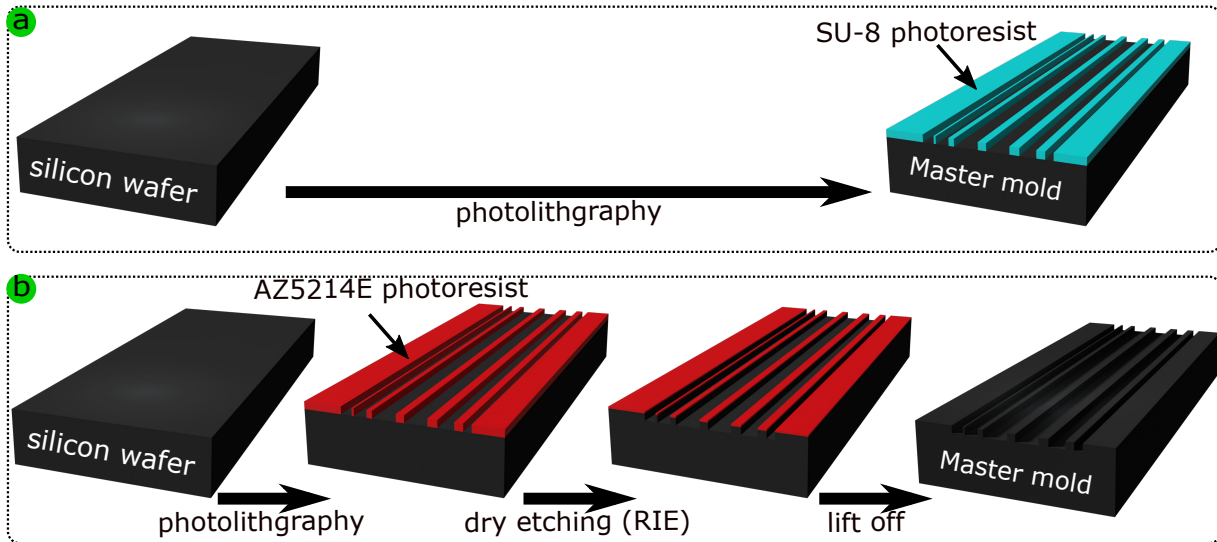


Figure 3.20: Two methods for master mold fabrication for PDMS replication a) SU-8 master mold and b) Silicon master mold.

silicon master mold fabrication

The silicon master molds are fabricated in three steps process as schematically shown in Figure 3.20-b.

1. **Photolithography of AZ5214E photoresist in negative mode:** The photoresist is spin-coated on a clean silicon wafer at 3000 rpm for 50 seconds to get $1.8\mu\text{m}$ photoresist film. After a soft baking at 110°C for 50 seconds on a hotplate, the photoresist layer is exposed to near-UV light exposure (intensity= 0.4mW , writing speed $5\frac{\text{mm}^2}{\text{min}}$, $\lambda = 365\text{nm}$)

using uPG 101 laser exposure system. The exposed photoresist is then post baked at 110°C for 60 seconds. Afterwards, the whole sample is again exposed to near UV light ($400\text{mJ}/\text{cm}^2$ at 365nm) using the exposure system (UV-KUB 2). The exposed photoresist film is developed in a solution (AZ 726 MIF) for 50 seconds. The developed sample is immersed in a glass container with water flow for 1 minute to clean and remove developer residue then dried with a nitrogen blower. The remaining photoresist patterns are the channel patterns with desired width that will be used as soft mask for dry etching in RIE.

2. **Dry etching of photoresist patterns by RIE:** The RIE process is performed using the same RIE equipment (Nextral NE110) and the same gas mixture ($\text{SF}_6:\text{O}_2$) that was used for ORMOSIL dry etching (see 3.2). After multiple of experiments, the processing parameters for silicon etching were optimized as follows: pressure = 50 mTorr , RF power = 50 watt , $\text{SF}_6 = 10\text{sccm}:\text{O}_2 = 10\text{sccm}$ flow rate. With these optimized parameters, $2.2 \pm 0.1\mu\text{m}$ of silicon is etched in 500 seconds with about 90° side wall angle.
3. **Lift off of the remaining photoresist:** After etching the silicon wafer, the sample is immersed in acetone in an ultrasonic bench to remove the remaining photoresist. At this stage, silicon patterns with a width defined by the photoresist and a height of $2.2 \pm 0.1\mu\text{m}$ are fabricated.

In Figure 3.21, we have shown an SEM image of the structure of a $2.2 \pm 0.1\mu\text{m}$ high and $2.7 \pm 0.1\mu\text{m}$ wide silicon channel fabricated using the previously described process. As can be seen in the figure, the sidewall and surface roughness of the channel are very low, which ensures the low roughness of the fabricated ORMOSIL channels.

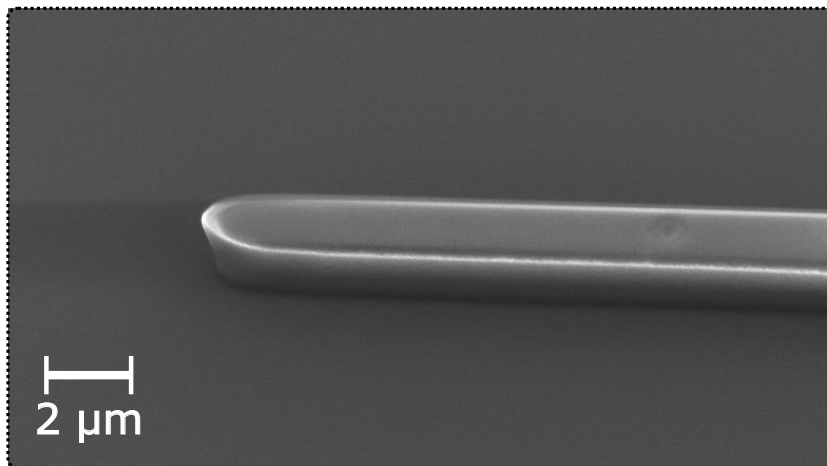


Figure 3.21: SEM image of silicon master mold fabricated by RIE. note that the the image is taken at 45° .

3.3.2 PDMS mold replication

PDMS is a silicon-based polymer that is transparent (compatible with UV-curable materials), elastic (compatible with all structures) and inexpensive. It is already used to reproduce patterns from a few nanometers to hundreds of microns [91, 92]. We used PDMS to obtain a negative image of the master mold structures for use in the imprinting process. The PDMS mold replication process is schematically shown in Figure 3.22, it consists of the following steps:

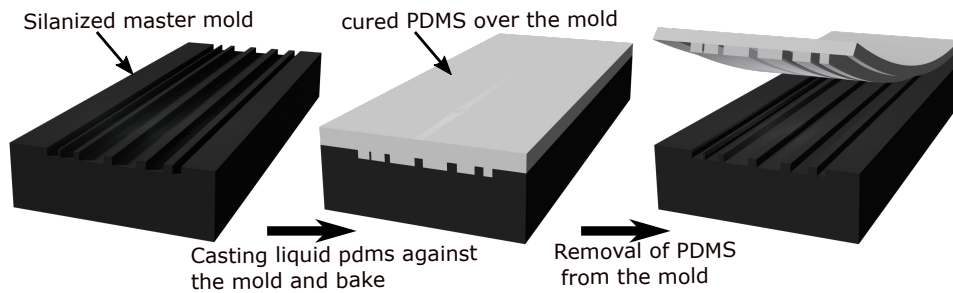


Figure 3.22: PDMS mold fabrication process flow.

1. **Master mold pretreatment:** This step is necessary if the substrate of the master molds is silicon, whether it is SU-8 patterns on silicon or pure silicon patterns. Silicon wafers are partially hydrophilic, which can lead to direct bonding of the silicon wafers to PDMS via the hydroxyl groups. It is therefore essential to make silicon-based molds hydrophobic by modifying the surface, which can be done by adding a silane function to the surface in a process known as silanization. To silanize the silicon mold, few microliters of a silanizing agent (TriMethylChloroSilane) is added to a small plastic cup and then, along with the silicon mold, placed in a vacuum desiccator. In Figure 3.23, we have shown the experimental facility used for silanization. The mold is left under vacuum for 3 hours so that the silanes form a monolayer on the silicon surface.



Figure 3.23: Photograph of the experimental facility for master mold silanization.

2. **Casting of liquid PDMS against the mold and bake:** This process is performed in five successive steps. Liquid PDMS is first prepared by mixing the PDMS base (Sylgard 184) and the curing agent with a plastic lab spatula in a 10:1 ratio (e.g. 20g of PDMS base with 2g of the curing agent). It is important during the mixing process to add the curing agent to the liquid Sylgard 184 and not the other way around, otherwise it may result in poor crosslinking of the polymer. Second, the silanized master mold was attached to the base of a petri dish to prevent the mold from floating in the liquid PDMS. Third, the liquid PDMS was poured onto the master mold in the petri dish. Four, the Petri dish containing the master mold and the liquid PDMS was placed under vacuum in a desiccator for 10-20 minutes to remove air bubbles produced during the preparation of the liquid PDMS. Five, the air bubbles-free liquid PDMS was placed in an oven set at 70°C for 4-5 hours to cure as shown in the Figure 3.24-a. Indeed, liquid PDMS can polymerize at room temperature but the curing time decreases with increasing temperature.
3. **Removal of PDMS from the master mold:** The cured PDMS was removed from the master molds by slowly pulling it from one edge of the petri dish. The replicated PDMS molds were then cut with a scalpel to the size of the master molds as shown in Figure 3.24-b.

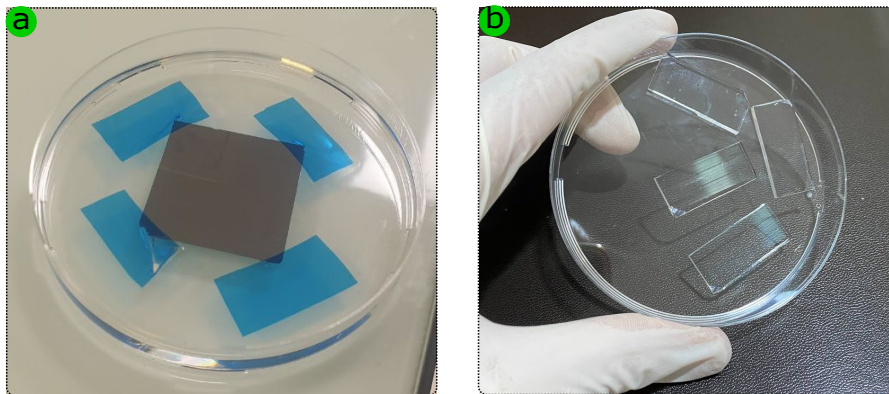


Figure 3.24: Photographs of last two steps in replicating the PDMS mold from the master mold a) Curing of the liquid PDMS on the master mold placed on a petri dish. b) PDMS molds removed and cut out.

In PDMS replication processes, the negative images of fabricated master molds are transferred into PDMS molds. Figure 3.25 shows a PDMS mold that replicated the negative image of three ridge structures of the same height but different width. The structures in the PDMS are trenches of the same size as the structures in the master mold. We used each PDMS mold multiple times for imprint lithography without noting any degradation in the performance of the fabricated ORMOSIL structures.

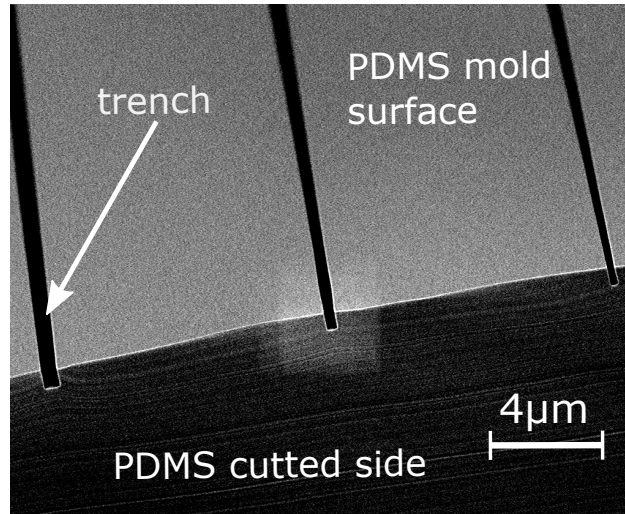


Figure 3.25: SEM image of a pdms mold

3.3.3 Fabricated ORMOSIL channel by imprint lithography

Figure 3.26 shows SEM images of ORMOSIL structures fabricated by imprint lithography. It can be seen that multiple structures of different sizes from the PDMS mold are well transferred onto the ORMOSIL layer. The sidewall and surface roughness of the structures are low enough that they are not sensed by a high-resolution SEM. During the time we used imprint lithography, we found no size limitations in this method. However, in the fabrication of the optical waveguides, we noticed that the process always ends with a small layer (d) below the fabricated channels as shown in Figure 3.26-b. This means that the fabricated optical waveguides

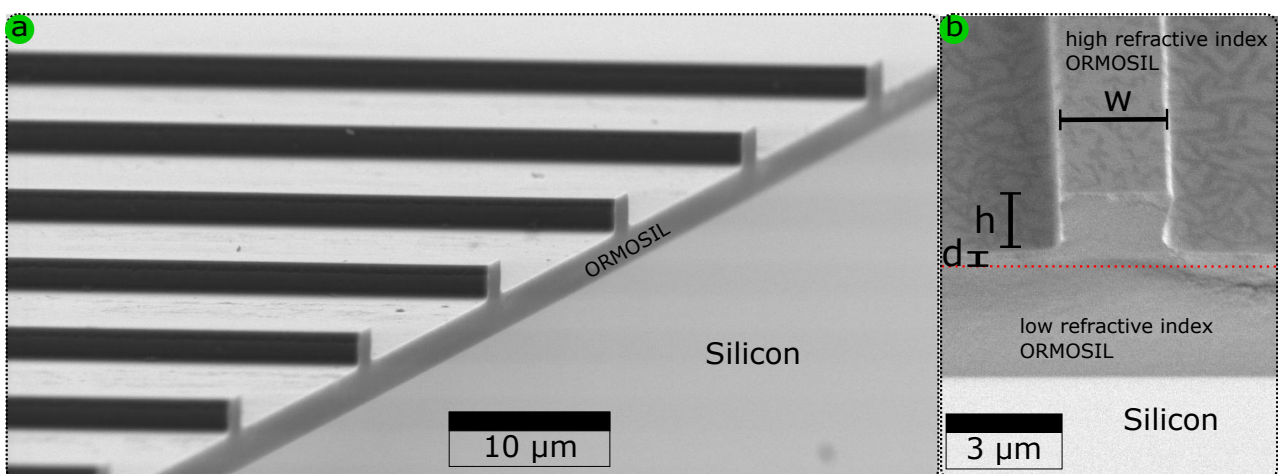


Figure 3.26: SEM images of ORMOSIL structures fabricated by imprint lithography a) rib waveguides with different width and b) a fabricated ORMOSIL channel with width ($w=2.7\pm 0.1\mu m$), height ($h=2.1\pm 0.1\mu m$) and rib slab thickness $d=0.2\pm 0.1\mu m$.

were always rib structures. The only drawback (to date) of this fabrication process is that the thickness of d layer could not be controlled.

In terms of optical performance, the waveguides fabricated by imprint lithography exhibit excellent optical performance (i.e., they easily guide light and exhibit low losses, as we will show in Chapter 5). In addition, the samples never cracked during the process, whereas cracking was the main problem with ORMOSIL microstructuring by RIE. Since this fabrication method allowed us to fabricate high quality optical waveguides, we decided to use only this method and abandon the previous methods.

3.4 Conclusion

In this chapter we have described three microfabrication methods for chirowaveguides channel fabrication. For each method we have discussed in details the principle of the method and the procedure to repeat such method. In Table 3.6, we have listed advantages and limitations for the three different methods.

Table 3.6: Comparison of different methods for the fabrication of channel chirowaveguides.

Fabrication Method	Advantages	Disadvantages	Choice
PLD deposition on patterned substrates	-Pure chirowaveguide -Simple process -Thickness control -Diffused and ridge channel	-Structure instability -Hard to couple light to the channels	Abandoned
ORMOSIL dry etching by RIE	-Thickness control -Ridge and rib channel	-High cost -High roughness -Complicated process -Structure cracking	Abandoned
ORMOSIL imprint lithography	-Simple process -Low cost -Thickness control -Stable structures -Low roughness	not controlled rib slab thickness	Selected

The first method was fabrication of channel chirowaveguide of pure chiral material deposited by PLD. The method included by the fabrication of SU-8 photoresist patterned substrate and then deposition of PLD layers on the patterned substrates to obtain PLD deposited structures. The second method was fabrication of channel chirowaveguides from sol-gel derived ORMOSIL films. This method was the conventional dry etching method for the fabrication of structures in

thin films. In the method patterns of AZ5214E photoresist are fabricated on ORMOSIL layers then they were transferred to the ORMOSIL layers in a reactive ion etching process. The last method was fabrication of channel chirowaveguides from sol-gel derived ORMOSIL by PDMS based imprint lithography. In the method structures of silicon or SU-8 molds were replicated by PDMS then they were transferred to the ORMOSIL layers.

For the three methods investigated, we were only able to use ORMOSIL channel waveguides fabricated by imprint lithography. This method was found to be much more efficient than the other two methods, so we concluded that we would only use imprint lithography to fabricate the channel chirowaveguides.

Development of Optical Setups for Waveguide Characterization

AFTER a year of study, we fortunately found a suitable method to fabricate good quality channel waveguides as attested by optical and scanning electron microscopes (see Figure 3.26). For our objective which requires a chirowaveguide with circularly polarized eigenmodes, the optical property of the waveguides can only be known by using optical characterization methods. An effective method to characterize the polarization properties of an optical system is to use classical Stokes polarimetry measurements [93]. By knowing the Stokes parameters of a laser beam and measuring the Stokes parameters of the same beam after interaction with the optical system, one can fully describe their optical properties in terms of polarization. In our case, we do not need simple classical Stokes polarimetry, such as bulk media polarimetry, but a polarimetry setup equipped with a technique to guide (couple) laser light into the waveguides and collect the output light out of the waveguides. In this chapter, we present the optical setups that we have developed and used for the characterization of our chirowaveguides by explaining the operating principle of the constituent optical elements as well as their advantages and limitations.

4.1 Waveguides input-output coupling

As discussed in Chapter 1, light is guided and propagates in waveguides as guided modes. To characterize waveguides, we need devices that convert a laser beam into guided modes, and also collect the light from the waveguides. These devices are known as waveguide light couplers. Researchers have developed three effective light waveguide couplers: prism coupler [57], grating coupler [94] and end-fire(direct) coupler [95].

4.1.1 Prism coupler

Prism coupler works by focusing a light beam onto the base of a high refractive index prism that is in proximity to a waveguide so that the evanescent field of the focused light beam tunnels to the waveguide. Figure 4.1 shows the schematic of an ideal prism coupler. One important condition for this technique to work is that the waveguide must be placed in contact with the base of the prism. To achieve the proximity between the waveguide and the prism, the waveguide must be pressed towards the base of the prism such that the evanescent field from the base of the prism overlap with the waveguide's guided modes. Light couples into the waveguide when phase velocity of the evanescent wave is equal to phase velocity of the waveguide's guided modes. The condition for phase matching is

$$k n_p \sin \theta = \beta_m \quad (4.1)$$

where ($k = \frac{2\pi}{\lambda}$) is the free-space wavenumber, n_p is refractive index of the prims, θ is angle of the light beam at the base of the prism, β is propagation constant of the guided modes, and $m = 0, 1, 2 \dots$ is guided mode order.

At certain values of θ the phase matching condition fulfills and light couples to the waveguide. The θ angles depend on the refractive index of the prism, the refractive index of the substrate (or buffer), the refractive index and the thickness of the waveguide. Thus, by knowing the refractive index of the prism and measuring the θ angles, calculation can be performed to obtain the thickness and refractive index of the waveguide. Indeed, to independently determine the thickness and refractive index of the waveguide, at least two coupling angles (i.e. two supported modes) are required.

Prism coupler is most suitable for thin films (planar waveguides) and is the coupler of M-line spectroscopy technique that is used to study the properties of optical thin films (thickness and refractive index). We have used M-line spectroscopy to measure refractive index and thickness of the planar chirowaveguides. However, the prism coupler is not suitable for studying channel waveguides; we avoided using such coupler to study the waveguides because:

- (i) Coupling of light into channel waveguides using a prism is a very challenging task [96].
- (ii) Pressing the channel waveguides to the base of the prism may destroy the channels.

4.1.2 Grating coupler

Grating coupling method uses periodic structures (grating) close to a waveguide guiding layer to couple the light diffracted by the grating to the waveguide as schematically shown in Figure 4.1-b. Light couples into the waveguide when the phase velocity of the diffracted light is equal to

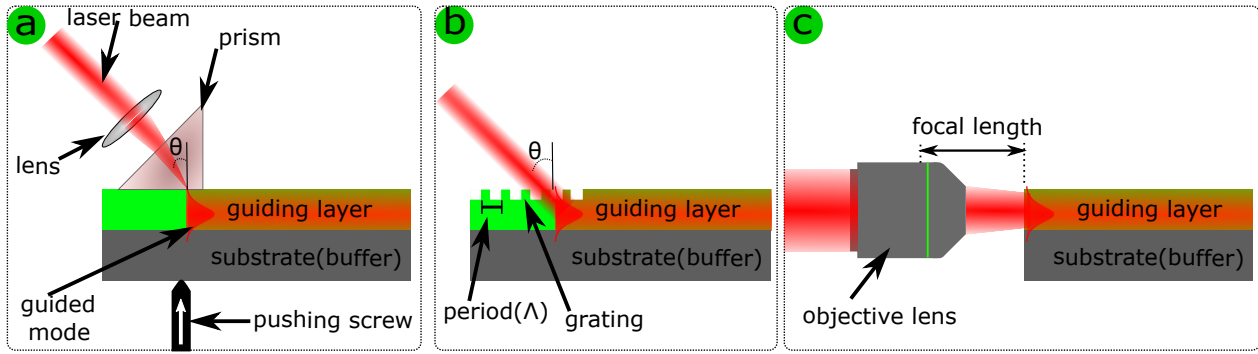


Figure 4.1: Schematic description of a) Prism coupler, b) Grating coupler, and c) End-fire coupler. The schematics are not to scale.

the phase velocity of a guided modes of the waveguide. The condition for phase matching is

$$k \sin \theta + p \frac{2\pi}{\Lambda} = \beta_m \quad (4.2)$$

where θ is angle of the light beam with respect to the normal line to the grating, p is diffraction order, and Λ is the grating period. From equation 4.2, to couple first order diffracted light (i.e. achieve high coupling efficiency), the grating must have a period less than the wavelength of the light.

Although the grating coupler can be integrated into channel waveguides, we did not use it in our characterization method because grating couplers are polarization sensitive and therefore not suitable for polarimetry studies [94].

4.1.3 End-fire(direct) coupler

For the whole polarimetry study we carried on the waveguides, we have only used end-fire(direct) coupling technique. As shown in Figure 4.2-c, an end-fire coupler directly couples a light beam into a waveguide by focusing the beam on the end faces of the waveguide using optical lenses. The first condition for this technique to work is that the waveguide must be prepared to have a flat input facet. This condition can be met by fabricating the waveguide on a silicon substrate and then cleaving the silicon. High coupling efficiency can be achieved by matching the focused beam profile to the guided modes profile. Since laser beams are Gaussian shape beams, they can be focused in a way that they match the fundamental modes of the waveguide (planar or channel).

Conditions for high coupling efficiency: Using appropriate optical lenses with right focal length and numerical aperture, one can focus a laser beam so that the beam intensity distribution (beam waist) at the entrance of the waveguide is as close as possible to overlap with the

field of the fundamental modes of the waveguide. For a laser light beam of diameter D and wavelength λ , the beam size d_f at the focal point is

$$d_f \approx \frac{4\lambda f}{\pi D} \approx \frac{2\lambda}{\pi N.A.} \quad (4.3)$$

where f and $N.A.$ are focal length and numerical aperture of the lens respectively. To avoid aberrations, we have used high numerical aperture objective lenses* instead of standard optical lenses for light coupling and collecting. With such objective lenses, we can image waveguides and guided modes, as well as couple (and collect) light simultaneously. However, end-fire coupling is rather delicate technique, any mismatch between the focused beam profile and the profile of the fundamental guided modes will lead to energy transfer into higher order or buffer leaky modes. To obtain high coupling efficiency, it is important to control position, size of the focused beam relative to the waveguide's edge facet and guided modes. Moreover, the coupling efficiency also depends on the angle of the focused beam with respect to the waveguide facet (maximum at right angles) and also on the cleanliness of the facet. Therefore, the objective lens and the laser beam require critical alignment and micro meter precision manipulation.

4.1.3.1 Experimental End-Fire coupler

Figure 4.2-a schematically represents our end-fire coupling setup. A light beam from a single-mode fiber-coupled laser-diode (5 mW, 635 nm-Roithner Laser Technik) is collimated using a regular beam collimator. To control the laser beam size, multiple lenses are used so that the beam size is equivalent to the aperture of the input coupling objective. The laser source is placed far enough away from the waveguide ($> 2\text{m}$) to have freedom in manipulating the beam. The height of the beam relative to the optical table is controlled with a mirror so that the beam is parallel to the optical table and arrives perpendicular to the waveguide entrance facet. The angle of the beam on the side of the waveguide is adjusted by controlling the reflection light on the side faces of the waveguides' silicon substrates. The light beam (Gaussian shaped, collimated, properly sized) arrives at the entrance of the objective, and it is focused at waveguide's input facet. To manipulate the focused beam at the micrometer scale, a waveguide alignment system (MDE881) is used. The MDE881 system allows us to control the position of the focused beam at the micrometer scale with several degrees of motion necessary for the type of critical alignment required for the end-fire coupler. It is composed of three parts, two parts controlling the (x, y, z) axes of input and collecting objective lenses, the middle part (the sample holder) has additional motions (rotation around the axes (x, y, z)) to ensure that the beam arrives at the waveguide facet at the correct angle. The light beam finally coupled to the waveguide then the output light is collected by the output objective and sent to a CCD camera (Stingray F201B).

*e.g. 20X Nikon CFI60 TU Plan Epi ELWD Infinity Corrected Obj.

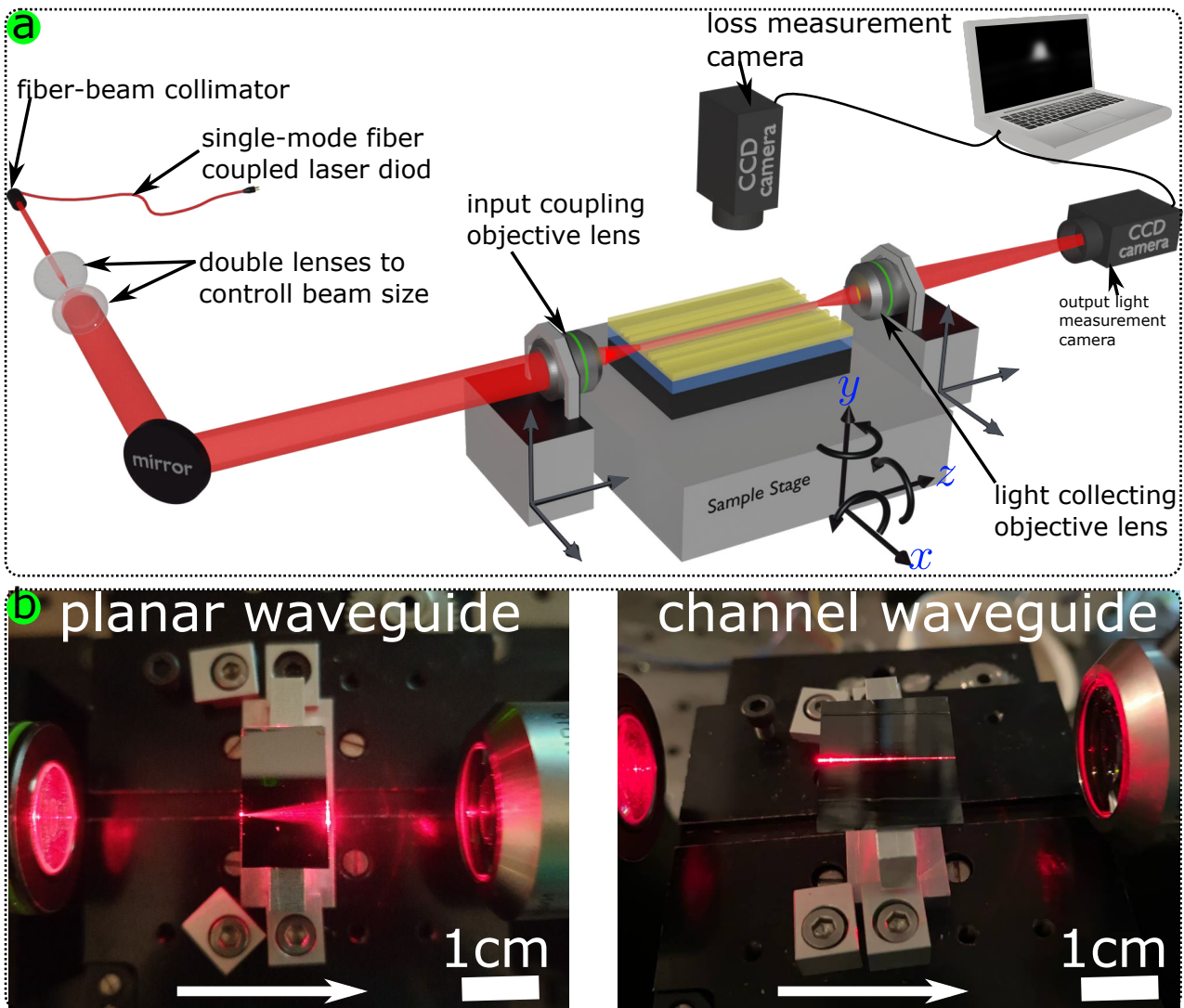


Figure 4.2: a) Schematic representation of the optical setup for light coupling using end-fire coupler. b) Photograph of guided light in planar (left) and channel (right) waveguides using the setup. Note that propagation direction is from left to right (white arrow).

4.1.3.2 End-fire coupler setup testing

The optical setup allowed us to couple light into planar and channel waveguides, as shown in Figure 4.2-b. As expected, the guided light in the planar waveguides is only confined in the plane parallel to the waveguide surface, it diverges laterally in the waveguide. On the other hand, the coupled light in the channel waveguide is confined in the x-y direction.

As the optical setup is equipped with a CCD camera, we can image the guided modes at output face of the waveguide. Figure 4.3 shows experimental images of guided modes' intensity profile of four channel waveguides of different sizes. The figure indicates that the setup can be used to guide fundamental modes of channels of different sizes. Furthermore, from the size

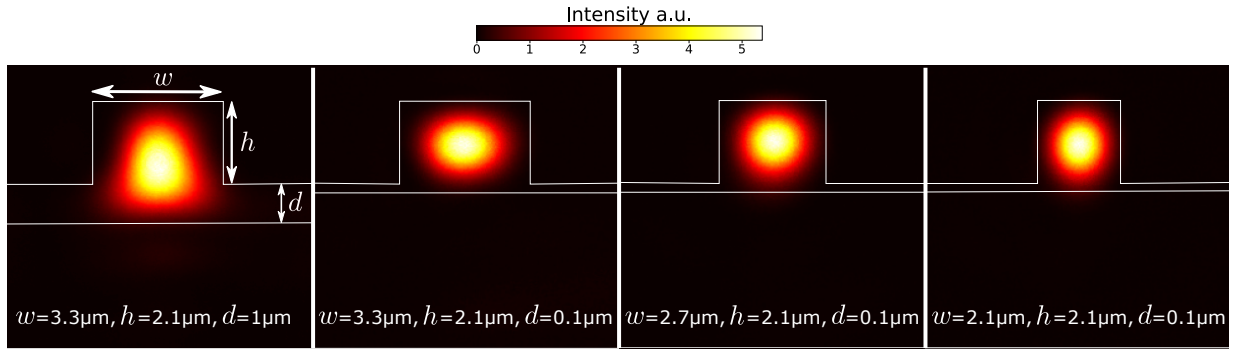


Figure 4.3: Experimental images of the intensity profile of guided modes in channel waveguides of different sizes. Note that the images are shown false colors

and shape of the measured modes, by comparing them with theoretically calculated ones, we can determine channel waveguides type (rib or ridge), the channel width (w), height (h) and rib channels slab thickness (d). Note that the identification of d shown in Figure 4.3-left in an optical waveguide in which the buffer and guiding layers are made of the same material with a low refractive index difference is not possible with either SEM or optical microscope. The scale bar in the images is calculated from the magnification of the system (focal length of the objective and the distance of the camera from the object), it is also verified using scale bar samples.

The only limitation of the setup, which is a basic limitation of the End-Fire coupler, is that the waveguide must have clean, flat input and output facets.

4.2 Waveguide loss measurement

After coupling light to the waveguides, the first optical characterization is the measurement of the optical losses of the waveguides. A simple method for measuring optical loss in a waveguide is to measure the intensity of light scattered on the surface of the waveguide [97]. The method works by assuming that the scattering centers in the waveguides are uniformly distributed. To measure the scattered light, a photodetector can be used at normal angle to the waveguide surface. We implemented this method in our optical end-fire coupler setup by simply placing a CCD camera over the waveguides to record images of the light scattered by the waveguides surface, as shown in Figure 4.2. The working principle of the method is simple, it is to record the images of the light scattered out of the surface of the waveguide and then calculate the decrease in light intensity with propagation length to obtain the losses.

Waveguide loss measurement setup testing

In Figure 4.4, we have shown images of the top surface and the relative intensity profile of light scattered when guided in a channel waveguide. The upper part of the figure is an

experimental photograph of the scattered light as it propagates through a 1 cm long, $2.1 \mu\text{m}$ high, $5.1 \mu\text{m}$ wide channel waveguide. The bottom part is obtained from the lateral intensity variation (propagation length) in the experimentally measured photographs. Due to the presence of some defects in the waveguide that scatter light, this method is not giving us an accurate measurement of optical losses. However, it can still be used to measure the overall optical losses, as the overall intensity of the scattered light decreases from the beginning to the end of the waveguides. The slope of the linear fit of the intensity profile in dB gives us the losses in dB/length. The setup can be used to measure losses higher than 1dB/cm with ± 1 dB/cm accuracy, if the light scattering sources are uniformly distributed in the waveguide.

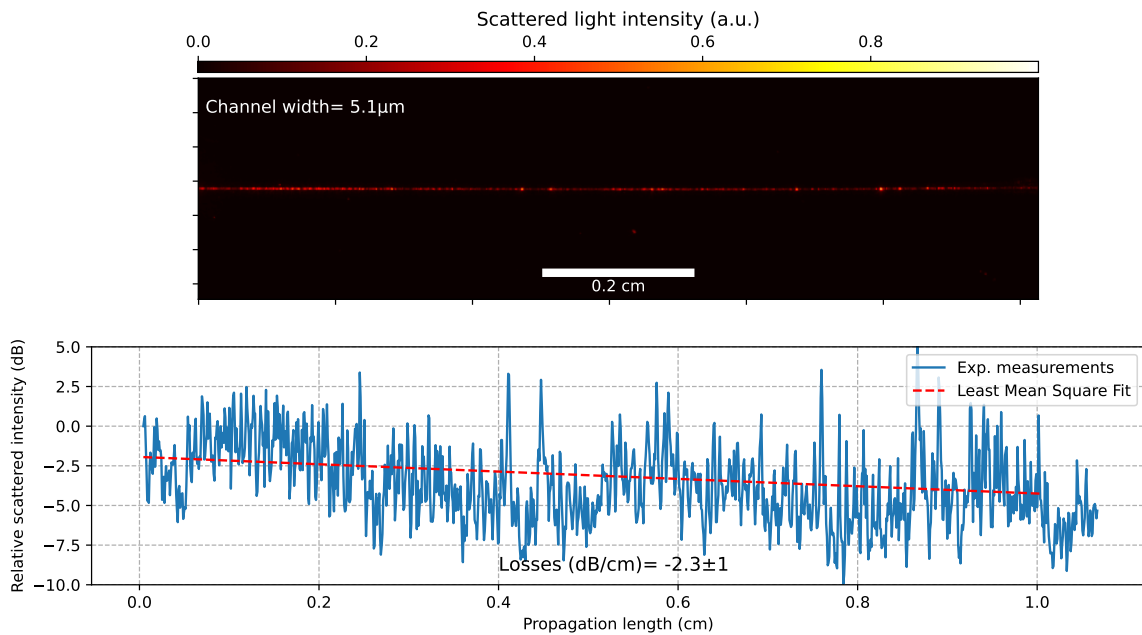


Figure 4.4: Losses measurement for a $2.1 \times 5.1 \mu\text{m}^2$ channel waveguide. top) Photograph of scattered light intensity in false color. bottom) Scattered light intensity variation with propagation length.

Although the method has an accuracy limitation, it can be partially resolved when long waveguides are used. The advantages of this setup are the simplicity and speed of the measurements. For our case study, the ± 1 dB/cm loss estimation was sufficient.

4.3 Polarimetry

In a laser polarimetry setup, a light beam of a known polarization state is passed through a sample to determine the polarization properties of the sample. It works by comparing the polarization state of the laser before and after its interaction with the sample. To build such a setup, we need an optical system to control (prepare) the polarization state of the laser light

beam and another optical system to analyze (measure) the polarization. During my thesis, we have built one optical system for polarization preparation and two systems for polarization measurements. In this section, we discuss the three optical systems by explaining the working principle of each optical element, showing step-by-step how the setups are constructed, and demonstrating their performance.

4.3.1 Polarization preparation

In the chapter 1, we explained that light can be linearly polarized if the oscillation of the electric field is confined in a plane. Such a polarization can be obtained by using optical elements called linear polarizers. Although linear polarizers are sufficient to obtain any linear polarization state by simply rotating them, to obtain nonlinear polarization states, an optical element capable of changing the phase of the electric field components of the light waves is required. Optical elements that are used to modify the phase of a light wave are generally called phase retarders or wave plates. In addition, some optical devices known as compensators are designed to produce a variable phase retardation. Using the polarization elements mentioned, any polarization state can be obtained. In our optical polarization setup, we chose to use combination of a linear polarizer (Glan-Laser polarizers) and a variable phase retarder (Babinet-Soleil compensator).

4.3.1.1 Glan-Laser polarizer

Glan-Laser polarizers consist of two prisms made of a linear birefringent material (e.g. calcite). As shown in Figure 4.5-a, the hypotenuses of the two prisms face each other with an air gap between them to form a rectangle. The prisms are oriented to have the same orientation of the optic axis, which is perpendicular to the direction of propagation of the light beam to be polarized. As described in the chapter 1, when a light wave enters a linear birefringent system, it decomposes into eigenmodes of the system which are two orthogonal linear polarizations and have different effective refractive indices. Glan-Laser polarizers are designed so that when the two eigenmodes encounter the glass-air interface between the prisms, one is totally reflected and the other is transmitted. This means that the transmitted light wave is one of the eigenmodes of the prisms and is therefore linearly polarized. Since the operating principle of the polarizer is total internal reflection, it is very important to control the input angle. Note that if the directed light wave forms an angle of 90° with the input face of the polarizer, 100000:1 extinction ratio of the two eigenmodes can be obtained.

4.3.1.2 Babinet–Soleil compensator

Babinet-Soleil compensator consists of three pieces of a linear birefringent material, a plane parallel plate (PP) and two wedges (WG1 and WG2), as shown in Figure 4.5-b. As indicated in the figure, the optic axes of the plane parallel plate and the two wedges are perpendicular to

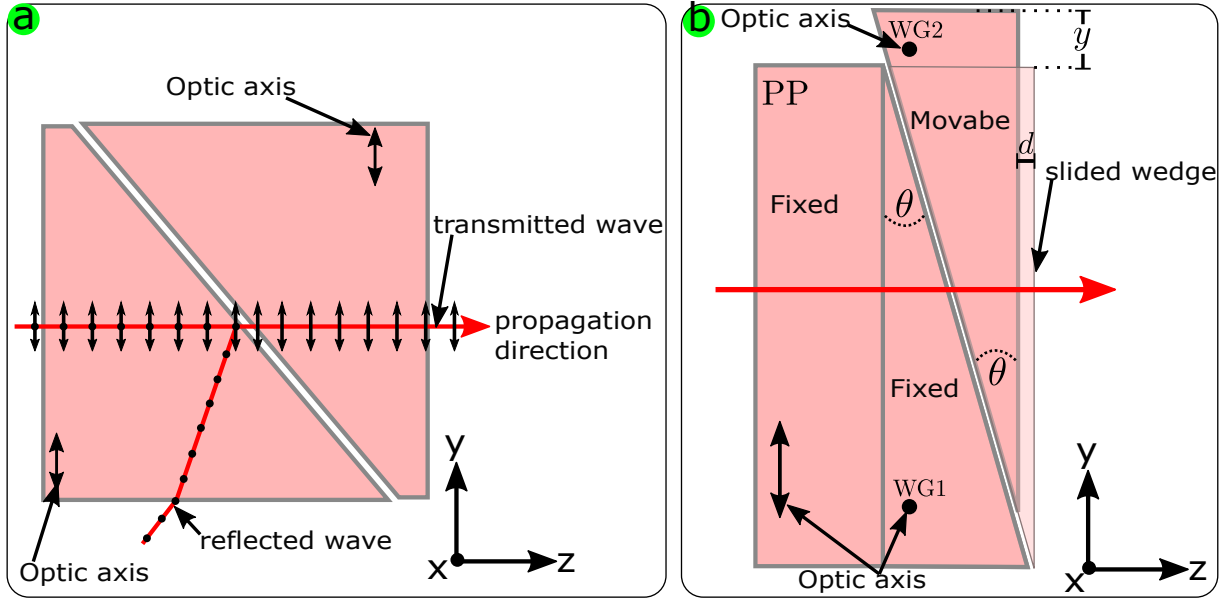


Figure 4.5: 2D schematic representation of a) Glan laser linear polarizer b) Babinet-Soleil compensator.

each other, all perpendicular to the direction of the light beam. The plane parallel plate and the first wedge are fixed while the second wedge is movable in y , so the effective thickness of the two wedges is adjustable. As the optic axis of the plane parallel plate is perpendicular to the two wedges, the wedges cancel out the phase retardation effect of the plane parallel plate [98]. When a light wave enters the Babinet-Soleil compensator, the phase of one of the eigenmodes of the system is retarded relative to the other, but when it reaches the two edges, it is the other eigenmode that is retarded. Therefore, if the effective thickness of the two wedges is equal to the thickness of the plane parallel plate, the net phase retardation is zero. In such a combined system, by moving the second wedge (sliding on the other wedge), one can control the net phase retardation. The variable phase retardation (ϕ) is proportional to the movement of the second wedge (variation in y)

$$\phi = \frac{2\pi(n_e - n_o)}{\lambda} \cdot d = \frac{2\pi(n_e - n_o)}{\lambda} \cdot \tan \theta \cdot y \quad (4.4)$$

where n_e and n_o are the effective refractive indices of the eigenmodes of the linear birefringent material, called here extraordinary and ordinary rays. d , y and θ are the variations of the effective thickness, the vertical movement of the movable wedge (WG2) and the angle of the two wedges respectively, as shown in Figure 4.5-b.

4.3.1.3 Polarization preparation experimental setup

Figure 4.6-a, schematically represents our polarization preparation system. A collimated 633nm laser light beam with an unknown polarization state is passed through a Glan-laser polarizer (10GL08AR.14 Newport) to obtain a linearly polarized light beam at azimuth 0. The

linearly polarized light beam is directed to a Babinet-Soleil compensator (Thorlabs SBC-VIS), which is oriented in such a way that its fast axis (eigenmodes axis) makes an azimuth angle of 45° with respect to the polarization axis of the input light beam. The phase retardation of the light beam after it passes through the Babinet-Soleil compensator is controlled by a computer-controlled motor. By moving the motor, i.e. moving the movable wedge, polarization states with any ellipticity from $\chi = -\frac{\pi}{4}$ to $\chi = +\frac{\pi}{4}$ but a constant azimuth can be obtained. The accuracy of Babinet-Soleil compensator in controlling phase retardation is found to be $\phi \approx 0.02^\circ$.

The principle of the setup can be explained using the Poincaré sphere. As the Babinet-Soleil compensator is a birefringent system, its eigenmodes create a diameter axis on the sphere as shown in Figure 4.6-b. The light coming from the polarizer is a horizontally polarized light wave ($\chi = 0$), it is represented by the green dot on the sphere. The variation of the position of the movable wedge of the Babinet-Soleil compensator creates a variation of the phase retardation. The variation in the phase retardation corresponds to a rotation of the input polarization state about the eigenmodes axis (i.e. rotation in $S_2 = 0$ plane). In Figure 4.6-b, we have plotted on the Poincaré sphere some possible polarization states (purple dots) that can be obtained

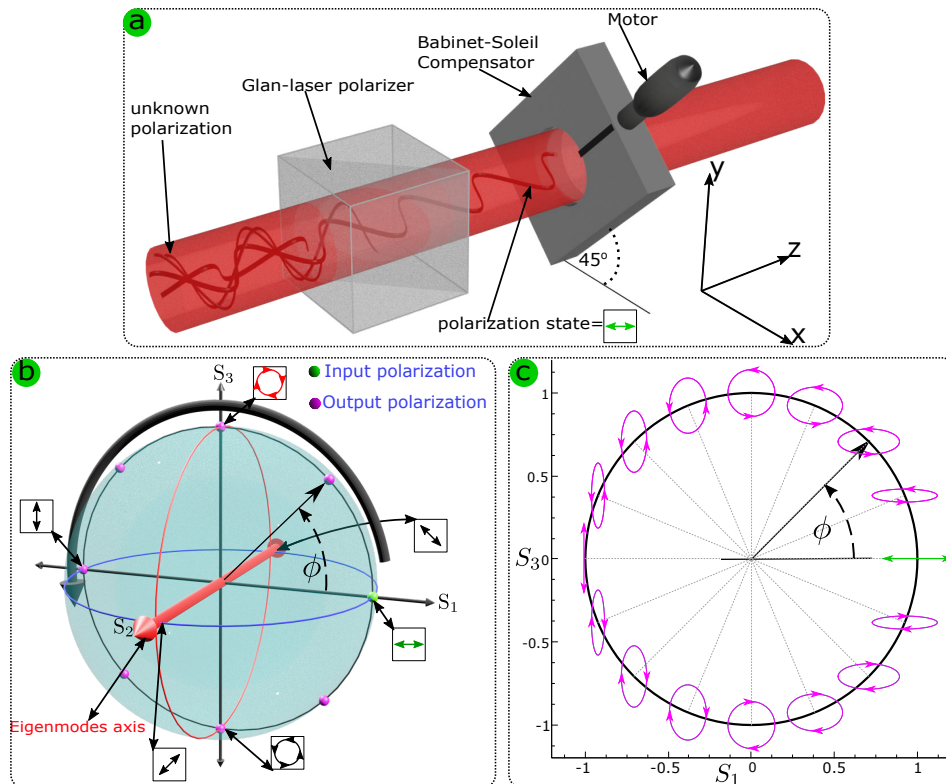


Figure 4.6: a) Schematic of Glan-laser polarizer and Babinet-Soleil compensator polarization preparation setup. b) Poincaré representation of the polarization modulation by a Babinet-Soleil compensator. c) Some possible polarization states prepared by the combination.

from the configuration of the optical system shown in Figure 4.6-a. According to the definition of the Poincaré sphere, the polarization states obtained by the configuration correspond to polarization with different ellipticity from $\chi = 0 \rightarrow \frac{\pi}{4} \rightarrow \chi = 0 \rightarrow \chi = -\frac{\pi}{4} \rightarrow \chi = 0$ as shown in Figure 4.6-c.

4.3.2 Polarization measurement by retarder and polarizer

Similar to the way we used a combination of phase retarder and polarizer to control (prepare) the polarization state of light, we can also design a combination to analyze (measure) the polarization state of a light beam. In chapter 1 section 1.1.5, we explained that when a light beam passes through polarization elements (e.g. a retarder or polarizer), its Stokes parameters change depending on the polarization element. The effect of the polarization element can be calculated using the 4×4 transfer matrix (Mueller matrix) corresponding to the element. In this section, using Mueller matrices, we investigate the design of an optical system for measuring the polarization state of light, consisting of a phase retarder and a linear polarizer.

4.3.2.1 General configuration

Let us assume that a light beam whose polarization we want to determine has Stokes parameters S_0, S_1, S_2, S_3 . If the beam passes through a combination of a retarder and a polarizer, its Stokes parameters become $S_0^*, S_1^*, S_2^*, S_3^*$. Let us also assume that the beam first passes through the retarder whose fast-axis is rotated by an angle α with respect to the x -axis of the input polarization, and it creates a phase retardation ϕ . Afterwards, the beam passes through a linear polarizer whose transmission axis is rotated by an angle ψ . The configuration is schematized in

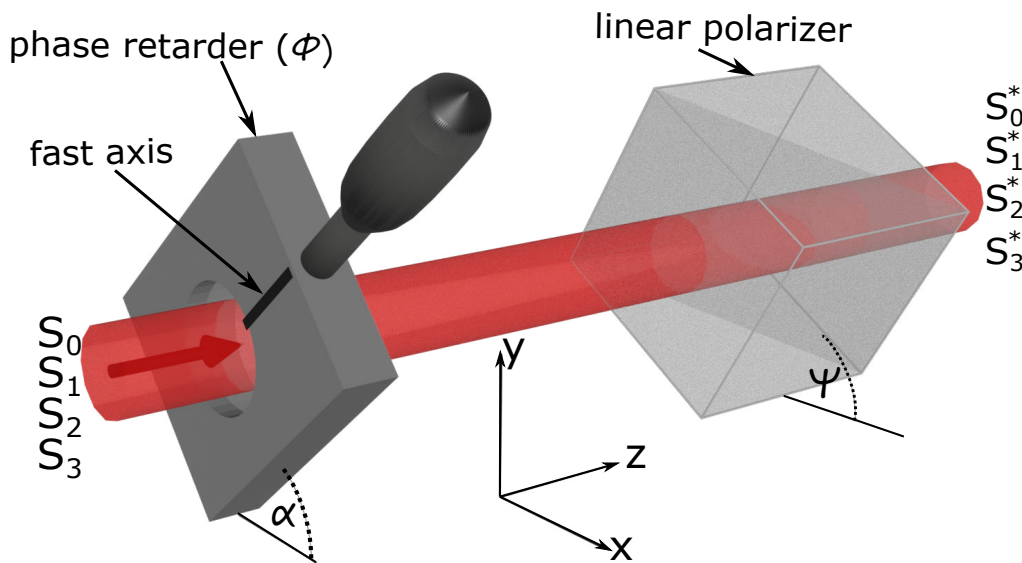


Figure 4.7: General configuration of retarder and polarizer for polarization measurement.

Figure 4.7. When the light beam with Stokes vector S_{input} passes through the phase retarder and the linear polarizer that have M_1 and M_2 Mueller matrices respectively, the output light Stokes vector is

$$S_{output} = M_2 \cdot M_1 \cdot S_{input} \quad (4.5)$$

Taking the Mueller matrices listed in Table 1.4 for the corresponding phase retarder and polarizer shown in Figure 4.7, Stokes vector of the output beam is

$$\begin{bmatrix} S_0^* \\ S_1^* \\ S_2^* \\ S_3^* \end{bmatrix} = \frac{1}{2} \begin{bmatrix} 1 & \cos 2\psi & \sin 2\psi & 0 \\ \cos 2\psi & \cos^2 2\psi & \sin 2\psi \cos 2\psi & 0 \\ \sin 2\psi & \sin 2\psi \cos 2\psi & \sin^2 2\psi & 0 \\ 0 & 0 & 0 & 0 \end{bmatrix} \cdot \begin{bmatrix} 1 & 0 & 0 & 0 \\ 0 & \cos^2 2\alpha + \cos\phi \sin^2 2\alpha & (1 - \cos\phi) \sin 2\alpha \cos 2\alpha & -\sin\phi \sin 2\alpha \\ 0 & (1 - \cos\phi) \sin 2\alpha \cos 2\alpha & \sin^2 2\alpha + \cos\phi \cos^2 2\alpha & \sin\phi \sin 2\alpha \\ 0 & \sin\phi \sin 2\alpha & -\sin\phi \sin 2\alpha & \cos\phi \end{bmatrix} \cdot \begin{bmatrix} S_0 \\ S_1 \\ S_2 \\ S_3 \end{bmatrix} \quad (4.6)$$

What we measure directly in experiments using photodetectors is the Stokes parameter S_0^* (i.e. the beam intensity). The results of equation 4.6 in terms of S_0^* is [99]

$$S_0^*(\alpha, \phi, \psi) = \frac{1}{2} \{ S_0 + [S_1 \cos 2\alpha + S_2 \sin 2\alpha] \cos 2(\psi - \alpha) + [(S_2 \cos 2\alpha - S_1 \sin 2\alpha) \cos\phi + S_3 \sin\phi] \sin 2(\psi - \alpha) \} \quad (4.7)$$

Equation 4.7 indicate that the output intensity of light as it passes through the combination of the phase retarder and the polarizer depends on its initial Stokes parameters (S_0, S_1, S_2, S_3), the phase retardation of the phase retarder (ϕ), the angle of the phase retarder (α), and the angle of the polarizer (ψ). Therefore, by measuring the intensity of the transmitted light for different values of (α, ϕ , and ψ), the initial Stokes parameters of the beam can be determined. The Equation 4.7 represents all the polarization measurement methods that can be built by the configuration shown in Figure 4.7.

4.3.2.2 Polarization measurement by rotating quarter-wave plate and polarizer

Looking at the Equation 4.7, we can notice that it is rather complicated equation and the parameters S_0, S_1, S_2 , and S_3 can not be easily determined if all the parameters (α, ϕ, ψ) change at the same time. However, if two parameters in the equation (e.g. ϕ, ψ) are chosen to be constant, S_0, S_1, S_2 , and S_3 can be determined by measuring the intensity of the output light as a function of the rotation of the phase retarder α . In our experimental setup, we chose to set the polarizer to $\psi = 0$ and use the quarter-wave plate (i.e. a fixed phase retarder $\phi = \frac{\pi}{2}$). Inserting the value of $\psi = 0$ and $\phi = \frac{\pi}{2}$ into equation 4.7, it simplifies to

$$S_0^*(\alpha, \phi = \frac{\pi}{2}, \psi = 0) = \frac{1}{2} [S_0 + \frac{1}{2}(S_1 + S_1 \cos 4\alpha) + \frac{1}{2}S_2 \sin 4\alpha - S_3 \sin 2\alpha] \quad (4.8)$$

4.3.2.3 Experimental setup

Figure 4.8 schematically represents our optical system for measuring polarization using the combination of a rotating quarter-wave plate and a linear polarizer at azimuth 0. The light beam whose Stokes parameters need to be determined first passes through a rotating wave plate (05RP04-24 Newport). Rotation of the wave plate is controlled by a motorized rotation plate (Newport-PR50CC). Then the light is passed through a Glan-laser polarizer (10GL08AR.14 Newport) and its intensity is measured with a CCD camera (Stingray F201B). The whole polarization measurement works by measuring the transmitted light intensity with the CCD for different rotation angles (α_i) of the wave plate. For each measurement, the camera takes a set of images at α_i and records the data which contain N intensity values corresponding to N angular positions of the wave plate ($i = 0$ to N-1). The length of the data (N) is usually a small fraction of 360° , for our case, we choose to take N=36 images ($\alpha=10^\circ$). The saved data are then analyzed using nonlinear least squares fitting of the data with the equation 4.8. By fitting the data with the equation, the four constants S_0, S_1, S_2, S_3 are determined which are the Stokes parameters of the input light beam. The advantage of using a camera to measure intensity is that when we analyze the data, we can choose precisely which part of the beam we want to analyze. The camera also allows to obtain polarization mapping of the beam (i.e. one polarization per pixel), as we will see in the setup testing section.

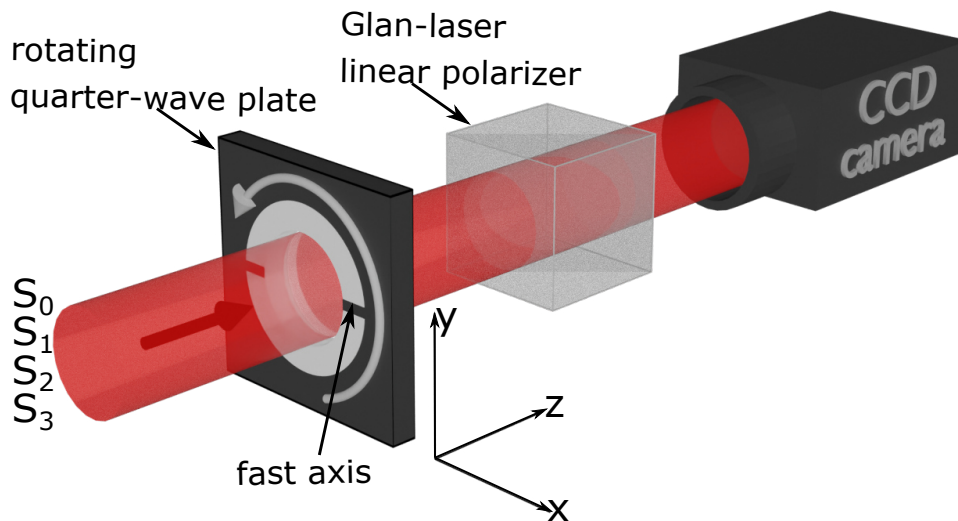


Figure 4.8: Rotating quarter-wave plate-polarizer optical system for polarization measurement.

4.3.3 Setup calibration

The main objective in developing the polarimetry setup was to characterize the fabricated chirowaveguides. We then incorporated the whole polarimetry setup into end-fire coupling one

as shown in Figure 4.9[†]. Before using the optical setup, all elements have to be calibrated. Therefore, we must

1. Define xyz axes of the whole system.
2. Find transmission axis of the two polarizers (polarizer I and polarizer II).
3. Find the fast axis of the Babinet-Soleil compensator.
4. Calibrate the variable phase retardation of the Babinet-Soleil compensator.
5. Find the fast axis of the quarter-wave plate.
6. Check phase retardation of the quarter-wave plate.

Based on the mentioned calibration requirements, we have calibrated the setup as explained in the following:

1. As indicated in Figure 4.9, the x , y , and z axes are defined as waveguide TE polarization mode axis, the TM polarization mode axis, and the propagation direction of the guided light, respectively.
2. To find the transmission axis of the first polarizer (polarizer-I), we coupled light into a single layer film on metal (doped silicon) and detected the output light from the CCD camera. Polarizer-I is then introduced into the setup and rotated until the output light is completely attenuated (minimum output), this angle corresponds to TM(y) axis, then the TE(x) axis is determined by rotating the polarizer by 90° . The polarization angle for which the transmission of the guided light is minimal corresponds to the TM axis because

[†]Note that the figure shows the setup after calibration.

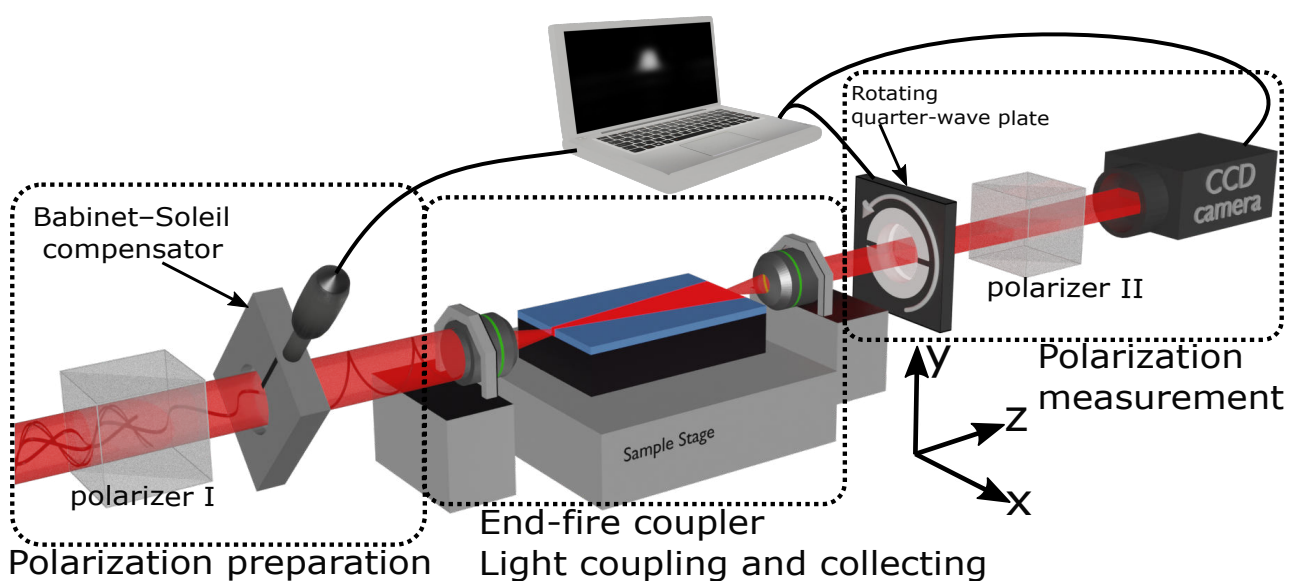


Figure 4.9: Polarimetry setup for waveguide characterization

the evanescent part of TM is longer and therefore strongly absorbed by the metal.

To find the transmission axis of the second polarizer, called polarizer-II in Figure 4.9, the waveguide is removed from the sample stage, then we just used the cross-polarizer technique. At this point, the transmission axes of polarizer-I and polarizer-II are determined, they are respectively at azimuth 0 and azimuth 90 and no light passes towards the camera.

3. To find the fast axis of the Babinet-Soleil compensator, it is placed between the two crossed polarizers and rotated until the minimum output intensity is measured, this angle corresponds to its fast axis.
4. To calibrate the Babinet-Soleil compensator (i.e. induced phase retardation as a function of the position of the computer-controlled motor), the compensator is rotated by 45° with respect to the x axis as shown in Figure 4.9. The computer-controlled motor is then moved to vary induced phase retardation until the minimum light is detected by the camera, the position is noted as zero phase retardation ($\phi = 0$). Then the motor continued to move until the second minimum light is detected by the camera, this position is noted as phase retardation of 2π . Once the motor position for the 0 and 2π phase retardations are known, any phase retardation can be obtained by taking the values between these two positions. For example, if the position of the motor for the phase retardations of 0 and 2π are p_1 and p_2 respectively, a phase retardation of $2\pi \cdot x$ can be obtained by moving the motor to $([p_2 - p_1] \cdot x + p_1)$ position.
5. To find the fast axis of the quarter-wave plate, the Babinet-Soleil compensator is set to 0 phase retardation, then the quarter-wave plate is added to the setup and rotated until the minimum intensity is measured again and this angle is noted as its fast axis.
6. To find the exact phase retardation by the quarter-wave plate, the quarter-wave plate is rotated by -45° with respect to the x axis such that its fast axis cross with the one of Babinet-Soleil compensator. In such configuration they cancel phase retardation of each other. Then phase retardation is modulated by the Babinet-Soleil compensator until minimum intensity is measured and that position of the Babinet-Soleil compensator is noted to be the phase retardation of the wave plate.

When all the optical elements were calibrated, the polarizer II is set back to 0 angle relative x -axis (remember we have crossed polarizer II with polarizer I at the beginning of the calibration) to satisfy the equation 4.8. At this point, all the optical elements are calibrated and the setup is ready to be tested.

4.3.4 Rotating quarter-wave plate and polarizer setup testing

The polarization measurement of the setup is tested by sending light with known state of polarization (SOP) and compare them with the measured ones. The known (reference) SOPs are prepared by the combination of the linear polarizer and the Babinet-Soleil compensator. In Figure 4.10-a we have plotted reference and measured polarizations on Poincare sphere. To know the accuracy of the system, we send light with a polarization of different ellipticity χ and azimuth ψ^\ddagger . The blue and green points in the figure represent the reference and the measured SOPs. We can clearly see that the accuracy of the setup is very high in the measurement of the Stokes parameters since the blue and green points coincide. This accuracy is also illustrated in the 2D plot shown in Figure 4.10-b by comparing reference and measured normalized Stokes parameter (S_1, S_2, S_3) separately. The accuracy of the system to measure Stokes parameters of any SOP is found to be $\pm 3\%$.

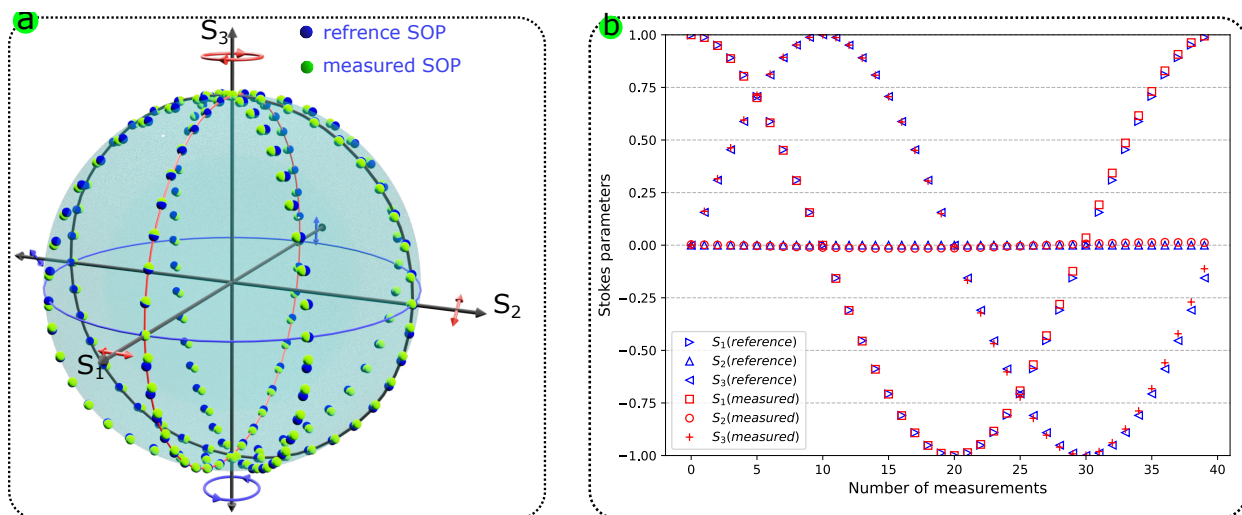


Figure 4.10: Comparison of reference and measured polarization states by the optical setup. a) Comparison plotted on Poincare sphere. b) Comparison of the Stokes parameters separately.

As the optical setup is equipped with a camera, it can be used to characterize separately any part of a light beam by analyzing the corresponding part from the images taken by the camera. We used the setup to obtain polarization mapping of light beams such that if the polarization of the beam is not homogenous it can be detected. Figure 4.11 shows an experimental measurement of polarization mapping of a laser light beam obtained by the setup. In the figure, we have shown in false color the normalized intensity of the laser beam (i.e. the beam profile) and SOP of light at different positions (pixels) of the beam represented by the polarization ellipses.

[‡]To obtain SOPs of different azimuth without rotating the Babinet-Soleil compensator, we used a half-wave plate by putting it after the Babinet-Soleil compensator.

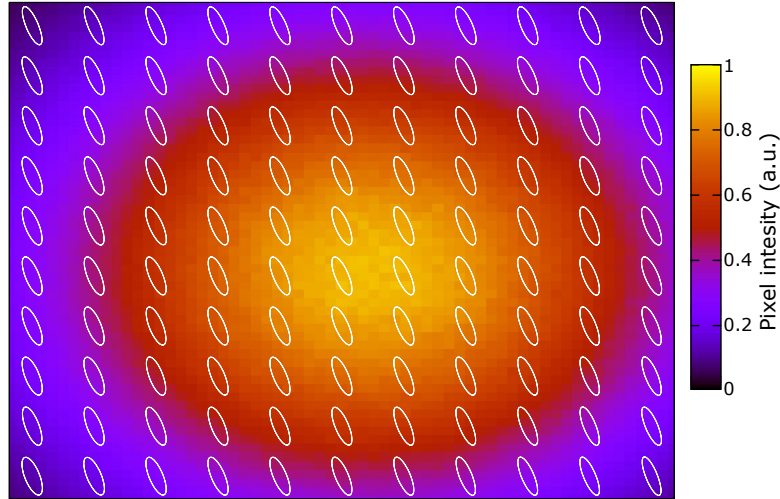


Figure 4.11: Polarization mapping of an elliptically polarized laser beam.

4.3.5 Birefringence measurement using the setup

Birefringence systems are characterized by two eigenmodes: the only SOPs that can pass through these systems without being modified. Therefore, determination of the eigenmodes of a birefringence system is enough to describe the system. To find the eigenmodes, we have sent different SOPs through the birefringence system and measured the corresponding output SOPs. We then used a computer model that compares the input SOPs with the output SOPs and determines phase retardation and the normalized Stokes parameters of the eigenmodes of the birefringence system. From the normalized Stokes parameters we can determine polarization ellipticity χ and polarization azimuth ψ of the eigenmodes using the equations 1.24-a and b (For normalized Stokes parameters the equations 1.24-a and b are $\tan 2\psi = \frac{S_2}{S_1}$ and $\sin 2\chi = \frac{S_3}{S_1}$ respectively).

We have tested our setup for determining eigenmodes of a known birefringence system (i.e. half-wave plate) that is designed to create a π phase retardation on a light beam. Figure 4.12 shows the Poincaré sphere representation of the half-wave plate behavior. The blue and green dots on the sphere represent the SOPs of the light beam before entering the half-wave plate (input) and after passing through it (output). The black points are fitted points to find the eigenmodes (and thereby eigenmodes axis) of the half-wave plate. We have also plotted by the cyan curves, the trajectory that connect input and output polarizations which means that the input SOPs went through the possible states shown by the cyan curve before arriving at final state. As can be seen the half-wave plate creates π phase retardation since it modifies a circular polarization to counterpart (orthogonal) circular polarization. It is not only phase retardation that we can find with the setup, it also gives azimuth (ψ) of the eigenmodes axis of the wave plate since it shows how horizontal and vertical linearly polarizations are modified.

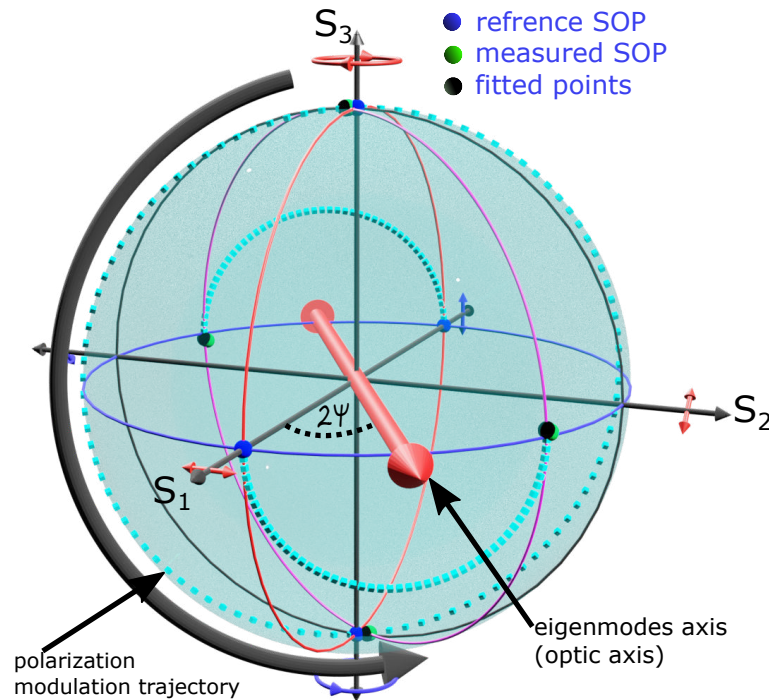


Figure 4.12: Poincaré sphere representation of the behavior of a half-wave plate.

Typically, a half-wave plate (half wavelength retardation) should create a π phase retardation, we found 182° phase retardation that corresponds to $\pm 1\%$ of error.

4.3.6 Advantages and drawbacks of the optical setup

During my thesis, we have mostly used this setup to characterize the samples. The advantages of the setup are:

1. The setup is equipped with a polarization preparation system that allows to produce any polarization state.
2. The End-fire coupler in the setup allows light to be guided and collected in optical waveguides. It can also be used to determine type and dimensions of channel waveguide from the guided modes.
3. The polarization measurement part of the setup can be used to analyze the polarization of an unknown light beam with accuracy of $\pm 3\%$.
4. The polarization measurement part of the setup can be used to analyze the polarization of an unknown light beam with accuracy of $\pm 3\%$. It can also be used to obtain the polarization mapping of a light beam.
5. The entire setup can be used to analyze the birefringent properties of any system, including waveguides and bulk media.

The only drawback of this setup is the measurement time, the combination of the rotating quarter-wave plate and polarizer takes ~ 1 minute to analyze one polarization state.

4.3.7 Dynamic polarization measurement

In order to overcome the only limitation of the polarization measurement part of the previous setup, namely the long measurement time, we have developed a new setup allowing instantaneous measurement of the SOP. The principle of this setup is simple: the light beam to be analyzed is divided into three parts so that each part can be used to measure a normalized Stokes parameter. To build the setup, we used non-polarizing beam splitters to split the light and Wollaston polarizing beam splitters to separate the orthogonal polarization states.

4.3.7.1 Optical elements working principle

Non polarizing beam splitter: Non polarizing beam splitter are cube beam splitters made by cementing together two right-angled prisms, the hypotenuse of each prism is coated with semi-reflective films. The films are designed such that one part of light is reflected at 90° while the other part is transmitted.

Wollaston polarizing beam splitter: In Figure 4.13, we have schematically shown a Wollaston polarizing beam splitter. It is made of two prisms of a linear birefringent material (e.g. calcite) cemented together on their hypotenuse. The two prisms are oriented such that their optic axes (eigenmodes axis) are perpendicular to each other and to the direction of propagation. When light enters at right angle into the first prism it decomposes into two eigenmodes without being refracted. As soon as the eigenmodes encounters the tilted interface of the two prisms, since the optic axes of the two prisms are perpendicular to each other, they are refracted as two beams in opposite directions, they are further refracted at the exit face. Therefore, the light coming out from the polarizer is made of two beams with orthogonal polarization states.

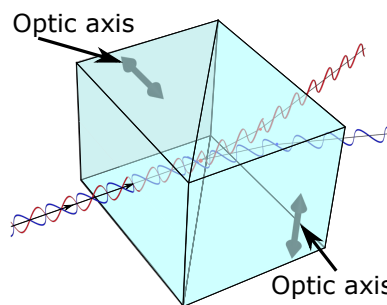


Figure 4.13: Schematic of Wollaston polarizing beam splitter.

4.3.7.2 Experimental setup

Figure 4.14 schematically represents the optical setup allowing the instantaneous measurement of the polarization state of light. A beam of laser light to be analyzed is split into three beams using a combination of a 30:70 non-polarizing beam splitter (NBS-1) and a 50:50 non-polarizing beam splitter (NBS-2). The 30% reflected beam from the NBS-1 is then sent through a Wollaston polarizing beam splitter (WPBS-1) which separates the horizontally and vertically polarized portions of the beam. The intensities of the separated beams are measured by two photodiodes (D_1 and D_2), then the value of the Stokes parameter S_1 is determined by the following formula:

$$S_1 = \frac{D_1 - D_2}{|D_1 + D_2|} \quad (4.9)$$

where D_1 and D_2 are intensities measured by the two photodiodes. The remaining 70% of the beam is split again into 35%:35% to be used for measurement for Stokes parameters S_3 and S_2 . The reflected 35% is sent through a quarter-wave plate oriented at 45° relative to the x -axis, the quarter-wave plate converts the left and right circularly polarized light into horizontal and vertical linear polarizations respectively. The horizontal and vertical linear polarizations are then separated by a Wollaston polarizing beam splitter (WPBS-2) to be detected by the D_3 and D_4 photodiodes. Then Stokes parameter S_3 is measured as:

$$S_3 = \frac{D_3 - D_4}{|D_3 + D_4|} \quad (4.10)$$

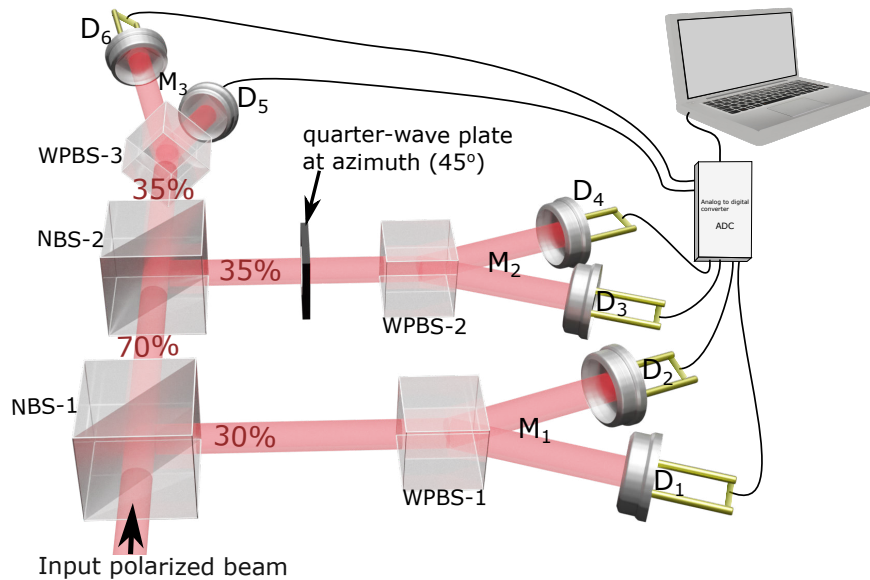


Figure 4.14: Schematic representation of the optical setup for instantaneous measurement of Stokes parameters. NBS, WPBS, D are abbreviations for non polarizing beam splitter, Wollaston polarizing beam splitter, and photo-diodes is polarizing beam splitter respectively.

Finally, the last 35% part of the beam is sent through a Wollaston polarizing beam splitter (WPBS-3) that is oriented at 45° to separate linear polarization at $+45^\circ$ and -45° relative to x -axis. The separated beams are measured by photodetectors D_5 and D_6 , and S_2 is measured as:

$$S_2 = \frac{D_5 - D_6}{|D_5 + D_6|} \quad (4.11)$$

It can be noted from equations 4.9-4.11 that the setup measures normalized Stokes parameters because they are determined by dividing the measured intensities by the total light beam intensity (i.e. S_0).

4.3.7.3 Setup calibration

In order to use the setup to accurately measure Stokes parameters, the following conditions must be met:

1. **Non-polarizing beam splitters should not change the polarization state of the light beams as they separate them:** We have used non-polarizing beam splitters (BS010 [50:50] and BS052 [30:70] Thorlabs). Since beam splitting is based on thin film coating, and generally (films) are sensitive to light polarization, the non-polarizing beam splitters were not a real non-polarizing beam splitters. Therefore, we had to determine Mueller matrices for the optical element encountered by each beam which are needed to be accounted during the measurement. The measurement of Mueller matrices for three beams as indicated by M_1, M_2 , and M_3 in Figure 4.14, is explained in Appendix A.
2. **Wollaston polarizing beamsplitters should separate two orthogonal polarizations in an ideal way[§]:** We have used Wollaston prism (Newport 10WLP08) that deviates the two polarizations at $\approx 20^\circ$ in wavelength of visible light. We verified the performance of this optical element using linear polarizers and found that the beamsplitter separates two orthogonal polarizations with an extinction ratio of $\sim 100000:1$.
3. **Each pair of photodiodes should measure the light intensity identically:** The sensitivity and response time for D_1 should be the same as for D_2 , the same for (D_3, D_4) and (D_5, D_6) . We used silicon photodetectors (Thorlabs FDS100-P10) which were all found to measure intensity identically. This can be verified by exchanging the photodiodes of the pair, if we exchange them we should get the same magnitude of the Stokes parameter but with an opposite sign.

[§]The first time we built the setup, we used prism polarizing beam splitters (Thorlabs PBS122), but their performance was not good. The polarization separation was partial, intensity of one of the polarizations was switching to the other which was changing the value of the measured Stokes parameter.

4.3.7.4 Dynamic polarization measurement setup testing:

As we did for the previous optical setup, we have also tested this setup by analysing a light beam with known (reference) Stokes parameters prepared by the combination of linear polarizer and the Babinet-Soleil compensator then compare them with the Stokes parameters measured by this setup. As the setup is not equipped with a camera but with photodiodes, it only gives the average polarization of a light beam; we cannot observe the intensity profile of the beam nor the polarization mapping. In Figure 4.15-a, we have plotted the reference and measured SOPs. The blue and green dots in the figure which represent the reference and measured SOPs of different ellipticity χ and azimuth ψ are very close to each other on the Poincaré sphere, attesting the accuracy of the setup. The accuracy is also verified by comparing reference and measured Stokes parameters separately as shown in Figure 4.15-b. The accuracy of this setup is found to be $\pm 6\%$ which is lower than the rotating quarter-wave plate polarizer setup (see 4.3.4). The important advantage of this setup is the instantaneous measurement of the light polarization.

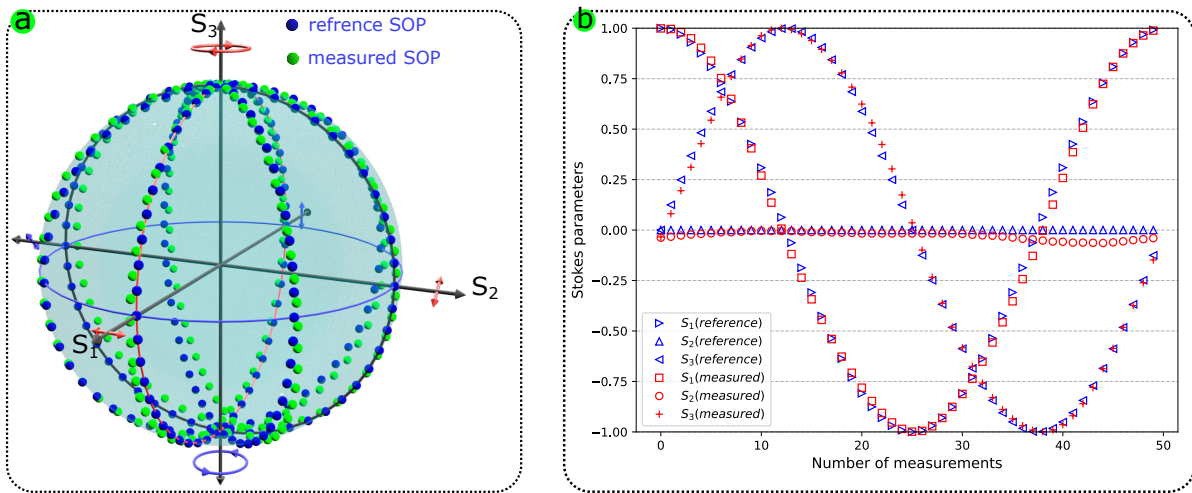


Figure 4.15: Comparison of reference and measured polarization states by the optical setup. a) Comparison on Poincaré sphere b) Comparison of the Stokes parameters separately.

4.4 Mach-Zehnder interferometer

When we were measuring the polarization properties of the waveguides, we noticed that the measurements were not reproducible. This is because, the ORMOSIL material of which the waveguides are made is sensitive to ambient humidity. We therefore had to set up an interferometric system to measure the effect of humidity on the samples. Indeed, interferometers have proven to be a very powerful tool to measure small changes in the optical properties of a material (e.g. refractive index) [100]. In this section, we explain the working principle of interferometers in general and the procedure for developing Mach-Zehnder interferometer.

4.4.1 Interferometry principle

An interferometer is an optical device that works on the principle of interference of light waves to measure any variation in the optical path length of one of the constituent waves, called measurement wave compared to the reference wave. The two constituent waves come from the same source of monochromatic light but travel two distinct paths. These two waves interfere when they are simultaneously present in the same region of space. The resulting intensity of their interference is a spatial redistribution of the total intensity in which it is higher/lower than the intensity of both waves (constructive/destructive interference) in certain positions.

Interference of two waves can be described by superposition principle which is an algebraic sum of the two waves [101]. For two plane waves propagating in free space, we can write their electric fields as

$$\begin{aligned}\mathbf{E}_1 &= \mathbf{E}_{01} e^{i(\mathbf{k}_1 \cdot \mathbf{r} - \omega t + \phi_1)} \\ \mathbf{E}_2 &= \mathbf{E}_{02} e^{i(\mathbf{k}_2 \cdot \mathbf{r} - \omega t + \phi_2)}\end{aligned}\quad (4.12)$$

where ϕ_1 and ϕ_2 are initial phases of each wave. Since the two waves are assumed to be coherent, their phase difference ($\phi_1 - \phi_2$) is constant. When we perform the vectorial sum of these two waves, the total electric field is written as

$$\begin{aligned}\mathbf{E}_{total} &= \mathbf{E}_1 + \mathbf{E}_2 \\ &= [\mathbf{E}_{01} e^{i(\mathbf{k}_1 \cdot \mathbf{r} + \phi_1)} + \mathbf{E}_{02} e^{i(\mathbf{k}_2 \cdot \mathbf{r} + \phi_2)}] e^{-i\omega t}\end{aligned}\quad (4.13)$$

We want to measure the beam intensity which is the absolute square of the complex amplitude of the electric field. The intensity of the two waves are $I_1 = |\mathbf{E}_{01}|^2$ and $I_2 = |\mathbf{E}_{02}|^2$, then the total intensity of the combination is

$$\begin{aligned}I_{total} &= |\mathbf{E}_1 + \mathbf{E}_2|^2 \\ &= |\mathbf{E}_{01}|^2 + |\mathbf{E}_{02}|^2 + |\mathbf{E}_1^* \mathbf{E}_2|^2 + |\mathbf{E}_1 \mathbf{E}_2^*|^2 \\ &= I_1 + I_2 + |\mathbf{E}_1^* \mathbf{E}_2|^2 + |\mathbf{E}_1 \mathbf{E}_2^*|^2\end{aligned}\quad (4.14)$$

Here we assume that the two waves have the same polarization state, then the interference terms are

$$|\mathbf{E}_1^* \mathbf{E}_2|^2 = \sqrt{I_1 I_2} e^{i[(\mathbf{k}_1 - \mathbf{k}_2) \cdot \mathbf{r} + (\phi_1 - \phi_2)]}, \quad |\mathbf{E}_1 \mathbf{E}_2^*|^2 = \sqrt{I_1 I_2} e^{-i[(\mathbf{k}_1 - \mathbf{k}_2) \cdot \mathbf{r} + (\phi_1 - \phi_2)]} \quad (4.15)$$

From the trigonometric identity $\cos \phi = \frac{1}{2}(e^{i\phi} + e^{-i\phi})$, we can rewrite the equation 4.13 as

$$I_{total} = I_1 + I_2 + 2\sqrt{I_1 I_2} \cos \phi \quad (4.16)$$

with

$$\phi = (\mathbf{k}_1 - \mathbf{k}_2) \cdot \mathbf{r} + (\phi_1 - \phi_2) \quad (4.17)$$

Equation 4.16 is called interference equation, it demonstrates that the final intensity of the interfered waves is not only sensitive to the initial intensity of the interferometer constituent waves but also to their phase difference (ϕ). The sensitivity of optical wave phases for environmental conditions makes interferometers a very sensitive tool for sensing background changes such as refractive index, distance encountered by the waves. For example, for two waves whose initial phase difference is zero ($\phi_1 - \phi_2 = 0$), the ϕ of the equation 4.16 ($\mathbf{k} \cdot \mathbf{r} = \frac{2\pi n}{\lambda} l$) change if one of the waves travels an additional distance l in a medium of index of refraction n . Therefore, any change in refractive index, wavelength or distance by one of the waves can be detected from the total intensity of the waves.

4.4.2 Mach-Zehnder interferometer experimental Setup

Figure 4.16 schematically shows a Mach-Zehnder interferometer setup to measure variation of refractive index in an optical waveguide. A collimated and polarized beam of light from a He-Ne laser (Uniphase 1507P-0) is split by an unpolarized beam splitter into two beams that constitute the two arms of the interferometer, called reference and measurement beams. The reference beam is reflected twice by two mirrors before being recombined with the measurement beam at the second non-polarizing beam splitter and sent to a CCD camera. The measurement light beam is coupled into the sample waveguide and collected with microscope objectives (end-fire coupler). As indicated in Figure 4.16-inset, the two beams are inclined (not parallel) by a small angle α when they are superimposed on the camera (detector), so they create interference fringes. Because of the inclination angle between the two beams the phase difference in Equation 4.17 become:

$$\begin{aligned} \phi &= \frac{2\pi}{\lambda} \cdot x \cdot \sin \alpha + (\phi_1 - \phi_2) \\ \phi &\approx \frac{2\pi}{\lambda} \cdot x \cdot \alpha + (\phi_1 - \phi_2) \quad \text{for small } \alpha \end{aligned} \quad (4.18)$$

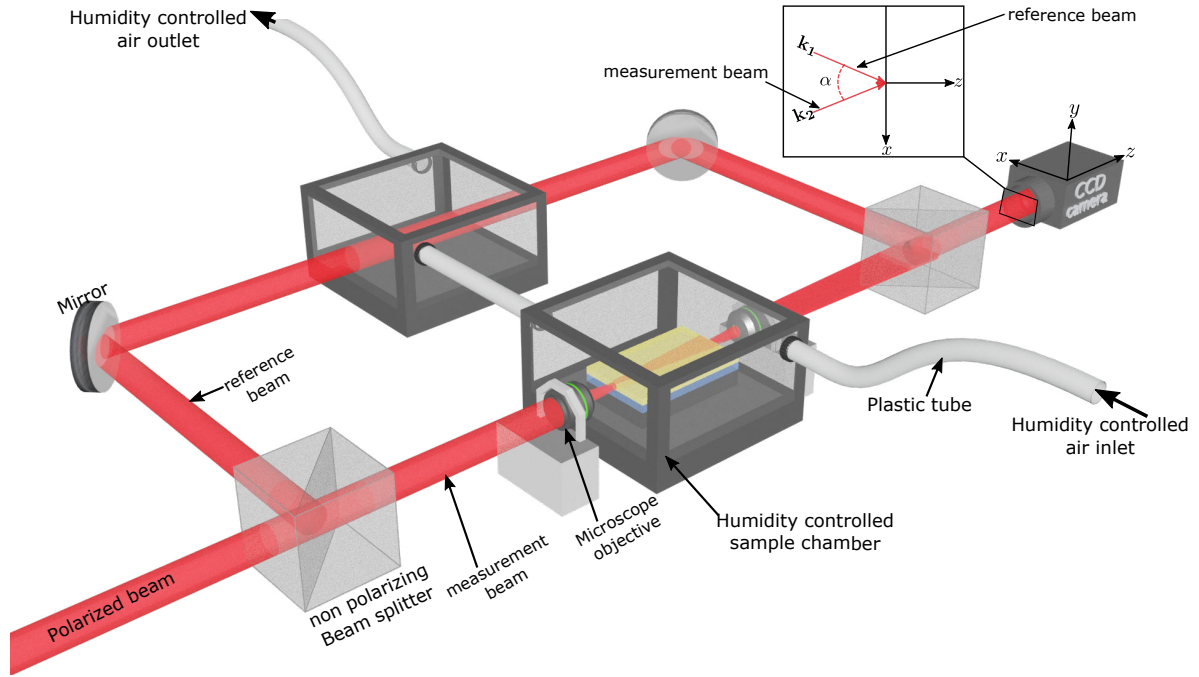


Figure 4.16: Schematic representation of the Mach-Zehnder interferometer optical setup.

Figure 4.17-a shows experimentally measured interference fringes resulting from the interference of the reference laser beam and the measurement beam that has been guided through a planar waveguide and collected. The distance between the interference fringes depends on the angle α as shown in Figure 4.17-b. As α is small, the fringe spacing (ξ) is defined as:

$$\xi = \frac{\lambda}{\alpha} \quad (4.19)$$

In principle ξ must be equivalent for all the fringes. However, as can be seen in Figure 4.17-b, the fringe spaces is higher in the left part of the figure compared to the right part ones. This is probably due to the divergence of the measurement beam, because when it exits the waveguide,

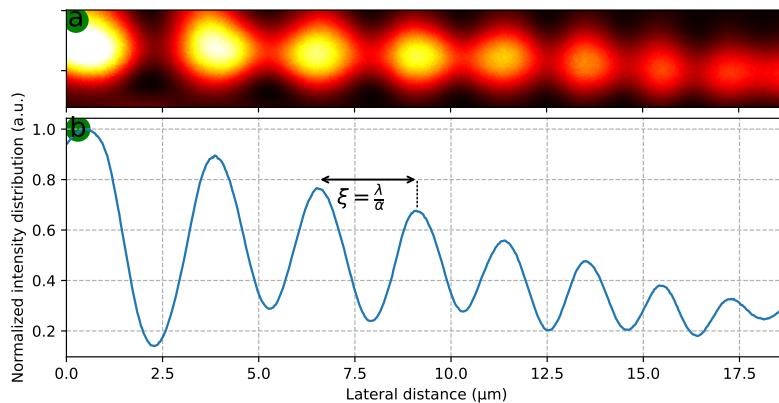


Figure 4.17: **a)** Interference fringes image. **b)** Interference fringes intensity profile.

it diverges. For our case study, the fringe space is not the parameter we want to measure but we measure the relative phase of the beams (i.e. the $\phi_1 - \phi_2$ term).

4.4.2.1 Measurement of humidity effect in planar waveguides

We used the Mach-Zehnder interferometer to measure effect of humidity in planar optical waveguides. As shown in Figure 4.16, the planar waveguides are studied in a controlled humidity chamber. An identical chamber is also put in the pass of the reference beam such that the only difference between the reference and measurement beam is the optical waveguide. When we modify humidity of the chamber, since the reference beam travels in a material that changes refractive index with humidity, the phase difference between the two beams vary as a function of humidity. The variation in refractive index of the material varies the phase of the measurement beam as:

$$\Delta\phi = \frac{2\pi}{\lambda} \Delta n_{guide} l_{guide} \quad (4.20)$$

where l_{guide} and n_{guid} are length and refractive index of the waveguide sample respectively. $\Delta\phi$ is only a function of the refractive index of the waveguide material if all other parameters (λ, l) are constant. The $\Delta\phi$ effect on the interference fringes is their redistribution such that they undergo a variation that they seem to move to the naked eye. If we measure the intensity at a constant position of the camera sensor, the resulting intensity with the variation of the refractive index, is a periodic variation of the intensity as shown in Figure 4.18. From the equation 4.20, we can calculate the variation in refractive index as:

$$\Delta n_{guide} = \frac{\lambda}{2\pi l_{guide}} \Delta\phi \quad (4.21)$$

Every peak in Figure 4.18 corresponds to change in $\Delta\phi$ by 2π . Therefore, the refractive index variation is given by:

$$\Delta n_{guide} = \frac{\lambda}{2\pi l_{guide}} 2\pi \cdot N = \frac{\lambda}{l_{guide}} \cdot N \quad (4.22)$$

where N is number of peaks. For instance, for the wavelength of red light (633nm) and the length of the sample (16mm), each peak corresponds to the change in the refractive index of the guided material (Δn_{guide}) by ($\sim 4 \times 10^{-5}$).

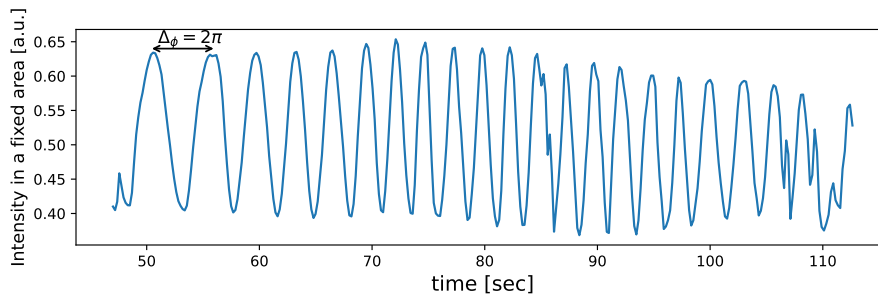


Figure 4.18: Intensity profile for interference fringes temporal evolution.

With this Mach-Zehnder interferometer setup we can measure in-plane refractive index (n_{TE}) and the out-of-plane refractive index (n_{TM}) of planar waveguides as a function of humidity. The precision of the measurement in refractive index variation is defined by the wavelength of light used in the setup and length of the waveguides (equation 4.22). In our measurements, we were able to measure refractive index variation with $\Delta n \sim 5 \times 10^{-5}$ in planar optical waveguides.

4.5 Conclusion

In this chapter, we have described the optical characterization setups developed and used to characterize optical waveguides during this thesis. In Table 4.1, we have listed all the optical setups with their functionality.

Table 4.1: Summary of optical characterization setups described in this chapter.

Optical setup	Functionalities
End-fire coupler	<ul style="list-style-type: none"> -Light guiding (coupling and collecting) in planar and channel waveguides. -Identification of waveguide types and dimensions.
Optical loss measurement	<ul style="list-style-type: none"> -Measurement of optical losses higher than 1dB/cm with ± 1 dB/cm accuracy.
Laser polarimetry	<ul style="list-style-type: none"> -Polarization preparation from unknown light beam with the precision of 0.02° in phase retardation. -Measurement of Stokes parameters of a light beam with accuracy of $\pm 3\%$ in ~ 1 minute. -Polarization mapping of a light beam in ~ 1 minute. -Instantaneous measurement of Stokes parameters of a light beam with accuracy of $\pm 6\%$. -Determining phase retardation and eigenmodes axis of any birefringent system with accuracy of $\pm 1\%$.
Mach-Zehnder interferometer	<ul style="list-style-type: none"> - Measurement of optical waveguides in-plane and out-of-plane refractive index variation (n_{TE} and n_{TM}) in the range of $\sim 5 \times 10^{-5}$ at wavelength of red light.

As shown in Table 4.1, the optical setups described in this chapter are sufficient to characterize optical waveguides in terms of polarization, optical losses, and also variation of optical properties of the waveguides material with changes in environmental conditions (e.g. humidity). For each optical setup, we have described the development details, including the working principle of the optical elements, the calibration of the setups, and the accuracy of the measurements.

be controlled is the LB from the waveguide geometry (shape). In chapter 1 (section 1.6), we have shown that LB can be controlled by fabricating channel waveguides with defined geometries. We have also shown that if low refractive index contrast buffer and guide layers are used in the fabrication of channel waveguides, low LB waveguides can be made with relatively high fabrication tolerance (less precision in size control). Low refractive index contrast waveguide layers are then obtained by using the ORMOSIL material in different compositions to fabricate the buffer and guide layers. The refractive indices of the ORMOSIL material that we used in this study are measured from planar waveguides using m-line spectroscopy, and they are found to be $n_b = 1.61$ and $n_g = 1.625$.

Regarding the channel type structure, we work with rib waveguides since our fabrication method (imprint lithography) allow us to easily fabricate rib structures (see section 3.3). In Figure 5.1-(inset) we have shown the cross-sectional schematic of the targeted rib waveguide. It is characterized by a rib width (w), a rib height (h), and a slab thickness (d). The guiding and the buffer layers have refractive indices n_g and n_b respectively ($n_g > n_b$). The refractive index of the cover layer (n_c) is set to 1 as refractive index of air.

Gathering these specifications, using numerical simulations, we have computed linear birefringence $LB_{\text{shape}} = n_{\text{TE00}} - n_{\text{TM00}}$ coming only from the shape of the waveguide. Figure 5.1 shows the computed LB_{shape} as a function of rib width w at constant $d = 0.2 \mu\text{m}$ and $h = 2.1 \mu\text{m}$ having $\Delta n = 1.625 - 1.61 = 0.015$. As it can be seen from the figure, the LB_{shape} varies with the rib width, and it intersects zero at $w = 3.25 \mu\text{m}$ (i.e. zero birefringence property). The yellow colored area in the figure delimit the range where $LB \leq CB$. This corresponds to the rib channel chirowaveguides with eigenmodes ellipticity $\chi \geq 22.5^\circ$. Intersections of the $LB \leq CB$ zone with the variation of LB_{shape} as a function of rib width w give us the fabrication tolerance in width of

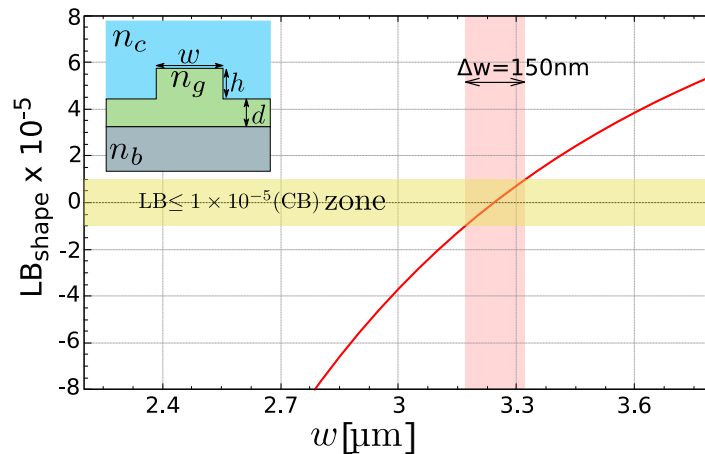


Figure 5.1: Computed shape birefringence LB_{shape} ($n_{\text{TE00}} - n_{\text{TM00}}$) for a rib waveguide (inset) as function of w but constant $d = 0.2 \mu\text{m}$ $h = 2.1 \mu\text{m}$, $n_c = 1$, $n_g = 1.625$, and $n_b = 1.61$.

the waveguides. To fabricate rib waveguides with targeted properties, the fabrication tolerance is $\Delta w = 150\text{nm}$.

In practice, LB_{shape} is not the only linear birefringence present in optical waveguides, some other sources of linear birefringence have often been reported and attributed to residual mechanical stress [27]. While LB_{shape} is possible to calculate theoretically and technologically tunable, the stress effect is difficult to predict and to control practically. Our strategy to get rid of this unpredictable contribution to the overall linear birefringence has been to elaborate on the same sample (wafer) series of rib waveguides with a constant slab thickness d and rib height h but with a various values of rib width w . Due to the fabrication tolerance shown in Figure 5.1, we have chosen to fabricate waveguides of different widths with a step of 300nm around the width in which the waveguides have zero birefringence property ($w = 3.25\mu\text{m}$). In doing so, it makes possible to end up with a w value where LB_{shape} is equal and opposite to the stress linear birefringence and thus cancels the overall linear birefringence of the channel waveguide.

5.2 Rib fabrication and testing

5.2.1 Rib fabrication

We have used imprint lithography to fabricate the channels. As explained in 3.3, the structures size is defined by the master mold. We thus fabricated a silicon master mold with several sets of channel structures, each set consisting of 11 channels with widths ranging from 1.8 to 5.1 μm in 300nm steps. Then, PDMS molds are replicated from the master mold, and they are used to fabricate ORMOSIL structures with the same structural design as the master mold.

In Figure 5.2, we have shown the fabricated rib waveguides. As it can be seen from the figure, the structures of the silicon mold (channels of $w=1.8, 2.1, 2.7, \dots 5.1 \mu\text{m}$) are well transferred by the PDMS mold to the ORMOSIL layer. The fabricated ribs have sidewall angles $80^\circ < \alpha < 90^\circ$ with a slight difference ($\leq \pm 4^\circ$) between the two sides of the channels (Figure 5.2-d). The sidewall angle comes from the silicon master mold as it is fabricated by reactive ion etching. The difference in sidewall angle between two sides may be due to the various anisotropic pressures used to press the PDMS molds during imprint lithography.

The channels widths and heights are found to be very similar to the initial master mold dimensions with a variation of $\pm 0.05\mu\text{m}$ from one waveguide to another. The fabricated structures w and h can be easily measured from the SEM images as it is shown for three different widths in Figure 5.2-b-d. However, because the compositions of ORMOSIL for the buffer and guide layers are relatively similar, the slab thickness d of the rib structures cannot be measured by either optical microscope or SEM. We have measured d of the structures from guided modes

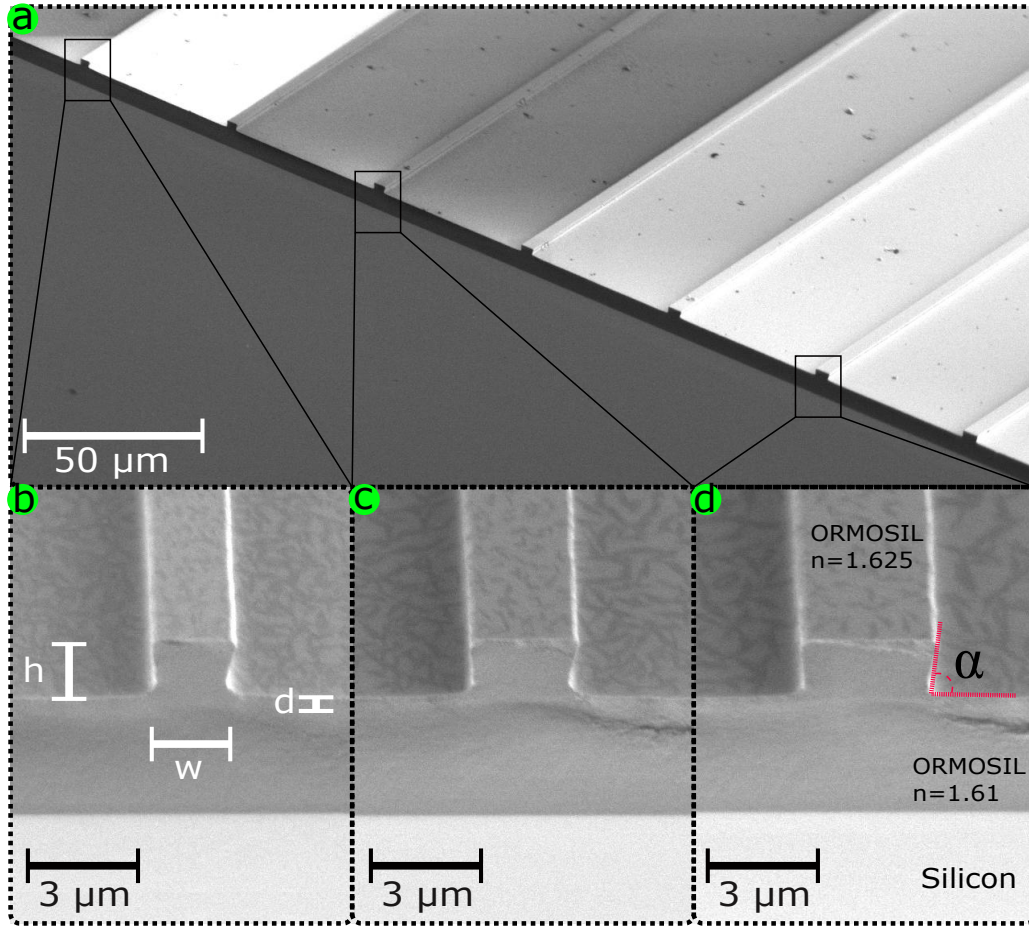


Figure 5.2: **a)** SEM image of ORMOSIL rib waveguides fabricated by imprint lithography which have same height $h = 2.1 \pm 0.1 \mu\text{m}$, same slab thickness $d = 0.2 \pm 0.1 \mu\text{m}$ but different width. **b), c), and d)** are rib channel waveguides with $w = 2.1 \pm 0.1 \mu\text{m}$, $w = 2.7 \pm 0.1 \mu\text{m}$, and $w = 3.6 \pm 0.1 \mu\text{m}$ respectively. The buffer layer is $6 \mu\text{m}$ thick with a refractive index contrast $\Delta n_g - n_b = 1.625 - 1.61 = 0.015$.

size as we will see in the next subsection. For a given channel waveguide, top view inspection with an optical microscope showed no variation in dimensions on a 2 cm long sample. In addition, polarization measurements on a 2 cm long waveguide before and after a half-cut showed no difference. This ascertains that the cross-sectional shape of the waveguides does not vary significantly along the sample.

5.2.2 Optical propagation

Samples are cleaved to have flat facets then fixed on our end-fire coupling setup (see Figure 5.5). Light is launched and guided into each channel independently. The modes measured at the waveguide output facets are seen to be properly confined in the rib structures and with an

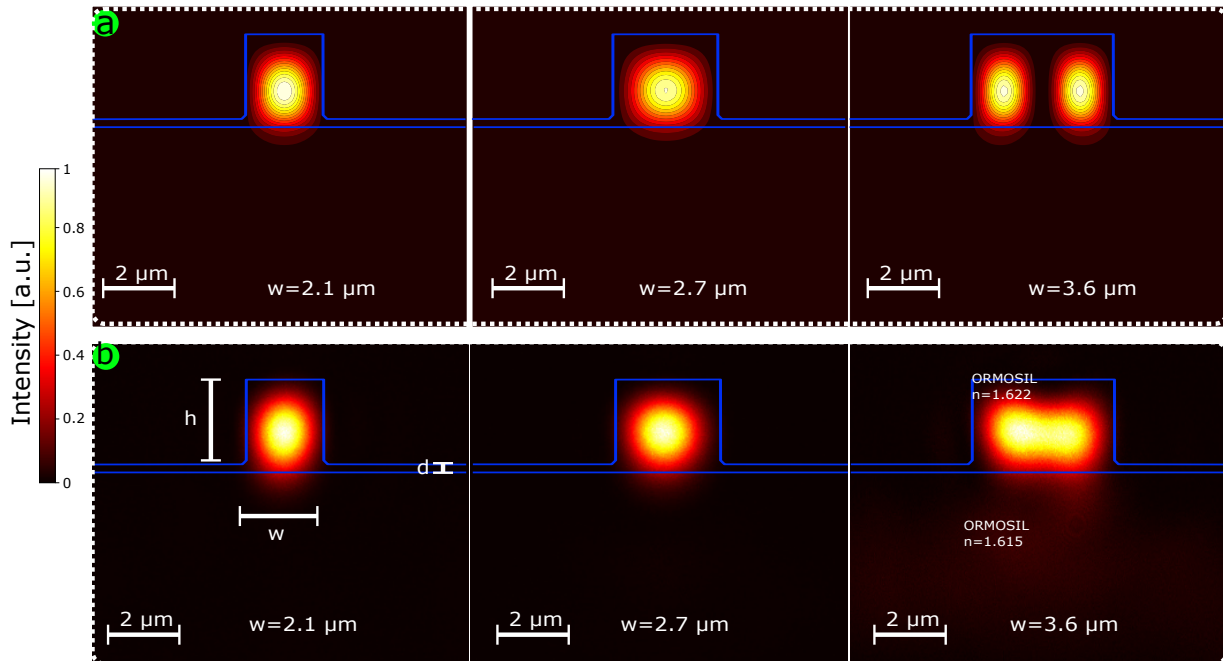


Figure 5.3: **a)** Simulated and **b)** Experimentally measured mode intensity profile for the three rib waveguides with same rib height $h = 2.1 \pm 0.1 \mu\text{m}$, same slab thickness $d = 0.1 \pm 0.1 \mu\text{m}$ but different width $w = 2.1, 2.7, 3.6 \pm 0.1 \mu\text{m}$ from left to right. Note that the intensity of the guided modes is shown in false color scale

intensity profile similar to the simulated one's as shown in Figure 5.3. After determining w and h from SEM measurements, comparing the experimental and theoretically calculated guide mode size, the slab thickness d of the fabricated ribs is determined to be $d = (0.2 \pm 0.01 \mu\text{m})$, as shown in Figures 5.3-a and b. Waveguides with widths less than $3.3 \mu\text{m}$ are single-mode (i.e., they support only the TE_{00} and TM_{00} guided modes which have a single-lobe intensity distribution). However, waveguides with widths greater than $3.3 \mu\text{m}$ (e.g., $w = 3.6 \mu\text{m}$), in addition to TE_{00} and TM_{00} modes, also supported higher order modes.

5.2.3 Waveguide loss measurements

Regarding the material losses, the rib waveguides are fabricated from ORMOSIL material in which losses of the material in planar waveguides are measured and estimated to be lower than 1 dB/cm [62]. However, fabrication of the channel may bring extra sources of losses such as sidewall and surface roughness. From the SEM measurements, we observed that the sidewall roughness was low, but this needs to be confirmed by the loss measurements.

Using the experimental setup explained in 4.2, we have measured losses by recording the images of the light scattering from the channels top surface. The images recorded by the CCD

camera are then treated to obtain the intensity profile of the scattered light as a function of the propagation length. Figure 5.4 shows top surface images and relative intensity profile (in dB) of the scattered light for three different width waveguides. The channels losses are seen to be in the range of the detection limit of the loss measurement method, as the presence of some non-uniformly distributed light scattering sources creates high noise in the measurement. However, a linear fit of the overall reduction in scattered light intensity allows to estimate the value of the losses in the channels. As shown in the figure, for the three waveguides the overall losses are always below $3dB/cm$ while the smaller width waveguide experience higher optical losses. In the $2.1\mu m$ wide channel, losses are $-2.9\pm 1dB/cm$, they reduce to $-2.6\pm 1dB/cm$ and $-1.9\pm 1dB/cm$ in the $2.7\mu m$ and $3.6\mu m$ wide channels respectively. The higher losses in small width channels can be attributed to the roughness of the sidewall created during the waveguide fabrication process. Indeed, the interaction between the guided modes and the waveguide sidewall is higher for smaller size channels [103].

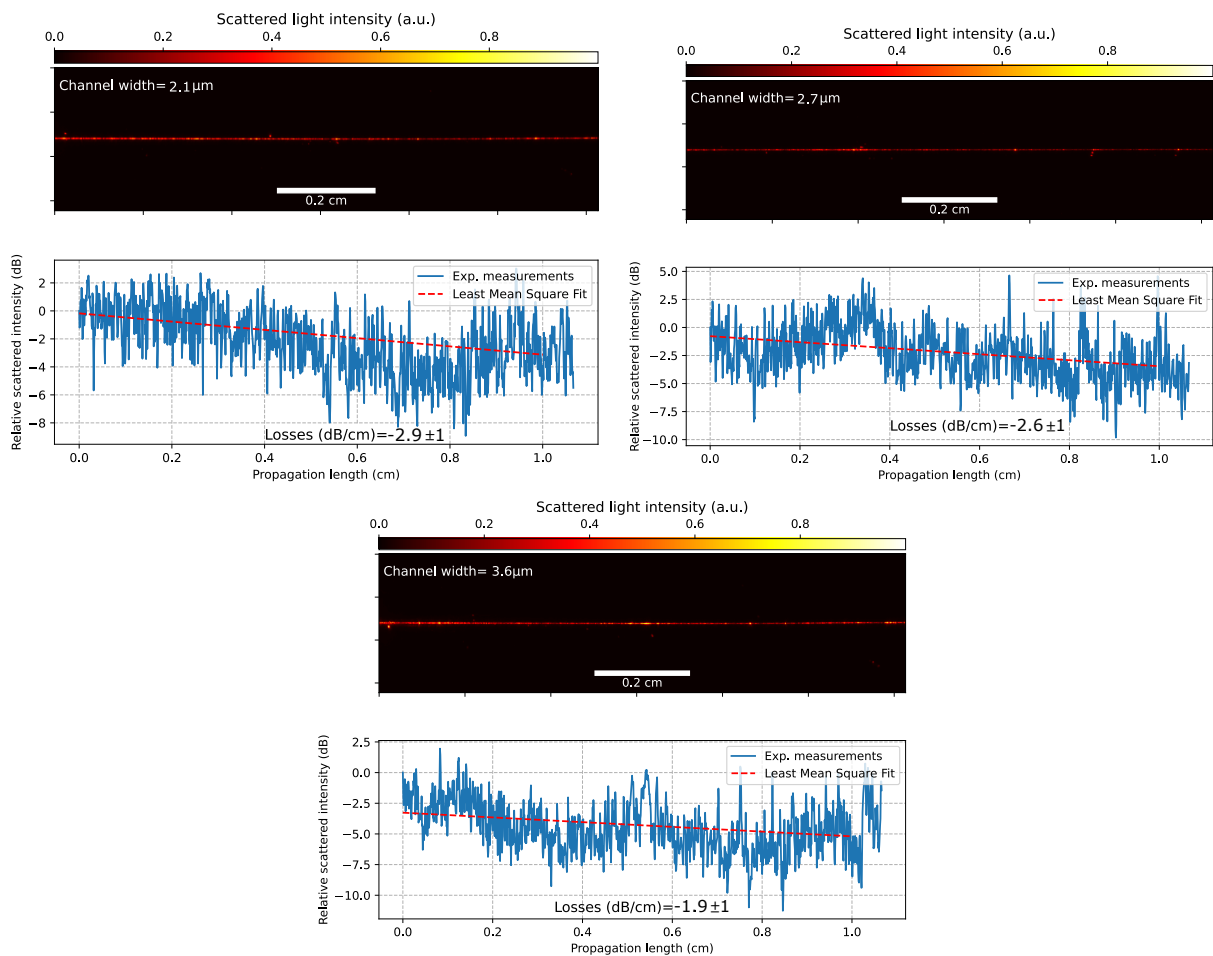


Figure 5.4: Top surface of image and losses measurement for ORMOSIL rib waveguides with same height $h = 2.1\mu m$ but different widths $w = 2.1, 2.4, 3.6 \pm 0.1\mu m$.

5.3 Polarization measurement results

In this section, we present polarization measurement results of the waveguides made of material with positive chirality ($CB=+1 \times 10^{-5}$), negative chirality ($CB=-1 \times 10^{-5}$), and racemic ($CB=0$) as a function of the channels' geometries. In measuring the polarization properties of the waveguides, we observed that they are sensitive to the ambient humidity. Therefore, the channels were studied in a controlled humidity chamber by keeping the relative humidity of the chamber at $57 \pm 2\%$. The details of the humidity effect on the waveguides' polarization properties are presented in the next chapter.

Figure 5.5 shows the optical setup used for waveguide characterization. A 633 nm laser beam is passed through a combination of a linear polarizer and a Babinet-Soleil compensator to control its polarization state (SOP), and then launched into the waveguides. The light collected from the waveguides is characterized in terms of Stokes parameters using the combination of a rotating quarter wave plate and a linear polarizer. By comparing the SOP of the input laser light with the SOP of the light measured at the output of the waveguides, the SOP of the waveguides eigenmodes represented by the normalized Stokes parameters is determined. From the normalized Stokes parameters we have determined polarization ellipticity χ and polarization azimuth ψ of the eigenmodes using the equations 1.24-a and b (For normalized Stokes parameters the equations 1.24-a and b are $\tan 2\psi = \frac{S_2}{S_1}$ and $\sin 2\chi = \frac{S_3}{S_1}$ respectively).

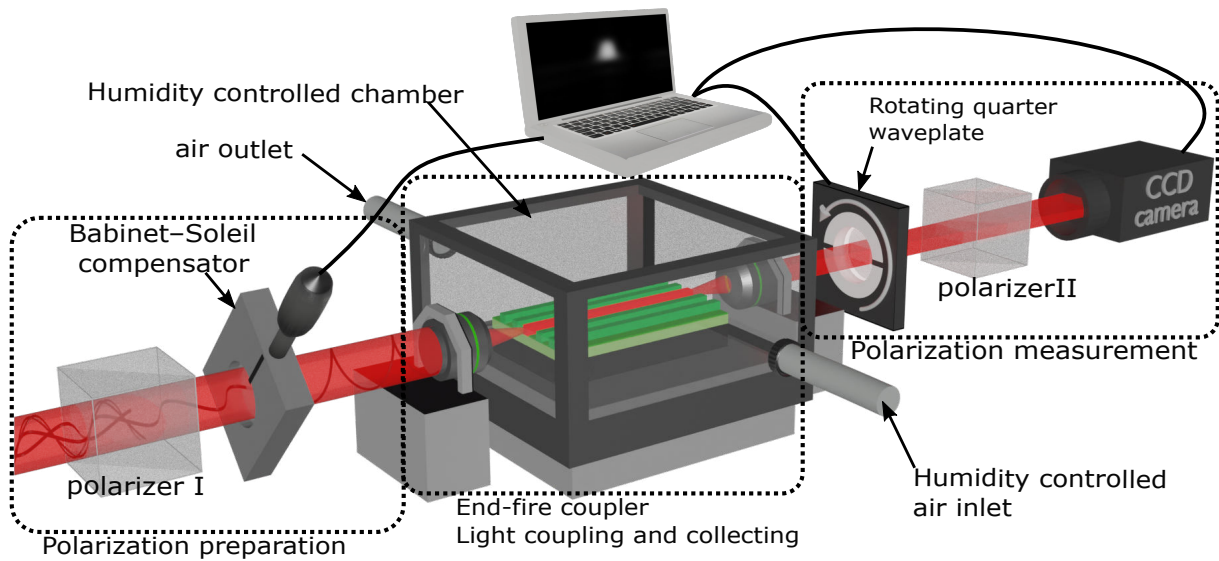


Figure 5.5: Optical measurement setup.

5.3.1 Elliptical birefringence modulation

First, we investigate the influence of the rib width (w) on the birefringence behavior of the waveguides. In Figure 5.6, we have shown the polarization ellipticity of the rib waveguides eigenmodes with corresponding ellipses as a function of the w for three samples: two with opposite chirality (+), (-) and one racemic (+/-). The measurements are repeated on at least five successive series of widths pattern for each of the samples, resulting in error bars that are twice the standard deviation of the measurements. For a given dimension, we retain only the best 70% of the ribs. The 30% remaining ribs present lower eigenmodes ellipticity that comes either from uncertainty in the fabrication process width or from additional deformations that induce higher linear birefringence.

As shown in Figure 5.6 by black squares, the racemic waveguides eigenmodes ellipticity are always null. Regardless of their width w , all these ribs behave as achiral waveguides that are linear birefringent. Adding chirality to these waveguides profoundly change their behavior. For the same rib structure, from $w=3.9\mu\text{m}$ down to $w = 2.7\mu\text{m}$, the eigenmodes ellipticity increases from conventional TE/TM ($\chi = 0$) to quasi-circular polarized eigenmodes ($\chi=32.5\pm 7^\circ$ and $29\pm 7^\circ$). Lowering the rib width from this optimized value, results in a high reduction of the eigenmodes' ellipticity down to 5° at $2.1\mu\text{m}$.

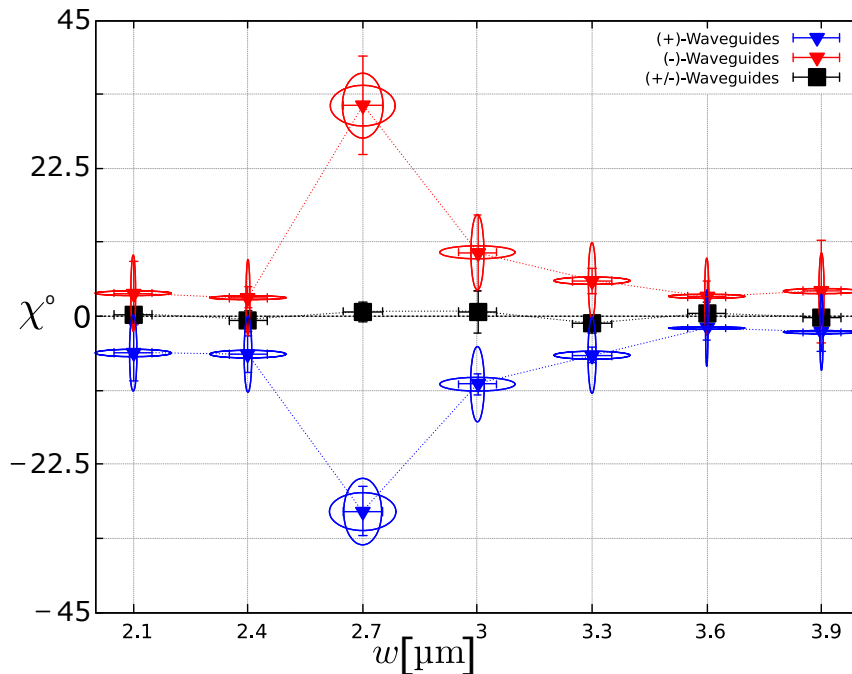


Figure 5.6: Eigenmodes ellipticity and polarization ellipses measured for different rib widths w at rib height $h=2.1\mu\text{m}$, slab thickness $d=0.2\mu\text{m}$, refractive index contrast is $\Delta n=0.015$, and working wavelength is 633 nm .

Since the waveguides' chirality (CB value) is independent of the size of the waveguides, the modulation of the eigenmode ellipticity as a function of w is related to the modulation of the LB of the waveguides as a function of w (i.e. $\chi(w) = 0.5 \arctan[\frac{CB}{LB(w)}]$). As predicted by numerical simulations, the LB depends on the width of the waveguides and has a minimum value at a certain width. However, as we have shown in Figure 5.1, the expected minimum LB is at $w=3.25\mu\text{m}$ while it is observed experimentally at $2.7\mu\text{m}$. This behavior of the eigenmodes indicates that the (LB_{shape}) coming from the geometrical size (shape) of the waveguides is not the only LB present in the waveguides.

5.3.2 Sources of linear birefringence

For further understanding, the magnitude and principal axis orientation of the experimentally measured LB were extracted from the normalized Stokes parameters of the waveguide eigenmodes. The magnitude of LB is calculated using equations 1.83 and 1.24-a[†], and the principal axis orientation is calculated using 1.24-b[‡].

In Figure 5.7-a, we have shown the experimental LB magnitude as a function of the waveguides widths. For all the rib widths, $|LB| \leq 1 \times 10^{-3}$ and is minimum at $w = 2.7\mu\text{m}$ where values as small as 3×10^{-6} are measured. We see that the minimum LB is at $w = 2.7\mu\text{m}$ whereas the minimum LB was expected by the numerical simulations at $w = 3.25\mu\text{m}$ (dashed line curves in Figures 5.7-a). However, the addition of a constant LB to LB_{shape} ($LB_{shape}(w)+1 \times 10^{-4}$) makes the numerical simulation model perfectly fit the experimental data (continuous line curves in Figures 5.7-a). Such additional LB contribution has been already observed in planar multi layers of polymers and is attributed to the stress induced linear birefringence [104,105]. Similarly, our fabrication procedure involves multiple layers of materials which may also add constant residual stress as they are fabricated by the sol-gel method and stress in sol-gel layers is a well known problem [89]. We therefore refer to this constant linear birefringence as stress linear birefringence (LB_{stress}).

Regarding the principal axis orientation of the LB as shown in Figure 5.7b, except for $w = 2.7\mu\text{m}$, it is around zero whatever the waveguides width and thereby, the eigenmodes of the linear birefringence are located on TE/TM axis. At $w = 2.7\mu\text{m}$, unexpectedly, the principal axis orientation of the eigenmodes is no more aligned to the TE/TM axis but tilted with an angle ($\psi \leq \pm 45^\circ$). Since the behaviour is also observed for the racemic rib waveguides, it can not be attributed to a chiral effect. Therefore, the waveguides exhibit additional linear birefringence that have eigenmodes not polarized like the TE/TM eigenmodes but polarized at

[†] $LB=CB/\tan[\arcsin(S_3)]$

[‡]Principal axis orientation is the orientation of the birefringent axis (eigen-axis) relative to x -axis which is defined by eigenmodes polarization azimuth $\psi = 0.5 \cdot \arctan \frac{S_2}{S_1}$

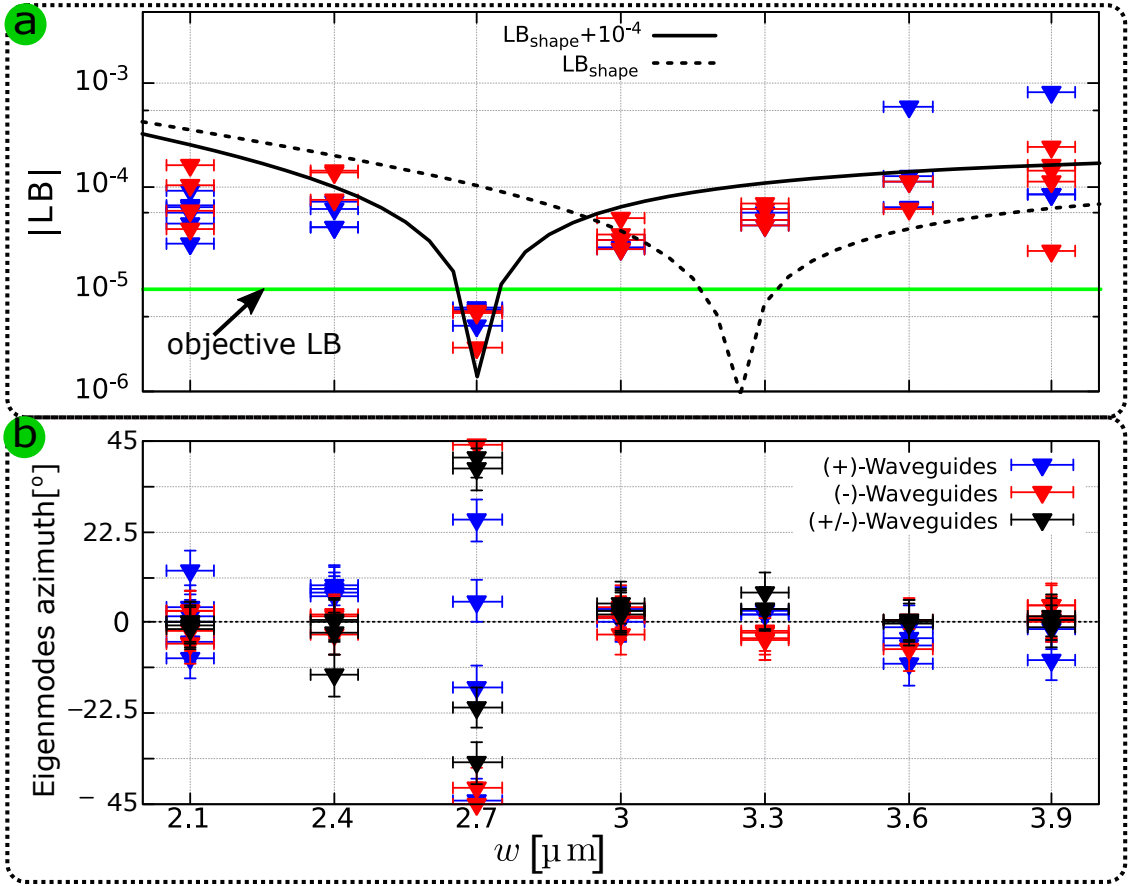


Figure 5.7: Experimental linear birefringence LB deduced from the eigenmodes polarization. **a)** Principal axis orientation of the linear birefringence as the orientation (azimuth) of the polarization ellipse of the eigenmodes. **b)** $|LB|$ deduced from the ellipticity of the eigenmodes. The green line is the CB value of our material.

$\pm 45^\circ$ with respect to TE/TM axis. We have calculated the magnitude of the additional linear birefringence ($LB_{\pm 45}$) at $w = 2.7\mu\text{m}$ and found that $LB_{\pm 45} \sim 4 \times 10^{-6}$. At this width, because LB_{shape} and LB_{stress} cancel each other, $LB_{\pm 45}$ becomes visible(measurable). The presence of $LB_{\pm 45}$ can be attributed to the small departure from the ideal rectangular symmetrical shape observed on some ribs [106], as can be seen on the SEM images shown in Figure 5.3-c.

Finally, the linear birefringence of the studied ribs can be assigned to three sources:

- (i) Shape linear birefringence $LB_{\text{shape}}(w)$, it is function of rib width and has TE/TM eigenmodes.
- (ii) Residual stress linear birefringence $LB_{\text{stress}} = 1 \times 10^{-4}$ which does not depend on waveguides' width and also has TE/TM eigenmodes.
- (iii) A low linear birefringence $LB_{\pm 45} \sim 1 \times 10^{-6}$ that is only measurable when the LB_{shape}

and LB_{stress} have opposite signs and cancel each other. $LB_{\pm 45}$ has eigenmodes that are polarized at $\pm 45^\circ$ with respect to TE/TM axis.

These results demonstrate the relevance of our design strategy to produce low LB waveguides by fabricating waveguides with different width on same sample. Indeed, it made it possible to achieve channel waveguides with low linear birefringence (less than our objective LB) and even find out and quantify other unpredictable birefringences arising in the waveguides.

5.3.3 Low linear birefringent chirowaveguides

Three examples of Poincaré sphere input/output trajectories for the three waveguides with $(-), (+)$ and $(+/-)$ chirality are shown in Figure 5.8, for the rib width $w = 2.7\mu\text{m}$. The blue and green dots in the figure show the SOP of the light before coupling into the waveguides and the SOP of the light measured at the waveguide output, respectively. The black dots are the best fitted SOP to the output polarization to find the eigenmodes. The cyan curve shows the trajectory of the polarization modulation of each input until it exits the waveguides and is measured as an output. The polarization trajectories of $(-), (+)$ samples show a clear rotation of the input SOP about a diameter axis of Poincare sphere (eigenmodes axis) that is out of the equatorial plane, attesting for an elliptical birefringence behaviour of the chirowaveguides. As expected, the racemic $(+/-)$ samples eigenmodes axis is located in the equatorial plane, its polarization behaviour is similar to linear birefringent waveguides.

For the $(-)$ waveguide, the input SOP are rotating "to the east" which corresponds to an anti-clockwise rotation in the laboratory space and with the location of the slow eigenmode in the north hemisphere as expected for a $(-)$ enantiomer in a chiral medium. The $(+)$ waveguide shows an opposite effect (mirror image) as expected for two enantiomers. Combining the measured eigenmode ellipticity and the rotation angle (guided light phase change ϕ in the Poincaré sphere), we calculated via equations 1.83 and 1.85 the two birefringence at this rib width $w = 2.7\mu\text{m}$ and obtained $CB=(1\pm 0.1)\times 10^{-5}$ and $LB=(4.5\pm 1)\times 10^{-6}$. This value of CB is very close to the CB measured at normal incidence for thick planar chiral films, which shows the validity of the coupled mode theory we used to determine polarization properties of the chirowaveguides eigenmodes.

Additionally, in Figure 5.8-a and b, we have shown the polarization modulation orbit for left-handed circularly polarized light by the cyan circle in the $(-), (+)$ samples. The position of polarization modulation orbit in the north hemisphere show that if circularly polarized light is guided in such waveguides its polarization handedness is conserved no matter how long the propagation length is. Furthermore, the eigenmodes of the chirowaveguides are quasi-circularly polarized as indicated in Figure 5.8-a and b by the red and blue ellipses, meaning

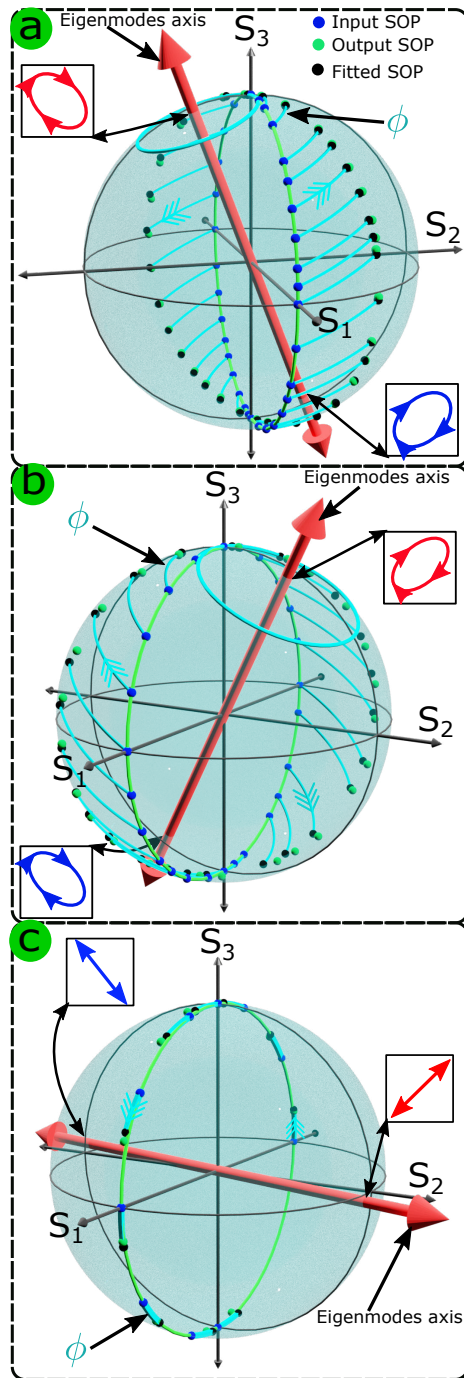


Figure 5.8: Poincaré representation of the transformations of input SOPs (blue points) into output SOPs (green points) after propagation in the chirowaveguides. The black points are the best fitted values for a rotation of angle ϕ about a diameter axis (red arrow). The cyan curves highlight the link between the input and output SOPs. **a)** (-) enantiomer waveguides, **b)** (+) enantiomer waveguides and **c)** (+/-) racemic waveguides. All waveguides are rib channels with $w = 2.7\mu\text{m}$, $d = 0.2\mu\text{m}$, and $h = 2.1\mu\text{m}$.

that quasi-circularly polarized light can be guided in these waveguides while its polarization remain unchanged. Therefore, in such chirowaveguides quasi-circularly polarized light can be used as chiral probe for chiral sensing. The polarization properties of these waveguides fulfill the conditions of our objective chirowaveguides that is “channel optical waveguides for enantioselective sensors”

5.4 Chiral evanescent wave sensor (Theoretical study)

One potential application of the waveguides presented in 5.3.3 is chiral sensing by probing chiral media with the evanescent waves surrounding the waveguides. In this section, we theoretically investigate the possibility of using the waveguides for chiral detection.

As we described in chapter 1 (in 1.5.1), a chirowaveguide is an elliptical birefringent system defined by the eigenmode ellipticity χ and the modal birefringence (MB).

$$\chi = \frac{1}{2} \arctan \left(\frac{\text{CB}}{\overline{\text{LB}}} \right) \quad (1.83)$$

$$\text{MB} = \sqrt{\text{LB}^2 + \text{CB}^2} \quad (1.81)$$

When a light wave propagates in a chirowaveguide, its SOP undergoes a phase change which is described on the Poincaré sphere as a rotation about the chirowaveguide’s eigenmodes axis by an angle

$$\phi = \frac{2\pi}{\lambda} \cdot \sqrt{\text{LB}^2 + \text{CB}^2} \cdot l \quad (1.85)$$

where l is the length of the waveguide. The CB in the equations 1.83,1.81, and 1.85 is the circular birefringence felt by the electromagnetic field according to

$$\text{CB} = \int \text{CB}(x, y) \cdot |\mathbf{E}(x, y)|^2 \cdot dx dy \quad (5.1)$$

where $|\mathbf{E}(x, y)|^2$ is modulus square of the normalized guided mode profile.

5.4.1 Effect of a chiral molecule on the chirowaveguide

Let’s assume that our device is in contact with a media containing chiral molecules. We schematized in Fig. 5.9 three scenarios for chiral molecules to change the chiral environment of the chirowaveguide

- (a) In the volume of the cladding layer of the waveguide, with CB that is denoted as CB_{clad} .
- (b) At the surface of the waveguide if the surface of the waveguides is functionalized, with CB that is denoted as $\text{CB}_{surface}$ over the length of the molecules’ binder.
- (c) Inside the waveguide if the chiral molecules diffuse into the waveguide layer through the pores of the sol-gel material with CB that is denoted as CB_{guide} .

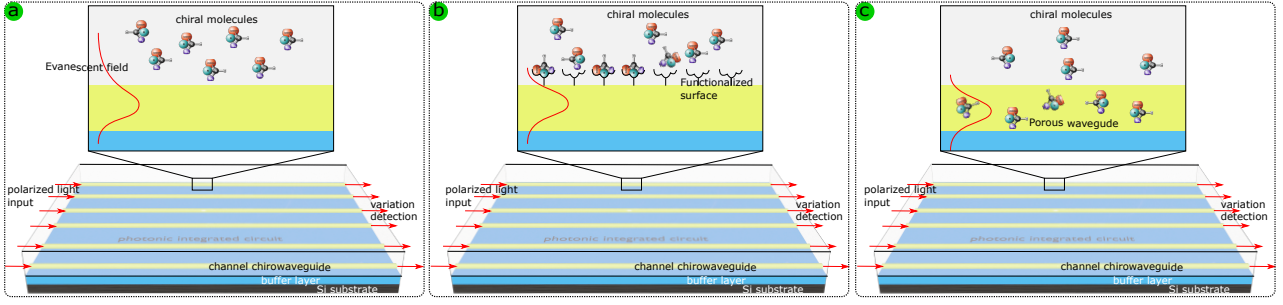


Figure 5.9: Different types of sensing in optical waveguides. a) Volume sensing: change of CB in the cladding layer of the waveguide. b) Surface sensing: targeted molecules are anchored on molecular binder resulting in a high CB enhance in the close vicinity of the waveguide. c) Molecular diffusion of the chiral molecules into the waveguide material.

According to Equation 5.1, the three scenarios change the CB of the elliptical birefringent waveguide from CB to $CB + \Delta CB$ by

$$\begin{aligned} \Delta CB = & \int_{outside} CB_{clad} \cdot |E(x, y)|^2 \cdot dx dy \\ & + \int_{surface} CB_{surface} \cdot |E(x, y)|^2 \cdot dx dy \\ & + \int_{inside} CB_{guide} \cdot |E(x, y)|^2 \cdot dx dy \end{aligned} \quad (5.2)$$

where the integral $\int_{outside}$ is taken outside the waveguide, $\int_{surface}$ is taken on the length of the molecule anchor, and \int_{inside} is taken inside the waveguide layer.

In order to get an idea of the change in CB during sensing, let's assume that we want to detect paracetamol. The specific optical rotation of paracetamol is $[\alpha] \sim 80$, it is the optical rotation for a path length of 10cm measured for a concentration of 1g per 100ml. The corresponding circular birefringence for a concentration C (g per 100ml) is therefore $CB = C \cdot \frac{80}{180} \cdot \frac{\lambda}{10cm} \approx C \cdot 2.8 \times 10^{-6}$ for $\lambda = 633nm$. A pill of 1000mg of paracetamol in one glass of water (200ml) results in $CB \sim 10^{-6}$. This CB corresponds to the condition where the electromagnetic field interacts fully with the paracetamol solution. However, for the waveguide, we must consider that the guided light partially interacts with the chiral solution (as indicated by Equation 5.2). We theoretically determined evanescent part of the guided modes of the chirowaveguides and found that it is only 0.1% of the total field which means that it is very low and needs to be optimized. However, we have also noticed that the waveguides are sensitive to humidity since the ORMOSIL material is porous (as we will see in chapter 6 water diffuses into the material pores). Thus, we assume that when the waveguides are used for sensing applications the analyte will diffuse into the material. Considering 0.1% of the evanescent of the guided modes and diffusion of the analyte into the material, we assume that 1% of the paracetamol solution is sensed by the guided modes corresponding to $\Delta CB \sim 10^{-8}$.

5.4.2 Measurement parameters of the sensor

Change CB of the chirowaveguide will induce at first order a change in the two parameters χ and ϕ :

$$\Delta\phi = \frac{\partial\phi}{\partial\text{CB}}\Delta\text{CB}, \quad \Delta\chi = \frac{\partial\chi}{\partial\text{CB}}\Delta\text{CB} \quad (5.3)$$

Inserting Equation 1.83 and 1.85 into Equation 5.3, we get:

$$\Delta\chi = \frac{\cos^2 2\chi}{2\text{LB}} \cdot \Delta\text{CB} \quad (5.4)$$

$$\frac{\Delta\phi}{2\pi} = \frac{l}{\lambda} \cdot \sin 2\chi \cdot \Delta\text{CB} \quad (5.5)$$

The Equation 5.5 can also be rewritten in terms of the optical rotation (OR):

$$\frac{\Delta\phi}{2} = \sin 2\chi \cdot \Delta\text{OR} \quad (5.6)$$

First, if we consider parameter $\Delta\chi$. Equation 5.4 states that the waveguides eigenmodes ellipticity change in the presence of additional chirality and the change χ is the product of two terms:

- (i) ($\cos^2 2\chi = S_1^2$) term vanishes for chiral material meaning this parameter can not be used in the chirowaveguides. However, it is maximum for achiral (racemic) waveguides ($S_1 = 1$) where a change in CB will induce the change in eigenmodes ellipticity χ .
- (ii) ($\frac{\Delta\text{CB}}{\text{LB}}$) is the angle measuring how far eigenmodes axis is from the equatorial plane in the Poincaré sphere. Paracetamol sensing with $\text{CB}=10^{-8}$ and our $\text{LB}=10^{-6}$ ends up with an angle of $\sim 10^{-2}$ which can not be reasonably detected.

Regarding the second parameter of the sensor that is $\Delta\phi$. Equation 5.5 states that the relative phase change ($\frac{\Delta\phi}{2\pi}$) of an input SOP will result in a change in rotation angle about the chirowaveguide eigenmodes axis in the Poincaré sphere. It shows that the sensitivity of our elliptical birefringent waveguide to a chiral change is the product of three terms:

- (i) ($\frac{l}{\lambda}$) term corresponds to the accumulation of the phase change along the length of the waveguide. This is a very important term for all interference-like measurements because it allows for a huge amplification of the signals.
- (ii) ($\sin 2\chi = S_3$) shows that chiral sensing requires an elliptical birefringent media. We can note that this term is the normalized $|S_3|$ Stokes parameter of the two eigenmodes. For circular polarized eigenmodes $|S_3| = 1$ is maximum. The low LB chirowaveguides presented in the previous section have $\chi = 32.5^\circ \equiv S_3 \approx 0.9$ which is very close to the maximum $|S_3|$ and therefore, they are very good candidates for chiral sensing. The achiral (racemic) waveguides which have $S_3 = 0$ are insensitive (at first order) to a CB change.

- (iii) (ΔCB) is the variation of the circular birefringence in the region of the guided modes' field. It requires optimization of the guided modes field/material interaction in order to get most of the field where the CB is changing.

This analysis shows that sensing chirality via a polarization change of the guided modes is well adapted for circular birefringent waveguides ($\sin 2\chi = 1$) by measuring the $\Delta\phi$ because it is amplified by phase change accumulation by the $\frac{l}{\lambda}$ term. Measuring the $\Delta\chi$ seems much more un-realistic because (i) there are no $\frac{l}{\lambda}$ amplification and (ii) the term $\frac{\Delta\text{CB}}{\text{LB}}$ is very small even for our low LB rib waveguides.

Chirowaveguide sensor

We first assume that the chirowaveguides behaves as pure chiral waveguides with circularly polarized eigenmodes (i.e. $2\chi \sim \frac{\pi}{2}$). The plane of polarization of a linearly polarized input light wave propagated in such chirowaveguides is rotated by an angle of $\phi/2$, as illustrated in Figure 5.10.

When such chirowaveguides are used for sensing, the effect of chirality from the analyte change the optical rotation as described by Equation 5.5 (expressed in CB) or Equation 5.6 (expressed in OR). Therefore, the chirality of the analyte can be measured simply as optical rotation as indicated in Figure 5.10 as $\frac{\Delta\phi}{2}$.

In a simple case, if the chirowaveguide is 1cm long, for the example of the paracetamol

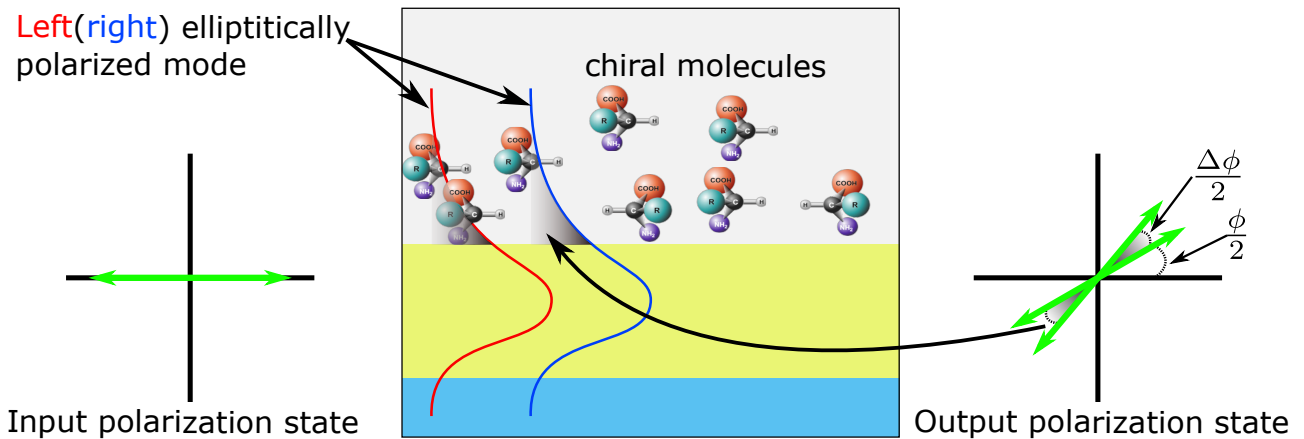


Figure 5.10: **Chirowaveguide evanescent sensor.** In red (blue) the field profile of the left(right)-handed elliptically polarized guided modes. While the guided modes acquire a phase change during their propagation in the chirowaveguide, a change of the chirality in the over-cladding induces an additional phase variation. The additional phase leads to a variation of the output polarization angle.

($\Delta\text{CB}=1 \times 10^{-8}$ at $\lambda=633\text{nm}$), the optical rotation coming from the chirality of the analyte is

$$\begin{aligned}\Delta\text{OR} &= \frac{\pi}{\lambda} \cdot \Delta\text{CB} \cdot l \\ \Delta\text{OR} &\sim 0.03^\circ\end{aligned}\tag{5.7}$$

This value of optical rotation is largely above the limit of detection of standard setups. We can then reproduce the instrumental strategy developed for bulk chiral polarimeters: modulation of the input polarization and Lock-in amplifier (leading to resolution of 0.0001° for commercial apparatus) [107].

5.5 Conclusion

In this chapter, we have presented the main results obtained in this thesis. First, we have shown the fabrication design rules to obtain channel waveguides with elliptically polarized eigenmodes. In the design, depending on the chirality of the material (CB), we defined a fabrication tolerance in the width of the waveguides. The numerical simulation model predicted only the LB_{shape} , to compensate unpredicted sources of LB such as $\text{LB}_{\text{stress}}$, we fabricated multiple waveguides of different widths on the same wafer.

Using imprint lithography method, we fabricated channel waveguides that showed to have low propagation losses ($< 3\text{dB/cm}$). Polarization measurements showed that the waveguides are elliptical birefringent. The eigenmode ellipticity was modulated by changing the width of the waveguides from linearly polarized eigenmodes to quasi-circularly polarized eigenmodes ($0 \leq \chi \leq 32.5^\circ$). Since the circular birefringence (CB) of the waveguides is constant and does not depend on the waveguide geometry, we deduced from these results the experimentally measured linear birefringence in the waveguides. By comparing the theoretically calculated and measured linear birefringence, we were able to deduce the different sources of linear birefringence in the waveguides and showed that LB in the channel waveguides is originated from three sources i) a variable LB_{shape} that is defined by the opto-geometrical properties of the channels ii) a constant $\text{LB}_{\text{stress}}$ coming from the residual stress of the waveguide layers which had magnitude of $\sim 10^{-4}$ and iii) a constant $\text{LB}_{\pm 45}$ that was a very low linear birefringence $\sim 10^{-6}$. The $\text{LB}_{\pm 45}$ being very small was only measurable when the LB_{shape} and $\text{LB}_{\text{stress}}$ were eliminated in the waveguides.

Afterwards, we showed that the chirowaveguides with the lowest linear birefringence (i.e. high χ) can be used to propagate circularly polarized light in integrated photonic chips without changing its polarization handedness. As these chirowaveguides had quasi-circularly polarized eigenmodes they can be used for quasi-circular polarization application such a chiral sensing. We have thus theoretically shown that such waveguides have the potential to be used in chiral sensing applications.

6.1 Experimental

Waveguide preparation

Thick layers ($> 5\mu\text{m}$) of ORMOSIL are prepared by dip coating of ORMOSIL solutions on silicon wafers, then they baked. These thick ORMOSIL layers are then used as buffer layers to deposit on them guiding layers with a higher refractive index than the buffer one's. The refractive index of the deposited layers is adjusted by adding a given amount of pre-hydrolyzed MTEOS into the ORMOSIL solution (see 2.4 for details). The thickness of the planar waveguide layer used in this study is measured by M-line spectroscopy and found to be $2\mu\text{m}\pm 0.1$. The refractive indices of the buffer (n_b) and guide (n_g) layers are 1.605 ± 0.001 and 1.618 ± 0.001 respectively.

Channel waveguides are prepared by the same procedure as the planar ones with the exception that the guiding layers are patterned using imprint lithography. All the channel waveguides analysed in this study are found to be rib channels with channel height $h = 2.1 \pm 0.1\mu\text{m}$, rib slab thickness $= 0.2 \pm 0.1\mu\text{m}$ but different width w . The refractive indices of the buffer and guiding layers of the channel waveguide samples are measured from planar waveguides made with same materials composition and found to be $n_b = 1.61\pm 0.001$ and $n_g = 1.625\pm 0.001$ respectively. The refractive indices of the planar and channel waveguides are measured at room temperature (from 20 to 27°C) and ambient relative humidity ($35\pm 5\%$).

Characterization setup

The waveguides are analyzed in a chamber, and the relative humidity (RH) is controlled by flowing RH-controlled air through the chamber. To control the relative humidity in the 11-75% range, a mechanical air pump and valves are used to control the flow of air bubbling through a saturated salt (LiCl) and water solutions into the sample analysis chamber. The air from the saturated LiCl solution has $\text{RH}=11\pm 5\%$ while the air from the water solution has $\text{RH}=75\pm 5\%$. The air mixture controlled by the mechanical valves is air with a $\text{RH}\in [11 \pm 5 : 75\pm 5\%]$. A commercial electronic humidity sensor (DHT11), placed next to the analyzed optical waveguides, is then used to measure the RH values. We calibrated the humidity sensor from the RH of air in equilibrium with different saturated salt solutions [117]. All measurements are performed at room temperature (from 20 to 27°C), but it only changed within $\pm 2^\circ\text{C}$ throughout any experimental run.

Mach-Zehnder interferometer is used to measure the evolution of in-plane refractive index (n_{TE}), out-of-plane refractive index (n_{TM}) in planar waveguides as a function of humidity. The

principle of the Mach-Zehnder interferometer measurement and the experimental setup are explained in detail in 4.4. Linear birefringence (LB) of the planar and channel waveguides is measured using a laser Stokes polarimetry setup which is explained in 4.3. To remind, the state of polarization (SOP) of a 633nm laser light is controlled, and then it is guided into the waveguides. At the output, the SOP of the collected light is measured. By comparing the SOP of the laser light before and after its passage through the waveguides, the eigenmodes phase (ϕ), SOP of the eigenmodes, and LB of the waveguides are determined.

6.2 Mach-Zender interferometer: n_{TE} and n_{TM} versus humidity for planar waveguides

M-line spectroscopy measurements performed on a thick film ($> 5\mu\text{m}$) showed that the ORMOSIL refractive index decreases before and after immersion in water. Relative variation of n_{TE} and n_{TM} of ORMOSIL planar chirowaveguides are then measured as a function of relative humidity, using Mach-zehnder interferometer. Figure 6.1 shows the dynamic evolution of n_{TE} and n_{TM} in a planar chirowaveguide when the humidity is changed from dry (RH=11%) to humid (RH=75%) air. It is seen that n_{TE} and n_{TM} decrease with increasing background humidity, indicating that the overall refractive index of the chirowaveguide decreases with humidity. The change in both n_{TE} and n_{TM} are reversible which means that the decrease in background humidity increases n_{TE} and n_{TM} . Figure 6.1 also shows that the variation of n_{TE} is higher than n_{TM} with the humidity variation. n_{TE} varies by $\sim 4.4 \times 10^{-3}$ in ~ 7 minutes when

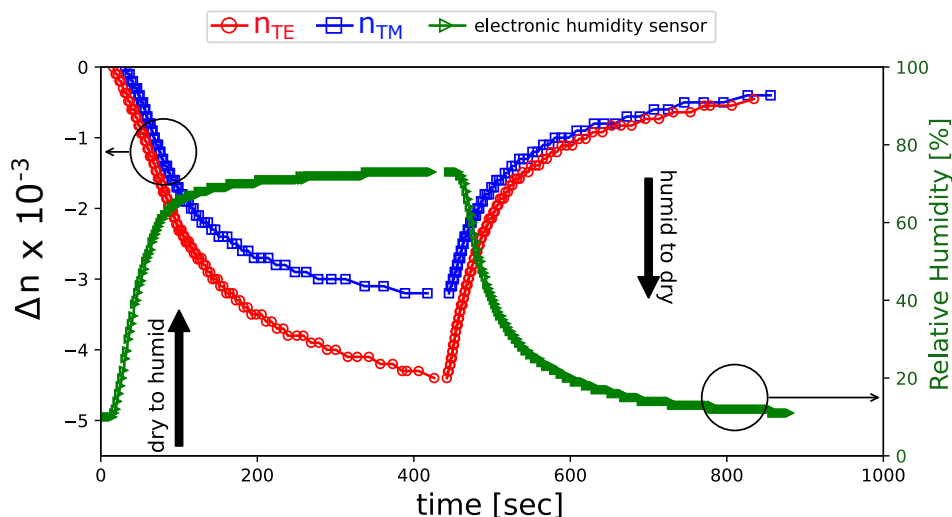


Figure 6.1: Dynamic evolution of in-plane refractive index (n_{TE}), out-of-plane refractive index (n_{TM}) versus humidity from dry air with (RH=11%) to humid air (RH=75%) and back cycle.

the dry background of the planar chirowaveguide becomes humid. However, n_{TM} varies by only $\sim 3.2 \times 10^{-3}$ during the same period of time in the humid air.

In order to understand the origin of the effective refractive index (RI) variation, we compute the variation of n_{TE} and n_{TM} for a planar waveguide made of two ORMOSIL layers with variable RI. We assume that with the increase of humidity water diffuses into the material pores and induces a RI variation Δn of either (i) only the guiding layer or (ii) the guiding and buffer layers. The results are plotted in Figure 6.2. They are almost similar for the two assumptions (i) and (ii): n_{TE} and n_{TM} depend linearly on Δn (Figure 6.2-a and b) and $\text{LB} = n_{\text{TE}} - n_{\text{TM}} \ll 10^{-3}$ (Figure 6.2-c and d). Therefore, the global effective refractive index ($n_{\text{TE}, n_{\text{TM}}}$) variation can be explained by the change of material refractive index of $\Delta n \sim 5 \times 10^{-3}$. However, the LB variation can not be attributed to the refractive index change of the layers since both n_{TE} and n_{TM} vary with the same ratio when the refractive index of the layers changes resulting in a LB change lower than 6×10^{-5} as shown in Figure 6.2-c and d.

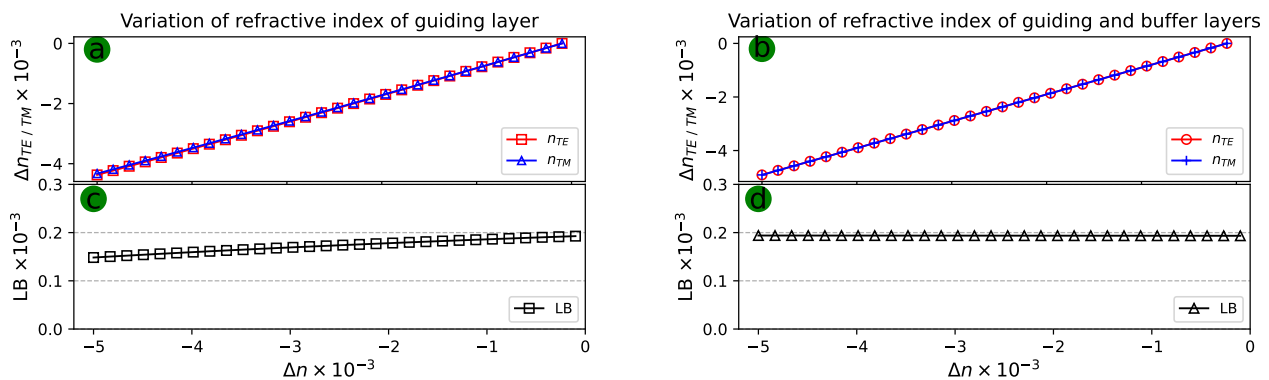


Figure 6.2: Calculated $n_{\text{TE}}(\Delta n) - n_{\text{TE}}(0)$, $n_{\text{TM}}(\Delta n) - n_{\text{TM}}(0)$, and $\text{LB} = n_{\text{TE}} - n_{\text{TM}} \ll 10^{-3}$ variation in a $2\mu\text{m}$ thick planar waveguide as a function material refractive index variation.

The variation of the refractive index of ORMOSIL layers can be due to the diffusion of water into the pores of the ORMOSIL material, which changes its refractive index [111]. The reason of which the refractive index decreases with humidity can be related to the presence of $\sim 20\%$ polyethylene glycol compound in the composition of the ORMOSIL material. Indeed, polyethylene glycol is known to be very hydrophilic and its refractive index has been shown to decrease with humidity [118].

The variation in LB cannot be attributed to the change in material RI. However, it has already been shown that the change in background humidity modifies the mechanical properties of sol-gel derived layers [119]. We believe that the mechanical stress present in the planar layers is modified by the adsorption of water in the material pores, resulting in a change of the measured LB.

6.3 Static birefringence measurement

6.3.1 Measurement technique

To further understand the effect of humidity on the birefringence in planar and channel chirowaveguides, we used Stokes polarimetry technique. From our elliptical birefringent description of chirowaveguides (see 1.5.1), a chirowaveguide is an elliptical birefringent system whose birefringence is composed of the LB of the waveguides and the CB of the chiral material. The LB and CB define the polarization ellipticity (χ) of the chirowaveguide eigenmodes and the magnitude of the phase variation between the two eigenmodes (ϕ) of the light as it propagates through the waveguide, according to the following relationships:

$$\tan 2\chi = \frac{\text{CB}}{\text{LB}} \quad (1.83)$$

$$\phi = \frac{2\pi}{\lambda} \cdot \sqrt{\text{LB}^2 + \text{CB}^2} \cdot l \quad (1.85)$$

where λ and l are free space wavelength and propagation length respectively. These two Equations allow us to determine birefringence variation in the chirowaveguides as a function of humidity if we determine χ and ϕ as a function of humidity. Since CB does not depend on humidity, measurements of χ and ϕ are indirect measures of LB in the waveguides.

We can determine χ and ϕ accurately by coupling light with at least four different SOP into the waveguides and measure the corresponding output SOPs. ϕ is the rotation angle between input and output vectors in the Poincaré sphere. 2χ is the inclination angle of the eigenmodes' axis. Since the angle ϕ is measured modulo 2π , the Equation 1.85 does not give the absolute value of $\sqrt{\text{LB}^2 + \text{CB}^2}$ because we do not know how many 2π must be added/subtracted to the measured ϕ . On the other hand, LB and χ are related by $\tan 2\chi$ which does not suffer from this problem (i.e. $\tan(2\chi + 2n\pi) = \tan(2\chi)$). Therefore, the measurement of LB is absolute once χ is known. However, the measurement of χ is only accurate for values of $\text{LB} \leq \text{CB}$ where χ departs significantly from zero. Based on this, our measurement strategy is the following:

- For each humidity we measure ϕ and χ .
- For the highest ellipticity ($2\chi \sim \pi/2$), we obtain an accurate (and absolute) value of LB: LB_{\min} . This value gives the minimum $\phi = \phi_{\min} \leq 2\pi$.
- The values of ϕ without the modulo 2π uncertainty are deduced from ϕ_{\min} step by step.
- LB is deduced from Equation 1.85.

From Equation 1.83, the results shown in Figure 6.3 indicate that at $RH < 61\%$ the LB of waveguide is high compared to CB ($LB \gg CB$). By increasing humidity the LB decreases while CB is constant. The fact that the maximum value of 2χ is measured at $RH \approx 65-66\%$ and it decreases after this RH value indicates that the waveguide $LB \approx 0$ around this RH, and it changes its sign (n_{TM} become higher than n_{TE}) before and after $RH \approx 65-66\%$. The direction of the evolution of the slow eigenmode towards the South Pole of the sphere is defined by the chirality of the waveguide: either the waveguide is (+)-enantiomer or (-)-enantiomer as we will see in the following sections. However, the plane in which the eigenmode vector evolves is defined by the LB of the waveguide. In Figure 6.3, the eigenmode vector evolution with humidity is confined the $S_2=0$ plane (red circle in the figure), which means that the main axis of the LB present in the planar waveguide always remains on the S_1 axis, regardless of the humidity.

45° polarization evolution

To measure magnitude of LB in the long range of humidity $11\% \leq RH \leq 75\%$ variation, we launched linearly polarized light at $+45^\circ$ with respect to the plane of the waveguide surface (x -axis) and measured the SOP of the output from the waveguide. Figure 6.4 shows the Poincaré sphere representation of the output SOP (green arrows) in a planar chirowaveguide as the background humidity varies for a $S_2 = 1$ input SOP (45° linear polarization- blue arrow).

At constant humidity ($RH=11\%$), the chirowaveguide modifies the $+45^\circ$ SOP input into a particular output SOP as indicated in Figure 6.4-a. From this measurement we can not determine absolute value of ϕ since its value repeats itself with a 2π period depending on length and birefringence of the waveguide. However, we can use the output SOP at $RH=11\%$ as a reference SOP for subsequent measurements to determine relative phase change $\Delta\phi$ as a function of humidity. From Figure 6.4-a, we can see that $\Delta\phi$ (and thereby SOP of the output light) varies with RH. The variation of the output SOP corresponds to the variation of the LB of the planar waveguide.

The output SOP variation, represented by the green arrows is a rotation in $S_1=0$ plane indicating that eigenmodes of the waveguide are TE/TM. After 5% change in relative humidity (at $RH=16$), the SOP output almost completes a full rotation about the eigenmodes' axis. Therefore, in the next measurement of the output SOP, 2π is added to the measured $\Delta\phi$ that defines the angle between the initial output polarization (SOP at $RH=11$) and the measured output SOP, as shown in Figure 6.4-b. During the measurements, RH is varied with a small step ($\sim 1\%$) to ensure that $\Delta\phi$ varies by less than 2π between two successive measurements. The polarization variation in the range (18% to 22%) is also a rotation about the TE/TM axis meaning the eigenmodes of the chirowaveguide still behave as TE/TM.

With the continuous increase in RH, after 8 rotations on the sphere (16π), at the 9th rotation

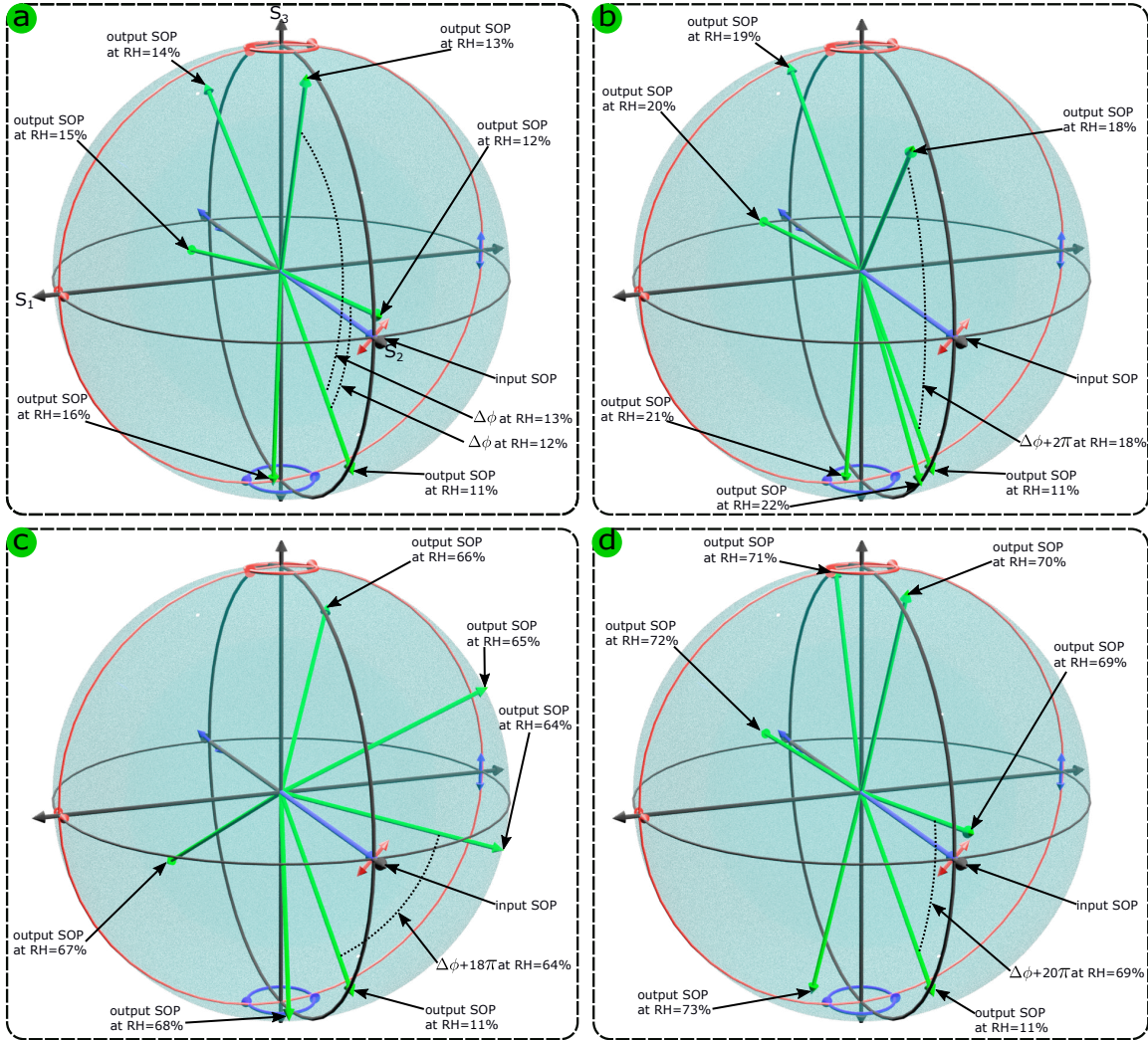


Figure 6.4: Poincaré representation of phase change for a linear polarization a $+45^\circ$ input as a function of humidity. a) RH=11% to 16%. b) RH=18% to 22%. c) RH=64% to 68%. d) RH=69% to 73%.

(18π), a rotation of the SOP output out of the $S_1=0$ plane is observed as shown in Figure 6.4-c. This out of the $S_1=0$ plane rotation is only observed for three values of RH (64-65-66%), and with continued increase in RH, the SOP rotation returns to the $S_1=0$ plane as shown in Figure 6.4-d. The out of the $S_1=0$ plane rotation can be explained by the following: at RH around (64-65-66%) the LB is small enough that the CB becomes a dominant effect and rotates the 45° input about the chiral eigenmodes (left and right-handed circular polarization). The return of the output SOP to $S_1=0$ after the further increase of RH, means that the waveguide goes through zero LB behavior while the LB is positive ($n_{TE} > n_{TM}$) at RH<64%, at RH \approx 64 ($n_{TE} \approx n_{TM}$) and at RH>64% ($n_{TE} < n_{TM}$). This means that the effect of humidity is a decrease in n_{TE} relative to n_{TM} , as it was observed from the eigenmode polarization measurements.

LB versus RH in planar waveguides

From the measurements of $\Delta\phi$ versus RH, with the absolute value $LB_{\min} \approx 2 \times 10^{-6}$ measured at RH=66% from $\chi \approx 39^\circ$, we obtain all the ϕ and LB versus RH. Figure 6.5 shows the variation of LB as a function of RH from 11 to 75%. It can be seen that the LB decreases linearly with RH over this range of measurements. Interestingly, it vanishes at RH \approx 65% meaning that at this value, the planar waveguide behave as a chiral bulk medium. We have also represented in the figure, the calculated LB for the planar waveguide considering that the material RI changes in the range 5×10^{-3} . The RI change is deduced from the Mach-Zehnder results (see Figure 6.1). As we have shown in Figure 6.2-c-d, the theoretically calculated LB is only function of the waveguide geometry (shape) and it is constant over the whole range of humidity variation. We can therefore write the measured LB as the sum of the shape linear birefringence (LB_{shape}), an offset LB at RH=0% (LB_{RH0}) and a humidity dependent LB $-\alpha[\text{RH}]$:

$$LB = LB_{\text{shape}} + LB_{\text{RH0}} - \alpha \cdot \text{RH}(\%) \quad (6.1)$$

From the experimental results $LB_{\text{RH0}} = 7.8 \pm 0.05 \times 10^{-4}$ and $\alpha = 1.2 \pm 0.01 \times 10^{-5}$. At RH=0%, the planar waveguide has $LB_{\text{shape}} + LB_{\text{RH0}}$. LB_{RH0} can be attributed to residual stress in the planar layers of the waveguide. Indeed, during evaporation of the sol-gel solution, tensile stress (positive sign) arises at the layer interfaces parallel to the substrate [120]. In addition, because the temperatures during deposition of the layers differ from those at which the films are used, thermal stress is also often reported due to the difference in thermal expansion coefficient between the waveguide layers and the silicon substrate [119].

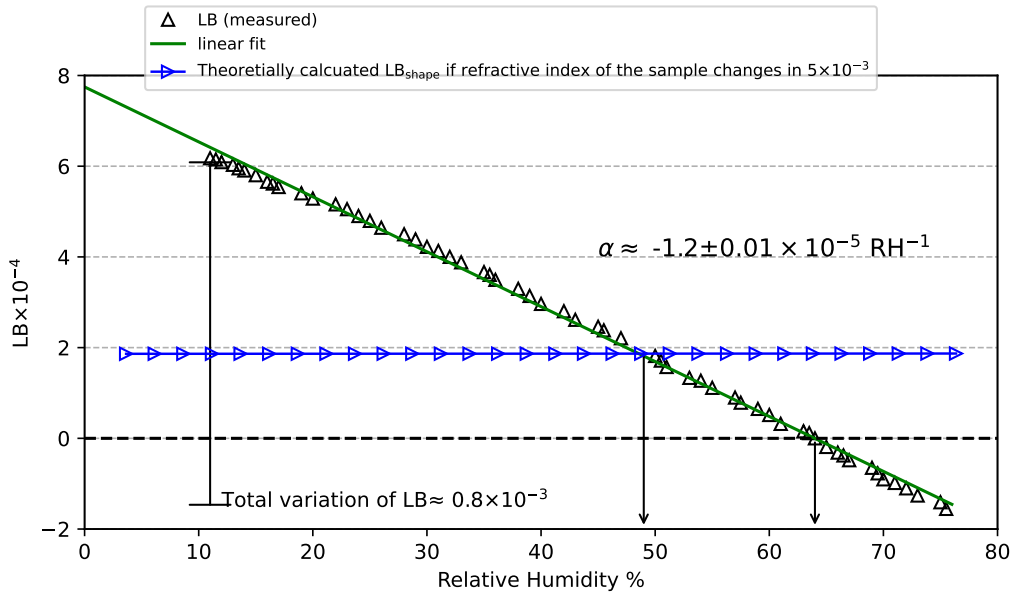


Figure 6.5: LB variation versus relative humidity for a planar ORMOSIL chirowaveguide.

As the relative humidity increases, water diffuses into the films and adsorbs on the pore walls, which causes the films to expand, resulting in a compressive stress in the waveguide layer [121]. We have observed such humidity-induced compressive stress in bad quality layers during our measurements. Figure 6.6 shows optical microscope images of the top surface of a planar waveguide before and after being placed in a high humidity environment. It can be seen that planar layers that have microcracks in their structure crack completely under the humidity induced stress.

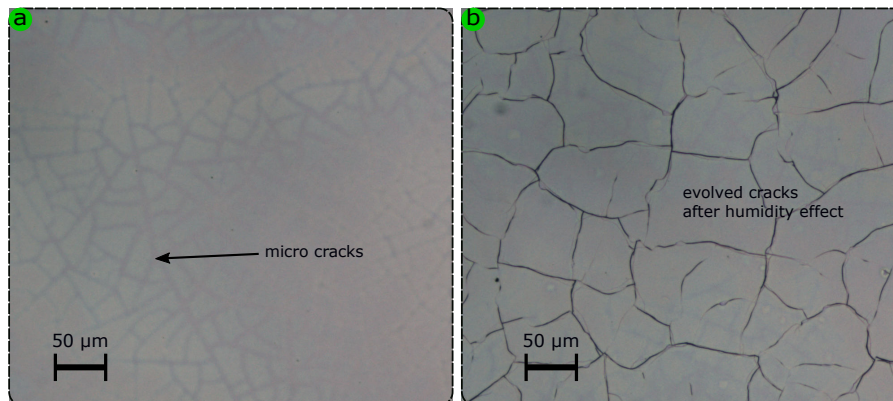


Figure 6.6: Optical microscope image of a planar ORMOSIL waveguides a) before and b) after humidity effect.

Figure 6.5 can be explained as following: The increase in humidity creates a compressive stress that creates a negative LB. At $RH \sim 50\%$, the humidity-induced compressive stress compensates the residual tensile stress in the waveguide layer, which means that the waveguide is stress-free and has only a LB_{shape} . For $RH > 50\%$, the humidity-induced compressive stress begins to compensate LB_{shape} , at $RH \sim 65\%$ the waveguide becomes a zero birefringence waveguide. The continued increase in humidity after $RH \sim 65\%$ introduces LB again but with a $(-)$ sign meaning that n_{TM} is higher than n_{TE} .

Finally, the LB of the studied planar layers can be assigned to three sources:

- (i) A constant LB_{shape} coming from finite planar shape of the waveguide that does not vary with humidity.
- (ii) A constant tensile stress ($LB_{RH0} = 7.8 \pm 0.05 \times 10^{-4}$), coming from the tensile stress induced during deposition of the planar waveguide.
- (iii) A variable compressive stress coming from the humidity diffusion into the material proportional to the humidity.

These results demonstrate the relevance of using chirowaveguides in the measurement of LB. Indeed, it allowed us to obtain absolute value of LB present in the planar waveguide and quantify the different sources of LB arising in the waveguide.

6.3.3 Humidity effect on channel waveguides

In this section, we present the results of polarization measurements obtained on the effect of humidity on three channel waveguides with the same geometry but consisting of material with positive chirality ($CB=+1 \times 10^{-5}$), negative chirality ($CB=-1 \times 10^{-5}$), and racemic ($CB=0$). The channel waveguides are rib waveguides with the following dimensions: width $w = 2.4 \pm 0.1 \mu\text{m}$, height $= 2.1 \pm 0.1 \mu\text{m}$, and slab thickness $d = 0.2 \pm 0.1 \mu\text{m}$.

Eigenmode evolution: Figure 6.7-a shows the evolution of the slow eigenmode as a function of humidity for an (-)-enantiomer channel waveguide plotted on a Poincaré sphere. For measurements made at $RH < 35\%$, the waveguide eigenmode is located on TE axis, which means that the waveguide behaves as a standard linear birefringent waveguide. Similar to what we observed in planar waveguides, we also see that the polarization ellipticity χ of the waveguide eigenmode increases with humidity. From $RH=40\%$, the eigenmode of the channel chirowaveguide are no longer linear but elliptically polarized. The increase in the ellipticity of the eigenmode is continuous with humidity until it becomes maximum around $RH=44\%$. Further increase in humidity leads to a decrease in the ellipticity of the eigenmode until humidity values $RH > 55\%$ where the eigenmode become linear again but this time the slow eigenmode behaves like TM. As we discussed for the planar chirowaveguide, this behavior of the eigenmode with humidity is an indication of the decrease in LB, so that around the humidity value $RH \approx 44\%$, the LB of the waveguide changes sign, meaning that n_{TM} becomes larger than n_{TE} .

For the (+)-enantiomer waveguide, the polarization ellipticity of the eigenmode also increases with humidity but in the opposite direction (i.e. towards the North Pole of the Poincaré sphere), as shown in Figure 6.7-b. This means that the eigenmode changes the polarization ellipticity from TE to a left-handed circular polarization, while for the (-)-enantiomer, it is from TE to a right-handed circular polarization. This is expected for two enantiomers because the effects of two enantiomers on the polarization of light are opposite.

The evolution of the two-enantiomer waveguides eigenmodes as a function of humidity does not resemble to the planar waveguide where humidity only changed the ellipticity of the eigenmode (χ); in the channel waveguides, as shown in Figures 6.7-a and 6.7-b, both the χ and azimuth (ψ) of the eigenmode change with the humidity. This unexpected evolution of the eigenmodes' azimuth cannot be attributed to the chirality of the materials, as it is also observed in the racemic waveguides, as shown in Figures 6.7-c. In the racemic waveguide, the humidity does not change the ellipticity since $CB=0$, the red arrows representing the slow eigenmode are always located on the equator of the Poincaré sphere attesting that they are linearly polarized no matter what humidity is. However, similar to the chiral waveguides, with the increase of humidity, the slow eigenmodes azimuth ψ of the racemic waveguide increases continuously.

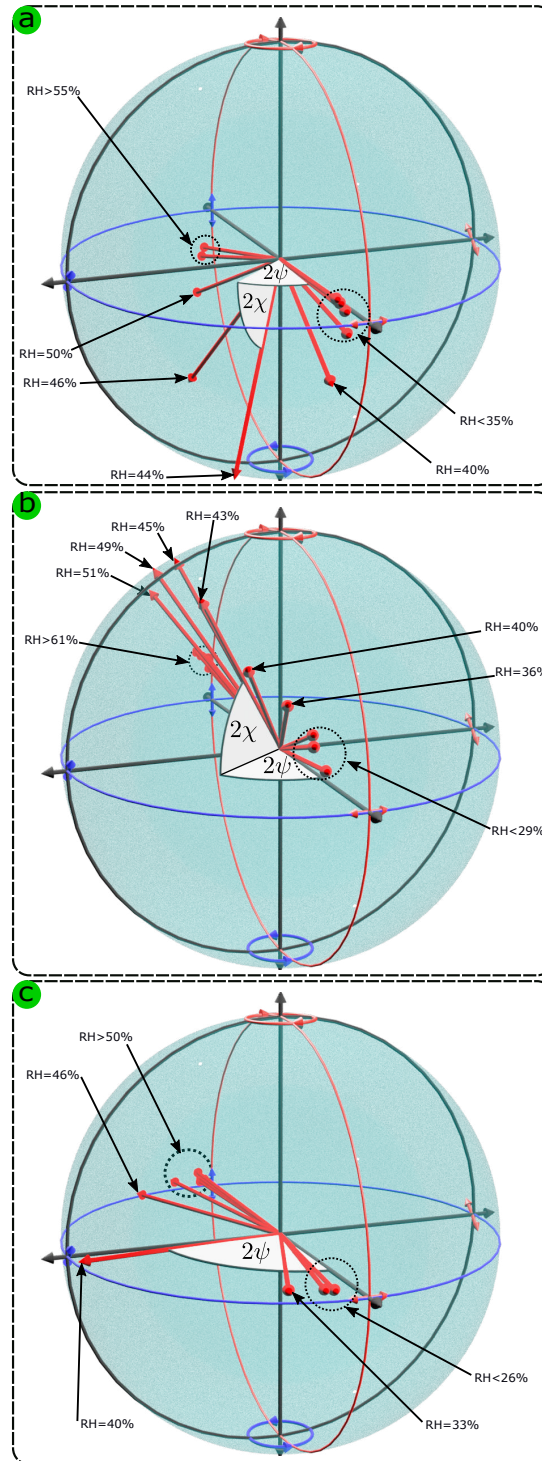


Figure 6.7: Channel chirowaveguides eigenmode evolution as a function of humidity plotted on Poincaré sphere. a) (-)-enantiomer , b) (+)-enantiomer, and c) (+)-racemic waveguide. With the exception of chirality, the other waveguides properties are similar with $w= 2.4\mu\pm 0.1m$, $h= 2.1\mu\pm 0.1m$, $n_g=1.618$, $n_b=1.605$.

45° oriented linear birefringence: The evolution of the eigenmodes can not be explained by only a coupling between chirality and TE/TM oriented LB. Indeed, in this case the eigenmodes only change χ , and in Poincaré sphere the change corresponds to movement of the eigenmode vector in $S_2=0$ plane. The movement out of $S_2=0$ plane comes from an additional LB oriented along the $S_2 = \pm 1$ axis. It is clearly exemplified with the racemic(achiral) case where the eigenmodes gradually rotate in the equatorial plane from the $S_1 = \pm 1$ to the $S_2 = \pm 1$ axis. In this case, without chirality, we can also apply the coupling mode theory with the coupling matrix

$$\begin{bmatrix} \text{LB}_{xy} & \text{LB}_{\pm 45} \\ \text{LB}_{\pm 45} & -\text{LB}_{xy} \end{bmatrix} \quad (6.2)$$

where $\text{LB}_{xy(\pm 45)}$ is the linear birefringence along the xy or ± 45 axis. This coupling results in a new linear birefringence (LB') having main axis that is oriented at an angle ψ

$$\text{LB}' = 2\sqrt{\text{LB}_{xy}^2 + \text{LB}_{\pm 45}^2}, \quad \tan 2\psi = \frac{\text{LB}_{\pm 45}}{\text{LB}_{xy}} \quad (6.3)$$

The evolution of the eigenmode azimuth resulting of the coupling of the two birefringences is plotted in Fig. 6.8 versus the ratio $\text{LB}_{\pm 45}/\text{LB}_{xy}$. The principal axis orientation moves progressively from 0 for $\text{LB}_{xy} \gg \text{LB}_{\pm 45}$ to 45° for $\text{LB}_{xy} \ll \text{LB}_{\pm 45}$. 40° is obtained for $\text{LB}_{\pm 45} = 6 \times \text{LB}_{xy}$. For the chirowaveguides shown in Figure 6.9-a and b, the evolution is thus a combination of two rotations on the Poincaré sphere: i) the first one coming from the coupling of CB and LB as expected by Equation 1.83 and ii) the second, coming from the coupling of LB_{xy} and $\text{LB}_{\pm 45}$ according to Equation 6.3.

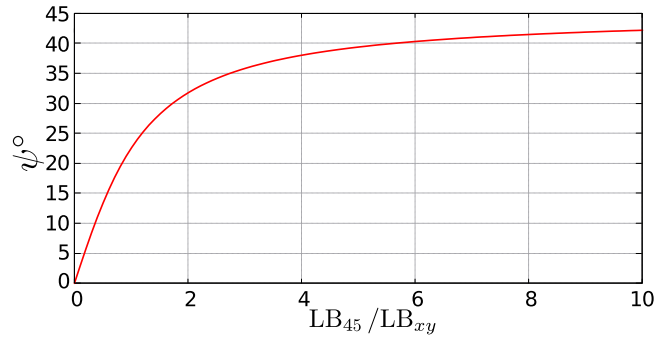


Figure 6.8: Calculated LB azimuth for a system mixing LB oriented at 0 and 45°.

LB versus RH in channel: As for the planar waveguides, we measured the eigenmodes and the rotation angle ϕ for different humidity. Again the absolute value of ϕ is deduced from the humidity where the eigenmodes are close to the North/South Pole. Then, from this value the phase retardation for humidity variation are recalculated. Finally, LB is deduced from $\phi(\text{RH})$. The LB that we describe here, is the combination of the two LB, one with principal axes at

$x=0$, the other at $x=45^\circ$ (LB_{xy} and $LB_{\pm 45}$). Figure 6.9-a and b show the variation of the LB and the LB azimuth as a function of humidity for three samples of different chirality. It can be seen that at low measured LB values, the azimuth ψ is $\sim 45^\circ$. It means that a low LB that is oriented at $\pm 45^\circ$ is present in the channels. This LB can only be observed when $LB_{xy} \ll LB_{\pm 45}$. We have calculated the magnitude of the additional linear birefringence for the three waveguides and found that $LB_{\pm 45} \sim 1 \times 10^{-6}$. As we discussed in the chapter 5, the presence of $LB_{\pm 45}$ can be attributed to the small departure from the ideal rectangular symmetrical shape of the channels [106].

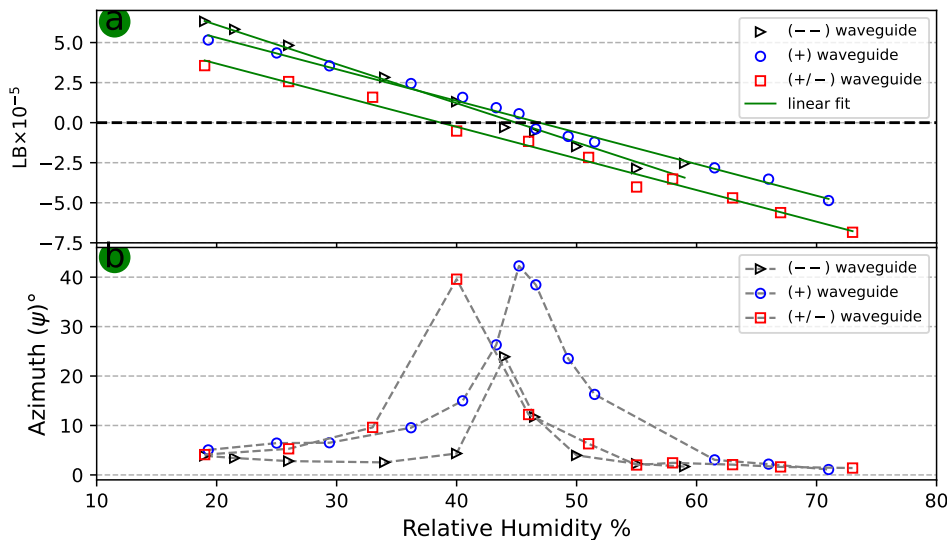


Figure 6.9: Channel waveguides a) LB variation and b) Eigenmodes polarization azimuth variation as a function of humidity for three waveguides with different chirality (- enantiomer, + enantiomer, and +/- racemic). Channels size $w = 2.4 \pm 0.1$, $h = 2.1 \pm 1$, $l = 0.2 \pm 0.1 \mu m$.

Similar to planar waveguides, in the channel waveguides, as shown in Figure 6.9-a, LB decreases linearly when humidity increases. Again, we can write

$$LB = LB_{\text{shape}} + LB_{\text{RH0}} - \alpha \text{RH}(\%) \quad (6.4)$$

We have shown that for the planar waveguide, the calculated LB_{shape} varies less than 1×10^{-5} for a material RI change of 5×10^{-3} . Therefore, the RH dependent variation (αRH) can be attributed to humidity induced stress. The tensile stress LB_{RH0} and the humidity dependent compressive stress factor α for the channel waveguides are listed in Table 6.1. LB_{RH0} and α are both approximately one order of magnitude lower in rib channels compared to planar waveguide. This shows that stress is released in the channel compare to non-structured planar layers as already reported [122]. Moreover, during the fabrication of the channel waveguides,

Table 6.1: Humidity LB parameters for channel waveguides of different chirality.

channel type	$LB_{\text{shape}} (\times 10^{-5})$	$LB_{\text{RH0}} (\times 10^{-5})$	$\alpha (\times 10^{-6})$
-	-17	11 ± 0.4	-2.4 ± 0.1
+	-17	7.7 ± 0.4	-2 ± 0.1
+/-	-17	9.2 ± 0.4	-2 ± 0.1

we did not observe any crack formation, whereas in the planar waveguides, cracks were always present. This also verifies the reduction of stress effects in micro-structured waveguides. Indeed, cracks in a waveguide layer are an indication of residual stresses.

Humidity effect on different size channel waveguides

We also studied the effect of humidity on ORMOSIL channel waveguides of different sizes on the same sample. Figure 6.10-a shows LB and eigenmodes azimuth variation with humidity for four different width w channel waveguides on the same sample having same channel height $h = 2.1 \pm 0.1 \mu\text{m}$ and rib thickness $d = 0.2 \pm 0.1 \mu\text{m}$. It can be seen that the three width 3.3, 3 and $2.4 \mu\text{m}$ present the same RH behavior that is a linear variation of LB and an azimuth increase when $LB \sim 0$. The fit parameters of the linear dependence (Equation 6.4) are listed in Table 6.2. The residual tensile stress at $\text{RH}=0$ (LB_{RH0}), is at least three times lower than the one measured on planar waveguide. However, LB_{RH0} increases with the rib width indicating a reduction in the residual stress with thinner structures.

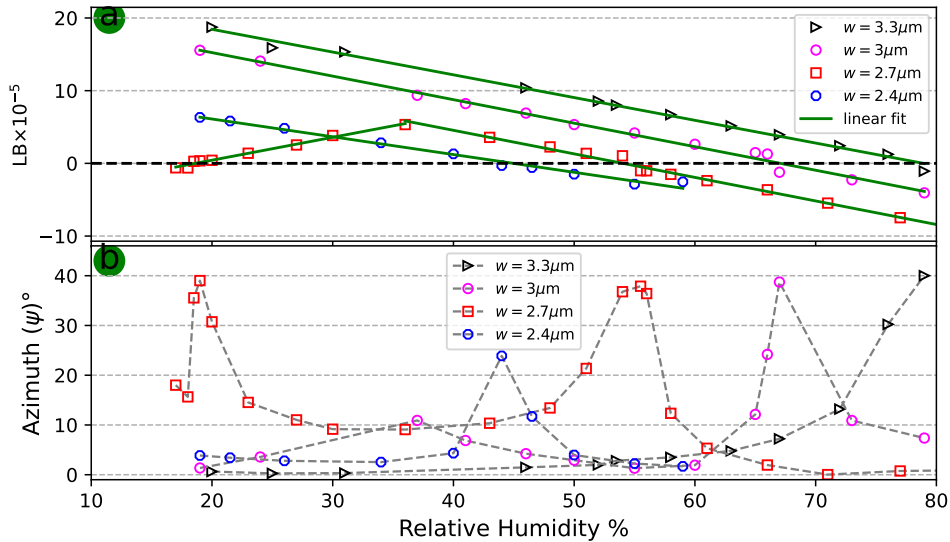


Figure 6.10: Channel waveguides a) LB variation and b) Eigenmodes polarization azimuth variation as a function of humidity for four waveguides with different width w but same height $h = 2.1 \pm 0.1 \mu\text{m}$, and rib thickness $d = 0.2 \pm 0.1 \mu\text{m}$.

Table 6.2: Channel waveguide of different width.

channel width $w[\mu\text{m}]$	$\text{LB}_{\text{shape}}(\times 10^{-5})$	$\text{LB}_{\text{RH0}}(\times 10^{-5})$	$\alpha [\text{RH}^{-1}](\times 10^{-6})$
3.3	+0.8	24 ± 0.4	-3.1 ± 0.1
3	-3.1	21.5 ± 0.4	-3.2 ± 0.1
2.7	-8.9	17.5 ± 0.4	-3.2 ± 0.1
2.4	-17	11 ± 0.4	-2.4 ± 0.1

For the channel waveguide with width $w = 2.7\mu\text{m}$, unexpectedly, the waveguide has a very low LB at RH=19%, and it increases with humidity up to RH=36% with a ratio of ($\alpha \approx 3.1 \times 10^{-6}\text{RH}^{-1}$). After RH=36%, LB starts to decrease with the same α value. This unexpected behaviour is seen for four channel waveguides with width $w = 2.7\mu\text{m}$ meaning this is not an artifact. To date, we have no explanation for this humidity-dependent behavior of some channel waveguides.

6.4 Dynamic birefringence measurement

Although the Mach-Zehnder measurements gave us a general idea of the dynamic effect of humidity on ORMOSIL waveguides, the measurements could only be performed on planar waveguides. To measure the dynamic effect of humidity on the channel waveguides, we used our Stokes polarimetry which has the ability to measure SOP of light instantaneously (see 4.3.7).

The dynamic effect of humidity on the ORMOSIL channel waveguides is characterized by launching left-handed circular polarization (LHCP) into the channels and measuring SOP of the output light. Figure 6.11-a shows the evolution of the output light SOP as the sample background humidity changes from dry air (RH=11%) to humid air (RH=75%) and then the cycle is reversed (from humid to dry air) for a channel waveguide of $w = 4.2 \pm 0.1\mu\text{m}$. When RH=11%, the channel waveguide modifies the LHCP input into a particular output SOP. With the change of humidity, the output SOP modifies continuously as a result of change in LB in the waveguide. The evolution of the output SOP with humidity is confined in $S_1 = 0$ plane, it means that the output SOP trajectory is a circular rotation about the $S_1 = \pm 1$ axis indicating that the waveguide eigenmodes are always TE/TM whatever the humidity. In other words, humidity changes LB of the waveguide but for the tested humidity range the eigenmodes stay TE/TM because of the high intrinsic LB of the waveguide. In each cycle of increasing and decreasing humidity, the output SOP rotates twice about the TE/TM axis but always remains in the $S_1 = 0$ plane.

The dynamic effect of humidity on channel waveguides which have low intrinsic LB is much complicated as shown in Figure 6.11-b for a $2.7 \pm 0.1\mu\text{m}$ width channel waveguide. The fact that the trajectory is not confined to a single plane shows that the output SOP comes from a

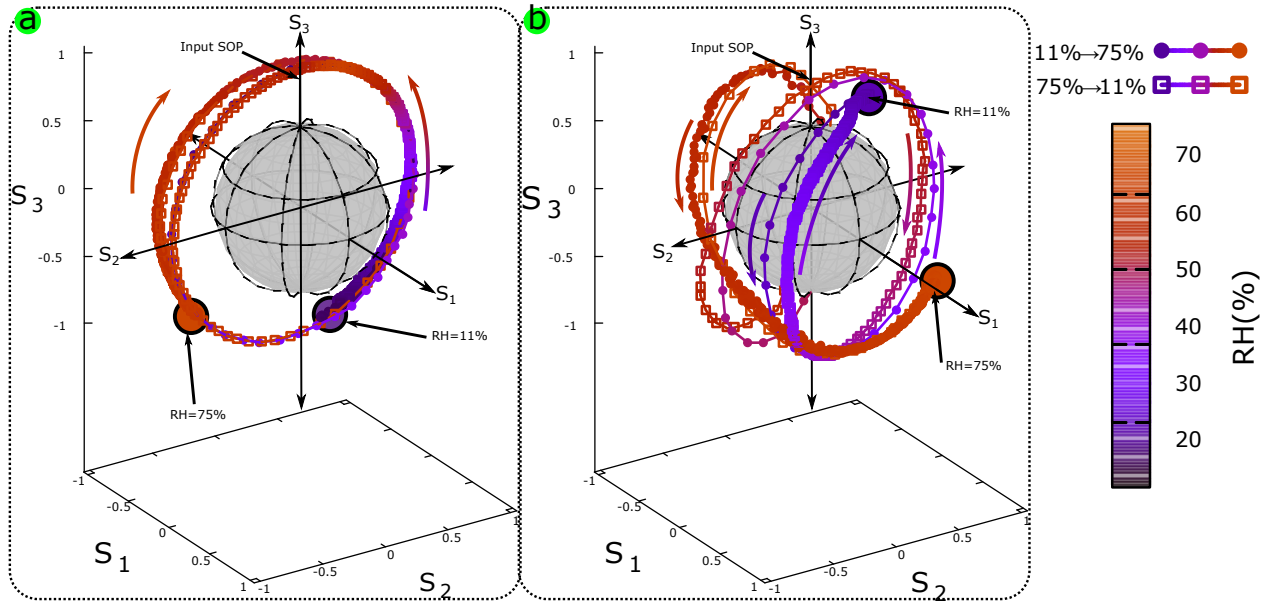


Figure 6.11: Poincaré sphere representation of the dynamic phase change for a left-hand circularly polarized input in an ORMOSIL channel waveguide as a function of humidity, from dry air ($RH=11\%$) to humid air ($RH=75\%$) and vice versa. Channel size properties are $h = 2.1 \pm 0.1 \mu\text{m}$, rib slab thickness $= 0.2 \pm 0.1 \mu\text{m}$, and a) $w = 4.2 \pm 0.1 \mu\text{m}$. b) $w = 2.7 \pm 0.1 \mu\text{m}$.

double movement: rotation about the eigenmodes axis and evolution of the eigenmodes' axis with humidity. Therefore, the effect of humidity on the LB leads to a modification of both the phase difference and the waveguide eigenmodes location in the Poincaré sphere as measured in the statics experiments. In addition, we can see that the trajectory when the background air changes from dry to humid is not the same as when the humid air changes to dry. The difference in trajectories is an indication of hysteresis in the waveguide which can be related to the difference in diffusion of water into and out of the waveguides.

From the results, we extracted the magnitude of LB variation (ΔLB) as a function of humidity. We assumed that the movement of the output SOP is mainly coming from the ϕ variation which is not completely exact for the double axis+ ϕ movement in the case of the small channel width. Results are shown in Figure 6.12 together with the dynamic response of the DHT11 humidity sensor. We can see that the LB in both channel waveguides changes and becomes stable as fast as the DHT11 humidity sensor. As we have seen in the Poincaré sphere representation, the effect of humidity on the channel waveguides is reversible.

The results presented in this section are preliminary results and work is ongoing to understand them. What we have deduced from these results so far, is that the effect of humidity on waveguides is very complicated.

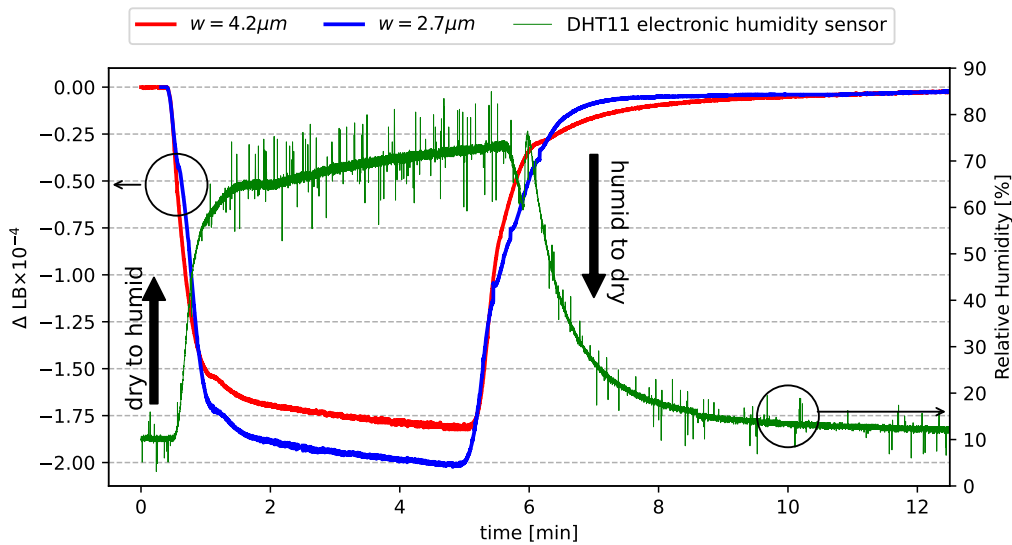


Figure 6.12: Dynamic evolution of channel chiro-waveguides LB as a function of humidity from dry air with ($RH=11\%$) to humid air ($RH=75\%$) and back cycle.

6.5 Conclusion

In this chapter, we have discussed in detail the humidity effect on planar and channel ORMOSIL waveguides.

The effect of humidity in planar waveguides was studied using the Mach-Zehnder interferometer and polarimetry measurements. Using the Mach-Zehnder interferometer, we observed that in a planar layer waveguide, the overall effective refractive indices n_{TE} and n_{TM} of the waveguides decreases by $\sim -5 \times 10^{-3}$ if the relative humidity changes from $RH=11\%$ to $RH=75\%$ at a temperature of $24 \pm 4^\circ\text{C}$. The theoretical calculation has shown that this variation can be attributed to material refractive index change about -5×10^{-3} between dry and wet environment. This change corresponds to water diffusion into the ORMOSIL which is known to be a porous material. The use of PEG which is very hydrophilic can also increase the affinity of our material with water [118].

LB ($n_{TE} - n_{TM}$) evolution versus the humidity put into evidence four sources of LB:

1. The shape birefringence, independent of the humidity.
2. A tensile birefringence LB_{RH0} induced during waveguide fabrication (sol-gel film contraction and substrate/ORMOSIL thermal expansion coefficient differences), independent of the humidity, its eigenmodes axis oriented as TE/TM axis. This birefringence is lower for the channel ($LB_{RH0} \sim 2 \times 10^{-4}$) compared to the planar waveguides ($LB_{RH0} \sim 8 \times 10^{-4}$).
3. A compressive birefringence, increasing with the humidity coming from the material

swelling. Its eigenmodes axis oriented as TE/TM axis but its magnitude is opposite to the tensile birefringence. This birefringence is also much smaller for the channels.

4. A very small birefringence ($\sim 1 \times 10^{-6}$) in which its eigenmodes axis oriented at $\pm 45^\circ$ with respect to the TE/TM axis. It was only observed in rib waveguides when the shape, tensile and compressive birefringences compensate each others. This LB comes from a deviation of the shape from the ideal rectangular symmetric shape of the channels.

In the last section of the chapter, we have presented some preliminary results on the dynamic effect of humidity on channel waveguides. We have observed complicate trajectories of the output SOP in the Poincaré sphere. From the results we could deduce that the humidity effect response time on the channel is in seconds which is as fast DHT11 electronic humidity sensor.

General Conclusion and Perspectives

Summary and accomplishments

IN this manuscript, we reported on the realization of integrated photonic waveguides having eigenmodes polarization other than the well known TE/TM polarization modes. The work consisted of theoretical study, design, fabrication and optical characterization of channel chirowaveguides.

The theoretical study of light propagation in optical waveguides was the first step of this work. We used the intuitive coupling mode theory to describe light polarization properties in chirowaveguides. The coupled mode theory enabled us to describe chirowaveguides by a simple coupling matrix from which we deduced the equation for the polarization ellipticity of the chirowaveguides eigenmodes. The results of the coupled mode theory have shown that chirowaveguides are not linear or circular birefringent systems, but elliptical birefringent systems with elliptically polarized eigenmodes whose ellipticity is proportional to the ratio between the circular and linear birefringence (CB/LB). Based on this description of chirowaveguides, for a given CB ($\sim 1 \times 10^{-5}$) related to the chiral material, we used numerical simulations to design channel waveguides with $LB \leq CB$ to obtain chirowaveguides with elliptically polarized eigenmodes. The numerical simulations showed that rib, ridge, and diffuse channel chirowaveguides can be fabricated with polarization eigenmodes varying from linear to quasi-circular, by varying the opto-geometrical parameters of the waveguides, such as channel width, height, and refractive index. A small refractive index difference between the guiding layer and the buffer layer has proven to be a very important parameter for obtaining low LB channel waveguides with a better fabrication tolerance.

In the fabrication part of this work, two previously developed chiral materials were used to fabricate channel waveguides. The two chiral materials were pure chiral organic films deposited by the pulsed laser deposition (PLD) technique and organically modified silica films (ORMOSIL) prepared by the sol-gel method and deposited by dip coating. Then, for the

fabrication of waveguides from these materials, we examined three different microfabrication methods, one for the pure chiral organic material and two methods for the ORMOSIL material. By fabricating SU-8 photoresist micropatterns on silicon wafers and depositing the PLD material on the patterns, we were able to fabricate channel waveguides made of a pure chiral material. However, the difficulties of cleavage in order to couple light into the waveguides as well as the degradation of the quality of the material with time prevented us to study the PLD waveguides.

For the ORMOSIL material, we investigated two lithography methods to fabricate the channels; reactive ion etching (RIE) and imprint lithography. The RIE method did not give us good results in terms of channel waveguides fabrication because of two limitations: i) the fabricated waveguides were rough, and ii) the majority of the ORMOSIL layers were cracking during the process. However, PDMS-based imprint lithography allowed us to fabricate high-quality rib channel waveguides. By fabricating silicon master molds with designed topological patterns, then replicating the PDMS molds and imprinting them on ORMOSIL gel layers, we were able to fabricate channel waveguides of different geometries. Our research on different microfabrication methods for waveguide fabrication resulted in a simple, fast, and cost-effective method that is the result of the synergistic combination of sol-gel process and PDMS-based imprint lithography.

In the optical characterization part, we first developed an optical setup to characterize the optical quality (guiding and optical losses) of the chirowaveguides. For this, we have developed an end-fire coupler for coupling and collecting light that allows light to be guided in any waveguide structure if the waveguides have flat, clean facets. Using the end-fire coupler, we were able to identify the shape, size, and order of modes in optical waveguides by comparing the intensity distribution of experimentally measured with theoretically calculated guided modes. Our method of waveguide loss measurement was based on the measurement of the intensity of the light scattered by the waveguide surface. It could only be used if the source of the scattered light in the waveguides is homogeneous and also with the limit of detection of 1 dB/cm.

To measure the polarization properties of optical waveguides, we have developed laser Stokes polarimetry setups. The polarization preparation part of the polarimeter can be used to obtain light with any polarization state from an unknown polarization state with an accuracy of $\pm 0.02^\circ$ in controlling the phase of the input light beam. For the polarization measurement, we developed two optical systems. The first one was composed of a rotating quarter-wave plate, a linear polarizer and a CCD camera which can be used to measure the Stokes parameters with an accuracy of $\pm 3\%$ in 1 minute and also to identify the polarization mapping of a light beam. The second polarization measurement consisted of non-polarizing beam splitters, Wollaston polarizing beam splitters, and photodetectors that can be used to instantly measure

the normalized Stokes parameters with $\pm 6\%$ accuracy. Using the laser Stokes polarimeter, we were able to measure phase retardation and eigenmodes axis of the birefringent systems with an accuracy of $\pm 1\%$. We have also developed a Mach-Zehnder interferometer that could be used to measure the in-plane and out-of-plane refractive index variation in planar optical waveguides with a detection limit of $\sim 5 \times 10^{-6}$.

Our research efforts to theoretically study chirowaveguides, experimentally find adapted channel fabrication method, and build characterization setups have resulted in the achievement of chirowaveguides with elliptically polarized eigenmodes, including waveguides with conventional TE/TM eigenmodes to quasi-circular polarized eigenmodes. These waveguides were obtained by using sol-gel process and the imprint technique to make channel chirowaveguides with different sizes and consequently modulate ellipticity of the eigenmodes from linear to quasi-circular. We have theoretically shown that the chirowaveguides can be used for chiral sensing by measuring optical rotation induced by a chiral solution in contact with surface of the waveguides.

As the sol-gel derived ORMOSIL waveguides that we fabricated were sensitive to ambient humidity, we studied the dynamic and static effects of humidity on the waveguides. Taking advantage of our experimental characterization facilities (Mach-Zehnder interferometer and laser polarimetry), we were able to accurately measure the effect of humidity on the refractive indices and polarization properties of the waveguides. By studying planar and channel waveguides, we have quantified different sources of birefringence in these two types of waveguides. The sources of LB in planar waveguides are identified to be i) a constant shape linear birefringence ii) a constant tensile residual stress induced during deposition of the waveguide layers iii) a humidity dependent compressive stress induced by adsorption of water molecules into material pores. In the channel waveguides, in addition to these three sources, a constant low LB $\sim 1 \times 10^{-6}$ was measured that was shown to have eigenmodes with principal axis located at $\pm 45^\circ$ relative to TE/TM axis.

Future perspectives

In the scope of the thesis, various research questions and ideas were raised but not addressed due to time constraints. Three future works are briefly described hereafter.

6.5.1 Chiral sensing using chirowaveguides

In chapter 5, we have theoretically shown that the channel chirowaveguides developed during this thesis have the potential to be used for chiral sensing. Therefore, the closest future perspective is to use the waveguide in an experimental study to detect chiral molecules in

solutions.

As the polarization behaviour of the channel chirowaveguides with quasi-circular eigenmodes is similar to bulk chiral medium, when a linearly polarized light propagates in the waveguides it undergoes an optical rotation (OR) that depends on the light wavelength (λ), waveguide propagation length (l), and circular birefringence (CB) of the waveguide

$$\text{OR} = \frac{\pi}{\lambda} \cdot l \cdot \text{CB} \quad (6.5)$$

where CB is defined by the interaction of the guided light and chirality of the waveguide.

In Figure 6.13, we schematized the experimental setup for using the chirowaveguides for sensing chiral solutions. It consists in bringing the chirowaveguides in contact with the chiral solutions to be sensed. As it is shown in the figure the waveguides are prepared by fixing four thin glass slides to the four sides of the waveguides samples such that the ensemble can be used as a solution container. The thin glass slides are connected to the input and output faces of the waveguides to avoid noise signal that can come from interaction of light with the chiral solution outside the waveguide. When the solution is added to the sample, as the small evanescent tail of the guided mode field is outside the waveguide, it interacts with the chiral solution and induces additional ΔOR to output light as indicated in the figure. It is therefore sufficient to develop an instrumental strategy to extract the ΔOR coming from the chirality of the solution from the OR induced by the chirality of the waveguide.

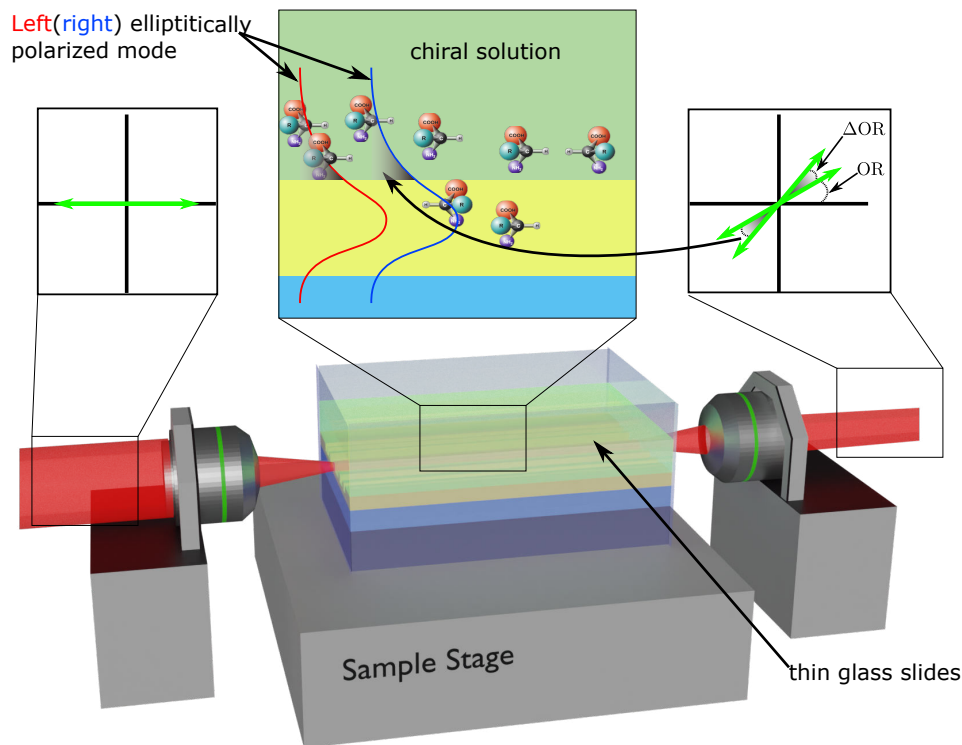


Figure 6.13: Optical experimental to use chirowaveguide for chiral sensing.

One limitation of the waveguides we developed in this study is that the evanescent part of guided light is found to be only 0.1%. However, it is possible for chiral molecules of the solution to diffuse into the material pores to enhance the ΔOR signal. In the case if ΔOR signal is very small and can not be measured, two solutions can be performed to enhance the signal

- (i) Design of optical waveguides having high evanescent field using numerical simulations.
- (ii) Design of spiral channel waveguides to obtain long propagation length.

6.5.2 Controlling LB of the waveguides by thermo-optics effects

In chapter 6, we have shown that the LB of the waveguides can be controlled by controlling background humidity. However, humidity is not an efficient parameter to control for experimental applications. Furthermore, if the waveguides are used for sensing application in water (or any solution) then the humidity parameter can not be used anymore. Another method to control LB in polymer layers on silicon substrates is using thermo-optics effects [123]. In Figure 6.14, we have schematized the experimental setup for LB control by thermo-optics effects. It consists of fixing the waveguides on a thermal heater panel from which temperature of the waveguides can be controlled. As the waveguides are made of ORMOSIL layers on silicon substrate and the thermal expansion coefficients of these two materials are different, a temperature-dependent stress will be induced if the waveguides are heated, i.e. thermal stress. Therefore, the thermal stress induced LB can be used to compensated intrinsic linear birefringence of the waveguides and obtain very low LB waveguides.

Thermo-optics effect study is already used to control LB in benzocyclobutene polymer channel waveguides and showed to be efficient to obtain low LB channel waveguides by changing the temperature of the waveguides between 20-90°C [122, 124].

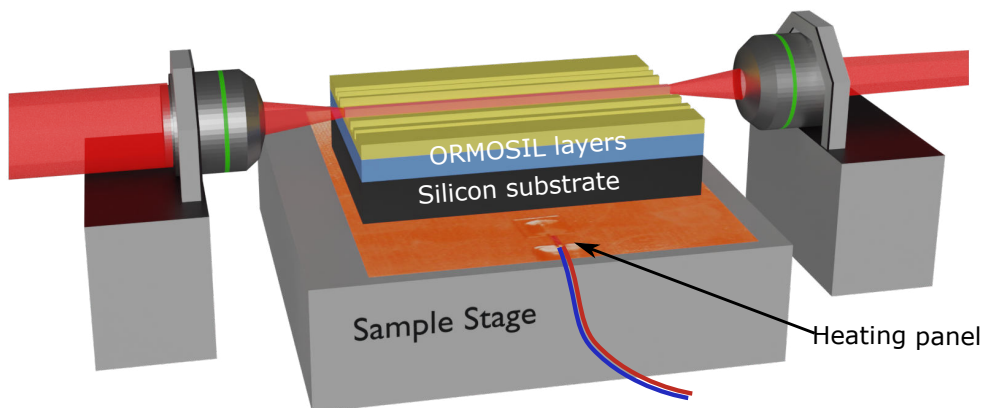


Figure 6.14: Experimental setup to control LB in the chiro-waveguides by thermo-optics effects.

6.5.3 Buried channel waveguides TE-TM mode convertors

Although the main objective of this thesis was to realize chirowaveguides with circularly polarized eigenmodes for sensing applications, the chirowaveguides can be used for other applications. One important application is using the chirowaveguides as polarization mode converters such as TE-TM mode converters. Muto et al. have experimentally demonstrated that TE-TM mode converters can be obtained by using planar chirowaveguides made of chiral polymers [29]. The working principle of a chirowaveguide TE-TM mode converter is simple, it is based on optical rotation of chiral materials. In other words, if the chirowaveguides with circularly polarized eigenmodes are obtained they can be used to rotate plane of polarization of TE mode by 90° and obtain TM mode or vice versa.

As TE/TM mode converters does not need cover free waveguides, the chirowaveguides can be buried by simply depositing an ORMOSIL layer with same refractive as the buffer that is smaller than the guiding refractive index. For TE/TM mode converters, such buried waveguides have two advantages over our current chirowaveguides:

- (i) Since the waveguides are covered with a layer, the TE/TM mode converter devices made of this buried waveguides are more robust and protected from undesired surrounding condition effect such as humidity effect.
- (ii) Numerical simulation results show that the fabrication tolerance in controlling size of waveguides is much better for buried waveguides compared to waveguides that have air as cover layer. Figure 6.15 shows the change of LB in buried and air cover rib waveguides as a function of rib waveguides width w if the remaining opto-geometric parameters are similar and constant (i.e. rib height $h = 2.1\mu\text{m}$, rib slab thickness $d = 0.2\mu\text{m}$, $n_c=1$, $n_g=1.625$, and $n_b=1.61$). It is seen that tolerance in waveguides width (Δw) to fabricate a rib waveguide with $\text{LB} \leq 1 \times 10^{-5}$ is $\Delta w \approx 150\text{nm}$ for air cover waveguides while it highly increase to $\Delta w \approx 980\text{nm}$ in the buried waveguide. Such high fabrication tolerance is due to the fact that the electromagnetic structure is more symmetric in the buried waveguide.

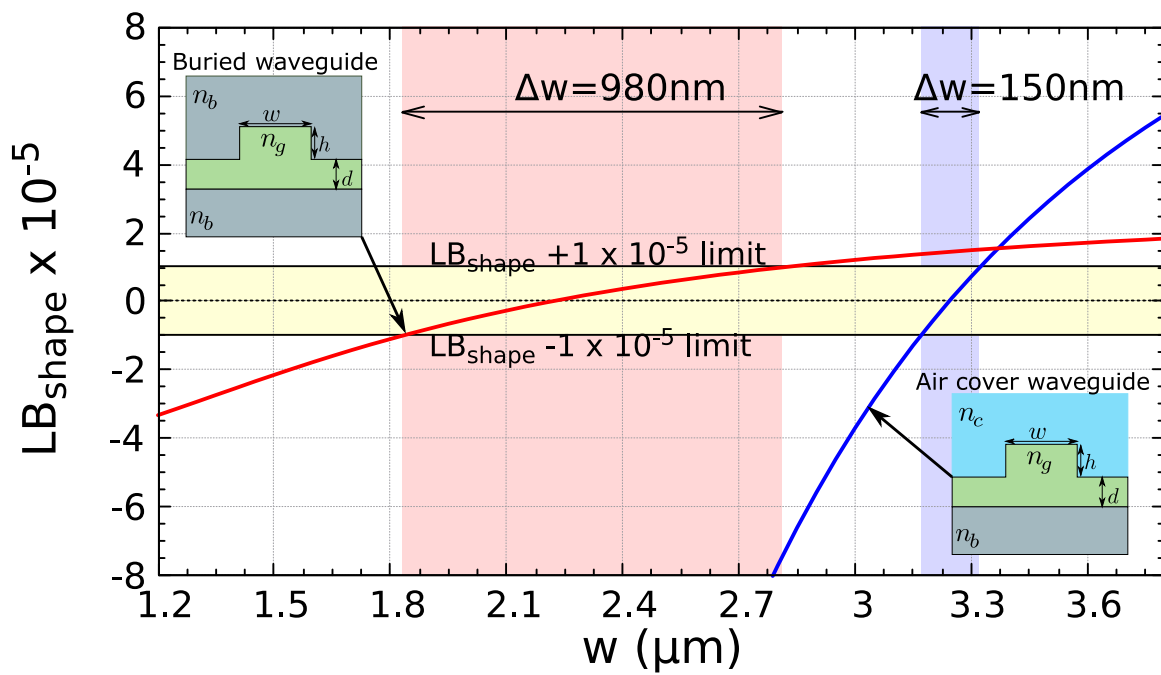


Figure 6.15: Computed shape birefringence LB_{shape} ($n_{TE00} - n_{TM00}$) for buried and air cover rib waveguides as function of w but constant $d = 0.2 \mu m$ $h = 2.1 \mu m$, $n_c = 1$, $n_g = 1.625$, and $n_b = 1.61$.

Appendices

Appendix A

Appendix

After using the setup to measure a known SOP of a beam, we found that the setup is not measuring the exact value of Stokes parameters. In an ideal case, the non polarizing beam splitters (NBS-1 and NBS-2) should not affect the state of polarization (SOP) of the light neither in the transmission nor in reflection. We found the effect of each beam splitters (non-polarizing and polarizing) by measuring the SOP before and after (transmission or reflection) and from that we calculated Mueller matrices related to each beam splitter. The input polarized beam (S_0, S_1, S_2 , and S_3) interacts with each beam splitter and the output beam is characterized by a new set of Stokes parameters S'_0, S'_1, S'_2, S'_3 . The linear relationship between input Stokes parameters and output Stokes parameters gives rise to a 4x4 matrix that is called Mueller matrix [39]:

$$\begin{bmatrix} S'_0 \\ S'_1 \\ S'_2 \\ S'_3 \end{bmatrix} = \begin{bmatrix} m_{00} & m_{01} & m_{02} & m_{03} \\ m_{10} & m_{11} & m_{12} & m_{13} \\ m_{20} & m_{21} & m_{22} & m_{23} \\ m_{30} & m_{31} & m_{32} & m_{33} \end{bmatrix} \begin{bmatrix} S_0 \\ S_1 \\ S_2 \\ S_3 \end{bmatrix} \quad (\text{A.1})$$

The Mueller matrix for the double transmitted light beam (M1) is give by:

$$\begin{bmatrix} S'_0 \\ S'_1 \\ S'_2 \\ S'_3 \end{bmatrix} = \begin{bmatrix} 1. & 0.043 & 0.021 & 0.007 \\ 0.02 & 0.975 & -0.02 & 0.004 \\ -0.01 & 0.034 & 0.945 & 0.305 \\ 0.011 & -0.015 & -0.3 & 0.958 \end{bmatrix} \begin{bmatrix} S_0 \\ S_1 \\ S_2 \\ S_3 \end{bmatrix} \quad (\text{A.2})$$

The Mueller matrix for the transmitted then reflected light beam (M2) is give by:

$$\begin{bmatrix} S'_0 \\ S'_1 \\ S'_2 \\ S'_3 \end{bmatrix} = \begin{bmatrix} 1. & 0.116 & -0.012 & 0.003 \\ 0.091 & 0.972 & 0.07 & 0.013 \\ 0.017 & 0.056 & -0.963 & 0.028 \\ -0.005 & 0.012 & 0.016 & -0.988 \end{bmatrix} \begin{bmatrix} S_0 \\ S_1 \\ S_2 \\ S_3 \end{bmatrix} \quad (\text{A.3})$$

The Mueller matrix for the first reflected light beam (M3) is give by:

$$\begin{bmatrix} S'_0 \\ S'_1 \\ S'_2 \\ S'_3 \end{bmatrix} = \begin{bmatrix} 1. & -0.058 & -0.018 & 0.005 \\ -0.079 & 0.977 & 0.069 & -0.01 \\ 0.012 & 0.057 & -0.89 & 0.4 \\ 0. & 0.014 & 0.404 & -0.907 \end{bmatrix} \begin{bmatrix} S_0 \\ S_1 \\ S_2 \\ S_3 \end{bmatrix} \quad (\text{A.4})$$

A.1 Measurement of Muller matrix of an optical element

Because Mueller matrix elements are practically measurable quantities, they can be practically determined from known polarization states of light. We can quantitatively determine the Mueller matrix of a medium by measuring the Stokes parameters of an input light and the corresponding Stokes parameters of the output. Here we use the six basic states of polarization of Stokes parameters ($\leftrightarrow, \updownarrow, \nearrow, \nwarrow, \circlearrowleft, \text{ and } \circlearrowright$) as input polarization states which will simplify the calculations

$$S_{output} = M \cdot S_{input}$$

for input \leftrightarrow :

$$S_{output} = \begin{bmatrix} m_{11} & m_{12} & m_{13} & m_{14} \\ m_{21} & m_{22} & m_{23} & m_{24} \\ m_{31} & m_{32} & m_{33} & m_{34} \\ m_{41} & m_{42} & m_{43} & m_{44} \end{bmatrix} \begin{bmatrix} 1 \\ 1 \\ 0 \\ 0 \end{bmatrix} = \begin{bmatrix} m_{11} + m_{12} \\ m_{21} + m_{22} \\ m_{31} + m_{32} \\ m_{41} + m_{42} \end{bmatrix} \quad (\text{A.5})$$

for input \updownarrow :

$$S_{output} = \begin{bmatrix} m_{11} & m_{12} & m_{13} & m_{14} \\ m_{21} & m_{22} & m_{23} & m_{24} \\ m_{31} & m_{32} & m_{33} & m_{34} \\ m_{41} & m_{42} & m_{43} & m_{44} \end{bmatrix} \begin{bmatrix} 1 \\ -1 \\ 0 \\ 0 \end{bmatrix} = \begin{bmatrix} m_{11} - m_{12} \\ m_{21} - m_{22} \\ m_{31} - m_{32} \\ m_{41} - m_{42} \end{bmatrix}$$

for input \nearrow :

$$S_{output} = \begin{bmatrix} m_{11} & m_{12} & m_{13} & m_{14} \\ m_{21} & m_{22} & m_{23} & m_{24} \\ m_{31} & m_{32} & m_{33} & m_{34} \\ m_{41} & m_{42} & m_{43} & m_{44} \end{bmatrix} \begin{bmatrix} 1 \\ 0 \\ 1 \\ 0 \end{bmatrix} = \begin{bmatrix} m_{11} + m_{13} \\ m_{21} + m_{23} \\ m_{31} + m_{33} \\ m_{41} + m_{43} \end{bmatrix} \quad (\text{A.6})$$

for input \nwarrow :

$$S_{output} = \begin{bmatrix} m_{11} & m_{12} & m_{13} & m_{14} \\ m_{21} & m_{22} & m_{23} & m_{24} \\ m_{31} & m_{32} & m_{33} & m_{34} \\ m_{41} & m_{42} & m_{43} & m_{44} \end{bmatrix} \begin{bmatrix} 1 \\ 0 \\ -1 \\ 0 \end{bmatrix} = \begin{bmatrix} m_{11} - m_{13} \\ m_{21} - m_{23} \\ m_{31} - m_{33} \\ m_{41} - m_{43} \end{bmatrix}$$

$$\begin{aligned}
\text{for input } \odot: \quad \mathcal{S}_{output} &= \begin{bmatrix} m_{11} & m_{12} & m_{13} & m_{14} \\ m_{21} & m_{22} & m_{23} & m_{24} \\ m_{31} & m_{32} & m_{33} & m_{34} \\ m_{41} & m_{42} & m_{43} & m_{44} \end{bmatrix} \begin{bmatrix} 1 \\ 0 \\ 0 \\ 1 \end{bmatrix} = \begin{bmatrix} m_{11} + m_{14} \\ m_{21} + m_{24} \\ m_{31} + m_{34} \\ m_{41} + m_{44} \end{bmatrix} \\
\text{for input } \ominus: \quad \mathcal{S}_{output} &= \begin{bmatrix} m_{11} & m_{12} & m_{13} & m_{14} \\ m_{21} & m_{22} & m_{23} & m_{24} \\ m_{31} & m_{32} & m_{33} & m_{34} \\ m_{41} & m_{42} & m_{43} & m_{44} \end{bmatrix} \begin{bmatrix} 1 \\ 0 \\ 0 \\ -1 \end{bmatrix} = \begin{bmatrix} m_{11} - m_{14} \\ m_{21} - m_{24} \\ m_{31} - m_{34} \\ m_{41} - m_{44} \end{bmatrix}
\end{aligned} \tag{A.7}$$

By measuring the output light and using equation A.5, we can calculate the first and second columns. The third and fourth columns can be calculated from equations A.6 and A.7 respectively.

Bibliography

- [1] James Hough. Polarimetry: a powerful diagnostic tool in astronomy. *Astronomy & Geophysics*, 47(3):3–31, 2006.
 - [2] Dongmei Song, Zongjin Zhen, Bin Wang, Xiaofeng Li, Le Gao, Ning Wang, Tao Xie, and Ting Zhang. A novel marine oil spillage identification scheme based on convolution neural network feature extraction from fully polarimetric sar imagery. *IEEE Access*, 8:59801–59820, 2020.
 - [3] Motahareh Peyvasteh, Alexey Popov, Alexander Bykov, Angelo Pierangelo, Tatiana Novikova, and Igor Meglinski. Evolution of raw meat polarization-based properties by means of mueller matrix imaging. *Journal of Biophotonics*, 14(5):e202000376, 2021.
 - [4] Alexandra S Maia, Ana R Ribeiro, Paula ML Castro, and Maria Elizabeth Tiritan. Chiral analysis of pesticides and drugs of environmental concern: Biodegradation and enantiomeric fraction. *Symmetry*, 9(9):196, 2017.
 - [5] Nozomi Nishizawa, Bassam Al-Qadi, and Takahiro Kuchimaru. Angular optimization for cancer identification with circularly polarized light. *Journal of Biophotonics*, 14(3):e202000380, 2021.
 - [6] Douglas G Jones, Dennis H Goldstein, and Jonathan C Spaulding. Reflective and polarimetric characteristics of urban materials. In *Polarization: Measurement, Analysis, and Remote Sensing VII*, volume 6240, pages 85–94. SPIE, 2006.
 - [7] Neil Purdie and Kathy A Swallows. Analytical applications of polarimetry, optical rotatory dispersion, and circular dichroism. *Analytical chemistry*, 61(2):77A–89A, 1989.
 - [8] W H Brooks, W C Guida, and K G Daniel. The significance of chirality in drug design and development. *Current topics in medicinal chemistry*, 11(7):760–770, 2011.
-

- [9] Frances O Kelsey. Events after thalidomide. Journal of Dental Research, 46(6):1199–1205, 1967.
- [10] Xinzhong Zhang, Fengjian Luo, Zhengyun Lou, Meiling Lu, and Zongmao Chen. Simultaneous and enantioselective determination of cis-epoxiconazole and indoxacarb residues in various teas, tea infusion and soil samples by chiral high performance liquid chromatography coupled with tandem quadrupole-time-of-flight mass spectrometry. Journal of Chromatography A, 1359:212–223, 2014.
- [11] Jing Ye, Meirong Zhao, Lili Niu, and Weiping Liu. Enantioselective environmental toxicology of chiral pesticides. Chemical Research in Toxicology, 28(3):325–338, 2015.
- [12] Xu Jing, Guojun Yao, Donghui Liu, Chang Liu, Fang Wang, Peng Wang, and Zhiqiang Zhou. Exposure of frogs and tadpoles to chiral herbicide fenoxaprop-ethyl. Chemosphere, 186:832–838, 2017.
- [13] S Evans, J Bagnall, and Barbara Kasprzyk-Hordern. Enantiomeric profiling of a chemically diverse mixture of chiral pharmaceuticals in urban water. Environmental Pollution, 230:368–377, 2017.
- [14] Stewart E Miller. Integrated optics: An introduction. The Bell System Technical Journal, 48(7):2059–2069, 1969.
- [15] Enrique AJ Marcatili. Dielectric rectangular waveguide and directional coupler for integrated optics. Bell System Technical Journal, 48(7):2071–2102, 1969.
- [16] Chen Sun, Mark T Wade, Yunsup Lee, Jason S Orcutt, Luca Alloatti, Michael S Georgas, Andrew S Waterman, Jeffrey M Shainline, Rimantas R Avizienis, Sen Lin, et al. Single-chip microprocessor that communicates directly using light. Nature, 528(7583):534–538, 2015.
- [17] R Wolfe, VJ Fratello, and M McGlashan-Powell. Thin-film garnet materials with zero linear birefringence for magneto-optic waveguide devices. Journal of Applied Physics, 63(8):3099–3103, 1988.
- [18] Kin Seng Chiang and Wa Peng Wong. Design of zero-birefringence semiconductor waveguides. In Integrated Optic Devices II, volume 3278, pages 168–178. International Society for Optics and Photonics, 1998.
- [19] SM Ojha, C Cureton, T Bricheno, S Day, D Moule, AJ Bell, and J Taylor. Simple method of fabricating polarisation-insensitive and very low crosstalk awg grating devices. Electronics Letters, 34(1):78–79, 1998.

- [20] L Vivien, S Laval, B Dumont, S Lardenois, A Koster, and E Cassan. Polarization-independent single-mode rib waveguides on silicon-on-insulator for telecommunication wavelengths. Optics Communications, 210(1-2):43–49, 2002.
- [21] E Lidorikis, ML Povinelli, SG Johnson, and JD Joannopoulos. Polarization-independent linear waveguides in 3d photonic crystals. Physical review letters, 91(2):023902, 2003.
- [22] Seong Phun Chan, Ching Eng Png, Soon Thor Lim, Graham T Reed, and Vittorio MN Passaro. Single-mode and polarization-independent silicon-on-insulator waveguides with small cross section. Journal of lightwave technology, 23(6):2103, 2005.
- [23] Takeshi Fujisawa and Masanori Koshiba. Polarization-independent optical directional coupler based on slot waveguides. Optics letters, 31(1):56–58, 2006.
- [24] Soon Thor Lim, Ching Eng Png, Eng Ann Ong, and Yong Long Ang. Single mode, polarization-independent submicron silicon waveguides based on geometrical adjustments. Optics express, 15(18):11061–11072, 2007.
- [25] Tymon Barwicz, Michael R Watts, Miloš A Popović, Peter T Rakich, Luciano Socci, Franz X Kärtner, Erich P Ippen, and Henry I Smith. Polarization-transparent microphotonic devices in the strong confinement limit. Nature Photonics, 1(1):57–60, 2007.
- [26] Milan M Milosevic, Petar S Matavulj, Branislav D Timotijevic, Graham T Reed, and Goran Z Mashanovich. Design rules for single-mode and polarization-independent silicon-on-insulator rib waveguides using stress engineering. Journal of Lightwave Technology, 26(13):1840–1846, 2008.
- [27] Md Faruque Hossain, Hau Ping Chan, and Abbas Z Kouzani. Efficient design of polarization insensitive polymer optical waveguide devices considering stress-induced effects. Optics Express, 22(8):9334–9343, 2014.
- [28] W.N. Herman, Y. Kim, W. L. Cao, J. Goldhar, C. H. Lee, M. M. Green, V. Jain, and M.-J. Lee. Amorphous thin films of chiral binaphthyls for photonic waveguides. J. Macromol. Sci., Part A: Pure Appl. Chem., 40(12):1369–1382, 2003.
- [29] Shinzo Muto, Tomoyasu Sakagami, Yoshihiko Sakane, Akira Namazue, Eisuke Nihei, and Yasuhiro Koike. TE-TM mode converter using optically active polymer. Optical Review, 3(2):120–123, mar 1996.
- [30] S Guy, A Bensalah-Ledoux, A Lambert, Y Guillin, L Guy, and JC Mulatier. Chiral organic thin films: How far pulsed laser deposition can conserve chirality. Thin Solid Films, 520(20):6440–6445, 2012.

- [31] Stéphan Guy, Bruno Baguenard, Amina Bensalah-Ledoux, Dalila Hadiouche, and Laure Guy. Full polarization control of optical planar waveguides with chiral material. ACS Photonics, 4(11):2916–2922, 2017.
- [32] Bipin Bhola, Pavel Nosovitskiy, Hari Mahalingam, and William H Steier. Sol-gel-based integrated optical microring resonator humidity sensor. IEEE Sensors Journal, 9(7):740–747, 2009.
- [33] Markku Penttonen, Anita Kamondi, Attila Sik, László Acsády, and György Buzsáki. Feed-forward and feed-back activation of the dentate gyrus in vivo during dentate spikes and sharp wave bursts. Hippocampus, 7(4):437–450, 1997.
- [34] Peter Kozma, Florian Kehl, Eva Ehrentreich-Förster, Christoph Stamm, and Frank F Bier. Integrated planar optical waveguide interferometer biosensors: A comparative review. Biosensors and Bioelectronics, 58:287–307, 2014.
- [35] B. E. A. Saleh and M.C. Teich. Fundamentals of Photonics. John Wiley and Sons, 2007.
- [36] R. Clark Jones. A new calculus for the treatment of optical systems. description and discussion of the calculus. J. Opt. Soc. Am., 31(7):488–493, Jul 1941.
- [37] Justi Peatross and Michael Ware. Physics of Light and Optics, chapter 6, pages 143–168. optics.byu.edu, 2015.
- [38] George Gabriel Stokes. MATHEMATICAL and PHYSICAL PAPERS vol III. Cambridge, 1901.
- [39] Dennis H Goldstein. Polarized light. CRC press, 2017.
- [40] Henri Poincaré and Jules Blondin. Leçons sur la théorie mathématique de la lumière: professées pendant le premier semestre 1887-1888, volume 1. G. Carré, Paris, 1889.
- [41] Hayao Kubo and Ryo Nagata. Vector representation of behavior of polarized light in a weakly inhomogeneous medium with birefringence and dichroism. JOSA, 73(12):1719–1724, 1983.
- [42] Henry F Taylor and Amnon Yariv. Guided wave optics. Proceedings of the IEEE, 62(8):1044–1060, 1974.
- [43] Arman B Fallahkhair, Kai S Li, and Thomas E Murphy. Vector finite difference modesolver for anisotropic dielectric waveguides. Journal of lightwave technology, 26(11):1423–1431, 2008.

- [44] L Bolla. Empy [computer software].
- [45] Lord William Thomson Kelvin. Baltimore lectures on molecular dynamics and the wave theory of light. CUP Archive, 1904.
- [46] A. H. Sihvola, A. J. Viitanen, I. V. Lindell, and S. A. Tretyakov. Electromagnetic Waves in Chiral and Bi-Isotropic Media. Artech Print on Demand, Boston, May 1994.
- [47] Kikuo Cho. Dispersion relation in chiral media: Credibility of drude–born–fedorov equations. In Electromagnetic Metamaterials, pages 189–199. Springer, 2019.
- [48] Craig F Bohren. Light scattering by an optically active sphere. Chemical Physics Letters, 29(3):458–462, 1974.
- [49] SV Demidov, KV Kushnarev, and VV Shevchenko. On mode dispersion properties of chiral optical planar waveguides. JOURNAL OF RADIOELECTRONICS, 1999.
- [50] Warren N Herman. Polarization eccentricity of the transverse field for modes in chiral core planar waveguides. JOSA A, 18(11):2806–2818, 2001.
- [51] Nader Engheta and Philippe Pelet. Modes in chirowaveguides. Optics Letters, 14(11):593–595, 1989.
- [52] Amnon Yariv and James F. Lotspeich. Coupled-mode analysis of light propagation in optically active crystals. J. Opt. Soc. Am., JOSA, 72(2):273–277, Feb 1982.
- [53] M Chien, Y Kim, and Haim Grebel. Mode conversion in optically active and isotropic waveguides. Optics letters, 14(15):826–828, 1989.
- [54] P. Pelet and N. Engheta. Coupled-mode theory for chirowaveguides. J. Appl. Phys., 67(6):2742–5, 1990.
- [55] Amnon Yariv. Coupled-mode theory for guided-wave optics. IEEE Journal of Quantum Electronics, 9(9):919–933, 1973.
- [56] Wei-Ping Huang. Coupled-mode theory for optical waveguides: an overview. J. Opt. Soc. Am. A, 11(3):963–983, Mar 1994.
- [57] PK Tien, R Ulrich, and RJ Martin. Modes of propagating light waves in thin deposited semiconductor films. Applied Physics Letters, 14(9):291–294, 1969.
- [58] Laure Guy, Maëlle Mosser, Delphine Pitrat, Jean-Christophe Mulatier, Mercedes Kukułka, Monika Srebro-Hooper, Erwann Jeanneau, Amina Bensalah-Ledoux, Bruno Baguenard, and Stéphan Guy. Modulation of chiroptical properties in a series of helicene-like compounds. The Journal of Organic Chemistry, 84(17):10870–10876, 2019.

- [59] H Schmidt. Organically modified silicates by the sol-gel process. MRS Online Proceedings Library Archive, 32, 1984.
- [60] MA Hernandez-Perez, C Garapon, C Champeaux, and JC Orlianges. Structural and optical properties of phenylalanine and tyrosine thin films prepared by pulsed laser deposition. In Journal of Physics: Conference Series, volume 59, page 154. IOP Publishing, 2007.
- [61] L. Guy, T. Vautey, and S. Guy. The use of LCMS as an analytical tool for hydrolysis/polycondensation monitoring of a chiral ormosil precursor. J. Sol-Gel Sci. Technol., 52:146–152, 2009.
- [62] D. Hadiouche, C. Le Luyer, L. Guy, A. Bensalah-Ledoux, S. Saoudi, H. Khireddine, and S. Guy. Optimization of optical properties of high chiral planar waveguides obtained from a non-aqueous sol gel method. Optical Materials, 36(5):885–891, March 2014.
- [63] Stephan Guy, Laure Guy, Amina Bensalah-Ledoux, Antonio Pereira, Vincent Grenard, Olivier Cosso, and Teophile Vautey. Pure chiral organic thin films with high isotropic optical activity synthesized by uv pulsed laser deposition. Journal of Materials Chemistry, 19(38):7093–7097, 2009.
- [64] Amina Bensalah-Ledoux, Delphine Pitrat, Thibault Reynaldo, Monika Srebro-Hooper, Barry Moore, Jochen Autschbach, Jeanne Crassous, Stéphan Guy, and Laure Guy. Large-scale synthesis of helicene-like molecules for the design of enantiopure thin films with strong chiroptical activity. Chemistry—A European Journal, 22(10):3333–3346, 2016.
- [65] James A Greer. In-situ growth of $y_1ba_2cu_3o_{7-x}$ thin films on three-inch wafers using laser-ablation and an atomic oxygen source. In Superconductivity and Applications, pages 117–126. Springer, 1990.
- [66] CJ Brinker, GC Frye, AJ Hurd, and CS Ashley. Fundamentals of sol-gel dip coating. Thin solid films, 201(1):97–108, 1991.
- [67] Dong Qin, Younan Xia, and George M Whitesides. Soft lithography for micro-and nanoscale patterning. Nature protocols, 5(3):491, 2010.
- [68] F Vroegindewij, EA Speets, JAJ Steen, J Brugger, and David HA Blank. Exploring microstencils for sub-micron patterning using pulsed laser deposition. Applied Physics A, 79(4):743–745, 2004.
- [69] Wenxiu Que, X Hu, and J Zhou. Sol-gel fabrication of ge_2 /ormosils organic-inorganic hybrid material channel waveguides. Thin Solid Films, 484(1-2):278–282, 2005.

- [70] Kurt Tiefenthaler, V Briguet, E Buser, M Horisberger, and W Lukosz. Preparation of planar optical sio₂-tio₂ and linbo₃ waveguides with a dip coating method and an embossing technique for fabricating grating couplers and channel waveguides. In Society of Photo-Optical Instrumentation Engineers (SPIE) Conference Series, volume 401, pages 165–173, 1983.
- [71] Amir Fardad, Mark Andrews, Galina Milova, Ali Malek-Tabrizi, and Iraj Najafi. Fabrication of ridge waveguides: a new solgel route. Applied optics, 37(12):2429–2434, 1998.
- [72] Inc Kayaku Advanced Materials. SU-8 » Kayaku Advanced Materials, Inc.
- [73] Bruno Bêche. Integrated photonics devices on Su8 organic materials. Int. J. of Phys. Sc, 5:612–618, 2010.
- [74] Maria Nordström, Dan A. Zauner, Anja Boisen, and Jörg Hübner. Single-mode waveguides with SU-8 polymer core and cladding for MOEMS applications. Journal of Lightwave Technology, 25(5):1284–1289, 2007.
- [75] Neil J Shirtcliffe, Sanaa Aqil, Carl Evans, Glen McHale, Michael I Newton, Carole C Perry, and Paul Roach. The use of high aspect ratio photoresist (su-8) for superhydrophobic pattern prototyping. Journal of Micromechanics and Microengineering, 14(10):1384, 2004.
- [76] Mirwais Aktary, Martin O Jensen, Kenneth L Westra, Michael J Brett, and Mark R Freeman. High-resolution pattern generation using the epoxy novolak su-8 2000 resist by electron beam lithography. Journal of Vacuum Science & Technology B: Microelectronics and Nanometer Structures Processing, Measurement, and Phenomena, 21(4):L5–L7, 2003.
- [77] Inc. Kayaku Advanced Materials. SU-8 2000 Permanent Epoxy Negative Photoresist PROCESSING GUIDELINES. <https://kayakuam.com/products/su-8-2000/>.
- [78] Thomas Aarøe Anhøj. Fabrication of High Aspect Ratio SU-8 Structures for Integrated Spectrometers. PhD thesis, Technical University of Denmark, 2007.
- [79] AZ Electronic Materials. Az 5200-e photoresist data package.
- [80] S Somekh. Introduction to ion and plasma etching. Journal of Vacuum Science and Technology, 13(5):1003–1007, 1976.
- [81] Sami Franssila and Lauri Sainiemi. Reactive Ion Etching (RIE), pages 1772–1781. Springer US, Boston, MA, 2008.

- [82] James A Bondur. Dry process technology (reactive ion etching). Journal of Vacuum Science and Technology, 13(5):1023–1029, 1976.
- [83] Henri Jansen, Han Gardeniers, Meint de Boer, Miko Elwenspoek, and Jan Fluitman. A survey on the reactive ion etching of silicon in microtechnology. Journal of micromechanics and microengineering, 6(1):14, 1996.
- [84] Sergi Gomez, Rodolfo Jun Belen, Mark Kiehlbauch, and Eray S Aydil. Etching of high aspect ratio structures in si using sf₆/o₂ plasma. Journal of Vacuum Science & Technology A: Vacuum, Surfaces, and Films, 22(3):606–615, 2004.
- [85] Rudolf AH Heinecke. Control of relative etch rates of sio₂ and si in plasma etching. Solid State Electronics, 18(12):1146–1147, 1975.
- [86] Khaled Ali Alshaltami and Stephen Daniels. Investigation of etching optimization in capacitively coupled sf₆-o₂ plasma. AIP Advances, 9(3):035047, 2019.
- [87] Kazuo Nojiri. Mechanism of dry etching. In Dry Etching Technology for Semiconductors, pages 11–30. Springer, 2015.
- [88] Gaëtan Cussac. Conception de guides chiroptiques canaux: photonique à polarisation contrôlée. Master’s thesis, Universite de Lyon, France, 2018.
- [89] Hiromiutsu Kozuka. Stress evolution and cracking in sol-gel-derived thin films. Handbook of Sol-Gel Science and Technology, pages 275–311, 2018.
- [90] Yu P Yampolskii, MV Motyakin, AM Wasserman, T Masuda, M Teraguchi, VS Khotimskii, and Benny D Freeman. Study of high permeability polymers by means of the spin probe technique. Polymer, 40(7):1745–1752, 1999.
- [91] Younan Xia and George M Whitesides. Soft lithography. Annual review of materials science, 28(1):153–184, 1998.
- [92] Ashish Pandey, Sivan Tzadka, Dor Yehuda, and Mark Schwartzman. Soft thermal nanoimprint with a 10 nm feature size. Soft matter, 15(13):2897–2904, 2019.
- [93] Dennis H Goldstein. Polarized light, chapter 16, pages 327–348. CRC press, 2017.
- [94] ML Dakss, L Kuhn, PF Heidrich, and BA Scott. Grating coupler for efficient excitation of optical guided waves in thin films. Applied physics letters, 16(12):523–525, 1970.
- [95] T. Tamir, editor. Integrated Optics. Topics in Applied Physics. Springer-Verlag, Berlin Heidelberg, 1975.

- [96] Kin-Seng Chiang and Sinyip Cheng. Technique of applying the prism-coupler method for accurate measurement of the effective indices of channel waveguides. Optical Engineering, 47(3):034601, 2008.
- [97] J. E. Goell and R. D. Standley. B.s.t.j. briefs: Sputtered glass waveguide for integrated optical circuits. The Bell System Technical Journal, 48(10):3445–3448, 1969.
- [98] Martin W McCall, Ian J Hodgkinson, and Qihong Wu. Birefringent thin films and polarizing elements, chapter 16, pages 310–313. World Scientific, 2014.
- [99] D Clarke and JF Grainger. Polarized light and optical measurement, volume 1. Elsevier, 1971.
- [100] Rami Reddy Bommareddi. Applications of optical interferometer techniques for precision measurements of changes in temperature, growth and refractive index of materials. Technologies, 2(2):54–75, 2014.
- [101] Grant R Fowles. Introduction to modern optics, chapter 3, pages 57–59. 1989.
- [102] Hoshang Sahib, Alban Gassenq, Amina Bensalah-Ledoux, Bruno Baguenard, Laure Guy, and Stephan Guy. Elliptical birefringent rib-channel chirowaveguides for quasicircularly polarized light applications in integrated photonics. Advanced Photonics Research, page 2100302, 2022.
- [103] Kevin K Lee, Desmond R Lim, Hsin-Chiao Luan, Anuradha Agarwal, James Foresi, and Lionel C Kimerling. Effect of size and roughness on light transmission in a si/sio₂ waveguide: Experiments and model. Applied Physics Letters, 77(11):1617–1619, 2000.
- [104] Shashikant G Hegde and Suresh K Sitaraman. Stress-induced birefringence in siloxane polymer waveguides. Applied Physics Letters, 91(8):081114, 2007.
- [105] A. Kilian, J. Kirchhof, B. Kuhlow, G. Przyrembel, and W. Wischmann. Birefringence free planar optical waveguide made by flame hydrolysis deposition (fhd) through tailoring of the overladding. J. Lightwave Technol., 18(2):193, Feb 2000.
- [106] Marie Fontaine. Theoretical approach to investigating cross-phase modulation phenomena in waveguides with arbitrary cross sections. JOSA B, 14(6):1444–1452, 1997.
- [107] ASCO Deutschland GmbH. A comprehensive range of high performance optical detectors. <https://www.jasco.de/Chromatography/LC-4000-Series/Detectors>.
- [108] C Jeffrey Brinker and George W Scherer. Sol-gel science: the physics and chemistry of sol-gel processing. Academic press, 2013.

- [109] Lin Yang, S Scott Saavedra, and Neal R Armstrong. Sol-gel-based, planar waveguide sensor for gaseous iodine. Analytical chemistry, 68(11):1834–1841, 1996.
- [110] Atsunori Matsuda, Yoshihiro Matsuno, Masahiro Tatsumisago, and Tsutomu Minami. Changes in porosity and amounts of adsorbed water in sol-gel derived porous silica films with heat treatment. Journal of sol-gel science and technology, 20(2):129–134, 2001.
- [111] W Lukosz and Ch Stamm. Integrated optical interferometer as relative humidity sensor and differential refractometer. Sensors and Actuators A: Physical, 25(1-3):185–188, 1990.
- [112] Dominic J Wales, Richard M Parker, James C Gates, Martin C Grossel, and Peter GR Smith. An investigation into relative humidity measurement using an aluminosilicate sol-gel thin film as the active layer in an integrated optical bragg grating refractometer. Sensors and Actuators B: Chemical, 188:857–866, 2013.
- [113] K Tiefenthaler and W Lukosz. Integrated optical humidity and gas sensors. In 2nd Intl Conf on Optical Fiber Sensors: OFS'84, volume 514, pages 215–218. International Society for Optics and Photonics, 1984.
- [114] Ze Bing Zhong, Zhi Cheng Fu, Jian Dong Shi, Qi Long Tan, Wo Bin Huang, and Xu Guang Huang. Measurement of modal birefringence in optical waveguides based on the mach-zehnder interferometer. Review of Scientific Instruments, 85(5):053104, 2014.
- [115] Damien Jamon, François Royer, François Parsy, Elise Ghibaudo, and Jean-Emmanuel Broquin. Birefringence measurements in optical waveguides. Journal of lightwave technology, 31(19):3151–3157, 2013.
- [116] Feng Yu, Li-Cheng Wang, Yang Chen, Qi-Dai Chen, Zhen-Nan Tian, Xi-Feng Ren, and Hong-Bo Sun. Polarization independent quantum devices with ultra-low birefringence glass waveguides. Journal of Lightwave Technology, 39(5):1451–1457, 2021.
- [117] Lewis Greenspan. Humidity fixed points of binary saturated aqueous solutions. Journal of research of the National Bureau of Standards. Section A, Physics and chemistry, 81(1):89, 1977.
- [118] Sabriye Acikgoz, Bukem Bilen, Mustafa Muamer Demir, Yusuf Ziya Menciloglu, Yani Skarlatos, Gulen Aktas, and Mehmet Naci Inci. Use of polyethylene glycol coatings for optical fibre humidity sensing. Optical review, 15(2):84–90, 2008.
- [119] K Bange. Characterization techniques applied to sol-gel derived coatings and products. In Sol-Gel Technologies for Glass Producers and Users, pages 417–437. Springer, 2004.

- [120] Michel A Aegerter. Characterization of the mechanical properties. Handbook of sol-gel science and technology. 2. Characterization and properties of sol-gel materials and products, 2:297, 2005.
- [121] Mickael Boudot, Hervé Elettro, and David Grosso. Converting water adsorption and capillary condensation in usable forces with simple porous inorganic thin films. ACS nano, 10(11):10031–10040, 2016.
- [122] SY Cheng, KS Chiang, and HP Chan. Birefringence characteristics of benzocyclobutene rib optical waveguides. Electronics Letters, 40(6):372–374, 2004.
- [123] John C Pincenti, Sanjay Goel, and David L Naylor. Thermally induced birefringence and stress in poly (methyl methacrylate) waveguides on oxidized silicon substrates. Applied optics, 32(3):322–326, 1993.
- [124] S Cheng, K Chiang, and H Chan. Birefringence in benzocyclobutene strip optical waveguides. In OFC 2003 Optical Fiber Communications Conference, 2003., pages 320–321. IEEE, 2003.

